Durham E-Theses

Gas sensing using an organic/silicon hybrid field-effect transistor

Paul Simon Barker

How to cite:

Barker, Paul Simon (1996) Gas sensing using an organic/silicon hybrid field-effect transistor. Doctoral thesis, Durham University.

Use policy

GAS SENSING USING AN ORGANIC/SILICON HYBRID FIELD-EFFECT TRANSISTOR

by

Paul Simon Barker B.Sc.

Grey College

A Thesis submitted in partial fulfilment
of the requirements for the degree of Ph.D.

School of Engineering and Department of Physics

University of Durham

September 1996

DECLARATION

I hearby declare that the work carried out in this thesis has not been previously submitted for any degree and is not currently being submitted in candidature for any other degree.

Signed............

Candidate

The work in this thesis was carried out by the candidate.

Signed............

Signed............

Directors of Studies

Signed............

Candidate

DEDICATION

This thesis is dedicated to my parents

ACKNOWLEDGEMENTS

Both of the research groups I have been a part of have provided many excellent friends and drinking buddies: Geoff Williams, John Cresswell, Mary Kilitziraki, Jason Wilde, Agbor, Carla Di Bartolomeo, Catia, Leonid, Igor, Julian and Vaughan from Mike's research group. Steve Pomfret, James (Eggie) Eggleston, Paul (Tallus) Laughlin, Ed Holland, Phil Adams, Pete Devasagayam, Anne Brassett, Stuart Dailey from Andy's research group. Dr's Doug Halliday, Graham Cross, Ken Durose, Andy Brinkman and Andy Fisher, not forgetting Prof. David Bloor have all made Applied Physics a great department to be involved with.

Friends from other research groups and departments who I would like to mention are: Harry Ramsbottom, Hayley Ash, Chris 'Mackam' Leighton, Dave Healey, Sue Cutbill, Des Ryan, Mark Docton, Steve Robinson, Mike Young, Rob Farr, Glyn Norris, Dave Bell, Mike Betteridge, Rory Barr, Martin Bradley, James Gourlay, Graham Dean-Hart, Hugh Bradley, Adam Parker, Steve Westwood, Chris Friend, Chris Gregory, Andy Perella, Alton, Caroline, Tom, Maria, Marcus, Tony, Marick, Anna, Pete Davies, Phil Thomas, Andy Fearnside, Debbie Hales, Chris Caulfield, Rick, Dan and Josep.

ABSTRACT

This thesis describes the fabrication and properties of novel organic/silicon hybrid field-effect transistor gas sensors. Whilst most of the work used the emeraldine base form of the conductive polymer polyaniline, the response of a device incorporating a metal-free phthalocyanine is also reported. Arrays of p-type transistors in which the gate electrodes were replaced by 'charge-flow' capacitors were fabricated using standard semiconductor processing techniques. Each array consisted of four devices in which the width of metallisation removed from the gate electrode (total width 72 µm) varied from 0 µm (i.e. the control device) to 35 µm. Thin films of the gas-sensitive organic materials were deposited by spin-coating, and chemically patterned within the holes in the gate metallisation. A delay, referred to as the 'turn-on' response, was observed in the drain current on application of a gate voltage. This was shown to depend on the temperature, level of humidity and the presence of certain gases.

The electrical operating characteristics of the hybrid device with and without the polyaniline were examined. These included capacitance-voltage measurements, the 'turn-on' response at different temperatures and the variation of threshold voltage with temperature. From these results an understanding of the effect of integrating polyaniline within a p-channel transistor structure was obtained.

The 35 µm gate-hole sensor incorporating polyaniline was found to be sensitive to NO_x and SO_2 at room temperature at concentrations as low as 1 or 2 ppm. Decreasing the gate-hole area, and therefore the surface area of polyaniline, reduced the sensitivity of the device. The reactions were found to be reversible, although complete recovery required approximately eight hours. A similar sensor incorporating a metal-free phthalocyanine compound was reversibly sensitive to 2 ppm NO_x with a more rapid recovery of five hours. There was no observable response to SO_2 or H_2S up to 30 ppm.

CONTENTS

CHAPTER 8   RESPONSE TO SO$_2$ AND H$_2$S: RESULTS AND DISCUSSION   120

CHAPTER ONE

INTRODUCTION

Over the last forty years, the research effort dedicated to the development of reliable gas sensors has significantly increased. Initial interest stemmed from a need to measure the concentrations of environmentally damaging and potentially toxic gases generated from industrial processes (e.g. NO_x, SO_2, H_2S, CO_2 and CO). Lately, this monitoring has become much more important with the introduction of stringent environmental controls on the levels of toxic emissions permitted both within the European Community and countries world wide. Occupational exposure standards are recommended for many toxic gases. These suggest a safe level for daily exposure over a fixed time period. Table 1.1 presents some of this available data. Gas sensors are also being developed to monitor the freshness of food stuffs such as meat and canned vegetables. A further application is in the brewing industry to ensure both consistency and quality in the flavour of beers and whiskies.

Gas	8 Hour Exposure Limit (ppm)	10 Minute Exposure Limit (ppm)
NO_x	3	5
SO_2	2	5
H_2S	10	15

Table 1.1 Safe exposure limits in parts per million (ppm) for the toxic gases used in this work. (Source: BOC Gases Speciality Gases Catalogue.)

Problems encountered with many sensors include poor sensitivity to low gas concentrations, cross-sensitivities to other gases (i.e. poor selectivity) and an incomplete reversibility of the response. Fluctuations in the operating temperature and humidity level can also affect the reliability of a device. The sensitivity and selectivity can often be improved by chemically modifying or doping the active material used within the sensor. A new approach to overcome the problem of cross-sensitivity has been to use an array

of devices.[1] By coating each sensing element with a different material the response to a particular gas will vary over the array. Using such an array, together with pattern-recognition software or a neural network simulator, a system may be produced that can detect a specific gas component from a sample containing a range of gases.[2,3]

In this work, a novel gas sensor has been fabricated with the aim of eliminating or reducing the effect of some of the problems highlighted above. The device is an organic/silicon hybrid field-effect transistor (FET) in which a section of the gate electrode is replaced by a thin organic film.[4] This sensor was first reported by Senturia et al. using a highly resistive polymer as the active material deposited within the gate electrode.[4] The major advantage of incorporating the gas-sensitive material within the FET structure, instead of using a simple electrode pair structure, is the level of current measured. Because organic films used are typically highly resistive, the currents measured using the electrode pair device are in the nanoampere to picoampere range, requiring complex detection and good shielding to avoid problems with noise. With the hybrid device the levels of current are comparable to those in conventional transistors - in the microampere to milliampere range - greatly reducing problems with noise. Additional benefits include a substantial reduction in the device size, the use of well-established semiconductor processing techniques and the possibility of integrating detection circuitry with the sensor device.

This thesis reports a detailed study on the hybrid transistor. Chapter Two provides a summary of existing research in the field of chemical sensing. In the first part, the various materials that have been used for gas sensing are described. This is followed by a review of device structures and the electrical parameters measured in the sensing process.

Chapter Three introduces the two organic materials used: polyaniline and a substituted phthalocyanine compound. A discussion of the basic physical and chemical properties of both materials is presented, with a summary of the effects of exposure to certain gases, water vapour and temperature. Chapter Four details metal-oxide-semiconductor theory, including capacitance-voltage effects to explain the operation of a simple p-channel metal-oxide-semiconductor field-effect transistor (MOSFET). The chapter closes with a

description of the charge-flow capacitor and how it is incorporated into the gate electrode of a MOSFET to create the organic/silicon hybrid FET gas sensor.

Chapter Five contains a detailed description of the experimental techniques used to produce an array of the FET sensors. These include microelectronic fabrication methods such as photolithography and wet chemical etching. The deposition and chemical patterning of the organic materials is also described. Finally, the experimental procedures for the characterisation of the devices are explained.

Chapters Six, Seven and Eight present the results obtained, with a discussion of their implications. Chapter Six is concerned principally with the electrical characterisation of the device. This includes the d.c. operating characteristics and capacitance-voltage measurements. Results for the dependency of film thickness on spin speed and the possible effects of chemical patterning on the chemical properties are also shown. Chapter Seven is concerned with the response of the various devices from the array, incorporating both polyaniline and phthalocyanine thin films, to various concentrations of NO_x. The recovery of the devices after termination of the test gas, the range of working sensitivities and the effect of different operating conditions are all discussed. Chapter Eight examines the response of some devices to SO_2 and H_2S, including comparisons with similar devices exposed to NO_x. A brief investigation into the effects of exposure to SO_2 and NO_x on the capacitance-voltage characteristic of one of the devices is shown. Optical absorption spectra of polyaniline films deposited on glass substrates are presented after exposure to the three gases. Finally, Chapter Nine draws together conclusions from the whole thesis and includes suggestions for further work.

REFERENCES

1. P.S. Barker, J.R. Chen, N.E. Agbor, A.P. Monkman, P. Mars and M.C. Petty, *Sensors and Actuators B*, **17** (1994) 143-147.
2. D. Hodgins, *Sensors and Actuators B*, **27** (1995) 255-258.
3. D. Bednarczyk and S.P. DeWeerth, *Sensors and Actuators B*, **27** (1995) 271-274.
4. S.D. Senturia, C.M. Sechen and J.A. Wishneusky, *Appl. Phys. Lett.*, **30** (1977) 106-108.

CHAPTER TWO

GAS SENSING REVIEW: MATERIALS AND SENSORS

There are two distinct elements that comprise a gas sensor: (i) the gas sensitive material and (ii) the sensor structure within which it is incorporated. This chapter summarises the different materials that can be used and the structures to which they can be applied.

2.1 GAS SENSING MATERIALS

It is possible to divide the types of gas sensitive materials used in to two categories:

- **Inorganic-** i.e. Metal oxides and catalytic metals, and

- **Organic-** i.e. Organic crystals (e.g. phthalocyanines and porphyrins) and conductive polymers.

2.1.1 Inorganic Materials

The majority of early research concentrated, with much success, on the use of inorganic materials. Semiconductor oxides and transition elements were, and still are, commonly used.

a) Metal Oxides

It has long been known that the absorption of a gas onto the surface of a semiconducting material generates, or modifies existing surface states, and the electrical properties of these surfaces, such as conductivity, change as a result of adsorption and/or reaction. This effect has been observed in many metal oxides

including ZnO,[1] TiO$_2$[2], WO$_3$[3] and SnO$_2$[4-6] etc. For this reason these materials are considered to act as n-type semiconductors.

SnO$_2$ surface after exposure to

oxygen   atomic hydrogen

Depletion   Accumulation
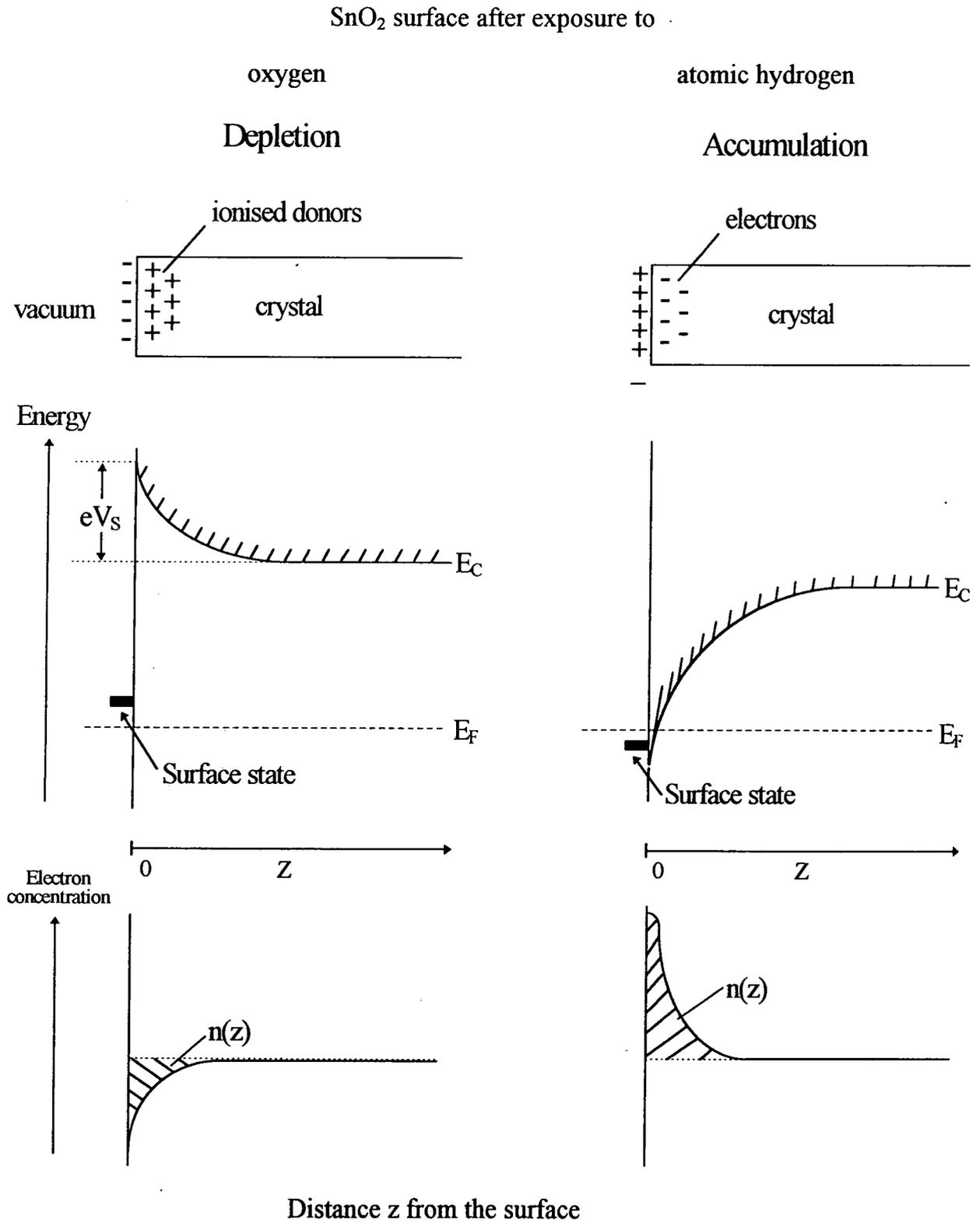
Figure 2.0 Space-charge modulation by adsorption in an *n*-type semiconducting oxide.

There are a finite density of electron donors (for absorbed hydrogen) or electron acceptors (for absorbed oxygen) bound to the surface of the oxide. They represent surface states which can exchange electrons with the interior of the semiconductor, thus forming a space-charge layer close to the surface (Figure 2.0). The position of the surface state relative to the Fermi level (E_F) depends on its affinity for electrons. For a low affinity it will lie below the Fermi level and donate electrons (reducing agent) to the space-charge region. If it is an acceptor, it will be positioned above the Fermi level and extract electrons (oxidising agent) from the space-charge region. By changing the surface concentration of the donors/acceptors the conductivity of the space-charge region is modulated.

The principles upon which tin, and other metal oxides act as gas sensitive materials can be summarised as follows. Initially, at elevated temperatures, there is a reversible reaction of atmospheric oxygen with lattice vacancies in the metal oxide leading to a reduction in the electron concentration to n_i. This reaction produces various oxygen species (denoted by the constant m) at different temperatures and oxygen pressures, i.e. O_2^-, O^-, O^{2-}, which can then react irreversibly with certain gaseous types (X). Typically these are reducing agents, gases that are oxidised by atmospheric oxygen, and those such as H_2, CO, hydrocarbons, and other organic gases and vapours. The following reaction scheme would apply

$$\frac{m}{2}O_2 + [\text{vacant site}] + e^- \xrightarrow{\ k_1\ } \left(O_m^-\right)_{\text{site}} \qquad [2.1]$$

$$X + \left(O_m^-\right)_{\text{site}} \xrightarrow{\ k_2\ } \left(XO_m\right)_{\text{site}} + e^- \qquad [2.2]$$
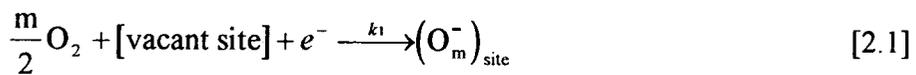
For example, the reaction between CH_4 and the lattice oxygen generates water vapour and CO_2 with an increase in the carrier concentration to n_f. Theory predicts an increase in the electrical conductivity $\Delta\sigma$ of the material which can be related to the change in the carrier concentration Δn (n_f-n_i) and, from simple reaction kinetics, to a fractional power λ of the gas concentration [X],

$$\Delta\sigma = \mu_n e \Delta n \ \propto [X]^{\lambda} \ ; \text{ where } 0.5 < \lambda < 1 \qquad [2.3]$$

In equation [2.3] e is the electron charge and μ_n is the electron mobility at the oxide surface. This modulation of carrier concentration can strongly affect the surface conduction in thin single-crystal films but it does not explain the similarly large effects observed in thick metal oxide layers. To account for this, it is necessary to extend the model of conduction and include a concentration-dependent mobility term. This arises from the fact that polycrystalline oxides have an open granular structure into which gas molecules can diffuse and react at the surfaces of discrete granules. The electron mobility μ_n is then governed by the potential barrier between neighbouring grains in a hopping model. The conductance G between grains now depends upon the height of the potential barrier ϕ_B, which in the simplest model is given by

$$G = G_0 \exp\left(-\frac{\phi_B}{kT}\right)$$
[2.4]

where G_0 is a weakly temperature-dependent constant, k is the Boltzmann constant and T the absolute temperature. The modulation of the barrier height $\Delta\phi_B$ on exposure to a gas can be related to the initial and final carrier concentrations by

$$\Delta\phi_B \approx \ln\left(1 + \frac{n_f}{n_i}\right)$$
[2.5]

where it is assumed that the bulk conductance is dominated by the gas-sensitive lattice sites. Finally, the carrier concentrations can be related by two reaction rates and the gas concentration, such that

$$\Delta G \propto \frac{k_2}{k_1}[X]^\lambda$$
[2.6]

where k_1 and k_2 are the reaction-rates in equations [2.1] and [2.2], respectively. Both the sensitivity and selectivity of the material are now determined by the reaction ratio (k_2/k_1).

To improve the selectivity and response time of metal oxide sensors, various approaches have been attempted including: pre-treatment of the material with certain gases (e.g. SO_2);[7] the use of molecular filters;[8] and by varying the film thickness.[9]

7

Selectivity to hydrocarbons (such as CH_4) can be enhanced by operating the sensor at high temperature; or to light gases (such as CO) by operating at low temperature. (This is thought to be because a light gas oxidises just before coming into contact with a hot metal oxide and so is not absorbed.)[10]

However, the most common technique to promote the specificity and rate of response is to add a low percentage of a catalytic metal, such as platinum, palladium, aluminium or gold, to the metal oxide film.[11,12] The promoting effects are related to the catalytic activities of the metals for the oxidation of the gases. In the case of SnO_2, there are two distinct mechanisms depending upon the metal type, i.e., electronic, for Ag and Pd promoters, and chemical for Pt promoters. For the chemical mechanism, the promoter activates a sample gas to assist in its catalytic oxidation on the surface of the semiconductor. The promoter has no direct effect on the conductivity of the metal oxide, but increases the sensitivity through the increase in the rate of the chemical process, leading to a decrease in the concentration of the negatively charged adsorbed oxygen (i.e. an increase in the reaction rate k_2 in equation [2.2]), with a concurrent increase in the carrier concentration.

The electronic mechanism for increased sensitivity involves a direct electronic interaction between the promoter and the metal oxide surface, leading to an increase in the work-function of the semiconductor. (For SiO_2 this corresponds to +0.7 eV for Ag and +0.3 eV for Pd.) The promoter then undergoes a change in its oxidation state by reaction with the surrounding atmosphere causing the electronic state of the semiconductor to change. Promoters of this type, such as Ag and Pd, are known to form stable oxides (Ag_2O and PdO) in air, but can easily be reduced to metals in the presence of certain gases. The work-function shifts observed indicate that the promoters in their oxidised forms produce a strongly electron-depleted space-charge layer within the semiconductor. When a reducing gas is introduced, the electronic interaction is disrupted as the promoter is reduced to the metal and the work function of the SiO_2 returns to its normal level.

Tin oxide sensors, doped with catalytic metals, have been commercially available since the early 1970s. A range of devices for the detection of combustible and toxic gases and organic vapours are manufactured by Figaro Engineering Inc. (Japan).

b) Catalytic Metals

Amongst the metallic elements that have been used for gas sensing are palladium, gold, platinum and nickel. In many instances, these have been utilised as gates on Metal-Oxide-Semiconductor Field-Effect Transistors (MOSFET). The first device of this type was a hydrogen sensor based on palladium which exhibited a threshold voltage shift ΔV_T that was dependent upon the concentration of hydrogen in an air mixture.[13]

The metal has three functions: it dissociates the incoming gas through its catalytic action; it transports hydrogen atoms to the metal-oxide interface; and it absorbs the hydrogen atoms at this interface as detectable dipoles. Hydrogen will diffuse very rapidly through the metal film since the hydrogen ion is a single proton. The dipole layer that is formed changes the difference of the electron work function between the metal and semiconductor and causes a shift of the threshold voltage of the MOSFET [§ 2.2.1 (a)].

The palladium based device is particularly sensitive to hydrogen, down to the parts per million (ppm) level,[14] as well as other hydrogen based compounds including H_2S and ammonia gas. It also demonstrates a certain degree of selectivity.[15] The use of other gate metals has led to reasonable specificity to other gases such as CO for nickel-gate devices[16] and CH_4 for platinum-gate MOSFETs.[17]

Gold is recognised for providing a highly efficient adsorption surface for mercury.[18] When adsorbed, there is a change in the surface electrical resistance of the film which can be used as the basis for a sensor. Generally, two thin gold films are connected in a Wheatstone bridge circuit. One of the films is made insensitive to mercury and acts as the reference arm. When mercury is adsorbed on the second film, the corresponding change in resistance unbalances the bridge circuit such that the measured voltage is proportional to the concentration of mercury. Gold films are also suitable sensing materials for halogens and hydrogen sulphide.[19]

Sensors based on inorganic materials suffer from a number of disadvantages. Amongst these is the requirement to operate at high temperatures (up to and greater than 400°C). This limits the portability of the device through the need to provide a quite substantial power source. A second problem is that of device drift, which can occur either when the device is stored in air, or may be induced by prolonged exposure to the test gas. This can only be overcome by frequent recalibration or by the use of a pulsed gas stream, both of which are inconvenient and costly. Further difficulties include a deactivation of the sensing material when stored in air or oxygen for long periods of time, without exposure to the gas it is required to detect. It is possible to overcome this by storing the sensor at high temperature in normal air conditions.

2.1.2 Organic Materials

More recently, organic compounds have been investigated as suitable materials for gas sensing. These materials have several advantages, including room temperature operation thereby reducing power consumption, a high sensitivity to many gases (parts per billion) but, perhaps most importantly, they are easy to modify chemically to enhance the sensitivity and selectivity. Finally, the processability of organic materials is often superior to that of inorganic oxides, allowing them to be deposited easily in thin film form.

The two main classes of organic materials used are organic molecular crystals and conductive polymer films.

a) Organic Molecular Crystals

(i) Phthalocyanines

Phthalocyanines form an important group of organic crystals. They are thermally stable up to approximately 450°C and essentially behave in the same manner as a metal oxide semiconductor (p-type). Figure 2.1 shows the structure of a typical phthalocyanine molecule.

The central ion, represented in the figure by an 'M', can be one of a number of metals, such as Pb^{2+}, Cu^{2+} or Mg^{2+}, or in the case of a metal-free phthalocyanine, atoms of hydrogen. The 'R' denotes a substituted organic side chain. By varying the metal ion and the side chain the response to a specific gas can be significantly improved.
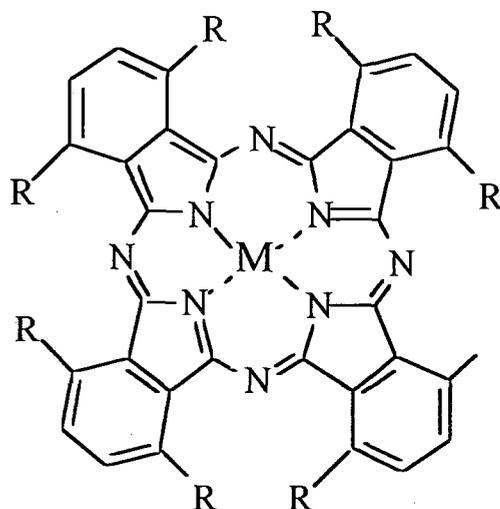
Figure 2.1 Structure of an octa-substituted phthalocyanine.

The conductivities of this family of materials are very sensitive to the presence of certain gases, particularly the oxides of nitrogen.[20,21] The conductivity can change by many orders of magnitude when a gas is adsorbed, making these compounds ideal for detecting very low gas concentrations (as low as one part per billion of NO_2).[22]

Thin phthalocyanine films can be prepared by vacuum sublimation[22] or spin-coating,[23] whilst ultra-thin films are deposited using the Langmuir-Blodgett technique.[24] The conductive properties of the material are initially affected at the surface. Then as gas molecules percolate through the film structure, the bulk conductivity is also seen to change.

Although phthalocyanine compounds operate well at room temperature, the recovery time is slow due to the presence of strongly absorbing sites. Raising the temperature to between 100 and 170°C greatly improves the rate of recovery,[22] as well as removing the effects of surface moisture. However, this does begin to limit the portability of a commercial device.

A more detailed discussion of the chemical and physical properties of phthalocyanines will be presented in Chapter Three.

(ii) Porphyrins

Porphyrin compounds are related to phthalocyanines. These comprise a hydrocarbon ring structure with a central metal ion and substituted organic groups around the periphery. Once again, the adsorption of certain electron-accepting gases (i.e. NO_2) causes a significant change in their electrical conductivities. Studies undertaken on these compounds have shown their interactions with gaseous molecules to be largely dependent on the electronegativity of the central metal ion.[25] It has also been demonstrated that the utilisation of porphyrins as gas sensing materials is dependent on factors such as the film thickness and also with the peripheral substituents on the porphyrin ring.[26]

Most reports have been based on the sensing of NO_2 utilising conductivity changes.[25-27] Response times have been shown to vary with film thickness and concentration of gas. For 39 layers of a symmetrically substituted cobalt porphyrin Langmuir-Blodgett film exposed to 5 ppm NO_2, the response and recovery times were 10 minutes and 1 hour, respectively.[27] The recovery time was found to decrease when the device was placed in a vacuum. In other work, the change in the measured fluorescence intensity of thin films of porphyrins has been used successfully as an NO_x sensor.[28]

b) Conductive Polymers

Conductive polymers are a relatively new class of organic material and have attracted considerable interest for their possible applications in gas sensing since their discovery in the early 1980s. They are readily processable in the form of thin films and, like phthalocyanines, offer near unlimited potential to chemically modify or dope the polymer to optimise the selectivity and sensitivity.

Conductive polymers are readily grown by electrochemical polymerisation of the monomer, examples of which are shown in Figure 2.2, under controlled conditions.[29]

Pyrolle   Thiophene   Indole   Furan
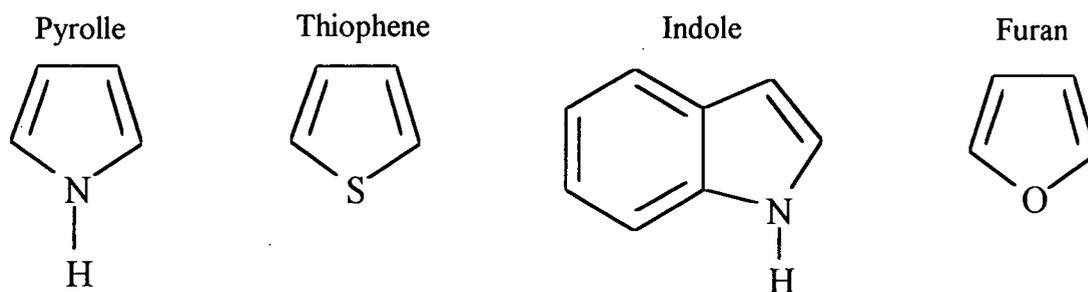
Figure 2.2 Chemical structures of some common monomers.

Polypyrrole has been extensively investigated for its gas sensing properties, in its pure form,[30] as a composite (polypyrrole-polyamide films),[31] and after chemical doping with ionic species (such as BF_4^-).[32] Polypyrrole is known to be a p-type semiconductor which, when exposed to electrophilic gases such as NO_2, showing an increase in conductivity. The opposite effect is observed when nucleophilic gases, such as NH_3, are adsorbed.[31]

The conduction mechanism is explained by a charge hopping process [§ 3.1.4], which can be enhanced by introducing a suitable doping anion, such as a sodium salt i.e. $NaClO_4$, during synthesis. The conductance and long-term air stability of materials such as $NaClO_4$-doped polypyrrole in thin film sensor form are sufficient, at ambient temperature, to reliably detect methanol as low as 10 ppm in concentration.[33]

Several other conductive polymers have been successfully used as sensing materials including, poly-5-carboxyindole for the detection of organic vapours,[34] polythiophenes used for NO_2 sensing,[35] polyimide for the detection of hydrogen,[36] and polyaniline for sensing gases including hydrogen cyanide,[37] ammonia[38] and organic vapours.[34,39]

Whilst the most common procedure for depositing these polymers is by electrochemical growth across an electrode structure, deposition by the Langmuir-Blodgett technique[35] or by thermal evaporation[36] is possible. Polyaniline is special in

that it can also be spin-coated from a solution of N-methylpyrrolidinone (NMP) to form thin uniform films.[40] (§2.2 introduces thin film deposition techniques). Polyaniline has been used in this work and will be discussed in greater detail in Chapter Three.

Neotronics Ltd. have developed a system using 12 polypyrrole sensors, doped so that the response of each to a certain gas is different. The system is being used by the brewing industry to monitor quality during the brewing process.

2.1.3 Adsorption of Gases

A material's suitability for sensing is very much dependent upon the rates of adsorption and desorption of the gases to which they are exposed. The free gas and the absorbed gas are in equilibrium, and the fractional coverage of the surface θ (defined below) depends on the pressure of the overlying gas.

$$\theta = \frac{\text{Number of adsorption sites occupied}}{\text{Number of adsorption sites available}} \quad [2.7]$$

The variation of θ with pressure at a fixed temperature is known as the adsorption isotherm. The simplest of these is the Langmuir isotherm which is based upon three assumptions:

1. Adsorption cannot occur beyond monolayer coverage.

2. All sites are equivalent and the surface is perfectly flat on a microscopic scale.

3. The ability of a molecule to adsorb at a given site is independent of the occupation of neighbouring sites.

Within a closed system the following dynamic equilibrium is achieved

$$A_{gas} + M_{surface} \Leftrightarrow AM_{surface}$$

with rate constants k_a for adsorption and k_d for desorption. The rate of change of surface coverage due to adsorption is proportional to the partial pressure p of A (the gas) and the number of vacant sites $N(1-\theta)$, where N is the total number of sites:

$$\frac{d\theta}{dt} = k_a p N (1 - \theta)$$
[2.8]

The rate of change of θ due to desorption is proportional to the number of adsorbed species, $N\theta$:

$$\frac{d\theta}{dt} = -k_d N \theta$$
[2.9]

At equilibrium the n et rate of adsorption is zero, and solving for θ gives the Langmuir isotherm:

$$\theta = \frac{Kp}{1 + Kp} \qquad \text{where } K = \frac{k_a}{k_d}$$
[2.10]

2.2 THIN FILM DEPOSITION TECHNIQUES

There are many ways of depositing thin films on devices. Three of the most established methods are: Langmuir-Blodgett deposition; thermal evaporation; and spin-coating. A brief, qualitative description of each method is given below.

2.2.1 Langmuir-Blodgett Deposition

Langmuir-Blodgett (LB) films are ultra-thin, highly ordered monolayers or multilayers of organic compounds deposited on a solid substrate. The technique is limited to materials that consist of amphiphilic long chain molecules with a hydrophobic molecule at one end and a hydrophilic molecule at the opposite end.

Using a specially constructed Langmuir-Blodgett trough, a small quantity of a material dissolved in a suitable solvent is deposited onto an ultra-pure water surface. As the

solvent evaporates, the material spreads out to form a monomolecular layer. By slowly compressing the film, the molecules undergo a transition to an ordered solidlike arrangement: in effect a two-dimensional analogue of a solid is created. The LB film is transferred onto the substrate by controlled dipping through the air-water interface at a constant speed and surface tension. In this way, films can be built-up with controlled symmetry, thickness and molecular orientation. The technique has been used to deposit both polythiophene[35] and phthalocyanine[20] films which have been shown to be sensitive to NO_2.

2.2.2 Thermal Evaporation

The deposition of thin films by thermal evaporation is performed at reduced pressure, typically 10^{-4} mbar or lower. This is a non-equilibrium process, involving several steps: evaporation; transfer of material to the substrate; condensation; nucleation and film growth.

The conversion of the solid to the vapour phase may take place at temperatures below the metal point through sublimation. In the vapour phase, the molecules travel at high velocities making frequent collisions with others in the system. The statistical average distance a molecule will travel before colliding with another is called the mean-free path, λ, and is defined as

$$\lambda = \frac{kT}{\sqrt{2}\pi\sigma^2 p}$$
[2.11]

where σ is the diameter of the molecule. From equation [2.11] it is evident that the mean-free path λ increases as the pressure p of the system is reduced.

As more material is evaporated, the vapour pressure of the evaporant above the source increases. When this pressure becomes greater than the equilibrium vapour pressure of the evaporant at the temperature of the substrate, condensation occurs. These molecules coalesce to form stable nucleation sites and act as centres for growth of the film. The monolayer then develops into a film covering the entire substrate. A

continuous film may not be formed until the film is many monolayers thick. This contrasts with LB film deposition in which complete coverage of the substrate can be achieved by a single monolayer. Sensors using evaporated films of a porphyrin compound have been shown to successfully detect 9.4 ppm NO_x.[28]

2.2.3 Spin-Coating

Perhaps the simplest and quickest means of depositing thin films is by spin-coating. The material to de deposited must first be dissolved in a suitable solvent, and then filtered to remove any particulate contamination. This is vital for producing good quality smooth films. The cleaned substrate is held in place on the rotating platform by a vacuum. The spinning process comprises three stages: the deposition and spreading of the material; generation of the thin film; and complete evaporation of the solvent. The speed and duration of the second stage is critical in determining the thickness of the resulting film. Materials deposited in this manner do not require to be amphiphilic, as for Langmuir-Blodgett films. Moreover, for organic materials, there are reduced possibilities of material decomposition than for thermal evaporation. This technique has been used in this work to deposit thin films of polyaniline and a phthalocyanine compound.

2.3 GAS SENSING DEVICES

There are four main methods for monitoring gas/material interactions. These can be broadly classified as electrochemical, optical, thermal and mass sensing techniques. The principles involved in each method will be outlined below with relevant examples.

2.3.1 Electrochemical Sensors for Gas Sensing

There are three types of electrochemical sensor that can be categorised by the physical parameter being measured. These are as follows,

- **Potentiometric**: The measurement of voltage,

- **Amperometric**: The measurement of current,

- **Conductimetric**: The measurement of conductivity.

a) Potentiometric Gas Sensors

In **potentiometric** gas sensors the potential change is obtained from the interaction of electrically neutral gas molecules with the sensor. To produce a potential difference requires charge separation. Therefore this type of sensor requires a mechanism linking the interaction of the gas molecules to generate ions or electrons at an interface within the sensor.

Within any electrochemical sensor there is a transfer of charge from an electrode to another phase, which can be either a solid or a liquid sample. During this process chemical changes occur at the electrodes, allowing the charge to be conducted through the sample phase (e.g. for an SO_2 sensor this will be an electrolyte of 0.01 M solution of $NaHSO_3$).[19]

The following describes a potentiometric gas sensor using a Severinghaus electrode, which can be used to detect many different gases by utilising different combinations of electrodes and electrolytes. The sensor, shown above in Figure 2.3, consists of two electrodes: an ion-selective electrode (Severinghaus electrode) to monitor the increase of a specific ionic species; and a reference electrode to form a closed electrical circuit. If we consider a carbon dioxide sensor, the dissolution of the gas into the electrolyte (in this case water) proceeds according to the equation

$$CO_2 + H_2O \Leftrightarrow HCO_3^- + H^+ .$$
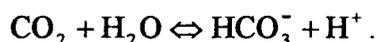
Using a hydrogen ion-selective electrode, i.e., a pH meter, the effect due to the H^+ ion can be measured. The reaction has a typical time constant of 10-20 seconds.[19] The sensitivity of this device can be increased by introducing a high concentration of bicarbonate (such as 0.1 M $NaHCO_3$) into the electrolyte so that the increase of

bicarbonate ions due to the dissolved CO_2 becomes negligible compared to the total concentration.
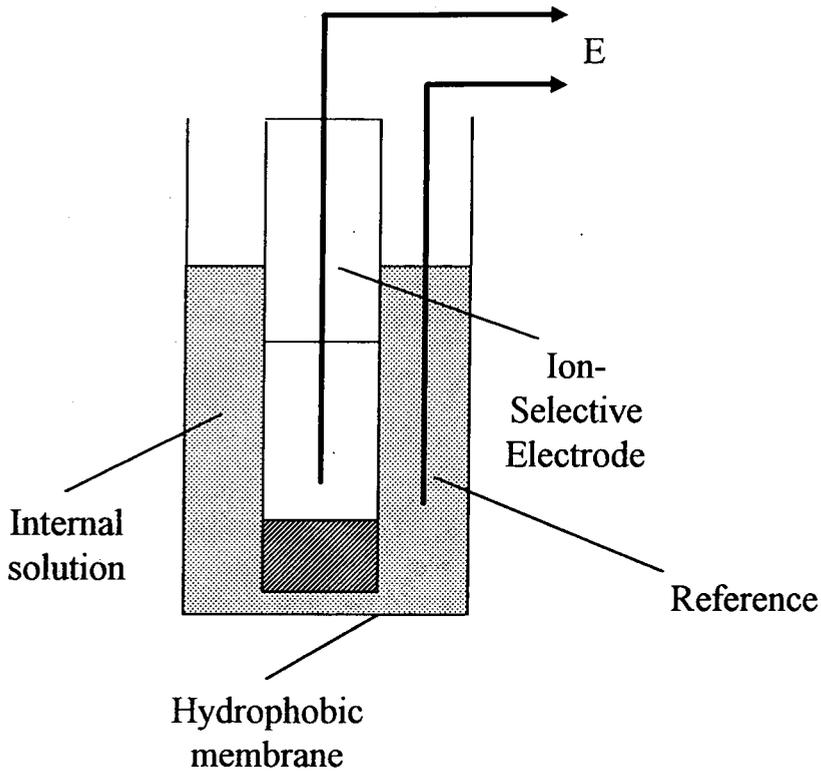
Figure 2.3 Schematic diagram of a Severinghaus electrode.

Table 1 summarises the ion-sensitive electrodes and electrolytes required to detect other gaseous species.

Species Detected	Sensor Electrode	Electrolyte
CO_2	H^+	0.01 M $NaHCO_3$
NH_3	H^+	0.01 M NH_4Cl
SO_2	H^+	0.01 M $NaHSO_3$
H_2S	S^{2-}	Citrate buffer (pH 5)
NO_2	H^+	0.02 M $NaNO_2$

Table 1. Specifications of some gas sensing electrodes [Ref. 19]

The use of a change in the work function of a material has long been established as a method for the detection of gases [§ 2.1.1 (b)]. A simple structure that exploits this effect is an inorganic Schottky diode. It comprises of a metallic electrode (e.g. palladium or platinum) and a semiconductor counter electrode (e.g. titanium oxide or cadmium sulfide). Figure 2.4 shows the electronic band structure for a metal-semiconductor diode. The barrier height ψ is the difference between the metal work function ϕ_M and the semiconductor electron affinity χ_S.
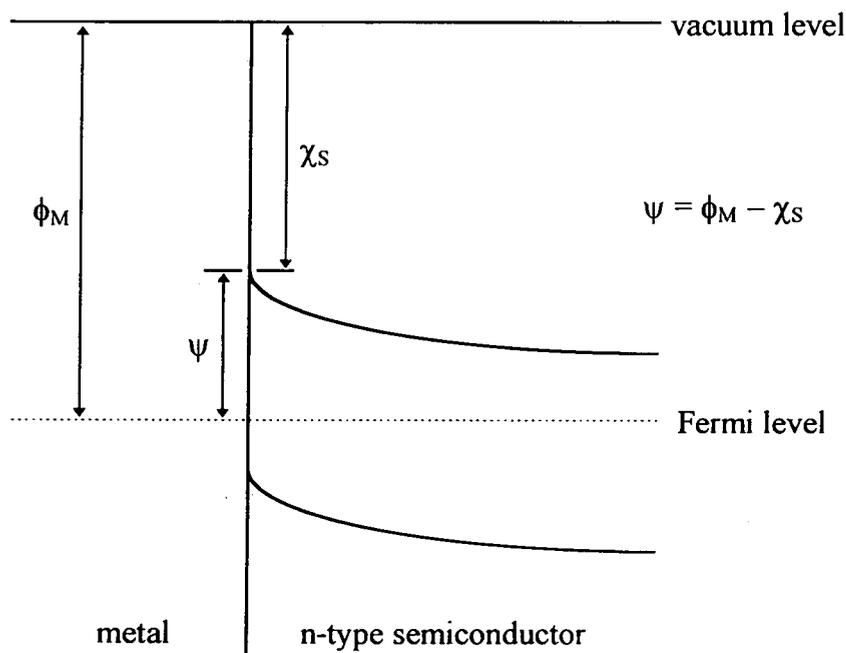
Figure 2.4 Band diagram of a metal-semiconductor diode. [Adapted from D.K. Schroder *Semiconductor Material and Device Characterization* (Wiley 1990) p 100]

Such a device for the detection of hydrogen is a palladium/cadmium sulfide Schottky diode.[41] Upon exposure to hydrogen the work function of the palladium is lowered, thus lowering the height of the junction barrier. This is reflected in the current-voltage characteristics of the diode. Unfortunately, the inorganic Schottky diode has both poor specificity and stability and requires an operating temperature of up to 150°C to increase the response time of the device to a practical level.

The alternative is to create an organic Schottky diode.[36] For example, a low work function metal (e.g. aluminium) forms a rectifying contact with a *p*-type polymeric semiconductor (e.g. polypyrrole), whilst gold provides the ohmic contact. Figure 2.5

shows the structure of an aluminium/poly(3-octylthiophene) device used for the detection of NO_x and ammonia.[42]
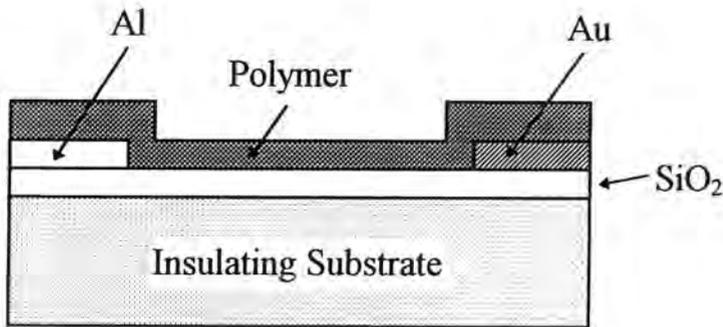
Figure 2.5 The cross-sectional structure of an organic Schottky diode [Ref. 42].

The diode I-V characteristics have been shown to be sensitive to 100 ppm NH_3 and 50 ppm NO_x at room temperature. Exposure to NH_3 decreases the forward-bias current in the Schottky diode, whilst NO_x enhances both the forward and reverse-bias currents.[42] This degree of selectivity demonstrates that the organic diode is a more practical device than the inorganic variant.

It is also possible to incorporate the gas sensitive material into a MOS capacitor structure.[43] (A more detailed explanation of MOS theory will be presented in Chapter Four.) Figure 2.6 shows the structure of a sensor using palladium as the top plate of the capacitor device. Absorption of hydrogen through the palladium electrode induces a dipole layer at the palladium-SiO_2 interface, changing the effective work function of the metal. This can be measured as a shift, ΔV_{FB}, in the flat-band voltage proportional to the concentration of hydrogen.
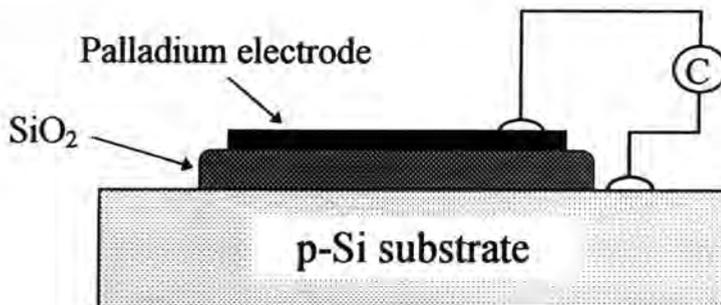
Figure 2.6 Cross-sectional structure of an MOS capacitor sensor.

Gases such as CO, CH_4 and C_4H_{10} can also be detected with this device by varying the gate metals (e.g. platinum or nickel) and using a different dielectric (e.g. Si_3N_4).[16]

Once again, a similar organic device can be fabricated by replacing the oxide layer with a conductive polymer and depositing a permeable gold electrode as the top plate of the capacitor. The advantages offered by this device are equivalent to those for the organic Schottky diode: room temperature operation and an enhanced selectivity.

A progression of the MOS capacitor structure is that of the MOSFET, where the reactive material, e.g. palladium, is used as the gate electrode of the device (Fig 2.7).
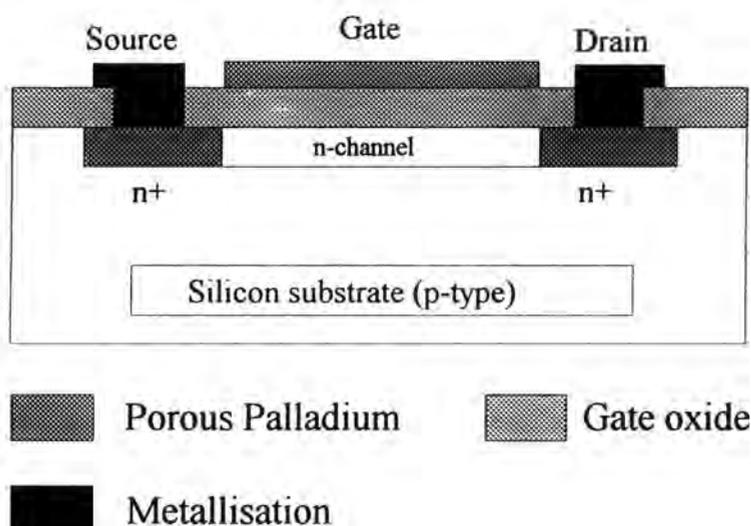
Figure 2.7 Structure of a palladium gate gas-sensitive MOSFET.
[Adapted from Ref. 43.]

These sensors, also referred to as Insulated-Gate Field-Effect Transistors (IGFETs) were first used to detect 40 ppm hydrogen when operated at a temperature of 150°C.[13] For this device, the threshold voltage V_T (i.e. the applied gate bias at which the transistor drain current begins to flow) is modulated by the variation of the metal-semiconductor work-function, which is proportional to the concentration of adsorbed hydrogen.

The factors affecting the response rate and selectivity of these devices include the choice of catalytic metal gate,[44] the method of the metal film deposition,[45] and the operating temperature.[46]

22

A limitation of the palladium IGFET is that only hydrogen and hydrogen-producing species can be detected. A Suspended-Gate Field-Effect Transistor (SGFET) offers the potential for any chemical species to interact with the electric field within the gate. The fundamental physical difference between the IGFET and SGFET is that there is an additional insulator present within the gate structure of the SGFET- an air gap between the metal and the insulator. The gap may be a vacuum, a gas or a non-conducting liquid depending on the gaseous species requiring detection. SGFET devices, coated with chemically modified polypyrroles, have been successfully used to detect aromatic compounds, including toluene, when operated at room temperature.[47]

The Open Gate Field-Effect Transistor (OGFET) sensor simply omits the gate metal from the MOSFET. Upon exposure to both polar and non-polar gases, a strong variation in the drain current is observed.[48] It is understood that a poorer quality of oxide layer is a contributing factor to the sensor's success. This allows the gases to be easily adsorbed creating charged particles which, under the influence of the electric field, increase the drain current.

A development of the OGFET is the Adsorption Field-Effect Transistor (ADFET) where the oxide thickness is limited to a maximum of 5 nm. The device responds to gases with a permanent net dipole, such as CO, NH_3, NO_2, and SO_2. This selectivity is explained by the fact that the drain current is determined by the fringing field of the adsorbed molecules.[48] A serious problem occurring with both the OGFET and ADFET sensor's is the open-gate construction, which makes the devices very sensitive to all kinds of electrical interference. This problem can be overcome by replacing the gate electrode, but creating a partial air gap by underetching the polysilicon gate. In this way the gas still has direct access to the silicon surface, but the gate now provides the necessary electrostatic shielding. This modified device is a Surface Accessible Field-Effect Transistor (SAFET) and has been shown to be sensitive to organic vapours, including methanol, ethanol and acetone.[49]

b) Amperometric Gas Sensors

An **amperometric** gas sensor uses the variation in current to evaluate the concentration or type of gas. The first device of this type was the Clark cell oxygen sensor, developed to determine oxygen levels in blood.

Another type of amperometric sensor is similar in construction and operation to the Severinghaus potentiometric gas sensor. An example of its kind is a fast-response oxygen sensor consisting of platinum working and counter electrodes, together with a silver reference electrode. The electrolyte is a layer of H^+-form Nafion gel coated evenly onto the electrode surface. This device differs from the standard amperometric sensors of this type in that "triple-points" exist where the electrode, electrolyte and gas phase meet. This eliminates the need for the gas to diffuse through a gas-permeable membrane, greatly reducing the response time. Oxygen is detected amperometrically by the reduction reaction

$$O_2 + 2H_2O + 4e^- \rightarrow 4OH^-$$
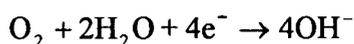
This reaction results in a steady-state oxygen reduction current, linearly proportional to the gas concentration, with a 90% response time of 300 ms, and a slightly longer recovery time of 400 ms.[50]

c) Conductimetric Gas Sensors

The chemiresistor is one of the simplest types of chemical sensor available, and is a classic example of a **conductimetric** gas sensor. A simple chemiresistor, illustrated in Figure 2.8, comprises of two electrodes deposited upon an inert substrate. The electrodes are usually made of gold or aluminium with dimensions of the order of microns. The chemically-sensitive thin film is deposited over the electrode structure. A variety of materials have been exploited including metal oxides,[11] organic crystals[24] and conductive polymers.[34]
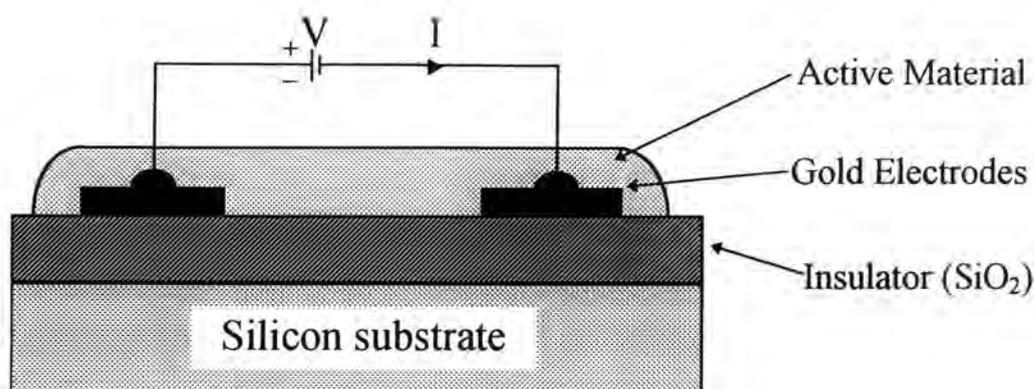
Figure 2.8 General structure of a chemiresistor gas sensor.

When a voltage is applied to the electrodes, the conduction electrons or holes travel through the thin film between the two electrodes. On exposure to an electroactive gas, a reduction or oxidation reaction takes place, changing the electrical conductivity of the active material. For example, a tin-oxide sensor exposed to 10 ppm of NO_2 can experience a fall in conductance of three orders of magnitude.[11] Such changes may be due to surface and/or bulk reactions and are required to be reversible for a practical sensor. Factors affecting the response of these devices include the quality and thickness of the sensitive material as well as the geometry of the electrode structure.

The charge-flow transistor (CFT) is another example of a modified MOSFET sensor.[51] The active material, typically a conductive polymer, is incorporated into the gate metal, which leads to a time delay between applying a bias to the gate electrode and the formation of a conducting channel between the source and the drain. The time delay depends predominantly on the conductivity of the film, which is modulated by the concentration of gas and/or humidity level. This sensor is the type used in this work and its operation will be discussed in greater detail in Chapter Four.

2.3.2 Optical Gas Sensors

Optical fibres and waveguides are able to transmit light over long distances with a minimal loss of intensity. This has allowed the development of remote sensors, with the data being propagated as a light pulse, in areas where the use of electric powered sensors would be hazardous. The sensors can be based on evanescent waves,

fluorescence measurements, infrared or ultraviolet-visible absorption and surface plasmon resonance.

Evanescent wave sensors comprise of an optical waveguide, say a fibre optic cable, over a section of which is coated the chemically sensitive material. Light transmitted through a waveguide generates an evanescent wave at the surface of the waveguide. Gas reacting with the sensitive medium leads to an attenuation of the evanescent component of the light, which can be detected using a phototransistor. A successful ammonia sensor has been developed based on this optical phenomenon.[52]

Fluorescence based sensors have been developed for the simultaneous detection of oxygen and carbon dioxide.[53] The tip of a fibre optic cable is coated with both oxygen and carbon dioxide-sensitive materials, entrapped in a polymer matrix. The two gases can be detected, and differentiated, by the two distinct emission bands generated by the excitation of the fluorescent indicators. This fibre optic device is a convenient sensor for the internal medical monitoring of these gases.

Infra-red absorption sensors operate on the principle that any compound with a covalent bond or net dipole moment will interact with infrared radiation at a characteristic frequency. When a gas reacts with a chemically sensitive layer the characteristic spectrum of the layer will change, with the formation of new and/or the suppression of old absorption bands. The sensitivity of this system is high and the selectivity can be enhanced by using narrow band optical filters or by restricting the wavelength region scanned. Both H_2S and NO_2 demonstrate characteristic changes in the infrared absorption spectra of powdered polythiophene pellets.[54]

Surface plasmon resonance (SPR) has been used to successfully detect NO_x at room temperature.[55] When a thin film of metal is irradiated with a coherent light source at a specific angle of incidence, oscillating charges are induced at its surface. These are called non-radiative surface plasmons. The effect is observed as a minimum on a plot of the intensity of the reflected light as a function of the angle of incidence. By coating the metal layer with a gas-sensitive film an optical gas sensor can be fabricated. Exposure to a gas results in a change in the refractive index of the overlayer, and hence, a shift in the point of resonance.

2.3.3 Thermal Gas Sensors

Thermal chemical sensors detect heat that is released or absorbed, ΔE_h, during a chemical reaction between the gas and the selective layer. This change in enthalpy causes a change in the temperature ΔT which can be monitored. For a thermally insulated system, the change in temperature is given by

$$\Delta T = \frac{-\Delta E_h}{C_p} \qquad\qquad [2.12]$$

where C_p is the heat capacity of the system at constant pressure. The two common types of thermal gas sensors are pyroelectric devices and catalytic gas sensors (also referred to as pellistors).

The **pyroelectric** effect is the property of certain crystalline, ceramic and polymeric materials to undergo a change in surface charge due to a variation in temperature between the two surfaces of the material. A gas sensor can be fabricated by evaporating two gold electrodes onto the measurement surface of a wafer of $LiTaO_3$ (a pyroelectric material). Over one of these electrodes is coated the chemically sensitive material, allowing the second electrode to be used as a reference. A heater element is attached to the reverse side of the $LiTaO_3$, allowing complete control of the temperature on one side of the pyroelectric material. The heat loss (or gain) associated with the reaction of the gas with the chemically sensitive material can be assessed by measuring the change in the electrical response. With charcoal as the chemically sensitive material, a sensor for monitoring residual gases (including oxygen) generated from an oil-pumped vacuum system has been demonstrated.[56]

Conventional catalytic gas sensors (**pellistors**) operate by the catalytic oxidation of combustible gases. The sensor consists of a platinum wire coil in an aluminium oxide bead covered with a porous thick film catalyst, such as platinum or palladium. The coil acts as both a heater and as a resistance thermometer. Catalytic combustion of the gas occurs when the catalyst material is heated to approximately 500°C. The increase in temperature due to the oxidation of the gas is then measured in terms of the resistance variation relative to a reference resistance. Typically, the pellistor is connected in one

arm of a Wheatstone bridge arrangement and the out-of-balance voltage measured across the circuit is a measure of the concentration of the gas.

The device can detect a wide range of combustible gases including methane, hydrogen and butane, but with a low specificity. Another problem is the quite large power consumption (~1 W) of the sensor, which can limit its portability. To overcome this difficulty pellistors have been developed utilising silicon technology to greatly reduce the size and, therefore, the overall power consumption to ~100 mW.[57]

2.3.4 Mass Gas Sensors

The most common gas sensors utilising the change in mass that occurs during a chemical reaction are piezoelectric and surface acoustic wave (SAW) devices. The change in mass Δm is generally converted to a shift in frequency Δf by an oscillator circuit. The basic equation that relates them is known as the Sauerbrey equation,

$$\Delta f = -\frac{1}{\rho_m k_f} \cdot f_0^2 \cdot \frac{\Delta m}{A} \qquad [2.13]$$

where A is the crystal surface area, ρ_m is the density of the gas sensitive coating on top of the piezoelectric substrate, f_0 is the resonance frequency of the uncoated crystal and k_f is a frequency constant.

A **piezoelectric** crystal has a resonant frequency that is directly proportional to its mass. By coating a sensitive material onto its upper surface a simple mass gas sensor can be created. The adsorption or desorption of gas molecules, resulting in a change in the overall mass of the sensor, alters the resonant frequency of the crystal according to equation [2.13]. This shift in frequency Δf is characteristic of the species and concentration of gas absorbed. By using an array of piezoelectric sensors with different coatings and pattern recognition software gases including toluene, chloroform and pentane have been successfully detected.[58]

A **surface acoustic wave** (SAW) sensor is a transmission (or delay) line in which an acoustic Rayleigh wave is piezoelectrically generated from a transmitter, propagated

along the surface of the substrate, and is transformed back into an electrical signal at the receiver (Figure 2.9).

Interactions of gaseous molecules with the selective material leads to an increase in the layer's mass, modulating the acoustic wave. This can be detected at the receiver as a variation in the amplitude ΔA, a shift in the frequency Δf, or as a phase shift $\Delta \phi$ in the electrical signal. Any of these parameters can be measured and expressed as a function of the gas concentration. The most common technique is to measure the change in frequency Δf.
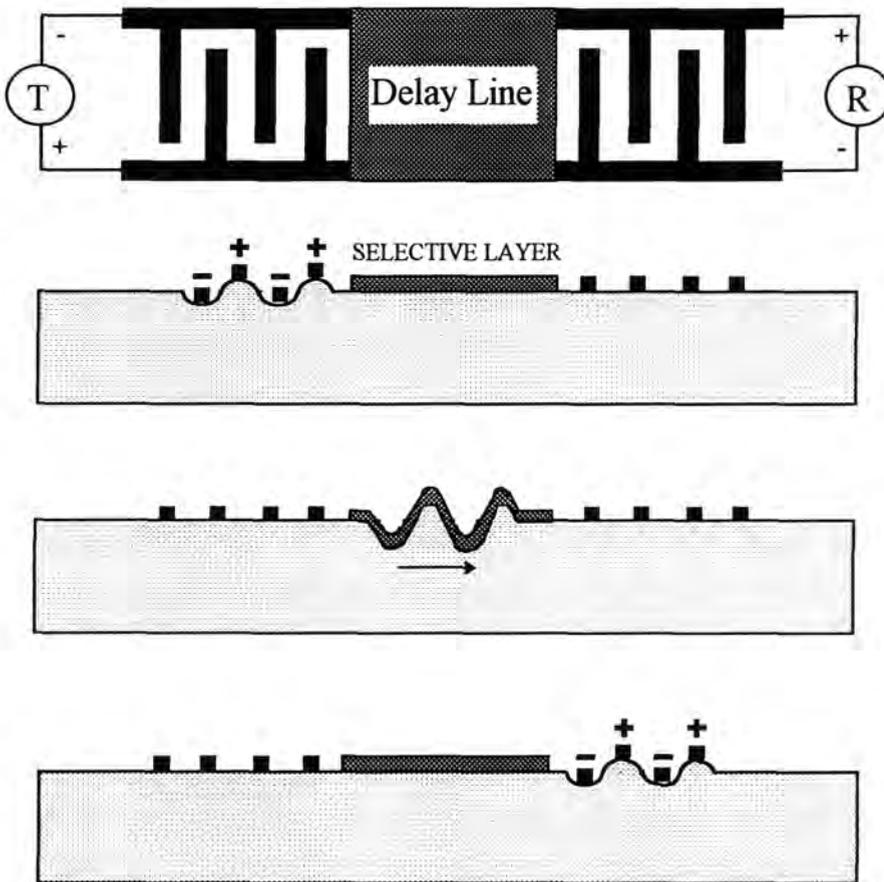
Figure 2.9 Schematic diagram of a SAW sensor with transmitter T, receiver R, with the chemically selective layer deposited on the delay line. [Ref. 59]

The selectivity of a SAW device is determined by the choice of chemically sensitive material used on the delay line. Langmuir-Blodgett films provide fast responses because the films are ultra-thin with a more ordered structure. Various polymer and phthalocyanine compounds have been applied to SAW sensors, for the detection of NO2,[60] ethanol and hexane.[61] The main problems with SAW sensors are a poor long-

term stability, a high dependence on temperature and a high sensitivity to ambient moisture. However, with signal processing and compensation techniques, these problems can be greatly minimised.

2.4 SUMMARY

A review of gas sensing materials, techniques for their deposition and the devices upon, or within which, they can be incorporated has been presented. The materials discussed included both inorganic and organic compounds. The advantages of organic materials, i.e. their simpler processability and the capability to chemically tailor the materials to improve selectivity, have been highlighted. Of the three methods for thin film deposition described, spin-coating is the simplest and more versatile process. A wide array of sensor devices have been introduced, some of which are more suitable for certain applications than others. The devices based on MOSFET technology have the advantage of in built signal amplification. In the next chapter the chemical and physical characteristics of the organic compounds used in this work will be discussed.

REFERENCES

1. T. Seiyama, A. Kato, K. Fujiishi and M. Nagatami, *Anal. Chem.*, **34** (1962) 1502-1503.

2. P.J. Shaver, *Appl. Phys. Lett.*, **11** (1967) 255-257.

3. D.J. Dwyer, *Sensors and Actuators B*, **5** (1991) 155-159.

4. P. Romppainen, V. Lantto and S. Leppävuori, *Sensors and Actuators B*, **1** (1990) 73-78.

5. G. Wiegleb and J. Heitbaum, *Sensors and Actuators B*, **17** (1994) 93-99.

6. L.I. Popova, S.K. Andreev, V.K. Gueorguiev and N.D. Stoyanov, *Sensors and Actuators B*, **19** (1994) 543-545.

7. R. Lalauze, N. Bui and C. Pijolat, *Sensors and Actuators*, **6** (1984) 119-125.

8. G. Tournier, C. Pijolat, R. Lalauze and B. Patissier, *Sensors and Actuators B*, **26** (1995) 24-28.

9. M. Ohnishi, C. Ishimoto and M. Aoki, *Jpn. J. Appl. Phys.*, **33** (1994) 5987-5994.

10. W.M. Sears, K. Colbow and F. Consadori, *Semicond. Sci. Technol.*, **4** (1989) 351-359.

11. G. Sberveglieri, S. Groppelli, P. Nelli, V. Lantto, H. Torvela, P. Romppainen and S. Leppävuori, *Sensors and Actuators B*, **1** (1990) 79-82.

12. N. Yamazoe, *Sensors and Actuators B*, **5** (1991) 7-19.

13. I. Lundström, S. Shivaraman, C. Svensson and L. Lundkvist, *Appl. Phys. Lett.*, **26** (1975) 55-57.

14. D. Xinfang, Y. Haiming and J. Hen, *Sensors and Actuators B*, **12** (1993) 1-4.

15. I. Lundström and C. Svensson in *Solid State Chemical Sensors* ed J. Janata and R.J. Huber (Academic Press 1985) 21.

16. T.L. Poteat and B. Lalevic, *IEEE Trans. Electron Devices*, vol.ED-**29**, 123-129.

17. A. Arbab, A. Spetz and I. Lundström, *Sensors and Actuators B*, **15** (1993) 19-23.

18. L. Ping and P.K. Dasgupta, *Anal. Chem.*, **61** (1989) 1230-1235.

19. J. Janata, *Principles of Chemical Sensors* (Plenum Press 1989) 218.

20. S. Baker, G.G Roberts and M.C. Petty, *IEE Proceedings*, Vol. **130**, Pt. I (1983) 260-263.

21. D. Crouch, S.C. Thorpe, M.J. Cook, I. Chambrier and A.K. Ray, *Sensors and Actuators B*, **19** (1994) 411-414.

22. B. Bott and T.A. Jones, *Sensors and Actuators*, **5** (1984) 43-53.

23. S.M. Critchley, M.R. Willis, Y. Maruyama, S. Bandow, M.J. Cook and J. McMurdo, *Mol. Cryst. Liq. Cryst.*, Vol. **229** (1993) 47-51.

24. A. Cole, R.J. McIlroy, S.C. Thorpe, M.J. Cook, J. McMurdo and A.K. Ray, *Sensors and Actuators B*, **13** (1993) 416-419.

25. M.M. Catalano, M.J. Crossley, M.M. Harding and L.G. King, *J. Chem. Soc., Chem. Commun.*, 1984, 1535-1536.

26. R.H. Tredgold, M.C.J. Young, P. Hodge and A. Hoorfar, *IEE Proceedings*, Vol. **132** (1985) 151-156.

27. L. Sun, C. Gu, K. Wen, X. Chao, T. Li, G. Hu and J. Sun, *Thin Solid Films*, **210** (1992) 486-488.

28. M.G. Baron, R. Narayanaswamy and S.C. Thorpe, *Sensors and Actuators B*, **11** (1993) 195-199.

29. P.N. Bartlett, P.B.M. Archer and S.K. Ling-Chung, *Sensors and Actuators*, **19**

(1989) 125-140.

30. P.N. Bartlett and S.K. Ling-Chung, *Sensors and Actuators*, **19** (1989) 141-150.

31. F. Selampinar, L. Toppare, U. Akbulut, T. Yalçin and S. Süzer, *Synthetic Metals*, **68** (1995) 109-116.

32. J.J. Miasik, A. Hooper and B.C. Tofield, *J. Chem. Soc., Faraday Trans. I*, **82** (1986) 1117-1126.

33. H. Nagase, K. Wakabayashi and T. Imanaka, *Sensors and Actuators B*, **14** (1993) 596-597.

34. P.N. Bartlett and S.K. Ling-Chung, *Sensors and Actuators*, **20** (1989) 287-292.

35. S.-R. Kim, S.-A. Choi, J.-D. Kim, K.J. Kim and S.B. Rhee, *Synthetic Metals*, **71** (1995) 2027-2028.

36. S. Nakagomi and T. Yamamoto, *Sensors and Actuators B*, **14** (1993) 617-618

37. J. Langmaier and J. Janata, *Anal. Chem.*, **64** (1992) 523-527.

38. M. Hirata and L. Sun, *Sensors and Actuators A*, **40** (1994) 159-163.

39. S. Sukeerthi and A.Q. Contractor, *Indian Journal of Chemistry*, Vol. **33A**, 565-571.

40. D. Chinn and J. Janata, *Thin Solid Films*, **252** (1994) 145-151.

41. M.C. Steele and B.A. MacIver, *Appl. Phys. Lett.*, Vol. **28** (1976) 687-688.

42. A. Assadi, A. Spetz, M. Willander, C. Svensson, I. Lundström and O. Inganäs, *Sensors and Actuators B*, **20** (1994) 71-77.

43. I. Lundström, M.S. Shivaraman and C. Svensson, *Surface Science*, **64** (1977) 497-519.

44. I. Lundström, C. Svensson, A. Spetz, H. Sundgren and F. Winquist, *Sensors and Actuators B*, **13** (1993) 16-23.

45. S. Formenko, S. Gumenjuk, B. Podlepetsky, V. Chuvashov and G. Safronkin, *Sensors and Actuators B*, **10** (1992) 7-10.

46. I. Lundström, A. Spetz, F. Winquist, U. Ackelid and H. Sundgren, *Sensors and Actuators B*, **1** (1990) 15-20.

47. M. Josowicz, J. Janata, K. Ashley and S. Pons, *Anal. Chem.*, **59** (1987) 253-258.

48. P. Bergveld, *Sensors and Actuators*, **8** (1985) 109-127.

49. M. Stenberg and B.I. Dahlenbäck, *Sensors and Actuators*, **4** (1983) 273-281.

50. M.J. Tierney and H.-O.L. Kim, *Anal. Chem.*, **65** (1993) 3435-3440.

51. S.D. Senturia, C.M. Sechen and J.A. Wishneusky, *Appl. Phys. Lett.*, **30** (1977) 106-108.

52. J.F. Giuliani, H. Wohltjen and N.L. Jarvis, *Opt. Lett.*, **8** (1983) 54-56.

53. O.S. Wolfbeis, L.J. Weis, M.J.P. Leiner and W.E. Ziegler, *Anal. Chem.*, **60** (1988) 2028-2030.

54. T. Hanawa, S. Kuwabata, H. Hashimoto and H. Yoneyama, *Synthetic Metals*, **30** (1989) 173-181.

55. J.P. Lloyd, C. Pearson and M.C. Petty, *Thin Solid Films*, **160** (1988) 431-443.

56. J.N. Zemel, in: *Solid State Chemical Sensors* ed J. Janata and R.J. Huber (Academic Press 1985) 196-204.

57. P. Krebs and A. Grisel, *Sensors and Actuators B*, **13** (1993) 155-158.

58. J. Auge, P. Hauptmann, J. Hartmann, S. Rösler and R. Lucklum, *Sensors and Actuators B*, **26** (1995) 181-186.

59. J. Janata, *Principles of Chemical Sensors* (Plenum Press 1989) 70.

60. C. Yuquan, Z. Wuming and L. Guang, *Sensors and Actuators B*, **20** (1994) 247-249.

61. M. Ohnishi, C. Ishimoto and J. Seto, *Thin Solid Films*, **210** (1992) 455-457.

BIBLIOGRAPHY

J.W. Gardener *Microsensors: Principles and Applications* (Wiley 1994).

J. Janata *Principles of Chemical Sensors* (Plenum 1989).

A.M. Azad, S.A. Akbar, S.G. Mhaisalkar, L.D. Birkfield and K.S. Goto '*Solid-State Gas Sensors: A Review*', J. Electrochem. Soc., Vol. **139** (1992) 3690-3704.

A.A. Saaman and P. Bergveld '*A Classification of Chemically Sensitive Semiconductor Devices*', Sensors and Actuators, **7** (1985) 75-87.

P. Bergveld '*The Impact of MOSFET-Based Sensors*', Sensors and Actuators, **8** (1985) 109-127.

D.K. Schroder *Semiconductor Material and Device Characterization* (Wiley 1990) Chapter 3

CHAPTER THREE

MATERIALS

Both of the main materials used in this work are organic compounds: polyaniline is a conductive polymer, whilst phthalocyanines are classified as molecular crystals. Each material demonstrates a change in its conductive properties upon exposure to certain gases, organic vapours and also water vapour. This chapter aims to summarise the important physical and chemical characteristics of each compound, outlining the mechanisms that make them suitable materials for gas sensing. The contrasting size of the two sections (§ 3.1 and § 3.2) reflects the quantity of research involving the two materials.

3.1 POLYANILINE

Following the successful synthesis of thin films of polyacetylene in 1974 [1] and its subsequent doping to a metallic-state in 1977,[2] electronic conductive polymers have generated much interest because of the many potential applications. One such conductive polymer, polyaniline (PANi), is considered attractive because aniline is a cheap product and polyaniline is an air-stable material. However, it is not a new material and its existence has been known for over 150 years. Early research was hindered by the uncertainty in the polymer's composition. But, during the mid-1980s research into the conductivity mechanisms and other physical characteristics greatly increased, due to better characterised materials of an established composition.

Polyaniline may exist in three different forms (Figure 3.1), each with a distinct backbone structure composed of different proportions of quinoid and benzenoid rings. The polymer may consist of reduced repeat units (Figure 3.1[a]) $[-(C_6H_4)-NH-(C_6H_4)-NH-]$ and oxidised repeat units (Figure 3.1[c]) $[-(C_6H_4)-N=(C_6H_4)=N-]$. If the polymer is composed of reduced units alone (benzenoid rings), it is referred to as the leucoemeraldine oxidation state of polyaniline; if it is composed of oxidised units only (one quinoid ring and one benzenoid ring), it is

known as the pernigraniline oxidation state. Intermediate between these two states is the semi-oxidised emeraldine base (Figure 3.1b). This form can be protonated (i.e. doped) by aqueous acids, leading to an increase in conductivity of over 10 orders in magnitude.[3]

3.1.1 Chemical Synthesis of Polyaniline

Polyaniline, until very recently, was not readily processible in its conductive state but needed to be in the emeraldine base form which has the structure shown in Figure 3.1(a). The molecular weight of the polymer used in this work exceeded a minimum value of 30,000, as measured by gel permeation chromatography, using polyvinylpyridine in solutions containing 0.1% lithium chloride in N-methyl-2-pyrrolidone as molecular weight standards.[4]

Leucoemeraldine Base

(a)

Emeraldine Base

(b)
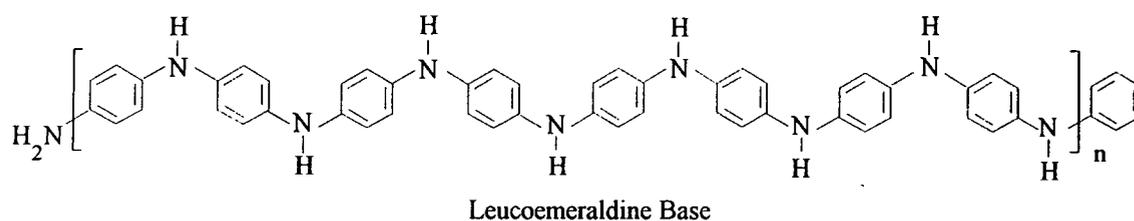
Pernigraniline Base
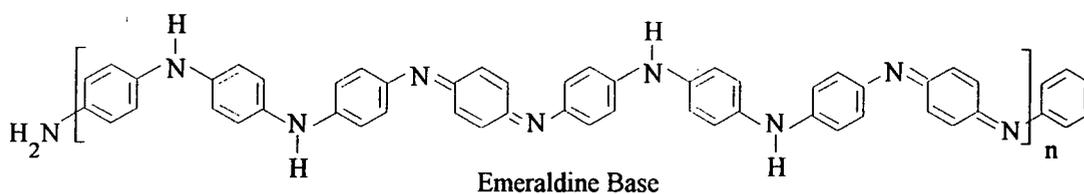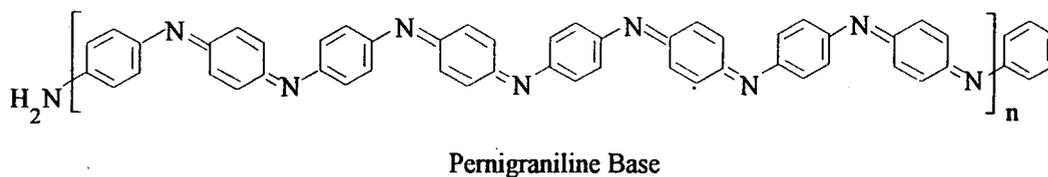
(c)

Figure 3.1 Chemical structure of (a) Leucoemeraldine Base; (b) Emeraldine Base; and (c) Pernigraniline Base.

The polymer used in this work was synthesised in the following manner. 12.96 grammes (0.100 mol) of aniline hydrochloride were dissolved in 150 ml of de-ionised water and stirred in a beaker at room temperature. 28.5 grammes (0.125 mol) of ammonium persulphate were then dissolved in 80 ml of de-ionised water and this solution added dropwise to the reaction mixture over a period of 4 hours. After stirring for a total of 24 hours, the reaction mixture was filtered under vacuum and washed with 3 x 100 ml of water. The filter cake was then stirred in 33% aqueous ammonia solution (to deprotonate the polyaniline) for 8 hours before refiltering, washing with 2 x 100 ml of water followed by 100 ml of isopropanol, and drying under vacuum at 60°C to give the emeraldine base form of polyaniline in approximately 90% yield. This material was soluble in a few selected solvents, of which N-methyl-2-pyrrolidone (NMP) was the most suitable.[3,5,6] To prepare a solution for spin coating, 0.40 grammes of emeraldine base were dissolved in 9.60 grammes of NMP to give a 4% by weight solution. This was homogenised at 20,000 rpm for 10 minutes, then centrifuged twice for 1 hour at 4000 rpm to give a lump-free solution.[†]

3.1.2 Morphology and Structure of Polyaniline

The chemical composition of polyaniline is dependent upon the method of synthesis (whether it is chemical or electrochemical) and also on the synthesis conditions such as pH, concentration of reactants and products, the oxidation potential, etc.

The structure of thin films of chemically prepared emeraldine base polyaniline have been investigated using Fourier Transform Infra-Red (FTIR) spectroscopy and both solid state[7] and solution state[8] ^{13}C magic angle spinning Nuclear Magnetic Resonance (NMR). The films examined were prepared by either spin-coating (similar to the films used in this work for optical studies), or casting onto glass substrates. The solvent was then removed by evaporation allowing free standing films of the polymer to be produced. Films of emeraldine base deposited in this manner were blue in colour in reflection.

[†] The emeraldine base form of polyaniline used throughout this work was chemically synthesised by Dr. Phil Adams of the Physics Department, University of Durham.

A typical FTIR reflectance spectrum for a cast film of the emeraldine base is shown in
Figure 3.2.
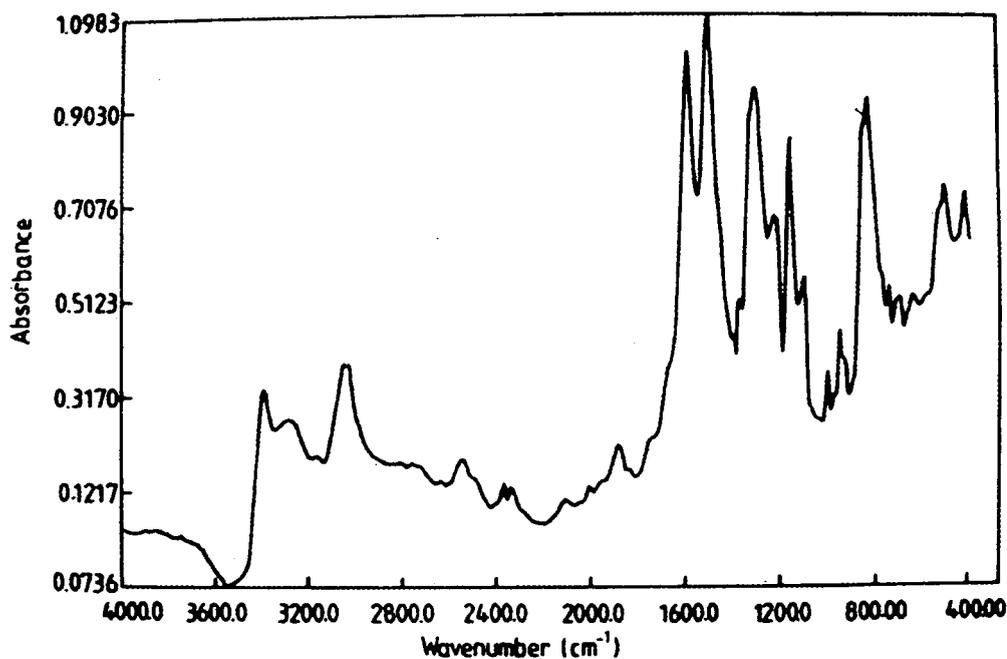
Figure 3.2 FTIR reflectance spectrum of an emeraldine base film [Ref. 7]

The characteristic absorptions observed in this type of spectra allows the identification
of the structure of a compound, in this case the emeraldine base form of polyaniline.[7,9]
Table 3.1 lists the important absorption peaks by wave number, and the associated
chemical groups.

IR BAND (cm^{-1})	ASSIGNMENT	COMMENT
3390	N – H	secondary amine
3283	H_2O	residual water
1310	C – N	secondary aryl amine
2363	CO_2	atmospheric CO_2
2333	CO_2	atmospheric CO_2
1595	C – N	iminoquinone
1508	C – C	aromatic
831, 1009, 1108, 3046	C – H	aromatic, para distribution

Table 3.1 FTIR peak assignments

Oxidation or reduction of the emeraldine base is known to affect the peak absorbances, particularly the N – H stretch at 3390 cm^{-1} and the C = N shoulder at 1670 cm^{-1}. These are used as an indication of the exact oxidation state of the material.[6] These results, and in particular those obtained from solution state ^{13}C magic angle spinning NMR, confirm the chemical structure of the emeraldine base to be that shown in Figure 3.1 (b).

3.1.3 Optical Properties

The optical spectra of spin-coated films of both the emeraldine base and salt form are shown in Figure 3.3.
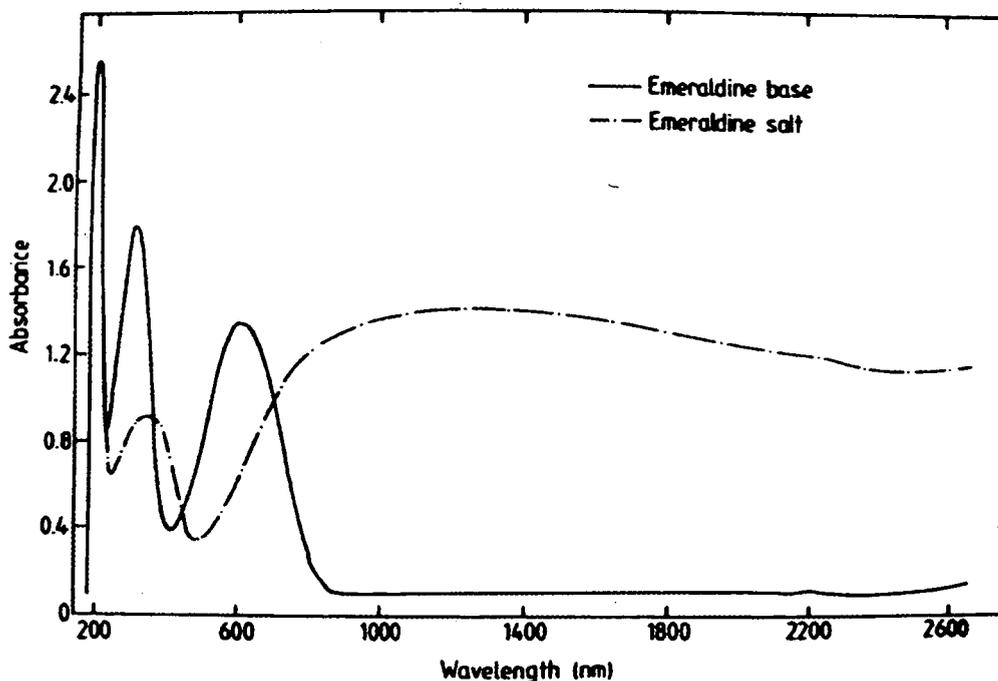
Figure 3.3 Optical absorption spectra of emeraldine base and salt films spin-coated onto quartz substrates [Ref. 7].

The absorption of ultraviolet or visible radiation generally results from excitation of bonding electrons; therefore the wavelengths of absorption peaks can be correlated with the types of bonds and functional groups that exist in the material. Absorption of

light for wavelengths greater than 185 nm is limited to functional groups (called chromophores) that contain valence electrons with relatively low excitation energies.

For polyaniline, it is necessary to consider absorbing species containing σ bonds and π bonds. For example, in ethane (C_2H_6) the four valence electrons of each of the carbon atoms are paired to the valence electrons of the four other atoms it bonds to, e.g. three hydrogen atoms and one carbon atom. Thus in this molecule all the valence (bonding) electrons are tightly bound in covalent bonds, termed σ bonds. These σ electrons are considered localised and require a significant amount of energy to excite one into a higher energy, antibonding orbital.

For a molecule containing a carbon-carbon double bond, e.g. ethene (C_2H_4), each carbon atom forms three σ bonds, two C–H bonds and one C–C bond. The remaining two unbonded valence electrons (one per carbon atom) form a second carbon-carbon covalent bond, with the electrons much less tightly bound than in the σ bond. This second type of bond is termed a π bond and the associated π electrons are thought of as being delocalised. In addition to σ and π electrons, many organic compounds contain nonbonding electrons. These unshared paired electrons are designated by the symbol n.

As illustrated in Figure 3.4, the energies for the different types of molecular orbitals differ significantly.
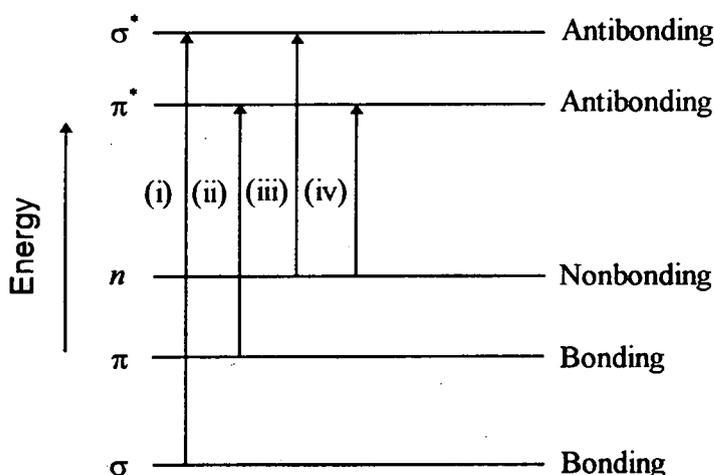
Figure 3.4 Electronic molecular energy levels and associated electronic transitions: (i) $\sigma \rightarrow \sigma^*$, (ii) $\pi \rightarrow \pi^*$, (iii) $n \rightarrow \sigma^*$ and (iv) $n \rightarrow \pi^*$ [Adapted from M.C. Petty *Langmuir-Blodgett Films: an Introduction* (Cambridge 1996) p 220]

Electronic transitions between different energy levels are induced by the absorption of radiation. Figure 3.4 shows the four possible electronic transitions.

For an unconjugated chromophore, the energy required for a $\pi \rightarrow \pi^*$ transition is typically 7 eV, which corresponds to an absorption at 180 nm. When the carbon-carbon double bond is part of a conjugated chain the energy level of the π^* orbital is lowered, giving it less antibonding character. As a consequence, the absorption band is shifted to longer wavelengths.

For the emeraldine base form of polyaniline there are two main absorption bands, centred on 320 nm ($\approx$3.8 eV) and 620 nm ($\approx$2 eV), shown in Figure 3.3. Both of these bands are attributed to $\pi \rightarrow \pi^*$ electronic transitions. The peak at 320 nm is an indication of the $\pi \rightarrow \pi^*$ transition of the polymer backbone.[6] The absorption at 620 nm has been ascribed [10,11] to the transition from a benzenoid-ring-based energy level to a quinoid-based energy level, and is evidence of exciton[†] formation.[7,11] This latter transition corresponds to the formation of a localised electron. The quinoid group effectively self-traps (localises) the exciton electron.[12,13] The presence of the nitrogen heteroatom along the polymer backbone induces trapping of the excitonic electron on the quinoid ring; hence its broadness.

Protonation of a thin film of the base material to the emeraldine salt form transforms the colour from blue to green in reflection. The optical spectrum (Figure 3.3) changes considerably: the 320 nm band greatly diminishes in intensity and, in this example, shifts to approximately 360 nm ($\approx$3.4 eV), whilst the peak at 620 nm is transformed into a very broad band, the onset of which starts at approximately 500 nm ($\approx$2.5 eV) and peaks at around 1230 nm ($\approx$1.0 eV).

Other reported spectra for fully protonated, chemically prepared emeraldine base show shoulders appearing at approximately 420 nm ($\approx$2.8 eV) [10,14,15] and 885 nm ($\approx$1.4 eV).[15,16] Whilst the absorption at 320 nm is shown not to shift with the protonation state, the absolute value does decrease with increasing protonation.[16,17]

[†] Absorption of a photon creates a bound electron-hole pair. An electron and a hole may be bound together by their attractive coulomb interaction, in the same way that an electron is bound to a proton to form a neutral hydrogen atom. The bound electron-hole pair is called an exciton.

The disappearance of the 2 eV exciton transition within the energy band and the formation of the two new ones (at 1.4 eV and 2.8 eV) are indicative of the disappearance of the localised quinoid structure (exciton absorption) of emeraldine base and the formation of a new polaron[§] lattice.[10,11]

The reduction in intensity of the absorption at 325 nm (characteristic of the $\pi \to \pi^*$ transition in the emeraldine base), tending towards the complete absence of the peak when fully protonated, is consistent with metallic-like behaviour, i.e. the oscillator strength has shifted into the infrared.[15]

Protonation produces semiquinone cation radicals which have a mixed benzenoid/quinoid nature; hence there is an increased π-orbital overlap between adjacent phenyl rings leading to subsequent charge delocalisation.[18]

3.1.4 Conductivity Mechanisms

Unlike conventional conductive polymers, polyaniline is unique in that the addition of a proton to an imine nitrogen causes the number of π electrons on the backbone to remain constant; however there is an increase in conductivity of many orders of magnitude.

Emeraldine base undergoes protonation when exposed to an aqueous protonic acid, such as hydrochloric acid. Original studies suggested that preferential protonation of imine sites occurred exclusively.[18] However, later results have shown that, depending on the pH of the acid, some amine sites are also protonated before all of the imine sites.

Figure 3.5 illustrates the change in the structure from the emeraldine base (Figure 3.5 a) to the fully protonated, i.e. *ca* 50% protonated, emeraldine salt (Figure 3.5 d). The suggested model is based on a two-step transition from the isolated, doubly charged, spinless bipolarons (Figure 3.5 b) to a polaronic metal (Figure 3.5 d).[10]

[§] In an insulator the combination of an excited electron and the strain field that its presence induces within an atomic lattice, is known as a **polaron**.
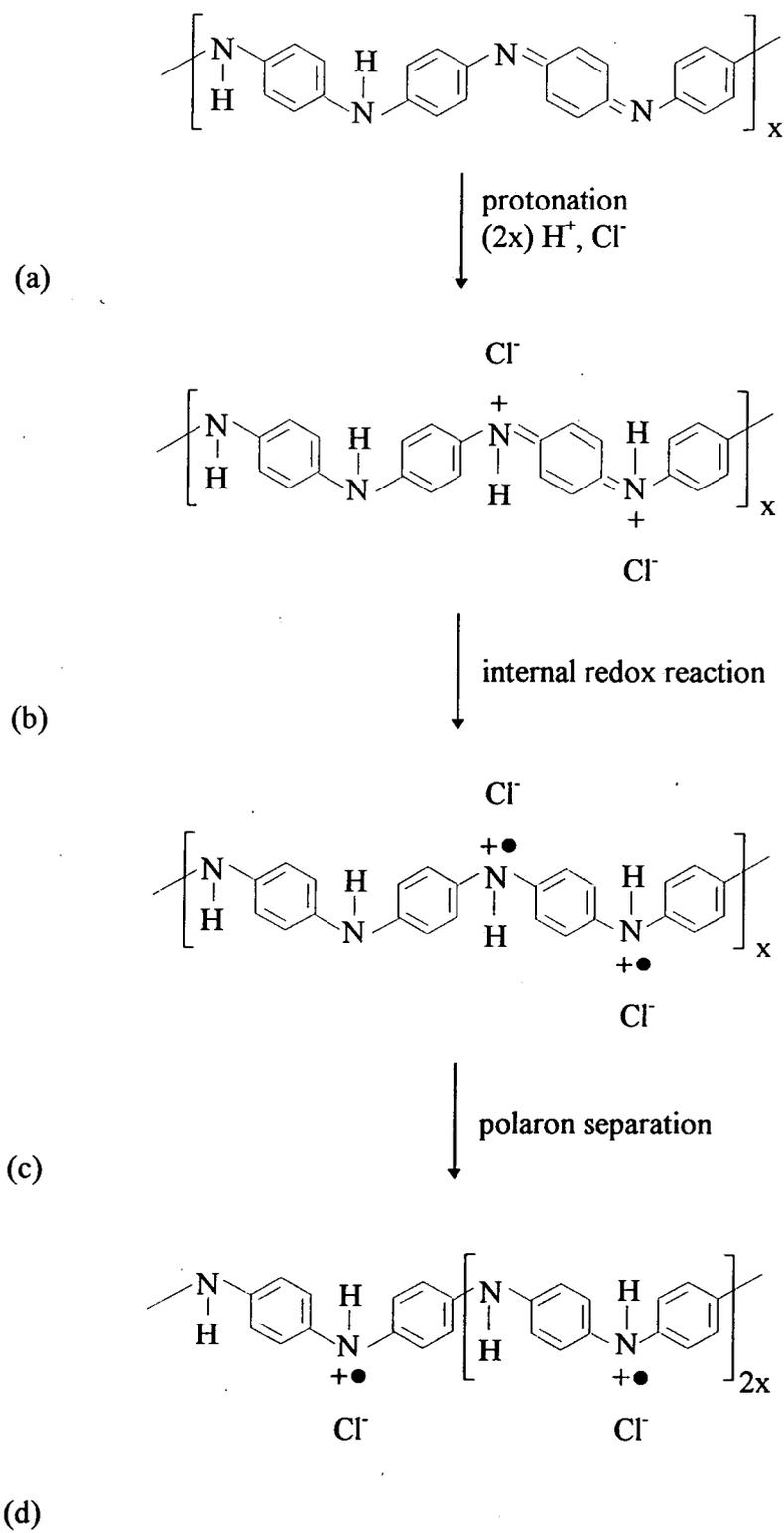
Figure 3.5 The geometric structure of emeraldine base (a) before protonation and (b)-(d) after 50% protonation. (b) Formation of bipolarons and (c) of polarons. (d) The polarons separate, resulting in a polaron lattice. [Ref. 19]

42

The first step relates to the instability of a bipolaron on the emeraldine chain with respect to the formation of two polarons. The second step is their subsequent separation to yield a highly conductive, polaron lattice.

3.1.5 Chemical Properties

a) Solubility

Complete solubility is possible for the emeraldine base using *N*-methyl-2-pyrrolidone, and such solutions have been used for the preparation of films in this work and elsewhere.[5-7] The material is also readily soluble, without degradation or cross-linking, in concentrated sulphuric acid at room temperature. Concentrations as high as 20% by weight have been reported, producing homogenous viscous solutions of a purple-black colour.[20]

b) Oxidation and Reduction

The oxidation and reduction of polyaniline can occur upon exposure to known oxidising and reducing reagents (gases or vapours). Nitrogen dioxide is an oxidising gas (i.e. an electron acceptor), which on contact with the π-electron network of polyaniline results in the transfer of an electron from the polymer to the gas, thus the polymer becomes positively charged. The positive charge created subsequently becomes delocalised along the polymer chain, producing an increase in conductivity. It has been shown that NO_2 interacts with the imine nitrogen in emeraldine base in an analogous manner to protons.[21] (Protonation of polyaniline as described in § 3.1.4.) Removing the presence of NO_2 will result in a reversal, over a period of time, of the above sequence of reactions as the gas dissociates from the surface of the polyaniline. This redox system can be represented by

$$PANi + NO_x \Leftrightarrow \left[PANi^{n^+} + NO_x^{n^-} \right] \qquad [3.1]$$
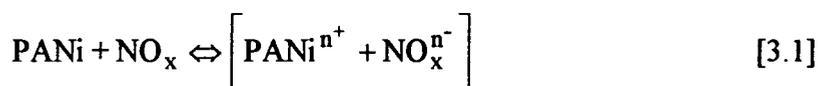
where n is an integer. For this interaction, the equilibrium is shifted to the right during exposure and to the left during recovery.[21]

Exposure to a reducing agent (i.e. an electron donor), such as ammonia vapour, reduces the number of available positive charge carriers along the polymer backbone, leading to a reduction in the conductivity of the material.[22]

c) Effect of Water Vapour on Electrical Conductivity

Water vapour absorbed by polyaniline has been found to increase the conductivity of both the emeraldine base and doped forms of chemically prepared compressed pellets, and free-standing films of polyaniline.[23-25] One suggested mechanism for the increase in conductivity for emeraldine salt with various degrees of protonation, is based on the existence of segregated 'metallic islands' within an insulating matrix.[23] It is proposed that the absorbed water greatly increases the interparticle conductance between the 'metallic islands' before it diffuses relatively slowly into the 'islands', which causes only a minor increase in the conductivity.

A second mechanism is based on the theory that protons are exchanged between the rigid polymer backbone and the mobile water phase.[24] The presence of an H_2O molecule in close proximity to a protonated amine group (NH_2^+) allows the transfer of an electron between the two. Initially a proton exchange takes place as shown:

$$NH_2^+ + H_2O \Rightarrow NH + H_3O^+ \qquad [3.2]$$

Following this, an electron is transferred from the NH site thus increasing the conductivity of the polymer. The role of the H_2O molecule is thought to be a depinning of the charge carried on the NH_2^+ site, through the temporary transfer of a proton.[24]

3.1.6 Thermal Stability and the Effects on Electrical Conductivity

Emeraldine base is known to be stable at high temperatures, up to 420°C.[26] When doped, polyaniline becomes considerably less thermally stable due to the presence of

the counter anion. The decomposition of the doped polymer occurs in two stages: the first step corresponds to the loss of the counter anion, with the decomposition of the backbone structure as the concluding step.

The specific counter anion present has a significant effect on the temperature at which decomposition begins. Results for chemically synthesised compressed pellets of emeraldine base doped with hydrochloric, methane sulphonic and sulphuric acid show that methane sulphonic acid doped polymer is notably more thermally stable than the other two.[26]

An increase in temperature for the same three samples reveals that the conductivities decrease with increasing temperature, though the sample doped with methane sulphonic acid has the greater thermal stability. All three samples show a decrease in conductivity of two orders of magnitude between 200 and 240°C.[26]

The temperature-dependent response for films of polyaniline synthesised electrochemically on gold electrodes differ from the pellets in that a small (two-to-three fold), reversible increase in the conductivity occurs in the temperature range 0≈70°C.[28] Above this temperature, a sharp and irreversible drop in the conductivity occurs. This lower threshold temperature for the onset of the decrease in conductivity (>70°C *cf.* >200°C) is assumed to be due to the difference in the thickness of the samples.

3.2 PHTHALOCYANINES

The observation that the semiconducting properties of phthalocyanines could be modulated by the absorption and desorption of gases has led to significant research toward their incorporation in chemical sensors.

The first reported synthesis of a phthalocyanine occurred in 1907 when Braun and Tcherniac heated *o*-cyanobenzamide at a high temperature.[28] It was much later before the structure of this metal-free, unsubstituted phthalocyanine was determined. Figure 3.6 illustrates the basic structure of a metal-free phthalocyanine (a) and a

metallophthalocyanine (b). The chemical and physical properties can be varied by the choice of metal ion 'M' and through substituent groups that can be added around the periphery of both the metal-free and metallo-phthalocyanine molecule.

(a)   **(b)**
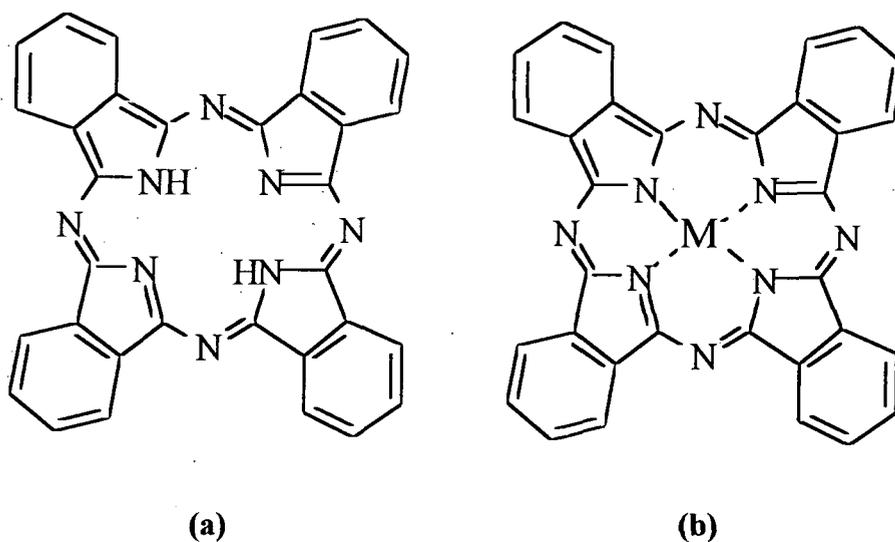
Figure 3.6 (a) Metal-free phthalocyanine and (b) metallophthalocyanine.

Phthalocyanines are polymorphic materials, and exist in one of three forms α, β and γ. Although each type possesses the same chemical composition, they exhibit different crystal lattice structures and physical properties such as density and melting point. The two most frequently observed forms depending on temperature are the α and β types, with only the β form stable at high temperatures (> 200°C).

3.2.1 Chemical Synthesis of Phthalocyanines

Phthalocyanines can be prepared from derivatives of phthalic acid by the reaction of a phthalonitrile with an alkoxide base. The metal-free octa-hexylphthalocyanine, as used in this work (Figure 3.7), is obtainable by two general routes.

R = C₆H₁₁, M = H,H.
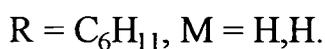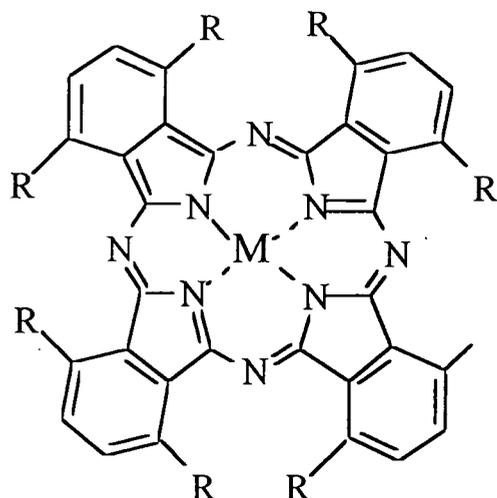
Figure 3.7 Octa-substituted metal-free phthalocyanine. [Adapted from Ref. 29.]

The first involves the reaction of phthalonitrile with lithium pentyloxide in pentanol. Treatment with acetic acid converts the initially formed lithium phthalocyanines to metal-free phthalocyanines. The second route entails the reaction of a substituted masked bis(3-carboxypropyl)phthalonitrile with the appropriate 3,6-dialkylphthalonitrile in a ratio of 1:9. This reaction produces two phthalocyanine derivatives, one of which is the metal-free octa-hexylphthalocyanine. (The compounds used in this work were supplied by Professor M.J. Cook, University of East Anglia. A full description of their synthesis can be found in Ref. 29, and those contained therein.)

Phthalocyanines are soluble in a range of solvents, including toluene and tetrahydrofuran (THF). This allows thin films of the materials to be deposited by the Langmuir-Blodgett technique and by spin-coating. Alternatively, thermal evaporation onto suitable substrates can be used to produce films of phthalocyanine compounds.

3.2.2 Optical Properties and Electronic Structure

The visible spectrum for a spin-coated film of octa-substituted phthalocyanine (full name- 1, 4, 11, 15, 18, 22, 25-octa-hexylphthalocyanine) is illustrated in Figure 3.8. The spectrum is characteristic of the α polymorph (i.e. demonstrates some crystalline
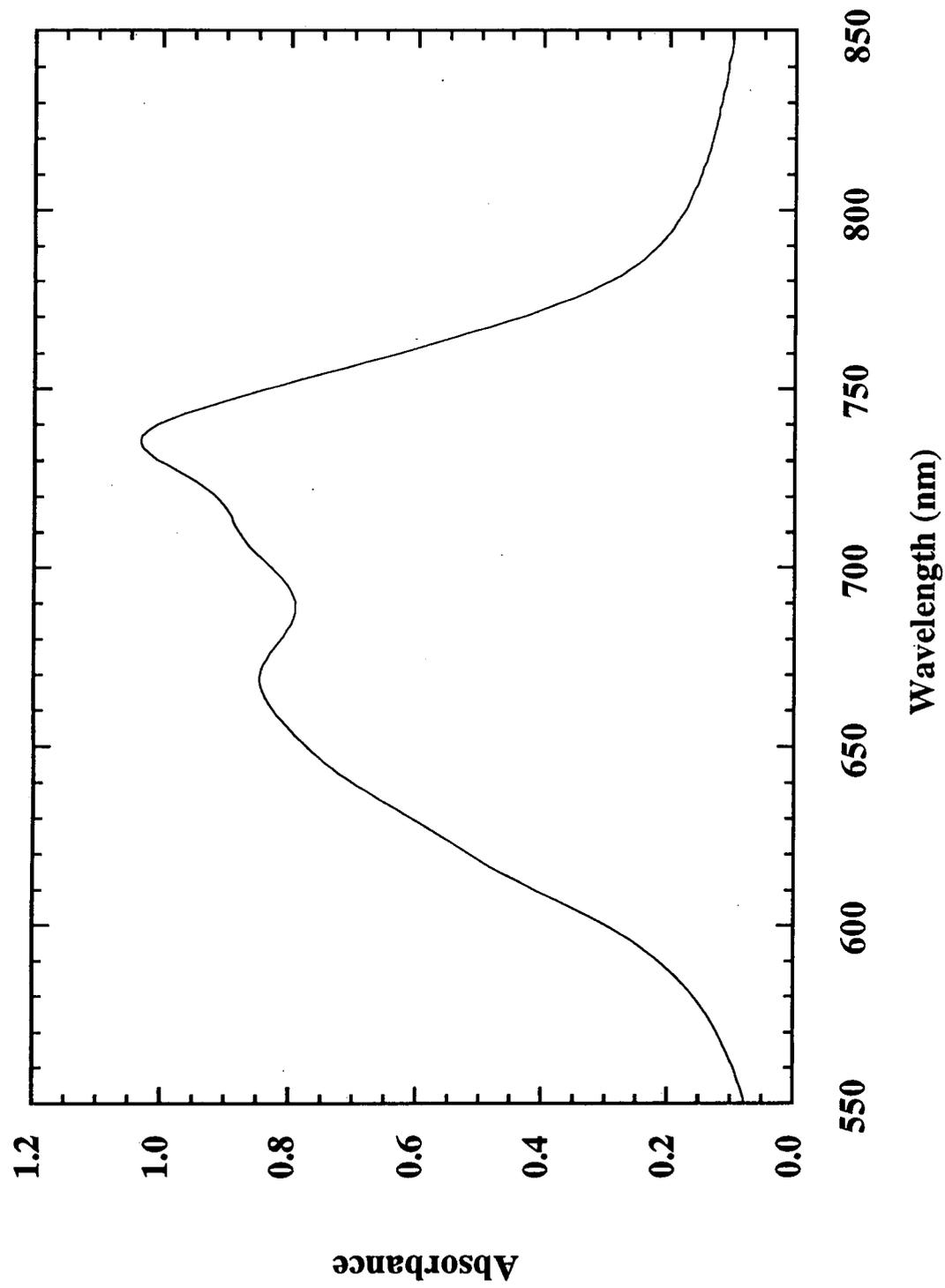
Figure 3.8 Visible region spectra of an octahexyl metal-free phthalocyanine

structure), which exhibits a very broad band in the 500- to 750-nm region (i.e. the visible band of the absorption spectrum, also referred to as the Q-band). These effects arise from extensive exciton coupling between adjacent π rings. The presence of both blue (hypsochromic) shifted and red (bathochromic) shifted bands, with respect to the solution phase Q-band, is evident in Figure 3.8. The band envelope is very similar to that observed for crystals of the same compound smeared onto a glass slide[30] and for a Langmuir-Blodgett film of a close analogue.[31]

3.2.3 Phthalocyanine-Gas Interaction and Conductivity Modulation

As a sensing material, it is the function of the phthalocyanine thin film to absorb or form weak bonds with gases. These surface reactions can result in a change in the conductive properties of the compound. The majority of phthalocyanines are classified as p-type semiconductors. i.e. Electron acceptor gases, such as nitrogen dioxide, cause an increase in the conductivity, whilst exposure to electron donor gases, such as ammonia, lead to a decrease. The conductivity of a thin film of a phthalocyanine compound, as measured on an interdigitated electrode structure, is approximately 10^{-12} S cm^{-1}. Exposure to NO_2 or N_2O_4 leads to an increase in surface conductivity of up to eight orders of magnitude.[32] The insertion of different metal-ions, or the attachment of alkyl groups around the periphery of the molecule, can modulate the ionisation potential (i.e. the ease of electron loss), and therefore the conductivity of the material.[33]

The increase in conductivity is attributed to a charge transfer interaction between the phthalocyanine (electron donor) and NO_2 or N_2O_4 (electron acceptor). Nitrogen dioxide is a π-electron acceptor, and the accepted electron would be delocalised over the planar NO_2 or N_2O_4 structure. Since the hole is also delocalised over the phthalocyanine structure, the coulombic force between the opposite charges is weakened, facilitating charge carrier movement. For certain metal-phthalocyanines such as lead-, cobalt-, and manganese-phthalocyanine, the metal ions can readily adopt oxidation states > +2, and can therefore donate electrons to the phthalocyanine π-system. This enhances the donor power, strengthening the chemisorption of electron-

acceptor gases and hence reducing the reversibility of the effect on removal of the gaseous species. This cannot occur for copper-, nickel-, zinc- and metal-free phthalocyanines, and the effect of oxidising gases, such as NO_2 and SO_2, is reversible for these materials.[32]

Changes observed in the UV-visible spectrum indicate the formation of a phthalocyanine radical cation taking place. Results from infra-red spectroscopy show that exposure of the phthalocyanine films to NO_2 causes the appearance of bands corresponding either to neutral NO_2 and N_2O_4 or to the NO_2^- ion depending on whether the spectrum is transmission or reflectance. Transmission spectra have indicated that NO_2 and N_2O_4 percolate into the phthalocyanine lattice interstices. The reflectance spectrum displays bands corresponding only to the NO_2^- ion, indicating that charge transfer occurs at the surface.[34] The quality and structure of the film's surface is also thought to be a determining factor in the rate of change of the surface conductivity and the subsequent increase or decrease in the bulk conductivity.[32] This is because the absorbing power for a gas is very dependent on the both the crystal form and crystal size.

3.2.4 Thermal and Chemical Stability

It is an established fact that phthalocyanines have excellent thermal and chemical stabilities. As discussed in the previous section, the reversibility of the conductance change induced by the absorption and/or desorption of oxidising gases depends on the central cation, the presence of substituent groups and the film structure.[35,36]

The majority of devices utilising phthalocyanines as gas sensitive materials operate at elevated temperatures to enhance the reversibility of the sorption-desorption process. Some phthalocyanines are known to have good thermal and chemical stability and sublime at 400°C or above in nitrogen. Analysis of the temperature at which a fixed percentage weight loss of phthalocyanine transpires after exposure to various gases can be used to determine if there is a change in stability. For a metal-free phthalocyanine the difference in temperature at which a 5% weight loss occurs in an air atmosphere,

compared to nitrogen, is less than 10°C (from 519°C down to 510°C).[36] The introduction of humid air induces a greater reduction in the thermal stability for metallophthalocyanines (particularly lead phthalocyanine), whilst the stability for all phthalocyanines decreases further in the presence of oxidising gases.[36]

The type of crystalline form adopted by a phthalocyanine is very dependent upon minor impurities, ambient gases and temperature. The temperature of the phase transition from the metastable α-form to the stable β-form is influenced by many factors, but is achieved by heating to above 300°C and is irreversible for most phthalocyanines.[36]

3.3 SUMMARY

A brief discussion of the chemical and physical properties of both polyaniline and phthalocyanines has been presented. The relevant qualities that make them suitable materials for gas sensing have been described. These include the ability to deposit thin films of the materials from suitable solvents and a conductivity mechanism that is enhanced (or inhibited) upon exposure to various gases and vapours. Both compounds demonstrate good chemical and thermal stability in gaseous environments which is a crucial characteristic for a sensing material. The synthesis of the compounds and the conductivity mechanisms have been explained for both materials. In the next chapter the operation of a metal-oxide-semiconductor field-effect transistor is described. The changes in the operating characteristics that occur when an organic material is incorporated into the gate electrode are also discussed.

REFERENCES

1. T. Ito, H. Shirakawa and S. Ikeda, *J. Polymer. Sci. :Polymer. Chem.*, **12** (1974) 11-20.

2. C.K. Chiang, C.R. Fincher, Y.W. Park, A.J. Heeger, H. Shirakawa, E.J. Louis, S.C. Gau and A.G. MacDiarmid, *Phys. Rev. Lett.*, **39** (1977) 1098-1101.

3. A.G. MacDiarmid and A.J. Epstein, *Faraday Discuss. Chem. Soc.*, **88** (1989) 317-322.

4. P.N. Adams, D.C. Apperley and A.P. Monkman, *Polymer*, **34** (1993) 328-332.

5. M. Angelopoulos, G.E. Asturias, S.P. Ermer, A. Ray, E.M. Scherr, A.G. MacDiarmid, M. Akhtar, Z. Kiss and A.J. Epstein, *Mol. Cryst. Liq. Cryst.*, **160** (1988) 151-163.

6. A.P. Monkman and P.N. Adams, *Synth. Met.*, **40** (1991) 87-96.

7. A.P. Monkman and P.N. Adams, *Synth. Met.*, **41** (1991) 891-896.

8. A.M. Kenwright, W.J. Feast, P. Adams, A.J. Milton, A.P. Monkman and B.J. Say, *Polymer*, **33** (1992) 4292-4298.

9. Y. Cao, S. Li, Z. Xue and D. Guo, *Synth. Met.*, **16** (1986) 305-315.

10. A.J. Epstein, J.M. Ginder, F. Zuo, R.W. Bigelow, H.S. Woo, D.B. Tanner, A.F. Richter, W.S. Huang and A.G. MacDiarmid, *Synth. Met.*, **18** (1987) 302-309.

11. A.J. Epstein, J.M. Ginder, F. Zuo, H.S. Woo, D.B. Tanner, A.F. Richter, M. Angelopoulos, W.S. Huang and A.G. MacDiarmid, *Synth. Met.*, **21** (1987) 63-70.

12. C.B. Duke, E.M. Conwell and A. Paton, *Chem. Phys. Lett.*, **131** (1986) 82-86.

13. M.G. Roe, J.M. Ginder, T.L. Gustafson, M. Angelopoulos, A.G. MacDiarmid and A.J. Epstein, *Phys. Rev. B.*, **40** (1989) 4187-4190.

14. S. Ghosh and V. Kalpagam, *Solid State Ionics*, **60** (1993) 149-152.

15. Y Cao, P. Smith and A.J. Heeger, *Synth. Met.*, **32** (1989) 263-281.

16. M. Wan, *J. Polymer Sci. Part A: Polymer Chem.*, **30** (1992) 543-549.

17. M. Wan and J. Yang, *J. Polymer Sci.*, **55** (1995) 399-405.

18. A.G. MacDairmid, J.C. Chiang, A.F. Richter and A.J. Epstein, *Synth. Met.*, **18** (1987) 285-290.

19. S. Stafström, J.L. Brédas, A.J. Epstein, H.S. Woo, D.B. Tanner, W.S. Huang and A.G. MacDairmid, *Phys. Rev. Lett.*, **59** (1987) 1464-1467.

20. A. Andreatta, Y. Cao, J-C. Chiang, A.J. Heeger and P. Smith, *Synth. Met.*, **26** (1988) 383-389.

21. N.E. Agbor, Ph.D. Thesis (University of Durham UK) 1993.

22. M. Hirata and L. Sun, *Sensors and Actuators A*, **40** (1994) 159-163.

23. M. Angelopoulos, A.J. Ray, A.G. MacDairmid and A.J. Epstein, *Synth. Met.*, **21** (1987) 21-30.

24. M. Nechtschein, C. Santier, J.P. Travers, J. Chroboczek, A. Alix and M. Ripert, *Synth. Met.*, **18** (1987) 311-316.

25. O.N. Timofeeva, B.Z. Lubentsov, Y.Z. Sudakova, D.N. Chernyshov and M.L. Khidekel, *Synth. Met.*, **40** (1991) 111-116.

26. V.G. Kulkami, L.D. Campbell and W.R. Mathew, *Synth. Met.*, **30** (1989) 321-325.

27. M. Probst and R. Holze, *Electrochemica Acta*, **40** (1995) 213-219.

28. A. Braun and J. Tchemiac, *Ber. Deut. Chem. Ges.*, **40** (1907) 2709-

29. N.B. McKeown, I. Chambrier and M.J. Cook, *J. Chem. Soc. Perkin Trans. I*, (1990) 1169-1177.

30. M.J. Cook, *J. Mater. Sci.: Mater. in Elect.*, **5** (1994) 117-128.

31. D. Crouch, S.C. Thorpe, M.J. Cook, I. Chambrier and A.K. Ray, *Sensors and Actuators B*, **19** (1994) 411-414.

32. R.L. Van Ewyk, A.V. Chadwick and J.D. Wright, *J. Chem. Soc., Faraday Trans. I*, **76** (1980) 2194-2205.

33. C.L. Honeybourne, R.J. Ewen and C.A.S. Hill, *J. Chem. Soc., Faraday Trans. I*, **80** (1984) 851-863.

34. A.W. Snow and W.R. Barger, in: *Phthalocyanines: Properties and Applications* ed C.C. Leznoff and A.B.P. Lever (VCH Publishers 1989) 349.

35. Y.Q. Liu, D.B. Zhu, T. Wada and H. Sasabe, *Synth. Met.*, **71** (1995) 2283-2284.

36. Y. Sadaoka, Y. Sakai, T.A. Jones and W. Göpel, *J. Mater. Sci.*, **25** (1990) 3024-3028.

BIBLIOGRAPHY

Phthalocyanines: Properties and Applications ed C.C. Leznoff and A.P.B. Lever (VCH Publishers 1989).

D.A. Skoog and D.M. West *Principles of Instrumental Analysis* (Second Edition, Holt-Saunders International Edition 1980) 148-202.

D.H. Williams and I. Fleming *Spectroscopic Methods in Organic Chemistry* (Third Edition, McGraw-Hill Book Company (UK) Ltd.1980) 1-34.

M.C. Petty *Langmuir-Blodgett Films: an Introduction* (Cambridge 1996) Appendix B.

CHAPTER FOUR

SENSOR DEVICE STRUCTURE

The molecular crystals discussed in Chapter Three are incorporated, as thin films, into the gate electrode of a metal-oxide-semiconductor field-effect transistor (MOSFET). The current that flows across the semiconductor is modulated by an applied transverse electric field. In a conventional MOSFET the current controlled by this field will reach an immediate maximum upon the application of a gate voltage. Inclusion of the organic material introduces a time lag in the saturation of this current because the highly resistive organic material inhibits the formation of the electric field. This chapter will present MOS semiconductor theory to explain the operation of a conventional MOSFET and also the differences introduced by incorporating the thin film of organic material into the gate electrode.

4.1 THE METAL-OXIDE-SEMICONDUCTOR CAPACITOR

A MOSFET is essentially a MOS capacitor combined with drain and source doped regions plus electrical contacts. Therefore, it is useful to examine first the electrical characteristics of a MOS capacitor in order to understand more fully the operation of a transistor. A cross-sectional view of the structure is illustrated in Figure 4.1.
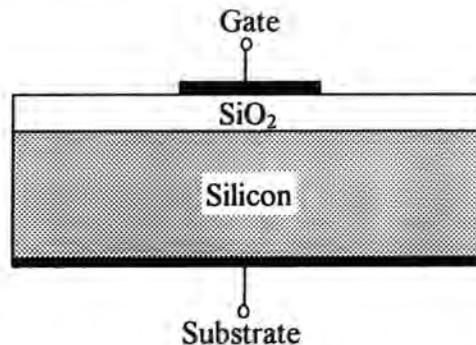
Figure 4.1 Cross-sectional view of a MOS capacitor

There are three distinct cases that can exist at the semiconductor surface; these are shown in Figure 4.2 for an *n*-type semiconductor.
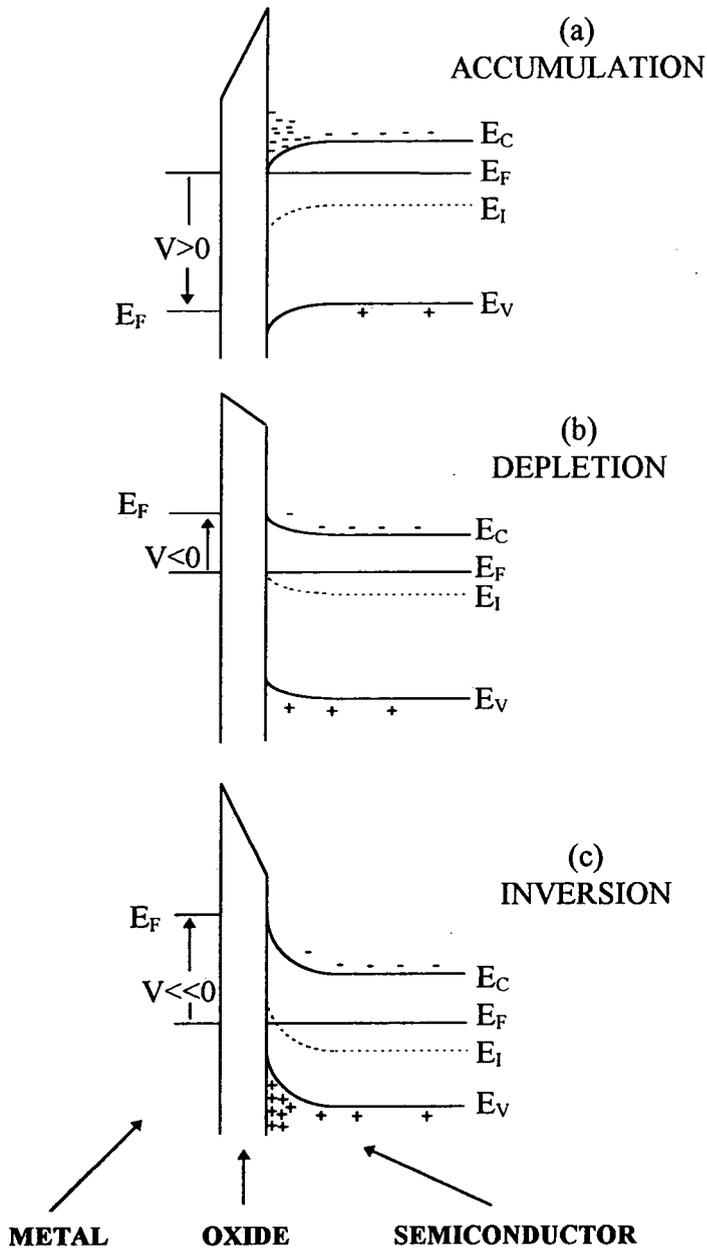
Figure 4.2 Energy band diagrams for an ideal *n*-type MOS capacitor when a bias voltage V is applied. (a) V > 0 surface accumulation occurs, (b) V < 0 surface depletion occurs and (c) V << 0 surface inversion occurs. [S.M. Sze *Physics of Semiconductor Devices* (Wiley 1967) p 428]

4.1.1 Accumulation

When a positive voltage (V>0) is applied to the gate electrode, Figure 4.2 (a), the top of the conduction band bends downwards and is closer to the Fermi level. For an ideal MOS structure there is no current flow so the Fermi level remains constant in the semiconductor. Because the carrier concentration depends exponentially on the energy difference (E_F - E_C), this band bending causes an *accumulation* of majority carriers (electrons) at the semiconductor surface.

4.1.2 Depletion

When a small negative voltage (V<0) is applied, Fig 4.2 (b), the bands bend upwards and the majority carriers are *depleted*. Under these conditions the Fermi level near the silicon surface moves to a position closer to the centre of the forbidden region.

4.1.3 Inversion

When a larger negative voltage (V<<0) is applied, Figure 4.2 (c), the energy bands bend further upwards such that the intrinsic Fermi level E_I at the surface crosses over the Fermi level E_F. At this point the number of minority carriers (holes in *n*-type silicon) attracted from the bulk of the semiconductor to the surface is larger than that of the majority carriers (i.e. electrons), thereby *inverting* the conductivity type of the material at the surface.

4.1.4 Capacitance-Voltage Characteristics of a MOS Capacitor

Ignoring surface states and fixed oxide charges, the theoretical total capacitance per unit area, C_T is given by

$$\frac{1}{C_T} = \frac{1}{C_S} + \frac{1}{C_{ox}},$$

[4.1]

where C_{ox} is the oxide capacitance per unit area, ε_{ox}/t_{ox} (where ε_{ox} is the oxide permittivity and t_{ox} the oxide thickness) and C_s is the semiconductor capacitance per unit area associated with the surface depletion region. This can be shown to be

$$C_s = \frac{\varepsilon_s}{x_d},$$ [4.2]

where ε_s is the permittivity of silicon and x_d is the width of the surface depletion region, which is a function of the applied gate voltage. Figure 4.3 shows the capacitance-voltage (C-V) relationship for a MOS capacitor fabricated on an *n*-type silicon substrate. C-V curves such as the one depicted in Figure 4.3 are obtained by applying a d.c. bias with a small-signal a.c. voltage superimposed to the gate electrode of the device. The rate at which the d.c. bias is ramped between the two extreme voltages +V_G and -V_G and the frequency of the a.c. signal determine the characteristics of C-V curves observed.
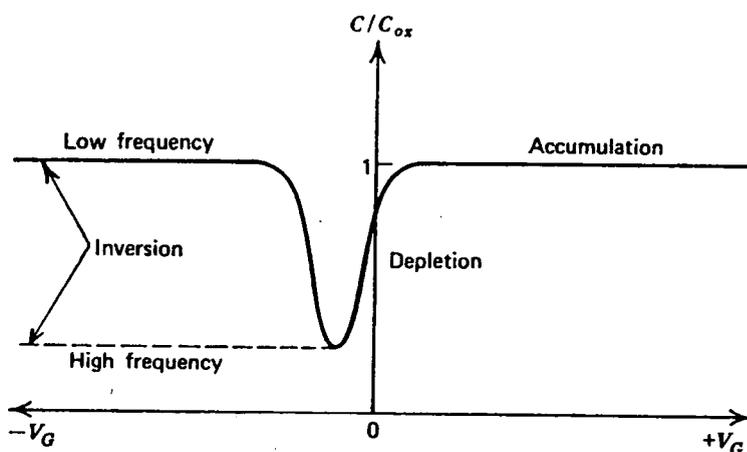
Figure 4.3 Typical capacitance-voltage relationship for a MOS capacitor fabricated on an *n*-type silicon substrate. [Ref. 1]

In the accumulation region (bias voltage > 0 for *n*-type silicon) majority carriers in the semiconductor are attracted to the interface with the metal contact. The carriers form a thin, highly concentrated layer which acts like a capacitor plate equal in area to the gate, effectively shorting-out the semiconductor capacitance (C_s). For this reason, the MOS device capacitance (C_T) in the accumulation region is due strictly to the device geometry as defined by the gate area and oxide thickness, i.e. C_{ox} multiplied by the area of the gate electrode.

The central region of the C-V curve, in which the capacitance changes rapidly with the applied gate bias, is known as the depletion region. As the magnitude of the applied

57

positive voltage is decreased, the electron concentration at the surface of the silicon will also decrease. As this depletion region widens the total capacitance (C_T) decreases, since the increasing surface depletion capacitance C_s is in series with the oxide capacitance C_{ox}, in accordance with Equation 4.1.

With increasingly negative applied gate bias, the surface depletion region continues to widen until the onset of surface inversion occurs (§ 4.1.3). After the formation of the inversion layer the width of the surface depletion region remains static, even if the gate bias is made more negative. This occurs for strong inversion when the potential at the semiconductor surface ψ_S becomes equal to twice the potential difference between the Fermi level E_F and the intrinsic Fermi level E_I, defined as ψ_B. An energy band diagram for this case is illustrated in Figure 4.4. In this state the semiconductor is effectively shielded by further penetration of electric field by the inversion layer such that a very small increase in band bending (corresponding to a very small increase in the depletion-layer width) will result in a very large increase in the charge density within the inversion layer.
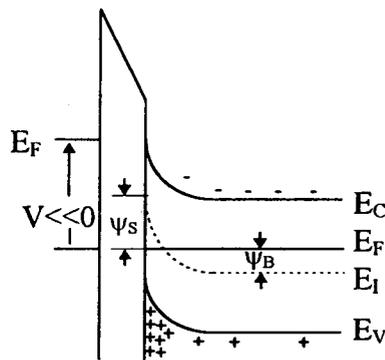
Figure 4.4 The energy band diagram for *p*-type silicon in strong inversion.

Because the mobility of the minority carriers is significantly less than that of the majority carriers, the capacitance is highly frequency dependent. At high frequencies (i.e. 1 MHz) the minority carriers are unable to respond, and so the capacitance is due only to the majority carriers and therefore remains at the depletion capacitance minimum (the dashed line in Figure 4.3). For low frequencies (i.e. 10 Hz) the minority charges are able to respond (i.e. exchange charge with the applied alternating current) and the capacitance saturates to C_{ox}, as shown by the solid line in Figure 4.3.

4.1.5 Deviations from Ideal Metal-Oxide-Semiconductor C-V Curves

In any practical MOS capacitor there exist many other states and charges which affect the ideal C-V curves shown in Figure 4.3. These are (i) surface states (or interface states) which are defined as energy levels within the forbidden band gap at the insulator-semiconductor interface which can exchange charges with the semiconductor, (ii) fixed surface charges which are located near to or at the semiconductor surface and are immobile under applied electric fields, (iii) mobile ions such as sodium which occur due to impurities during the oxide growth and (iv) ionised traps which can be created by X-ray radiation.

The presence of these states can cause a shift of the ideal MOS curve along the voltage axis. This is because, when surface states are present, the electric field in the oxide is higher than the field in the semiconductor surface, and more charges on the metal plate are necessary to create a given surface field in the semiconductor.[2]

A second effect is the hysteresis phenomenon illustrated in Figure 4.5. This occurs in the inversion region and is characteristic of the trapping of mobile ions within states in the oxide layer.[3,4]
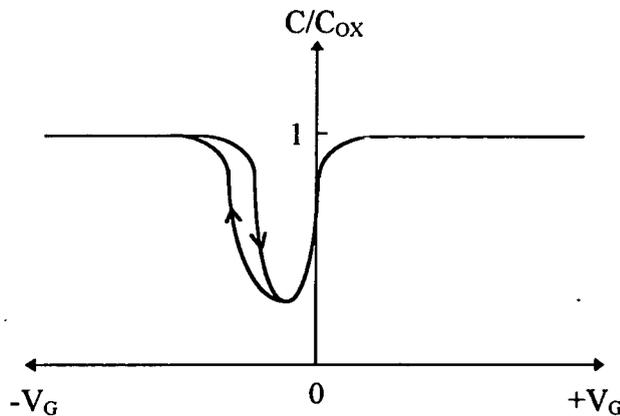
Figure 4.5 An example of hysteresis effects in a low-frequency C-V curve for an n-type MOS capacitor. [Adapted from Ref. 1.]

As the bias voltage is ramped into the inversion region ($V<0$ for an n-type MOS capacitor) these ions drift towards the oxide-gate metal interface, where they become trapped in surface states. When the applied bias is swept back towards more positive

voltages, this charge remains trapped until a more positive voltage is applied. Hence for a particular voltage in the inversion region, the total capacitance on the reverse sweep is greater than on the forward sweep because of the trapped charge.

4.2 THE METAL-OXIDE-SEMICONDUCTOR FIELD-EFFECT TRANSISTOR

Figure 4.6 illustrates the cross-sectional view of a *p*-channel MOSFET. In this device the carriers are positively charged 'holes' flowing from the heavily doped p^+ source region to the similarly doped drain region.
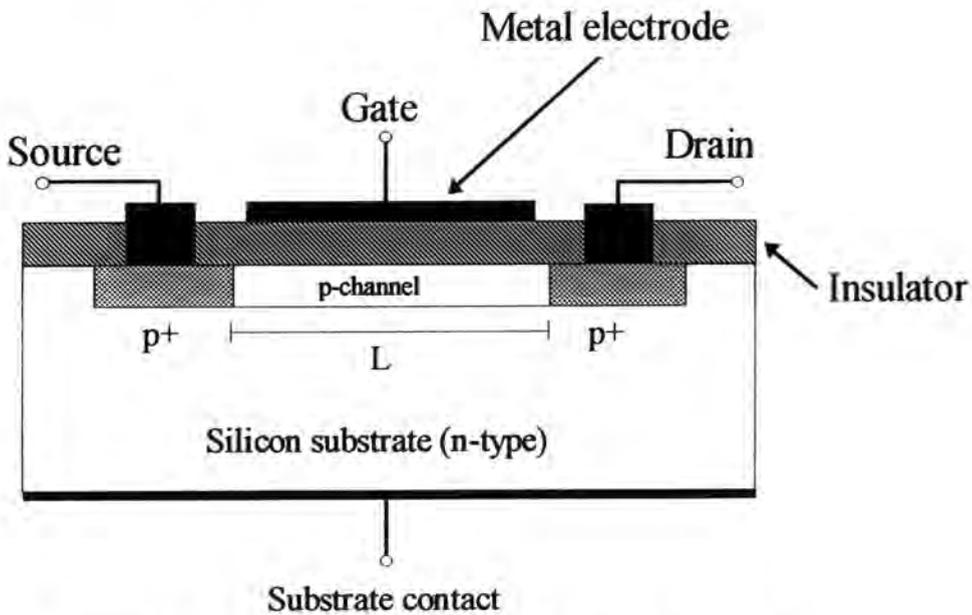
Figure 4.6 Cross-sectional view of a *p*-channel MOSFET

The quantity of charge passing between these two regions, and hence the magnitude of the corresponding drain current, is controlled by a transverse electric field applied via the gate electrode. The drain current flows along an induced channel at the silicon-silicon oxide interface. For an enhancement-mode *p*-channel MOSFET a drain current will only flow when a negative gate bias is applied. Figure 4.7 shows the output characteristics for a typical *p*-channel MOSFET.
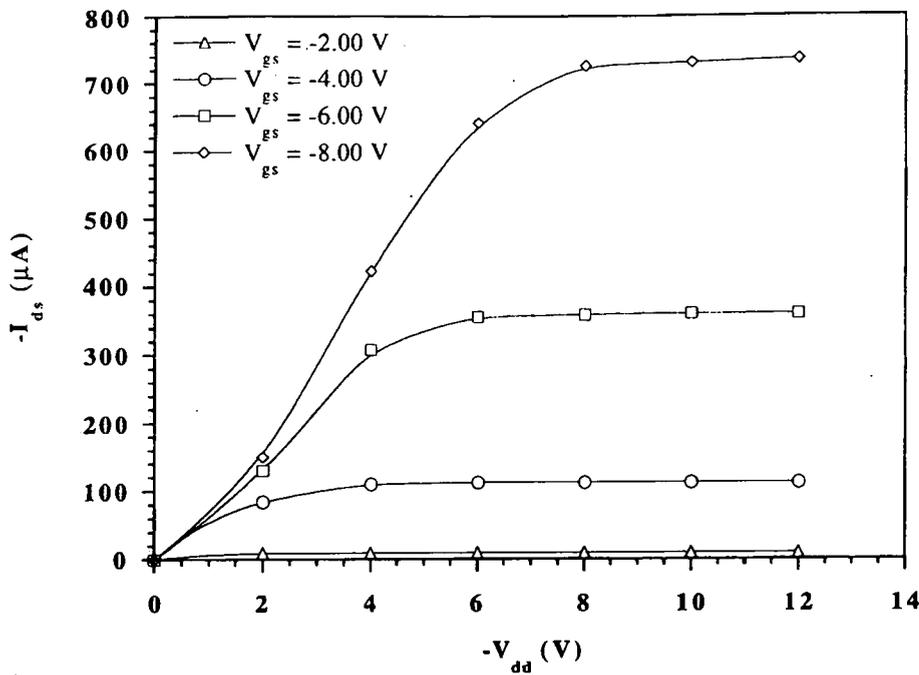
Figure 4.7 Drain current I_{ds} vs. drain voltage V_{dd} for a p-channel MOSFET with a threshold voltage of -1.8 V. [Experimental data obtained from the 15 μm gate-hole device with polyaniline deposited, illustrated in Chapter Five, Figure 5.4 (d).]

4.2.1 DC Operating Characteristics

For an enhancement-mode device a drain current will flow only when the applied gate voltage V_{gs} exceeds the threshold voltage, V_T. This is the gate voltage at which a significant density of charge carriers, holes in a p-channel device, are induced into the channel. For a gate bias less than the threshold voltage insufficient holes are available in the channel to allow a substantial drain current to flow. For a transistor with a threshold voltage of -1.8 V, a drain current can be observed for gate voltages of -2.0 V or greater (Figure 4.7).

Figure 4.8 illustrates the stages of operation for an enhancement-mode MOSFET that lead to the output characteristics shown in Figure 4.7. In Figure 4.8 (a), with no gate voltage applied, there are very few holes in the channel, (only those thermally generated in the n-type substrate) so when a negative voltage V_{dd} is applied to the drain, a negligible drain current flows. In Figure 4.8 (b) a voltage of -6 V is applied to

the gate electrode. This creates an electric field across the substrate which repels electrons from near the oxide and also induces holes just under the oxide. This phenomenon, when the density of holes exceeds that of electrons at the silicon-silicon oxide interface, is referred to as an *inversion layer* (previously discussed in § 4.1.3). The dashed line shows the edge of the transition region, which after the application of the negative gate voltage joins similar transition regions around the source and drain regions. Holes are now able to flow along the channel under the influence of the lateral electric field created by the drain-source voltage, V_{dd}. If the magnitude of the gate voltage is increased, more holes are attracted into the channel generating a larger drain current for the same value of drain voltage.

Increasing the magnitude of the drain voltage, as shown in Figs 4.8 (c) and 4.8 (d), increases the drain current. But increasing the drain voltage reduces the potential difference between the gate and drain electrodes. In Figure 4.8 (c) it has fallen to 3 V and in Figure 4.8 (d) it has been reduced to zero. This results in a reduction in the density of holes induced into the drain-end of the channel, forming a depletion region. (This is represented schematically by a narrowing of the channel.) The effect on the output characteristic of the MOSFET (Figure 4.7) is the onset of saturation of the drain current. In Figure 4.8 (d) the potential difference is zero volts, thus the channel is more than 'pinched-off' and the drain current reaches its saturation value, $I_{ds_{sat}}$.

Increasing the drain voltage further, extends the depletion region towards the source-end of the channel, whilst the drain current remains at the saturation value (as can be seen in Figure 4.7). Saturation of the drain current occurs when

$$V_{dd} \cong V_{gs} - V_{T}.$$

[4.3]
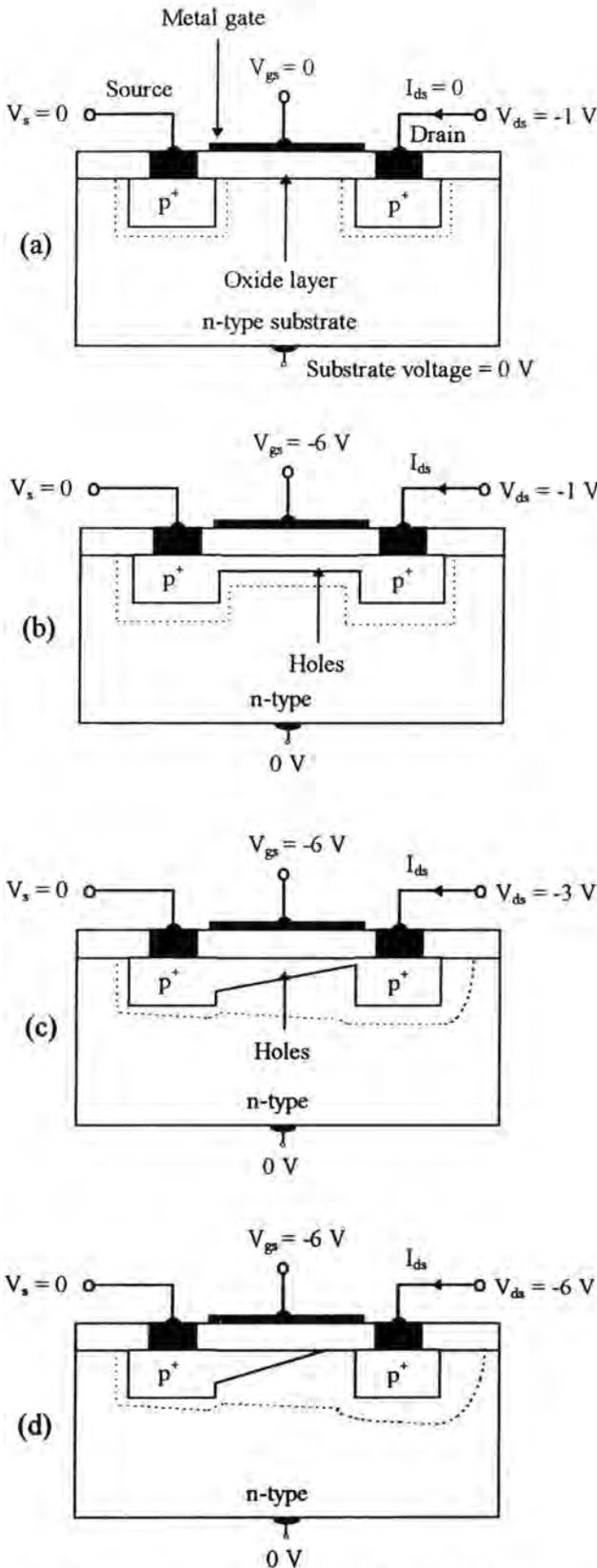
Figure 4.8 A schematic for the operation of a p-channel enhancement mode MOSFET, with a threshold voltage of -2 V. (a) With $V_{gs} = 0$ V a channel is not formed. (b) With $V_{gs} = -5$ V a channel of mobile holes is induced under the oxide which can carry a current. (c) & (d) As the drain voltage is increased the channel becomes progressively depleted of carriers. Pinch-off occurs when $V_{dd} = V_{gs} - V_T$. [Adapted from Ref. 5.]

4.2.2 Factors Affecting the Threshold Voltage

The threshold voltage is defined as the voltage at which the density of mobile holes (for a p-channel device) induced in the channel is equal to the equilibrium electron density in the n-type substrate before a voltage is applied.

An approximation of the threshold voltage can be obtained from a low-frequency C-V plot of the transistor. The gate bias at which the onset of strong inversion occurs (i.e. when the capacitance is observed to increase again) indicates when a conducting channel has been established at the oxide-semiconductor interface.

Two significant factors that influence the value of the threshold voltage are *surface states* that occur in the oxide layer and the difference in the *work function* of the metal and the semiconductor (i.e. silicon).

(i) Surface States

Surface states in metal-insulator-semiconductor devices arise because of the amorphous nature of silicon dioxide. A mismatch in the number of silicon and oxygen atoms lead to 'dangling' chemical bonds which act as donor atoms in the silicon. They can be defined as energy levels within the forbidden band gap at the insulator-semiconductor interface which are able to exchange charges with the semiconductor in a short time. (See also § 4.1.5.)

These states create a layer of fixed positive charges in the oxide which electrically isolate the gate from the substrate. Therefore, sufficient negative charge must be applied to the gate to balance this positive layer before the field can penetrate the substrate and form a conducting channel. The density of surface states can be reduced by the careful growth of high quality oxide layers on the silicon.

(ii) Work Function

The work function of a material is defined as the energy required to remove an electron from the Fermi level to the vacuum level. The work functions of the metal gate contact and the silicon are different. The metal-silicon contact potential, inherent from the difference in the work functions of the materials, creates an electric field across the

oxide. In a MOSFET this field must be overcome by the gate voltage before a field can be established in the semiconductor substrate.

Equation 4.4 defines the threshold voltage for a *p*-channel MOSFET, illustrating the contribution from the effects of surface states and the work function difference between the metal and the silicon.[8]

$$V_T = 2\phi_F - \frac{Q_{SS}}{C_0} + \phi_{ms} - \frac{\sqrt{2\varepsilon qN}}{C_0}\sqrt{2\phi_F} \qquad [4.4]$$

In this equation the symbols are defined as follows:

ϕ_{ms} metal-semiconductor work function difference

ϕ_F Fermi potential (the potential difference between the Fermi level and the intrinsic level)

Q_{SS} extrinsic charge due to surface states, interface energy states, oxide traps etc.

C_0 gate oxide capacitance

N impurity concentration

ε dielectric permittivity of the medium.

4.2.3 Temperature Effects on the Electrical Characteristics of MOSFETs

Changes in the operating temperature of a transistor produce variations in the electrical output characteristics of the device. One reason is the effective mobility of the carriers in the inversion layer is found to depend upon the temperature as given by

$$\mu_{eff} \propto T^{-1} \qquad [4.5]$$

in the temperature range -55°C to +125°C.[6]

The threshold voltage V_T (defined in Equation 4.4) is another temperature dependent parameter.[6-8] Although all the terms in Equation 4.4 are temperature dependent, the two terms with a significant dependency are the work function difference ϕ_{ms} and the associated band bending ϕ_F. Results show that the threshold voltage is approximately a

linear function of temperature for both *n*- and *p*-channel devices over the temperature range -55°C to +125°C.[6] For a *p*-channel MOSFET increasing the operating temperature reduces the negative gate bias required to create the conducting channel (i.e. lowers the threshold voltage.)

The variation of the threshold voltage and the inversion layer mobility with temperature lead to a change in the channel conductance and hence, the drain current.[9] The drain current temperature coefficient is positive at low current levels and negative at high currents. The positive coefficient at low current levels is determined by the threshold voltage shift: a greater current can flow for the same gate bias as the threshold voltage goes down with temperature. At higher current levels, the current decreases because of the decrease of the effective mobility. There does exist a zero temperature coefficient point, where for a fixed drain voltage a gate bias exists for which the drain current is unaffected by fluctuations in the temperature.[10]

4.3 THE CHARGE-FLOW CAPACITOR

To integrate the organic material into the MOSFETs used in this work required a charge-flow capacitor[11] to be incorporated into the gate electrode of the transistor. Figure 4.9 illustrates the charging mechanism of a charge-flow capacitor.

The silicon substrate is semi-conducting and the two sections of the metallic electrode are connected together. The thin film of organic material (polyaniline in this work) is deposited within the gap in the metallic electrode. When a voltage is applied between the electrode and the substrate, the capacitor charges in two steps. First, the metallic sections charge very rapidly to the applied voltage, as shown in Figure 4.9 (i). Charge then begins to flow through the highly resistive (in comparison to the metal) polymer film until a state is reached where the organic region of the capacitor is uniformly charged to the applied voltage, illustrated in Figure 4.9 (ii) and (iii). The time required for this charging process depends on the sheet resistance of the film, the area of the gap in the gate electrode and the thickness of the insulator.

Metal Contact

Polyaniline

Insulator

Silicon Substrate

$+$

V_o

$-$

(i)

(ii)

(iii)
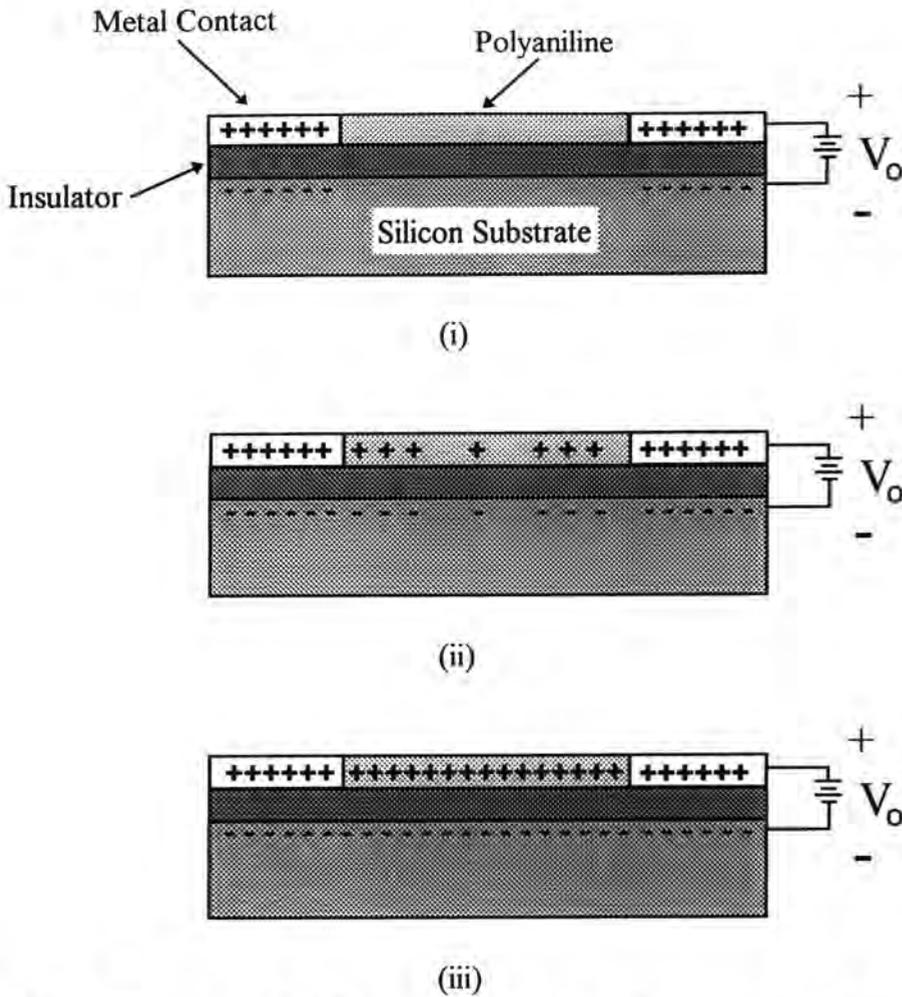
Figure 4.9 An illustration of the charging of a charge-flow capacitor. (i) immediately after V_o is applied; (ii) partially charged; (iii) completely charged.

4.4 THE CHARGE-FLOW TRANSISTOR

The organic/silicon hybrid FET used in this work was a standard *p*-channel enhancement mode MOSFET incorporating the charge-flow capacitor in the gate electrode, as illustrated in Figure 4.10.

Incorporating a charge-flow capacitor into the gate electrode of a *p*-channel MOSFET has been shown to modulate the time response of the drain current.[12] When a gate voltage greater than the FET threshold voltage is applied, a complete conducting channel is not formed until the FET threshold voltage is exceeded along the whole film, resulting in a significant delay between the application of the gate voltage and the drain current reaching its saturation value. This time delay in the formation of the conducting

channel and hence the saturation of the drain current, is known as the 'turn-on' response of the device.
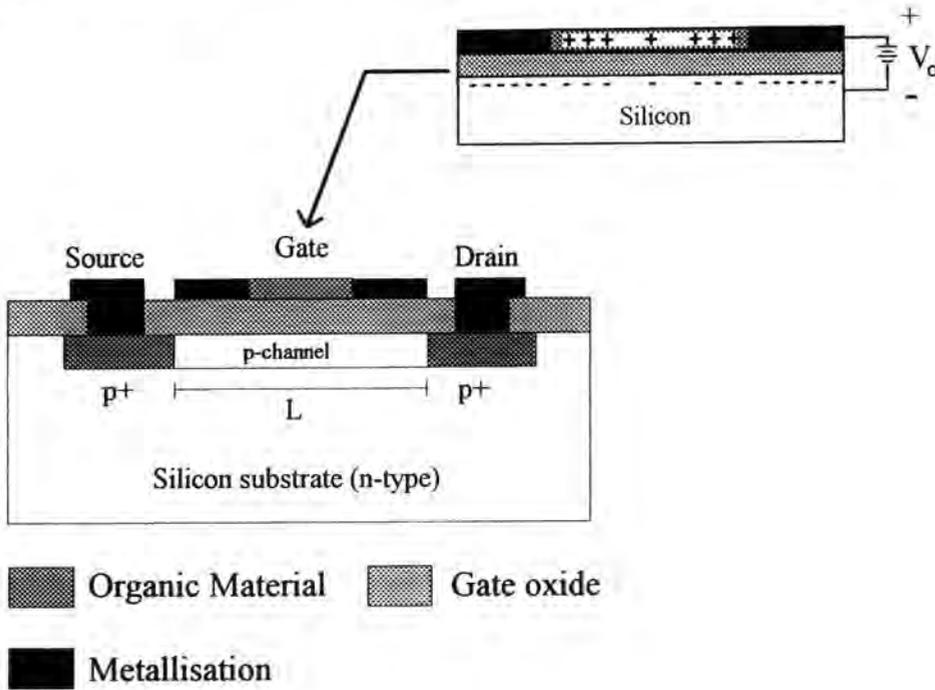
Figure 4.10 The integration of a charge-flow capacitor into a MOSFET to create an organic/silicon hybrid FET.

Figure 4.11 shows a comparison of the 'turn-on' responses for a polyaniline/silicon hybrid FET with and without the polymer deposited.
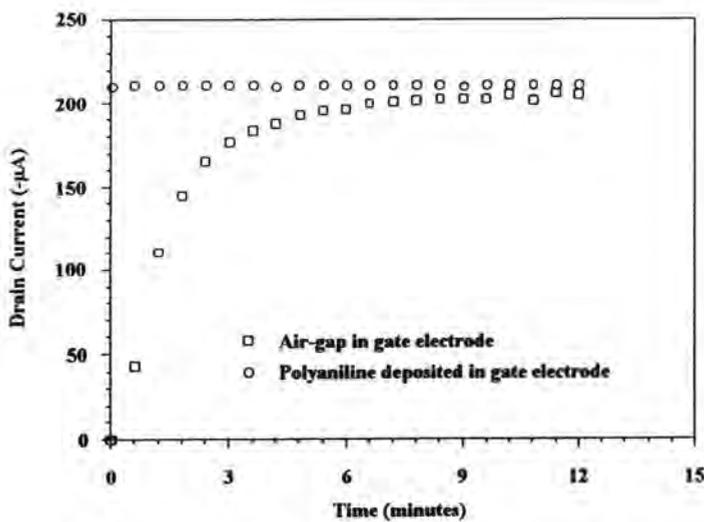
Figure 4.11 Drain current vs. time for a polyaniline/silicon hybrid FET with and without polyaniline deposited. [Experimental data that will be presented in § 6.6.1.]

68

It is clearly evident from Fig 4.11, that the formation of the conducting channel is greatly enhanced by the presence of the conductive polymer.

4.5 SUMMARY

A review of metal-oxide-semiconductor theory has been presented to aid in the understanding of the operation of a MOSFET. The capacitance-voltage characteristics of a MOS capacitor were introduced, highlighting the three electrical states that an applied bias can induce at the silicon-silicon oxide interface: accumulation, depletion and inversion. This theory was then applied to explain the operation of an enhancement mode p-channel MOSFET. The effects of device temperature and oxide defects (impurities) on both the C-V characteristics and MOSFET response, including the threshold voltage, were also explained. Finally, the charge-flow capacitor incorporating the sensing material was introduced and an explanation of its inclusion in a MOSFET to create the organic/silicon hybrid sensor given. In the next chapter the fabrication of such a transistor will be presented along with the methods used to characterise the devices in gaseous ambients.

REFERENCES

1. P. Richman *MOS Field-effect Transistors and Integrated Circuits* (Wiley 1973) 53.

2. S.M. Sze *Physics of Semiconductor Devices* (Wiley 1967) 447.

3. A. Goetzberger, E. Klausmann and M.J. Schultz, *CRC Critical Review in Solid-State Science*, **6** (1976) 1-43.

4. D.W. Greave and V.R. Hay, *J. Appl. Phys.*, **61** (1987) 1176-1180.

5. J.J. Sparkes *Semiconductor Devices* (Van Nostrand Reinhold 1987) 90.

6. L. Vadasz and A.S. Grove, *IEEE Trans. On Electron Devices*, **ED-13** (1966) 863-866.

7. F.M. Klaassen and W. Hes, *Solid-State Electronics*, **29** (1986) 787-789.

8. R. Wang, J. Dunkley, T.A. DeMassa and L.F. Jelsma, *IEEE Trans. On Electron Devices*, **ED-18** (1971) 386-388

9. A. Blicher *Field-Effect and Bipolar Power Transistor Physics* (Academic Press 1981) 302-303.

10. K. Singh, *Discovery and Innovation*, **6** (1994) 245-247.

11. S.D. Senturia, C.M. Sechen and J.A. Wishneusky, *Appl. Phys. Lett.*, **30** (1977) 106-108.

12. S.D. Senturia, J. Rubinstein, S.J. Azoury and D. Adler, *J. Applied Phys.*, **52** (1981) 3663-3666.

BIBLIOGRAPHY

J.J. Sparkes *Semiconductor Devices* (Van Nostrand Reinhold 1987) 84-107.

P. Richman *MOS Field-Effect Transistors and Integrated Circuits* (Wiley 1973) 47-72.

P. Richman *MOS Field-Effect Transistors and Integrated Circuits* (Wiley 1973) 125-135.

R.S.C. Cobbold *Theory and Applications of Field-Effect Transistors* (Wiley 1970) 181-271.

S.M. Sze *Physics of Semiconductor Devices* (Wiley 1967) 425-504.

A. Goetzberger, E. Klausmann and M.J. Schultz, *CRC Critical Review in Solid-State Science*, **6** (1976) 1-43.

CHAPTER FIVE

EXPERIMENTAL TECHNIQUES

The metal-oxide-semiconductor field-effect transistors (MOSFETs) used for the sensor arrays were produced using conventional techniques of microelectronic device fabrication. The gas sensitive organic materials were deposited by spin-coating over the entire device, and then patterned by the use of chemical etching. The characterisation of the sensors was carried out using a purpose-built electrical measurement system, with computer controlled data acquisition software. The optical properties of the organic films deposited on glass substrates were examined, both before and after exposure to gases, using ultraviolet/visible (UV-vis) spectroscopy.

5.1 SILICON DEVICE PROCESSING

The most common procedure for the fabrication of semiconductor devices is the collection of steps known as the planar process. It is based on the use of photolithography to define selected areas of silicon for the addition of donor or acceptor impurity atoms as well as the other necessary structures, including oxide layers and metal interconnections. The following sections outline each of the steps used in this work.

5.1.1 Sample Preparation

The MOSFETs were fabricated on 2″ (100) n-type silicon wafers with a substrate resistivity of 2 - 4 Ω cm. Initially the wafers were thoroughly cleaned to remove all surface contaminants. The slice was boiled in 1,1,1 trichloroethane, a powerful organic solvent, to remove surface grease, and rinsed in propan-2-ol. Following this, the silicon was transferred to a mixture containing equal measures of concentrated ($\approx$98%) sulphuric acid and 30% hydrogen peroxide solution. This solution is a very strong oxidising agent, used to remove any organic contamination. After rinsing in deionised

water the wafer was dipped in 10% hydrofluoric acid (HF) to remove the thin surface layer (15-20 Å) of silicon dioxide until the surface became hydrophobic. This layer grows during the cleaning process as well as upon exposure to air. Finally, the wafer was thoroughly washed in deionised water and transferred to a water recirculating system. The resistivity of the water leaving the recirculator was continuously measured, and the silicon was considered to be clean when the resistivity reached approximately 10^7 Ω cm. Once this had been achieved the wafer was clean enough to begin the fabrication process.

5.1.2 Thermal Oxidation of Silicon

The thermal oxidation of silicon was carried out in quartz furnace tubes at temperatures around 1000°C in an atmosphere of oxygen (dry oxidation) or water vapour (wet oxidation). This allowed relatively dense, trap-free layers of SiO_2 to be grown on the surface of the wafer. These films served as masks for the diffusion processes, as gate or field oxide films and as passivation layers, protecting the silicon from contamination during further processing.

Silicon is oxidised at its surface. Therefore, for continuing oxidation the oxidising species must penetrate through the growing oxide layer in order to combine with the silicon atoms at the wafer surface. Equations [5.1] and [5.2] show the chemical reactions that occur when silicon reacts with oxygen and water vapour, respectively.

$$Si + O_2 \Leftrightarrow SiO_2 \tag{5.1}$$

$$Si + 2H_2O \Leftrightarrow SiO_2 + 2H_2 \tag{5.2}$$

Using calibration charts[1-3] it was possible to quite accurately calculate the time required in the furnace to grow an oxide layer of a certain thickness at a set temperature.

Wet oxidation was carried out by allowing a carrier gas, a mixture of nitrogen and oxygen, to flow through a water bubbler maintained at 95°C. Wet thermal oxidation is a rapid process, but results in relatively porous films. It is used to grow relatively thick oxides for masking purposes. Dry oxidation is a slower process involving only dry

oxygen, but produces better quality oxide films with a relatively low concentration of traps and interface states. Dry oxidation procedures were used in the fabrication of gate oxides.

5.1.3 Photolithography

During all stages of the device fabrication it was necessary to pattern the wafer so that each section of the MOSFET structure was defined. Processes including the diffusion of dopants, the opening of contact windows and defining the metal contacts on the device all required photolithography.

The patterns that were required for each photolithographic stage were first drawn to scale. A reduction (from the original design to the mask) of 1:134 was possible, giving a resolution of the order 5-10 μm for the smallest feature of the device. An alignment mark is a necessary part of every mask created. This allows the exact alignment of all subsequent masks during the fabrication of the device. The design was then transferred to a sheet of Rubylith (opaque ruby coloured plastic) by tracing the scale drawing and cutting the Rubylith with a scalpel. This was then attached to a light box and photographed onto a high resolution plate. When developed, a negative, reduced image of the pattern was produced. The final reduction stage was carried out using a step-and-repeat camera to generate an array of aligned images onto a single photographic plate.

Figure 5.1 (steps 1 to 4) illustrates the transfer of a pattern onto a wafer using the photolithographic process. The surface was first coated with a light-sensitive polymer solution known as photoresist. The Shipley Microposit S1800 series photoresist used in this work is a positive resist system. That is, upon exposure to UV light cross-links within the polymer are broken, such that any exposed areas will be washed away when the wafer is developed.
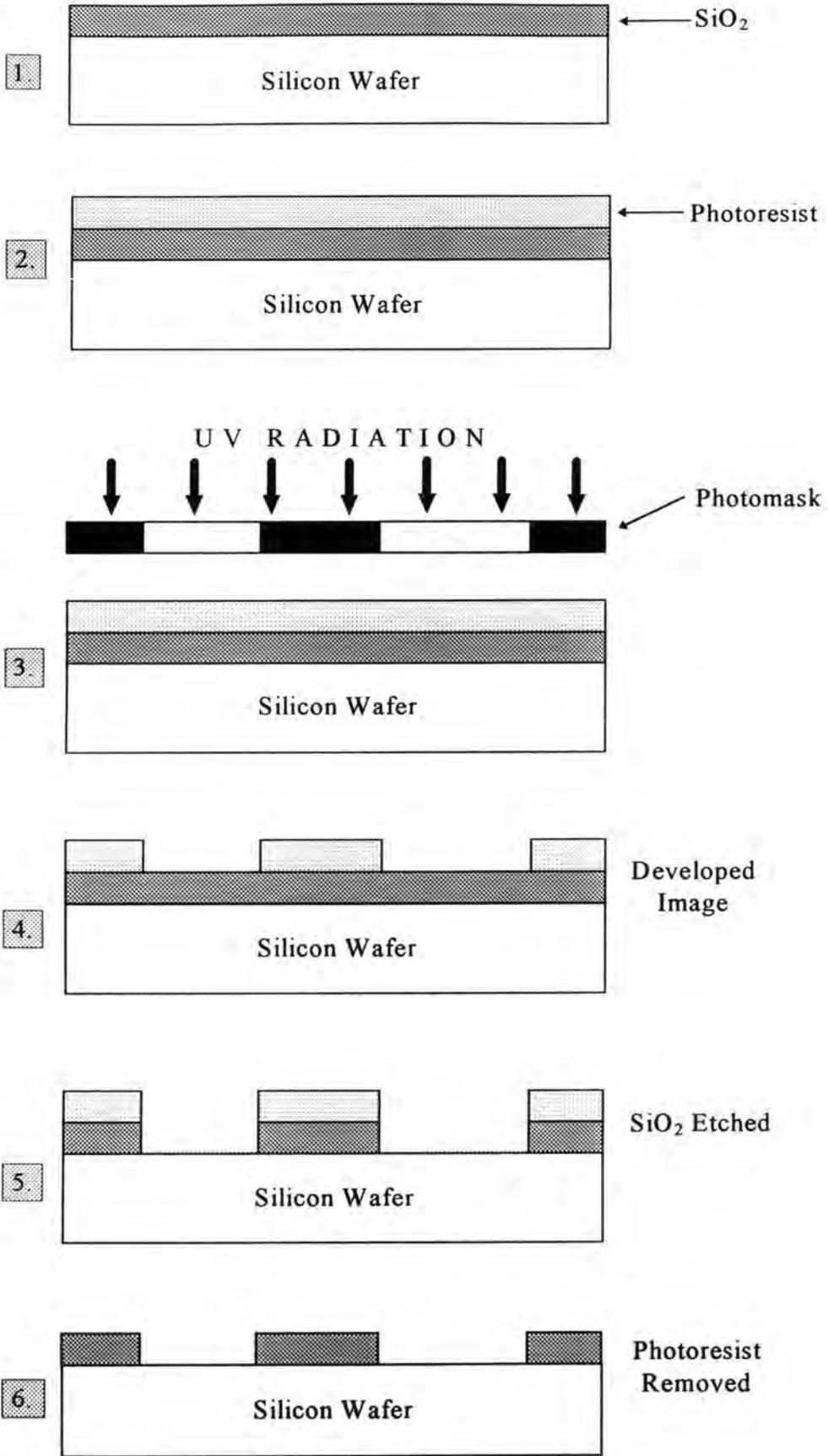
Figure 5.1 The six steps involved in the photolithographic and etching process

The photoresist (Microposit S1813) was spin-coated onto the wafer at 4000 rpm, producing a uniform layer 1.5 μm in thickness. This was then soft-baked at 80°C for 10 minutes to promote adhesion and eliminate any remaining solvent. The mask and wafer were then loaded into a mask alignment and exposure system (Kasper wafer aligner model 17A). Exposure of UV light for between 8-10 seconds through the mask, was sufficient to break the cross-links within the photoresist film.

The wafer was developed for approximately 45 seconds in Shipley Microposit (MF312) Developer solution that had been diluted to half its original concentration with pure water. The developed wafer was then rinsed thoroughly in deionised water and dried in a stream of compressed nitrogen gas. Finally, to maximise the reliability of the resist in subsequent processing steps, the wafer was hard baked at 120°C for 30 minutes. To remove the photoresist after etching (or patterning of the metallisation), the wafer was placed in acetone in an ultrasonic bath for approximately 30 seconds (or until visibly clean).

5.1.4 Wet-Chemical Etching

The rate at which a material would be etched in a particular etchant was an important consideration when calculating the strength of etchant, and the time the sample would require in the solution to remove the necessary amount of material. An etchant will etch both vertically and laterally at different rates. Within the time limit of the etching procedure, it was required that the vertical etch rate greatly exceeded the lateral, to give a virtually straight-edged profile perpendicular to the surface of the wafer. If the lateral etch rate was too great, serious under-etching of the material would have occurred, leading to the possibility that the fabricated device would not properly function.

Wet-chemical etching involved the exposure of the wafer to chemical solvents in order to induce the conversion of the unprotected material into soluble compounds, which could be dissolved by the chemical etchants. Although dry-etching procedures, such as plasma etching,[4] allow smaller feature sizes to be patterned without undesirable

75

undercutting of the material, they were considered too costly and non-essential for the size of devices fabricated in this work.

Silicon dioxide layers were etched using buffered solutions of HF acid (1 part of 40% HF acid to 4 parts of 40% ammonium fluoride) to reduce the etching to a controllable rate. The etch rate also depended upon the quality of the oxide layer. Thus, the poorer quality field oxide layer with its more porous structure etched more rapidly than the better quality gate oxide.

5.1.5 Diffusion

The dopants that were required for the source and drain regions of the MOSFET were added by solid-state diffusion into regions defined by photolithography. Openings were etched through the layer of SiO_2 that covered the surface and the dopants were added to the substrate by chemical means. Common n-type dopants used include phosphorous, arsenic and antimony, whilst boron is the most widely used p-type dopant. All of these dopants are substitutional diffusers, that is they move through the crystal lattice by hopping from one lattice site to another.

To dope n-type silicon, an activated wafer of boron nitride was held in close proximity to the silicon. Both wafers were loaded into a diffusion furnace at a temperature of 990°C, and left for a period of 45 minutes with a continuous flow of nitrogen gas. After etching the sample in buffered HF to remove the boron glass from the surface of the silicon, the dopant was 'driven-in' during the deposition of the gate oxide, in the dry oxidation furnace.

5.1.6 Metallisation

The contact pads and interconnections required to complete the device were provided by conductive metallic films. The films were required to satisfy several criteria: the material had to be highly conductive; form low-resistance ohmic contacts; adhere well

to silicon dioxide; and be capable of withstanding high current densities. The two most common metals used are aluminium and gold.

The metal was deposited by physical vapour deposition (i.e. evaporation), using an Edwards model 306 coating system. The wafer was clamped in the vacuum chamber, above a rotating turret source holding four tungsten boats containing the evaporation source materials. This arrangement allowed multi-layer deposition in a single vacuum cycle.

The system was initially pumped-down to approximately 3×10^{-1} millibar with a rotary pump, and then down to 10^{-4} millibar (or lower) with a diffusion pump. For the MOSFETs used in this work gold was chosen for the metallisation. Because gold does not adhere well to silicon, a thin layer of chromium was first evaporated onto the wafer before the deposition of the thicker gold film.

Evaporation was achieved through direct resistance heating; by passing a large current (60-80 Amps) through the tungsten boats containing the source metals (chromium and gold). The rate of deposition and the thickness of the film were monitored electronically during the evaporation.

5.2 FABRICATION OF A P-CHANNEL MOSFET

Figure 5.2 illustrates the six main steps required for the fabrication of a MOSFET device. After the initial cleaning of the silicon slice a field oxide was grown over the entire wafer by the wet-oxidation process (Step 1). A four hour oxidation produced an oxide layer 0.465 μm thick. Diffusion windows were cut into the field-oxide for the source and drain contacts (Step 2). Photoresist was deposited and exposed to the first mask; and then developed ready for the etching process. This required four minutes in a buffered solution of HF (until the surface was visibly hydrophobic), followed by rinsing in deionised water. After removal of the photoresist the wafer was placed in the recirculator until the resistivity of the water reached 10^7 Ω cm.
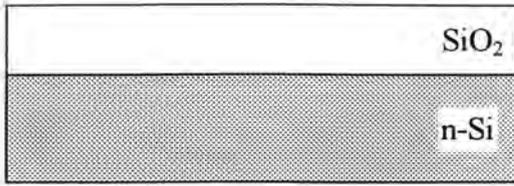
Step 1: Grow the field oxide.
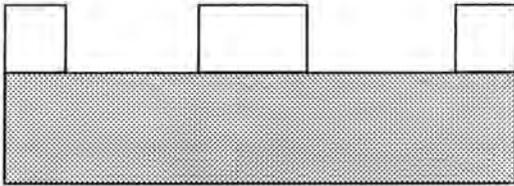
Step 2: Etch the diffusion windows.
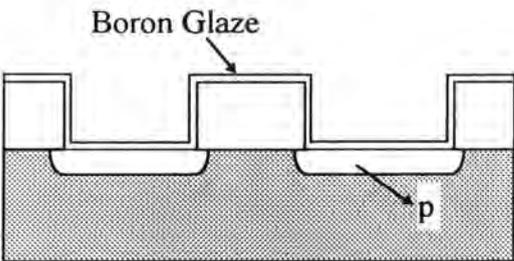
Step 3: Diffuse the source and drain regions.
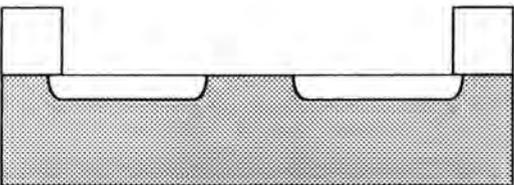
Step 4: Remove the boron glaze and then etch the contact and gate windows.
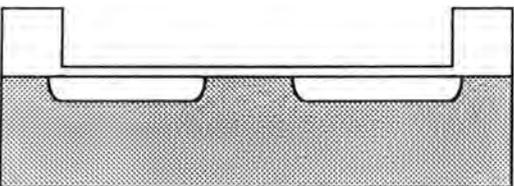
Step 5: Grow the gate oxide.
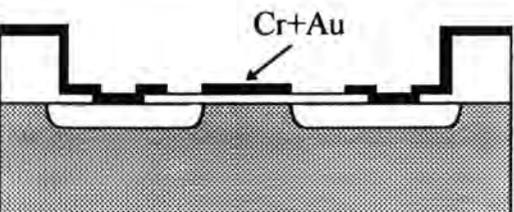
Step 6: Re-etch the contact windows and evaporate and pattern the metallisation.

Figure 5.2 P-MOS transistor fabrication stages.

The silicon wafer and the activated boron nitride wafer were placed in the boron diffusion furnace for a period of 45 minutes (Step 3). During the diffusion the whole wafer became covered with a boron glaze. This was removed by first dipping the slice into 5% HF for one minute. After rinsing, the wafer was boiled in a 1:1:1 mixture of nitric, hydrochloric and sulphuric acids (all concentrated) until the solution became colourless, indicative of the complete removal of the glaze. To conclude this process, the slice was again dipped in 5% HF and thoroughly rinsed, before being placed in the recirculator until the resistivity of the water exceeded 5×10^7 Ω cm. Using the second mask to pattern the photoresist, the gate and contact windows were etched in buffered HF (for approximately four minutes) until the silicon surface became hydrophobic (Stage 4). After rinsing and removal of the photoresist, the wafer was placed in the recirculator until the resistivity of the water reached approximately 10^7 Ω cm.

Prior to growing the gate oxide by dry oxidation (Step 5), the slice was dipped in 10% HF for a few seconds to remove any residual oxide from the surface. The wafer was then placed in propan-2-ol in the ultrasonic bath for 30 seconds, then dried in a stream of compressed nitrogen gas. The period of dry oxidation was 110 minutes; and during this time the boron diffusion was 'driven-in'.

To complete the device fabrication it was necessary to re-cut the contact windows for the source and drain regions and deposit the metal contacts (Step 6). Using the third mask to pattern the photoresist, the contact windows were etched using buffered HF (for approximately one minute) until the wafer became hydrophobic. After rinsing and removal of the photoresist, the slice was placed in the recirculator as before.

At the beginning of this project, a suitable chemical etchant for chromium had not been discovered. This enforced an alternative method of photolithographic patterning to be used known as the lift-off technique,[5] illustrated in Figure 5.3 (b).

In lift-off, the inverse pattern is formed by lithography and the metal is deposited on the masked substrate. Then the desired pattern is revealed by lifting the mask and the unwanted metal. The lifting is accomplished by using a standard solvent (e.g. acetone) to dissolve the photoresist, thus undercutting the overlayer of metal. The metal

deposited through the openings in the lithographic mask adheres directly on the substrate surface, and thus remains after lifting.
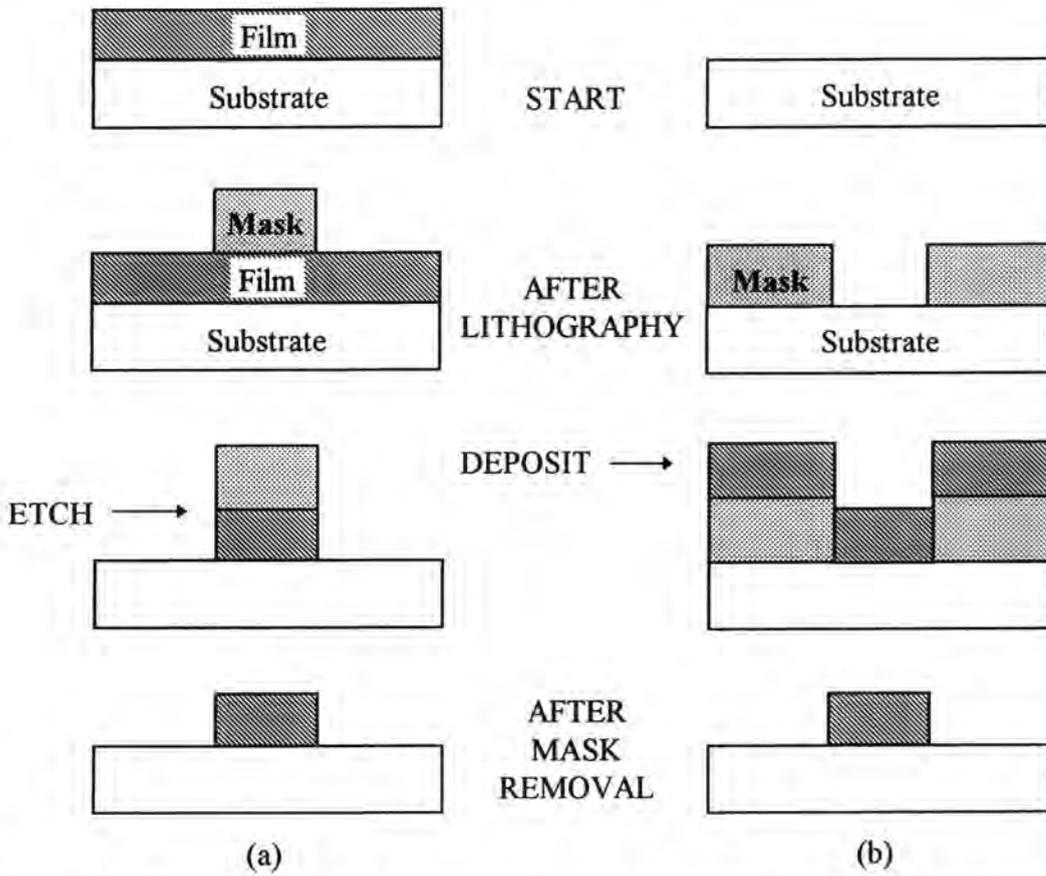
Figure 5.3 Comparison of (a) subtractive and (b) additive (lift-off) methods of photolithographic patterning.

Using the fourth mask (with an inverse pattern to allow lift-off), the photoresist was deposited and patterned before the sample was placed in the evaporator. Once pumped down to between 10^{-5} - 10^{-6} millibar, the thin chromium layer was deposited, followed by the thicker gold layer. Although it was not possible to deposit the same amount of each metal during successive evaporations, the approximate thickness of the chromium layer was 20 nm ± 5 nm and for gold the target was for between 80 nm and 100 nm.

The photoresist was removed, thereby removing the unwanted metallisation, by placing the wafer in acetone in an ultrasonic bath for 30 seconds, or until all the unwanted metallisation had been removed. An assessment of the quality of this procedure was obtained by examining the sample under an optical microscope.

5.3 FABRICATION OF AN ARRAY OF GAS SENSING DEVICES

In this project, rather than produce single p-channel MOSFETs, an array of four devices were fabricated. Three of the four gate electrodes had holes of different dimensions patterned onto them (Figure 5.4) to allow for the incorporation of the active sensing material within the device. The width of metallisation removed from the gate electrode (total width 72 μm) varied from 0 μm (i.e. the control device) to 35 μm. One silicon wafer contained a 4 x 7 arrangement of FET arrays. A cross-section of such a wafer is illustrated in Figure 5.5. Table 5.1 summarises the properties and dimensions of the array of FET devices.

Silicon Wafer [Orientation]	n-type [100]
Resistivity (ρ)	2 – 4 ohm cm
Channel Length (L)	52 μm
Channel Width (W)	260 μm
p-type Doping (N)	7×10^{15} cm^{-3}
Field Oxide Thickness	465 nm
Gate Oxide Thickness	85 nm
Chromium Film Thickness	20 nm $\pm$ 5 nm
Gold Film Thickness	80 – 100 nm
Width of Gate Hole	0 μm, 15 μm, 25 μm & 35 μm

Table 5.1 Summary of the properties and dimensions of a standard array of devices.
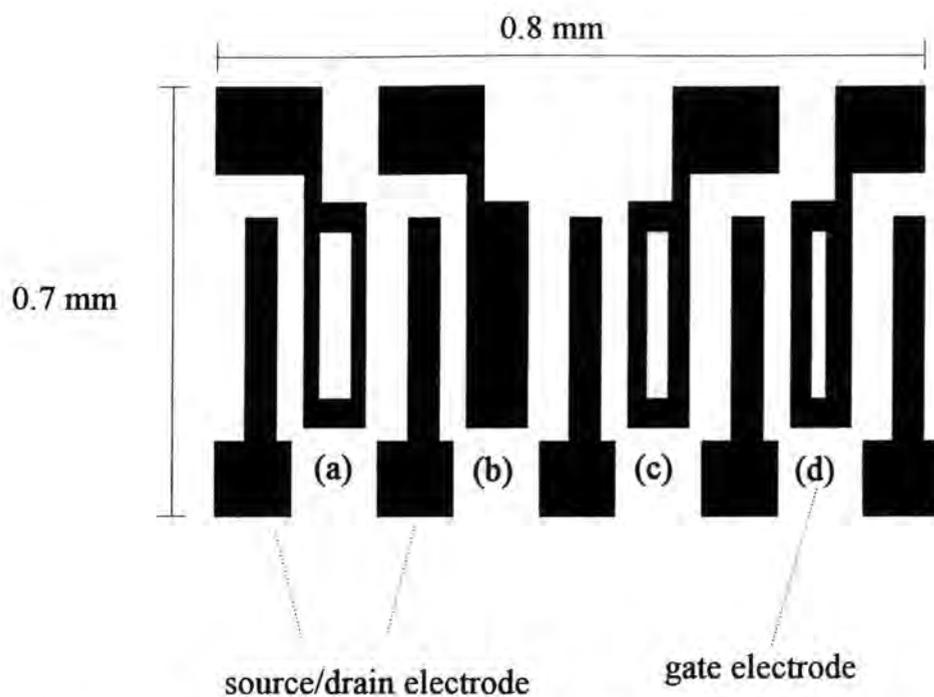
Figure 5.4 A plan of the electrode arrangements of the four FET devices: (a) 35 μm gate-hole; (b) control FET; (c) 25 μm gate-hole; (d) 15 μm gate-hole metallisation.
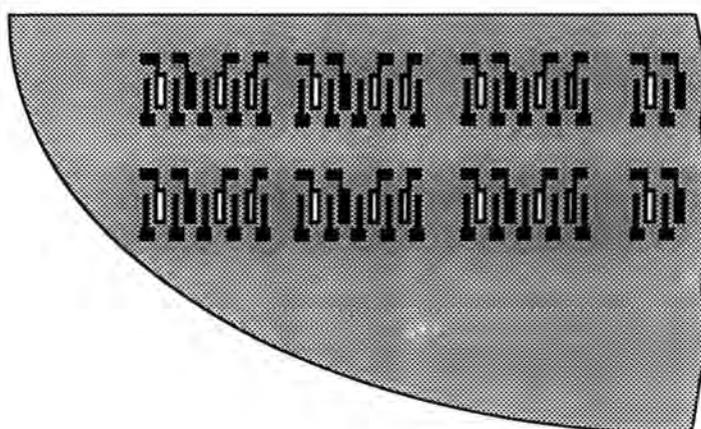
Figure 5.5 A cross-section of a 2" silicon wafer with a 4 x 7 arrangement of FET arrays (as shown in Figure 5.4).

5.3.1 Deposition of the Organic Sensing Material

The organic compounds were deposited from solution using the spin-coating technique.[6,7] For polyaniline the solvent was N-methyl-2-pyrrolidinone (NMP), whilst tetrahydrofuran (THF) was used for the phthalocyanine compound. A programmable

82

spinner, allowing control of the velocity, duration and acceleration of three separate but successive stages was used (Model 4000-Solent Semiconductor Services). An optimum program was devised to produce good quality uniform films.

Before deposition, the wafers were cleaned by stirring in chloroform and then washing in pure water. The dried substrate was placed on the central rotating platform and sufficient solution pipetted onto the surface for complete coverage. The first spin-stage, to spread the material evenly over the surface, was a 50 second cycle at 500 rpm. The critical second stage, which determined the thickness of the resulting film, was varied from 1285 rpm to 3230 rpm (for 50 seconds) until an ideal value was determined. The final deceleration stage was a 50 second cycle at 300 rpm. For these last two stages an infra-red heat lamp, set to 80°C, was positioned directly over the wafer to ensure the rapid evaporation of the remaining solvent. The results for the variation in film thickness with the second stage spin speed for polyaniline, will be presented in Chapter Six.

To pattern the organic material a fifth mask was prepared and the photoresist was deposited and processed in the normal manner. The mask was designed so that photoresist covered the four gate electrodes in each array. Exposed areas of the organic layer were then etched away by gently stirring in 35% nitric acid.[6] The sample was visually inspected under a microscope to ensure that all the exposed material had been etched away before rinsing with distilled water and drying under compressed nitrogen gas. The remaining unexposed photoresist overlying the patterned gas-sensitive material was removed by stirring the slide in Shipley 1112A Microposit remover that had been diluted to one-third of its original concentration with water. (Using acetone in an ultrasonic bath was found to be too aggressive; removing the polyaniline/phthalocyanine as well as the photoresist.) The wafer was then rinsed in pure water and dried under compressed nitrogen gas.

Figure 5.6 shows the results of a surface profile (Tencor Alphastep) scan across one of the FET devices; this structure had a 25μm gate hole. The top (dashed curve) scan is for the final patterned polymer-coated structure. The two deep troughs in the plot correspond to the source and drain contact holes. The middle plot (full curve) is for the same device but after the polyaniline layer has been removed by dissolving in NMP.
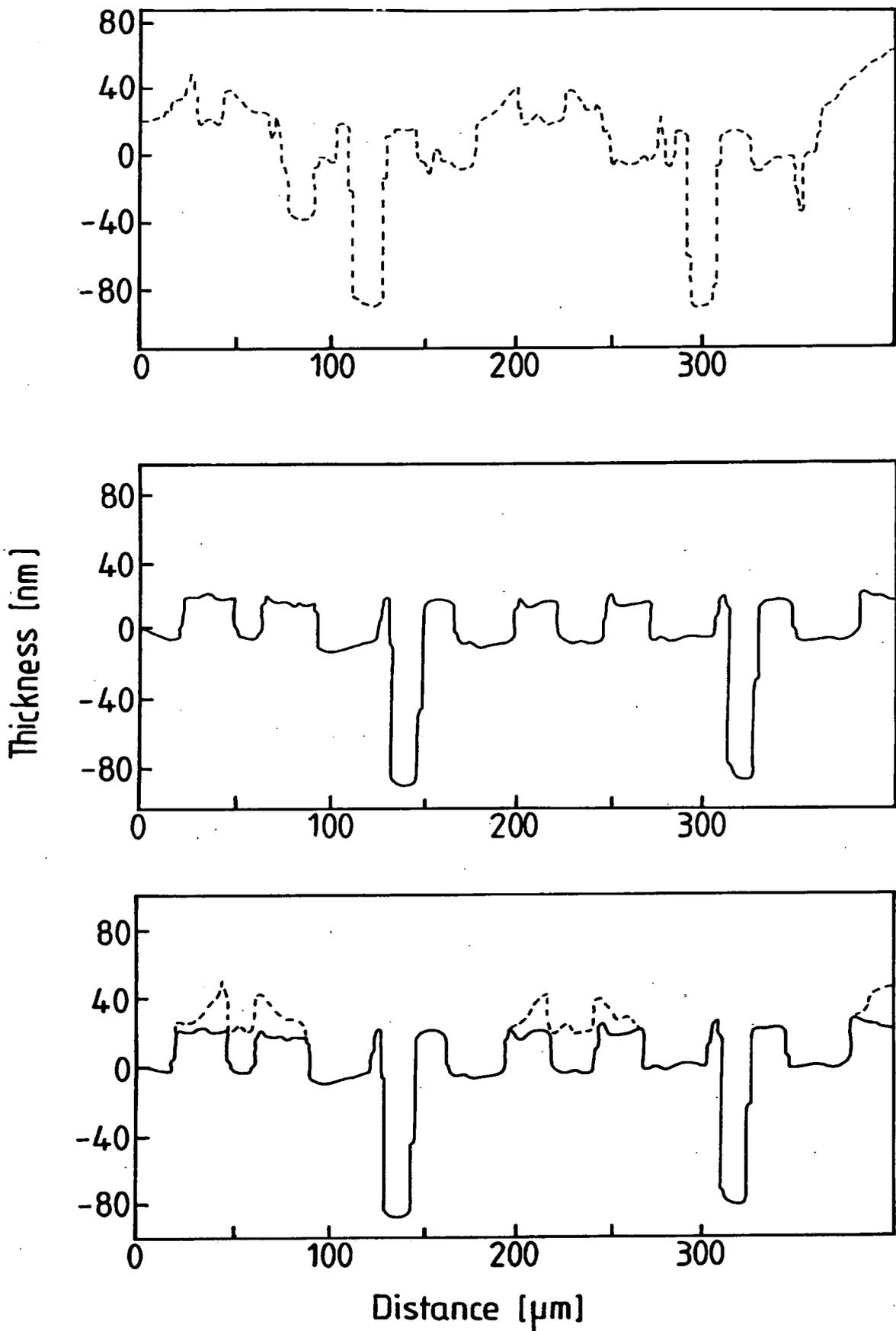
Figure 5.6 Surface profile scan across the 15 μm and 25 μm FET devices. Top: with final patterned polyaniline layer. Centre: with polymer layer removed. Bottom: difference scan.

The difference in these two scans is highlighted in the bottom plot in Figure 5.6 revealing the presence of the polymer in the hole in the gate metal. Figure 5.7 illustrates a schematic cross-section of a completed sensor device.
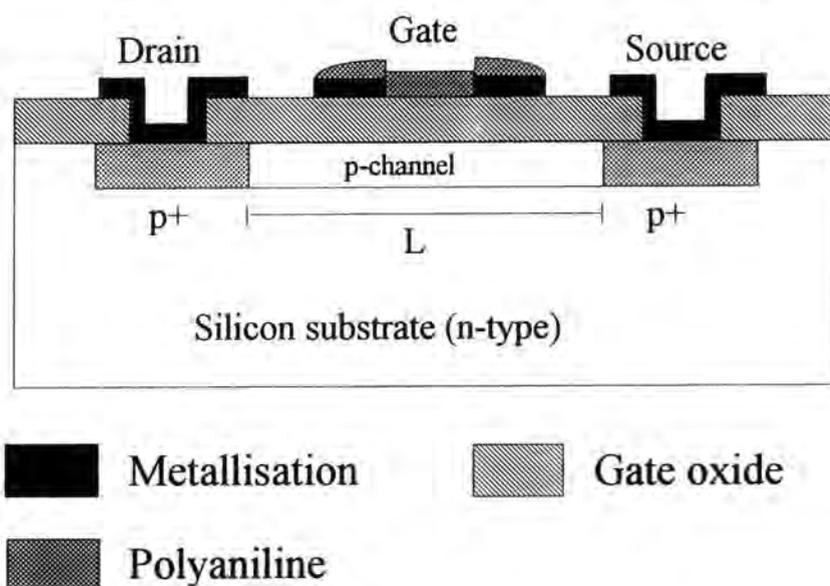
Figure 5.7 A schematic cross-section of an organic/silicon hybrid FET sensor.

5.4 DEVICE CHARACTERISATION

The electrical characteristics of the devices were examined both before and after the deposition of the organic material. This allowed an assessment of the effect of the organic on the operation of the transistor. The gas sensing experiments were accomplished in a custom-built system as described below.

5.4.1 Gas Sensing System

To characterise the sensors, a purpose-built electrical measurement system was used (Figure 5.8). This comprised a gas-tight chamber, within which the sensor was mounted. A Peltier effect heat-pump coupled with a CAL 9900 programmable temperature controller allowed the device to be operated from room temperature up to approximately 75°C. A Lutron HT-3003 humidity/temperature meter was used to monitor the humidity level within the chamber. For the majority of the work, the
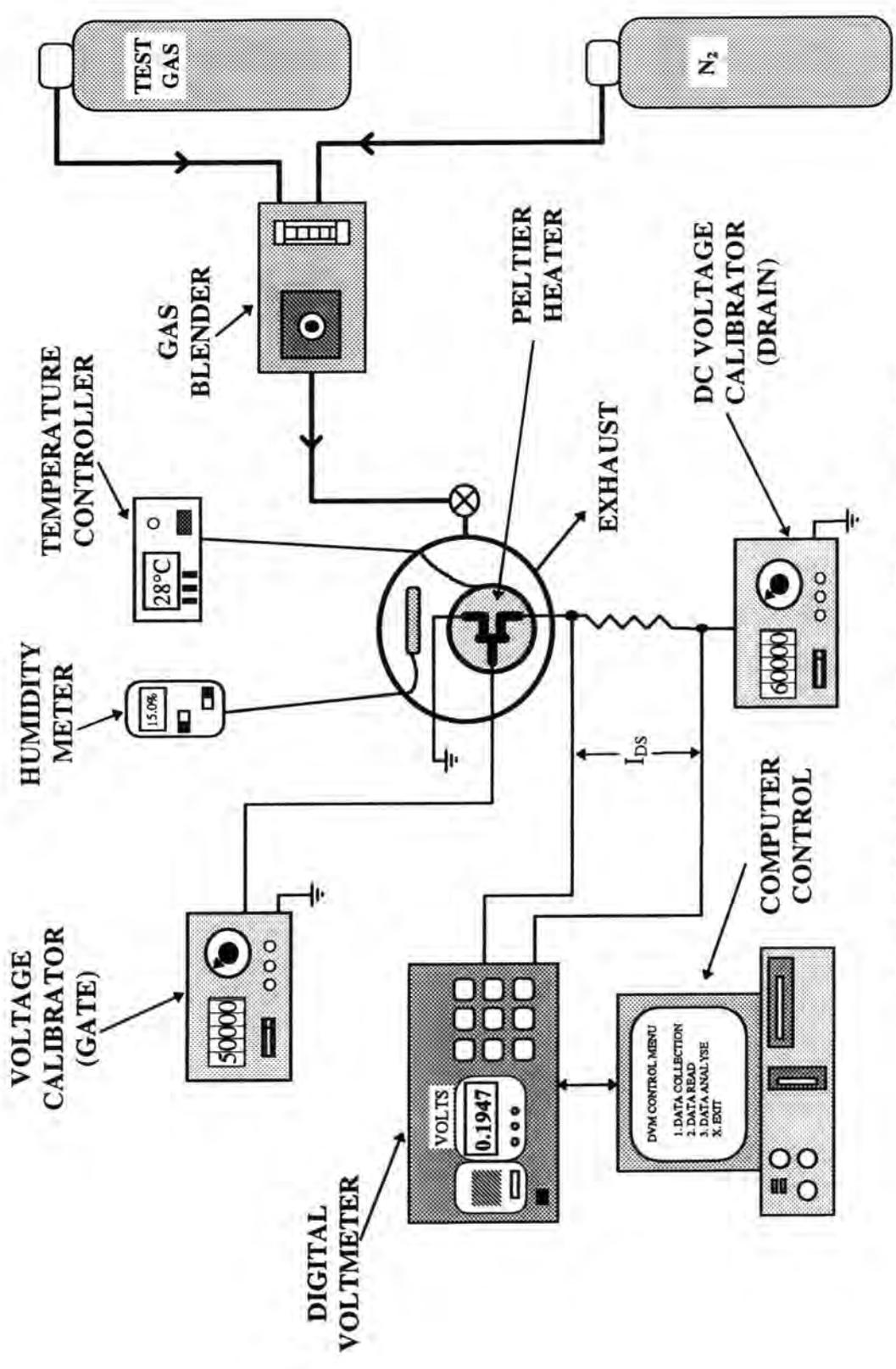
Figure 5.8 The Gas-Tight Electrical Measurement System

humidity was controlled, and kept approximately constant by using desiccant and allowing the atmosphere within the chamber to re-stabilise after opening to air.

Contacts to the drain, source and gate electrode were made using microprobes with X-, Y- and Z-axis control. The concentration of the gas was varied by using a Signal series 850 gas blender, which mixed the test gas with an inert balance gas, in this case nitrogen. The electrical characteristics were recorded using a Hewlett-Packard 3437A digital voltmeter linked to a computer-controlled data-acquisition program (see Appendix A for Turbo Pascal source code).

The procedure for testing a device required that a steady baseline response was first achieved in an inert nitrogen ambient, i.e., that consecutive 'turn-on' responses differed by no more than ± 2 μA (< 1%). Following this, the test gas was introduced and blended to the required concentration. To be certain of having a uniform atmosphere within the chamber, a period of one hour, whilst the gas was flowing, was allowed to elapse before recording the next 'turn-on' response. Subsequently, the supply of the test gas was terminated and pure nitrogen passed through until the baseline was re-established. Figure 5.9 contrasts the 'turn-on' response for an FET with an entirely metallic gate, to a hybrid device with a section of the gate metal replaced with an organic compound.
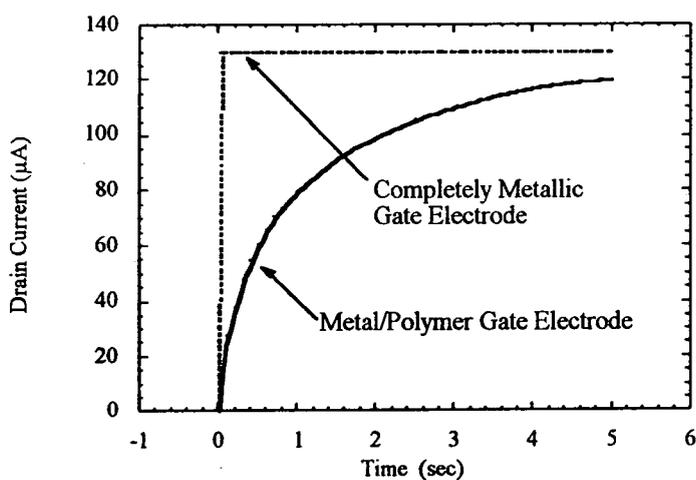
Figure 5.9 Illustration of the 'turn-on' effect for (i) a metallic-gate FET and, (ii) a metal/organic gate FET. The gate voltage, V_{gs}, is applied at time t = 0 seconds.

5.4.2 Capacitance-Voltage Measurements

The capacitance versus voltage (C-V) characteristics of MOS capacitors have been shown to be extremely useful in the evaluation of the electrical properties of the insulator-semiconductor interfaces. Before the devices in this work could be analysed, an ohmic-contact was required on the underside of the silicon wafer.

The surface was initially cleaned using 10% HF to remove any contaminants and/or oxide layer. The wafer was mounted and clamped in the evaporator above a metal mask with a rectangular section removed. This allowed the deposition of a metallic contact across the rear surface of the silicon. To create a good ohmic-contact to n-type silicon it is necessary to create a more heavily doped n^+ region adjacent to it, thus narrowing the space-charge region sufficiently to allow charge to tunnel through the Schottky barrier.[8] For this reason gold with trace amounts (1%) of antimony (an electron donor) was used as the source metal.

Figure 5.10 illustrates the electrical circuit used to measure the differential capacitance, $\frac{\partial Q}{\partial V}$, and hence determine the C-V characteristics.
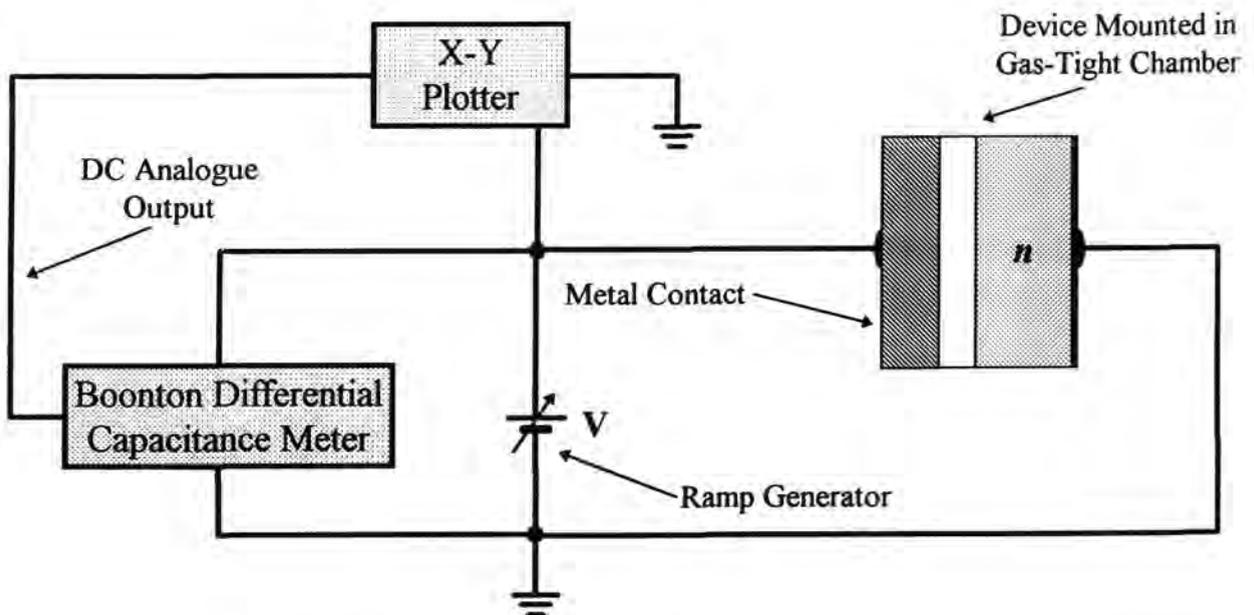
Figure 5.10 Representation of the configuration for measuring the C-V characteristics of the sensor.

The capacitance of the devices, at 1 MHz, was measured with a Boonton 72 BD capacitance meter. The measurement frequency must be high enough so that the relaxation times of interface states can be ignored.[9] The a.c. voltage for the capacitance measurement should be less than 18 mV rms to avoid non-linear effects, and in this case was 15 mV rms. The rate at which the bias voltage is ramped must be slow enough so that thermal equilibrium is maintained. Typical values are in the range between 1 mV s^{-1} and 100 mV s^{-1}.[9]

The C-V characteristics of devices with and without polyaniline deposited; in dark and light conditions were obtained at room temperature and in standard atmospheric conditions. Experiments to evaluate the effect on the C-V response upon exposure to different gases (NO_2, SO_2 and H_2S) were also carried out.

5.5 OPTICAL CHARACTERISATION OF THIN-FILMS

Samples of the organic material were prepared on glass substrates and used to determine the characteristics of the film before and after exposure to a gas.

5.5.1 Ultraviolet/Visible Spectroscopy

The changes in the optical characteristics, and hence the chemical properties of the organic films after exposure to the test gas, were monitored. Glass substrates approximately 1 cm^2 in size were cleaned by scrubbing with Decon 90; then rinsed thoroughly in pure water; before a 20 minute ultrasonic agitation in pure water. After drying in a stream of compressed nitrogen, the organic materials were deposited by spin-coating as previously described (§5.3.1).

The optical absorption spectra were recorded using a Perkin-Elmer Lambda 19 ultraviolet/visible/near-infrared spectrophotometer. An uncoated glass substrate placed in the reference beam was used for the background correction. The sample was exposed to a known concentration of a gas by placing it in the gas-tight sample chamber for a set period of time.

5.6 SUMMARY

The methods of silicon device fabrication and the technique of deposition by spin-coating of thin films of organic materials have been described. The FET sensors have been electrically characterised (by the 'turn-on' response and through C-V measurements) in various, well controlled gaseous ambients. The optical characterisation of thin films deposited on glass substrates, and the effect of exposure to different gases, has been summarised. In the following chapter the results for the electrical characterisation of the devices will be presented.

REFERENCES

1. B.E. Deal, *J. Electrochem. Soc.*, **110** (1963) 527-533.

2. C.R. Fuller and F.J. Strieter, *Extended Abstracts of Electronic Division*, **13** (1964) 180-181.

3. Motorola Semiconductor Products Inc., Research and Development for Surface Protection of Semiconductor Devices, by M.A. Hall, H.W. Cooper and S.S. Flaschen, AF CRL-64-188, Final Report, Contract No. AF 19(604)-8358, Phoenix, Arizona, 14 Dec. 1963 (U) AD 437 399.

4. M. Pons, J. Pelletier, O. Joubert and P. Paniez, *Jpn. J. Appl. Phys.*, **34** (1995) 3723-3730.

5. T. Sakurai and T. Serikawa, *J. Electrochem. Soc.*, **126** (1979) 1257-1260.

6. C. Di Bartolomeo, P.S. Barker, M.C. Petty, P. Adams and A.P. Monkman, *Advanced Materials for Optics and Electronics*, **2** (1993) 233-236.

7. M. Scully, M.C. Petty and A.P. Monkman, *Synth. Met.*, **55** (1993) 183-187.

8. D.K. Scroder *Semiconductor Material and Device Characterisation* (Wiley 1990) 100-104.

9. A. Goetzberger, E. Klausmann and M.J. Schulz, *CRC Critical Reviews in Solid State Sciences,* **6** (1976) 1-43.

BIBLIOGRAPHY

J.W. Gardener *Microsensors: Principles and Applications* (Wiley 1994) 36-58

R.J. Huber, in: *Solid State Chemical Sensors* ed J. Janata and R.J. Huber (Academic Press 1985) 119-162

S. Middelhoek and S.A. Audet: *Silicon Sensors* (Academic Press 1989) 287-330

D.A. McGillis, in: *VLSI Technology* ed S.M. Sze (McGraw-Hill 1983) 267-301

C.J. Mogab, in: *VLSI Technology* ed S.M. Sze (McGraw-Hill 1983) 303-345

D.B. Fraser, in: *VLSI Technology* ed S.M. Sze (McGraw-Hill 1983) 347-384

CHAPTER SIX

DEVICE CHARACTERISATION: RESULTS AND DISCUSSION

This chapter describes the physical and electrical characterisation of the organic/silicon hybrid field-effect transistor. Results are presented for devices with and without polyaniline deposited. The electrical performance over a range of temperatures, and the effect of humidity on both the polyaniline and the phthalocyanine devices are also discussed.

6.1 SPIN-COATED POLYANILINE THIN FILMS

To understand the effects of the various parameters involved during the spin coating and chemical patterning of polyaniline films, the processes were first performed on glass substrates to allow the analysis of changes, if any, in the film thickness and chemical properties.

6.1.1 Dependence of Film Thickness on Spin Speed

Polymeric materials have been shown to behave as non-Newtonian fluids during spin-coating.[1,2] It has been established that the initial volume of fluid dispensed onto the substrate, and whether it is deposited whilst the substrate is static or rotating has a negligible effect on the final film thickness.[3] The two parameters that determine this value are the viscosity of the solution and the final spin speed.

It had already been shown that 6% by weight solutions of polyaniline dissolved in N-methyl-2-pyrrolidone (NMP) produced good quality thin films that could be successfully patterned using photolithographic techniques.[4] Before attempting to deposit 4% by weight solutions of polyaniline onto the FET devices, an investigation

into the variation of resultant film thickness with spin-speed was undertaken using 1 cm^2 glass substrates.

Having carefully scored through each film to the glass substrate, a Tencor Alpha Step was used to accurately measure the thickness. Figure 6.1 shows how the thickness of the spin-coated films varied with spin speed in the range 1285 rpm to 3230 rpm. To minimise error, three sets of data were collected in identical conditions and the average value used for each point.

Previous work on the spinning of polymers has revealed both exponential [2] and linear [5] dependencies of film thickness and spin speed. It is evident from Figure 6.1 that polyaniline does not fit into either of these categories. In this case the thickness of the film varied with spin speed such that,

$$\text{Film Thickness} \propto (\text{Spin Speed})^{-1}.$$

It was found that faster spin speeds (> 1200 rpm) produced more uniform films. It is thought that this was due to the polyaniline behaving more like a Newtonian fluid.[1]

6.1.2 Optical Characterisation of Polyaniline Films Before and After Patterning

To assess the effects, if any, of device processing on the physical or chemical properties of the polyaniline, the patterning procedure was repeated for a thin film of polyaniline deposited onto a cleaned glass substrate. Figure 6.2 shows the optical absorption spectra for the film before and after the patterning process. There are two main absorption bands, centred on 315 nm and 615 nm. These are due to $\pi \rightarrow \pi^*$ electronic transitions, which have already been described in § 3.1.3. It can be seen that there are no differences in the two spectra (within experimental error), confirming that the polymer has not undergone any significant changes during the patterning process. These spectra are in good agreement with results presented in the literature for the optical spectra of thin films of polyaniline in the emeraldine base form.[6,7]
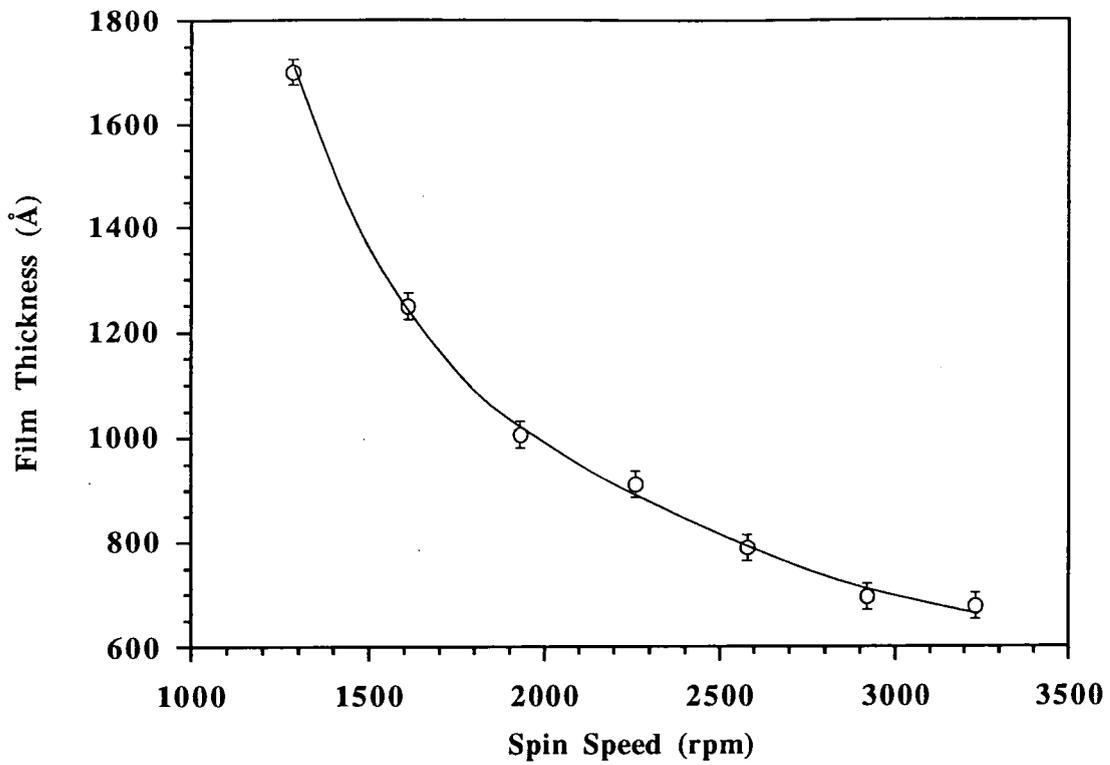
Figure 6.1 The variation of film thickness with spin speed for 4% by weight solutions of polyaniline.
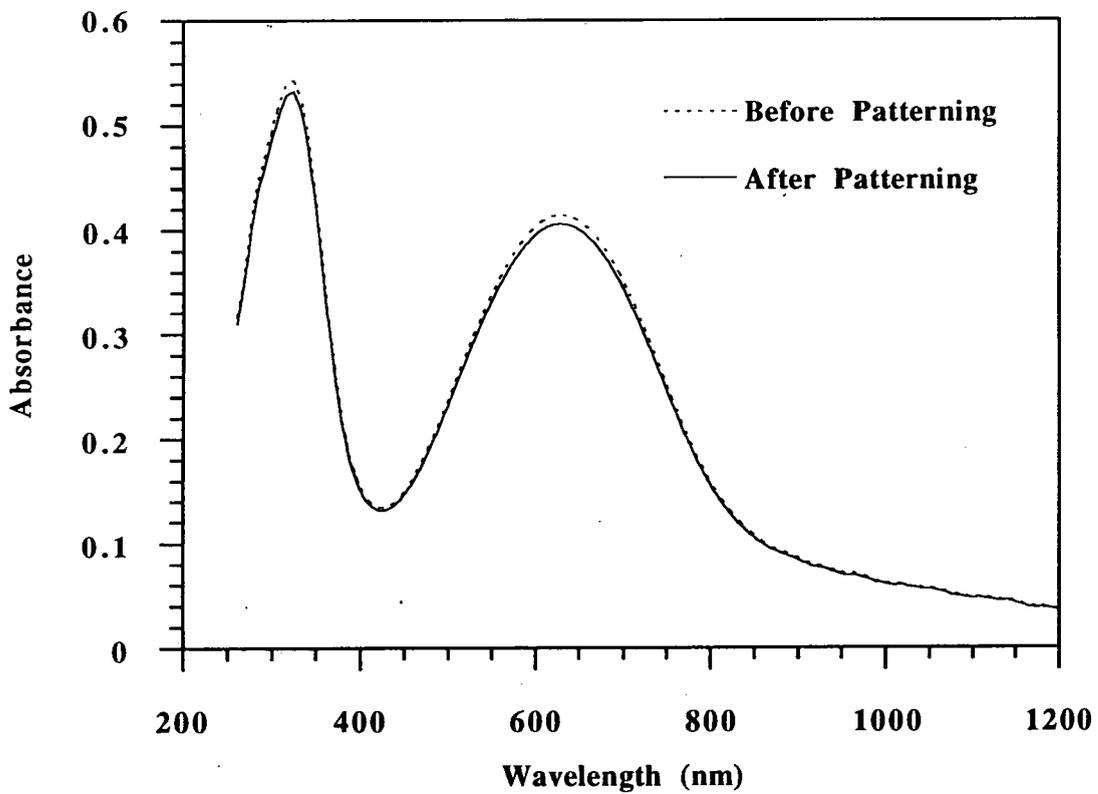
Figure 6.2 Ultra-violet-visible spectra of a 80 nm thick polyaniline film before and after chemical patterning.

6.2 CAPACITANCE-VOLTAGE MEASUREMENTS

The capacitance versus voltage (C-V) characteristics of MOS capacitors that result from the modulation of the width of the surface space charge region by the gate field have been found to provide a valuable insight into the electrical properties of insulator-semiconductor interfaces.

Figure 6.3 shows the C-V relationship, measured at 1 MHz, for the four different FET structures without polyaniline deposited within the openings in the gate metallisation. The decreasing value of the oxide capacitance, C_{ox}, in the accumulation region (i.e. > +2 V) with the increasing area of gate metallisation removed is entirely expected. This is because majority carriers are only attracted to the oxide/silicon interface at points where charged metallisation exists.

Table 6.1 shows the comparison of the theoretical values of C_{ox} with the measured data. In strong accumulation, the total capacitance per unit area, C_T, as defined in Equation [4.1] is equal to the oxide capacitance, C_{ox}. This is because the large density of majority carriers attracted to the oxide-semiconductor interface effectively shorts out the semiconductor capacitance. The oxide capacitance per unit area is given by

$$C_{ox} = \frac{\varepsilon_{ox}}{t_{ox}}, \qquad\qquad [6.1]$$

where ε_{ox} is the oxide permittivity and t_{ox} is the oxide thickness. For silicon oxide, ε_{ox} is 3.45×10^{-11} F m^{-1} and t_{ox} for these devices was 85 nm. The product of the oxide capacitance per unit area and the area of metallisation for each device gives the absolute value of capacitance shown in Table 6.1.

Comparison of the theoretical values with the measured data shows the calculated figures to be between 26% (for the control device) and 31% (for the 35 μm gate-hole device) lower than the measured values. These apparently significant differences can be placed into perspective when it is noted that the maximum oxide capacitance was only 11.9 pF for the control device and 7.4 pF for the 35 μm gate-hole device. It is thought that parasitic capacitance due to the measuring circuit results in the observed increase in C_{ox} for all four devices.
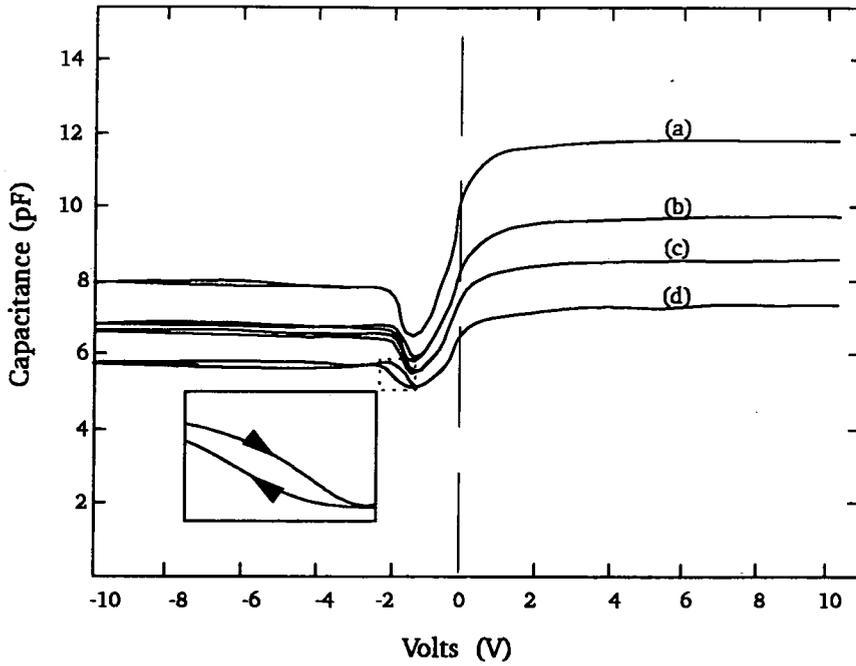
Figure 6.3 Room temperature capacitance - voltage curves for the
four FET devices without polyaniline deposited: (a) control FET;
(b) 15 μm gate - hole; (c) 25 μm gate - hole; (d) 35 μm gate - hole.
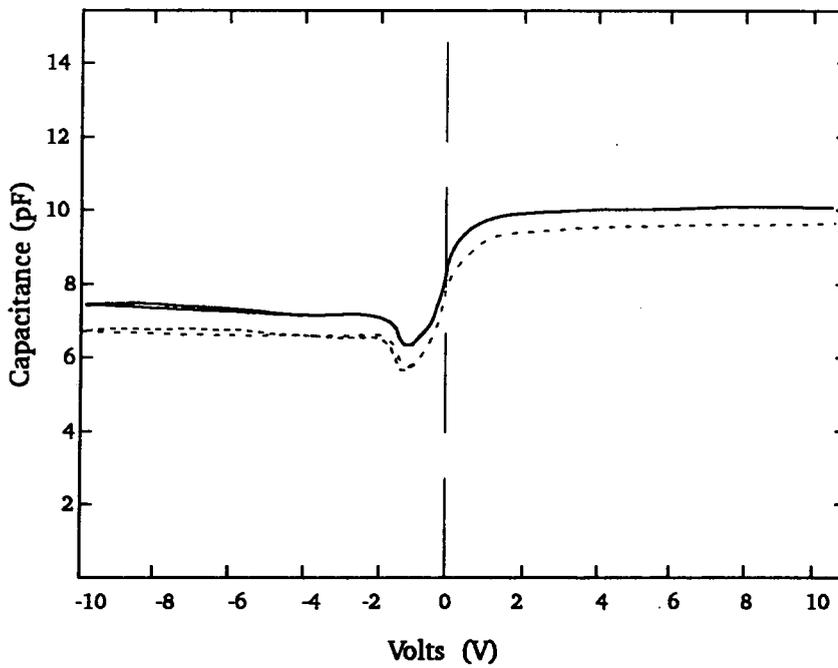
Figure 6.4 Room temperature capacitance - voltage curves for the
15 μm gate - hole FET with (full) and without (dashed curve)
polyaniline deposited.

Gate-hole (μm)	Measured C_{ox} (pF)	Theoretical C_{ox} (pF)	% Reduction (from measured)
0	11.9 ± 0.1	8.8	26
15	9.8 ± 0.1	7.2	27
25	8.6 ± 0.1	6.1	29
35	7.4 ± 0.1	5.1	31

Table 6.1 A comparison of the theoretical and measured values of the oxide capacitance, C_{ox}.

6.2.1 Deviation from the Theoretical High Frequency Response

It is evident from Figure 6.3 that there is a deviation from the expected high frequency response in the inversion region. For a p-type device this could be explained by the presence of lateral alternating current flow in the inversion layer due to positive charges in the insulator and/or on the surface.[8] This effect is only observed for p-type silicon devices where the presence of positive oxide charge induces an inversion layer in all regions underlying the oxide, including those not covered by the gate metal. The inversion layer can be considered to consist of two parts: an intrinsic section lying directly beneath the metal and an extrinsic section consisting of those areas of the semiconductor covered by the oxide but not the metal. Obviously, for an n-type device, the positive oxide charge induces an n^+ layer instead of the inversion layer and the high frequency response corresponds to that predicted for an ideal device.

The capacitors used in this work were constructed from a single array of transistor devices with the addition of an ohmic back contact. Therefore two p^+ doped regions (source and drain) existed beneath the oxide layer. For this reason a lateral alternating current flow could occur in the inversion layer due to a coupling effect between the

positive charge attracted to directly below the gate electrode at the silicon-oxide interface, and the p^+ doped source and drain regions.

The inversion layer is essentially connected with minority carriers present across the entire surface of the capacitor. The flow lines of the alternating current are shown in Figure 6.5. The current flows across the insulator as a displacement current (i.e. equivalent to the current flow in the dielectric of a charging capacitor), then spreads out in the high-conductivity inversion region (channel region) and finally flows across the depletion capacitance in an area much larger than the metal plate. This channel connection greatly enhances the response time of the minority carriers, and the cut-off frequency of the channel becomes considerably higher (as large as 50 MHz) than that for minority carriers under equilibrium condition.
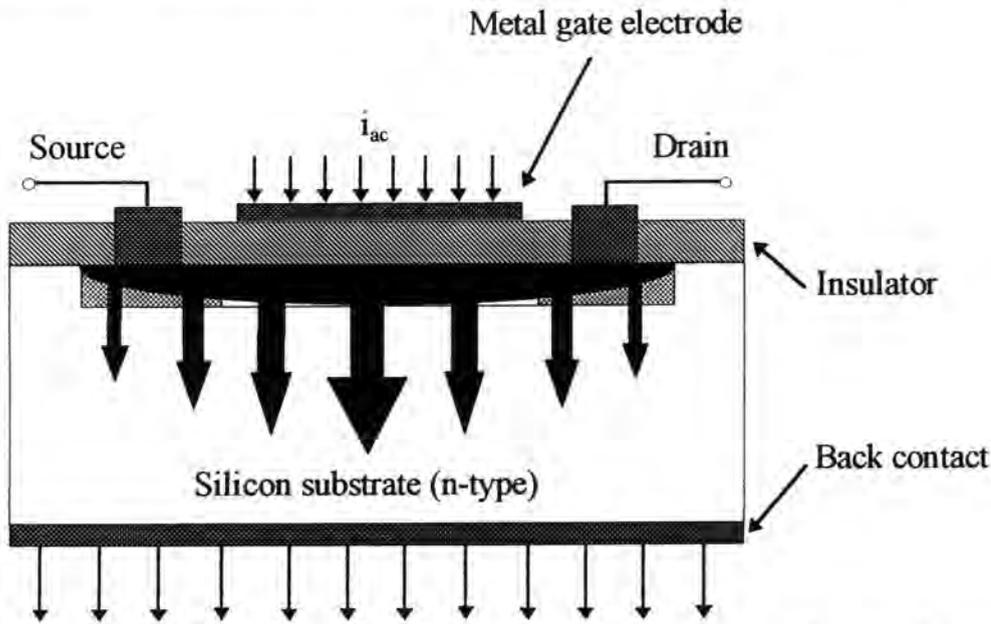
Figure 6.5 A schematic diagram of the a.c. current flow at zero d.c. bias between the field plate and the silicon. The radial decrease of the current along the channel is depicted. [Adapted from Ref. 8.]

6.2.2 Effects Due to Surface States and Mobile Ions

In a typical MOS capacitor there exist many states and charges which affect the ideal MOS characteristics. These include surface states and mobile ions due to oxide

impurities (as discussed in § 4.1.5). One of the consequences of the presence of these states is the hysteresis highlighted in the inset shown in Figure 6.3.

Hysteresis can be seen in the inversion region for the three MOS capacitors with metallisation removed from the gate electrode, the effect becoming greater as the area of the gate-hole is increased. This phenomenon is characteristic of the trapping of mobile ions in states in the oxide layer.[9]

For the entirely metallic electrode, all the mobile ions within the oxide will be influenced directly by the image charge created on the field-plate. In contrast, for those electrodes with some metallisation removed (creating an oxide-air interface surrounded by two metal-oxide interfaces), there is a central region of oxide containing mobile ions not under the direct influence of an image charge. As the bias voltage is ramped into the inversion region (bias voltage < 0) these ions drift towards the oxide-air interface, where they become trapped in what are effectively potential wells. When the applied bias is swept back towards positive voltages, this charge remains trapped until a more positive voltage is applied. Hence for a particular voltage in the inversion region, the total capacitance on the reverse sweep is greater than on the forward sweep because of the trapped charge. As the area of metallisation removed increases, the number of ions available to drift and subsequently become trapped also increases. This explains why the hysteresis effect becomes progressively greater as the size of the gate-hole is increased.

Figure 6.4 shows a comparison of the C-V responses for the 15 μm gate with (full line) and without (dashed line) polyaniline deposited within the hole in the gate metallisation. With polyaniline present, the total capacitance in all regions of the trace is greater in comparison to the air-gap response. This increase in capacitance occurs because the thin film of polyaniline is less resistive than the air-gap, allowing partial charging as the gate bias is swept from +10 volts to -10 volts. Because the polymer does not possess metallic-like conductivity, the increase in the total capacitance is unable to approach that measured for the entirely metallic gate electrode MOS capacitor. The hysteresis effect is reduced to negligible levels when the polymer is present in the air-gap. This was also found to be the case for the 25 μm and 35 μm

gate MOS capacitors. Again, this is because the polymer is able to conduct some charge from the surrounding metallic regions of the electrode and thus drive mobile ions away from the polymer-oxide interface at a gate bias that is independent of its direction of sweep.

6.3 DC OPERATING CHARACTERISTICS

Figure 6.6 shows the room temperature d.c. operating characteristics for the 15 μm p-channel enhancement mode MOSFET, with polyaniline deposited within the gate hole. These curves are of the same general form as for an entirely metallic gate electrode device. It was important to allow sufficient time for the metallisation and polyaniline to acquire a uniform charge for each applied gate bias. If not, hysteresis effects were observed in the curves, increasing as the ratio of polymer-to-metal increased. Without the polymer present in the gate electrodes it was not possible to obtain reasonable d.c. operating characteristics. This was because the conducting channel could not be readily formed without the polymer present to charge to the applied bias. This effect will be described later (§ 6.6.1) with reference to the 'turn-on' (§ 4.4) response of the device.

Figure 6.7 displays a comparison of the dc operating characteristics for the complete array of devices (again with polyaniline deposited) for an applied gate bias of -4.0 V. It can be seen that the drain current saturates at a significantly larger value for the entirely metallic gate electrode FET, in comparison to those with polyaniline deposited within the air-gap. The polymer-metal contact is the critical factor that determines the electrical response of the other three devices. The ability for charge-transfer from the highly conductive metallic areas of the gate electrode to the more resistive organic regions was crucial in the formation of a complete conducting channel between the drain and source regions. For this reason it was not possible to fabricate arrays of FETs with identical electrical characteristics even on the same silicon wafer.

Figure 6.7 illustrates this difficulty by the variation in the d.c. response of the 15-, 25- and 35 μm gate-hole devices. It can be seen that the saturated drain current is greater
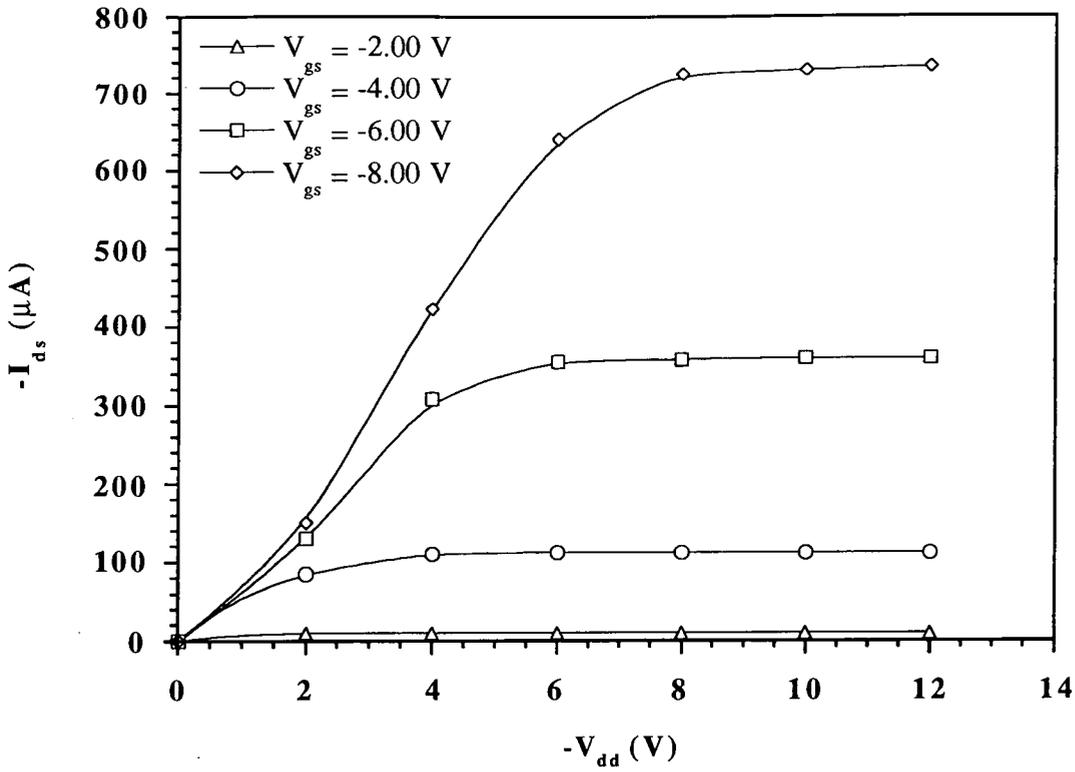
Figure 6.6 Source-drain current I_{ds} vs. drain voltage V_{dd} at room temperature for a 15 μm FET with polyaniline deposited.
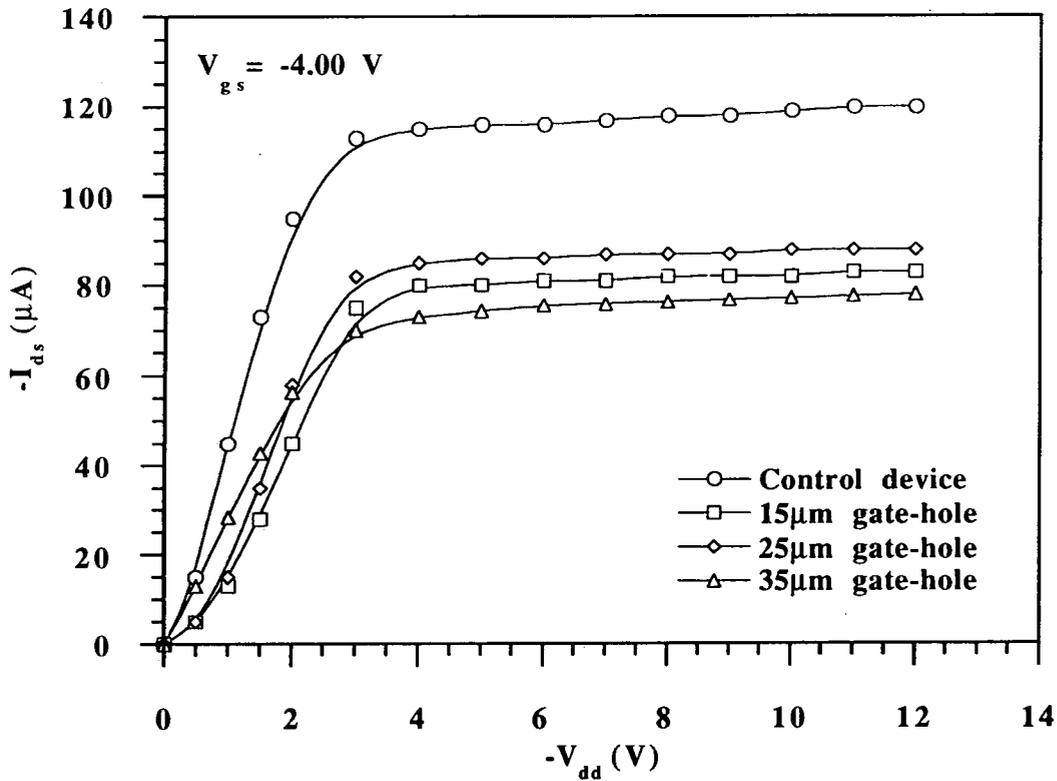
Figure 6.7 Source-drain current I_{ds} vs. drain voltage V_{dd} for a fixed gate bias ($V_{gs} = -4.0$ V) at room temperature for a complete array of devices with polyaniline deposited.

for the 25 μm gate-hole device than for the 15 μm device, whilst the 35 μm FET saturates at the lowest value. For a different array of devices, on the same silicon wafer, a different set of responses for the same operating conditions could be observed. For an ideal array of sensors, it may be expected that the characteristics would be dependent on the ratio of the surface area of polyaniline to that of the metal, the total of which would comprise the gate electrode. It is apparent that the uniformity of the film deposited within the air-gap, and the quality of the contact with the metallisation, varies in each gate electrode.

6.4 THRESHOLD VOLTAGE

The threshold voltage, V_T, associated with a MOSFET is the minimum gate voltage required to create an inversion layer at the silicon-silicon oxide interface, inducing a conducting channel between the drain and the source regions (§ 4.2.1). It can be determined experimentally by examining the low-gate-voltage behaviour of the device either at low values of drain voltage, well below 'pinch-off', or within the region of saturated drain current.

Below 'pinch-off' the threshold voltage can be obtained from the variation of the drain current as a function of the gate voltage (with the drain voltage held constant) and extrapolating the resulting curve to obtain the gate voltage intercept (equal to the threshold voltage). Alternatively, the threshold voltage may be established in the saturated drain current region by measuring the square root of the drain current as a function of gate bias at a constant drain voltage well beyond the 'pinch-off' region. Once again, the extrapolated gate voltage intercept is equal to the threshold voltage. When measured using either of these techniques, the threshold voltage is independent of the ratio of the channel width to the channel length of the MOSFET.

Using the second technique, Figure 6.8 shows the square root of the saturated drain current versus the gate bias at various substrate temperatures. From the extrapolated gate voltage intercepts, the variation of the threshold voltage with substrate temperature was evaluated, as illustrated in Figure 6.9.
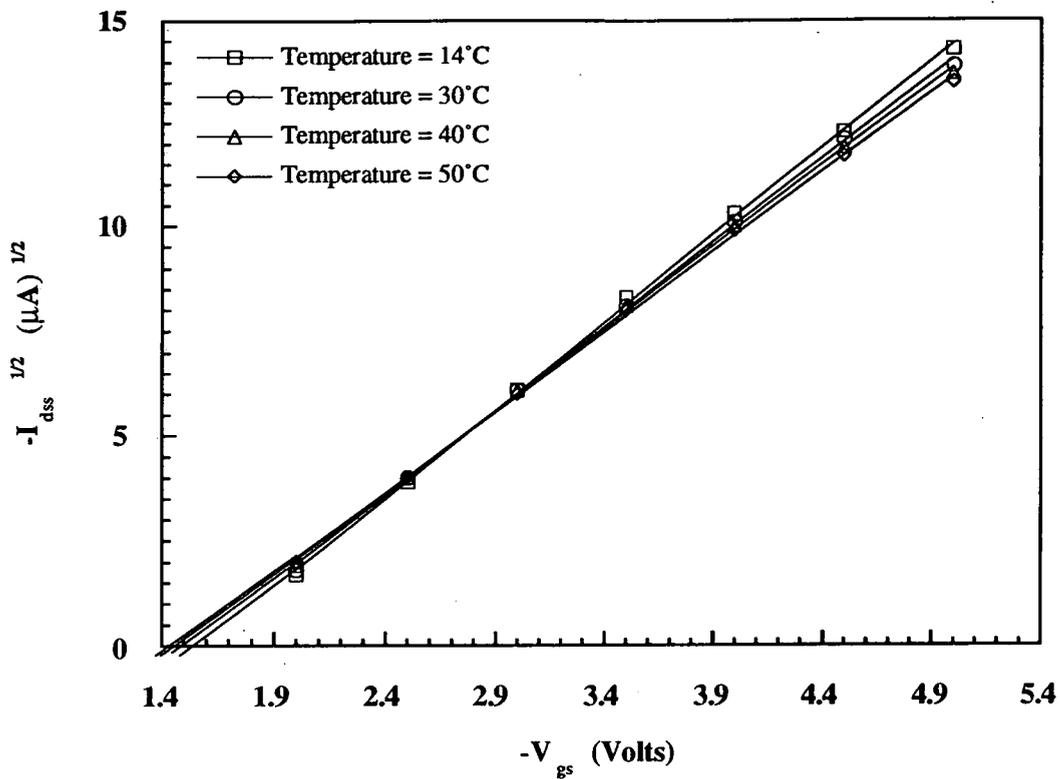
Figure 6.8 A plot of $(I_{dss})^{1/2}$ vs. V_{gs} at various substrate temperatures for the control device.
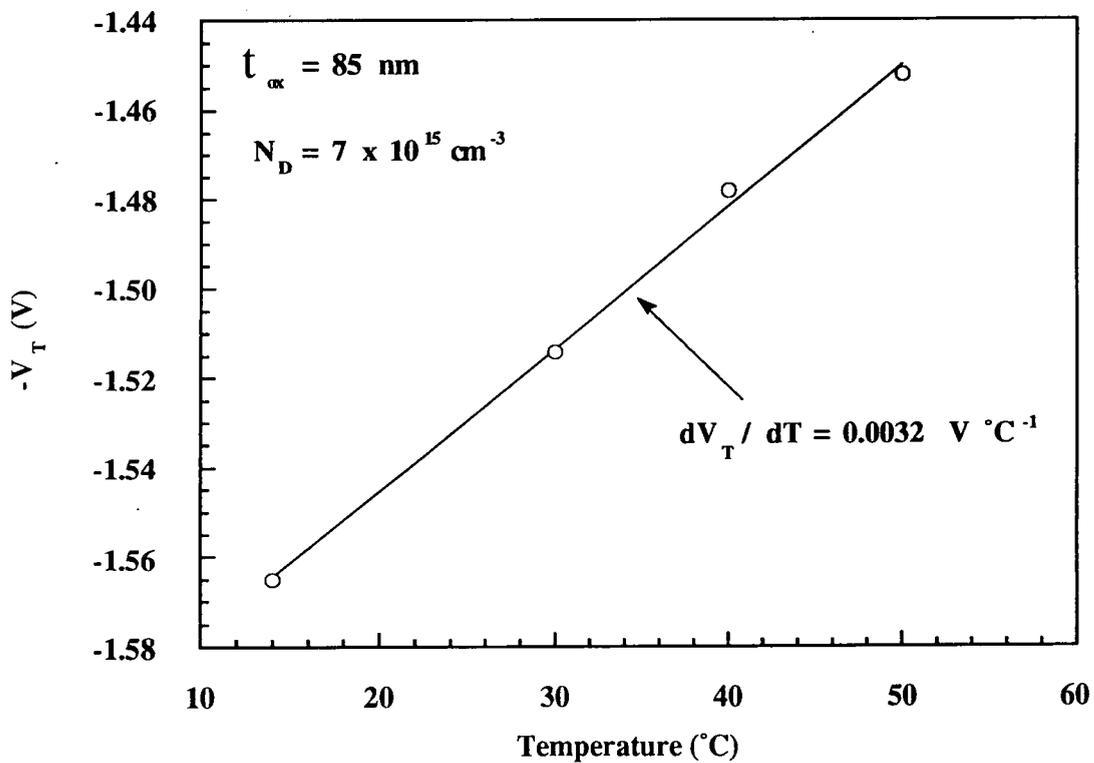
Figure 6.9 The variation of the threshold voltage V_T with substrate temperature for the control device.

The threshold voltage was found to be approximately a linear function of temperature, over the range + 20°C ($V_T \approx$ -1.54 V) to + 50°C ($V_T \approx$ -1.45 V). In comparison, for the 35 μm gate-hole FET device with polyaniline deposited, the threshold voltages for the two extremes of operating temperature were evaluated to be $\approx$ -1.50 V at +20°C and $\approx$ -1.35 V at +50°C. For the control device the rate of change of threshold voltage with substrate temperature, $\frac{dV_T}{dT}$, was found to be equal to 0.0032 V °C^{-1}. This is in agreement with results published for a comparable p-channel device with an oxide thickness of 900 Å and a similar doping concentration of 3 x 10^{15} cm^{-3}. [10] (The value usually taken for the threshold voltage temperature coefficient is between -2 mV °C^{-1} and -4 mV °C^{-1} for doping concentrations between 3 x 10^{16} cm^{-3} and 10^{15} cm^{-3}.)[11] This result demonstrates that increasing the device temperature lowers the threshold voltage (because the decrease in the mobility of the charge carriers with increasing temperature, is more than compensated for by the increased number of mobile carriers generated by the ionisation of surface states).

6.5 ISOTHERMAL OPERATING POINT

The drain current of an FET is particularly sensitive to operating temperature variations because of the effect on the carrier mobility and the modification in the number of available charge carriers generated through the ionisation of surface states. There does exist a zero temperature coefficient point, where the drain current is unaffected by fluctuations in the temperature. This point can be determined from a plot of the transfer curves for a fixed drain voltage, as depicted in Figure 6.10 for the 35 μm gate-hole FET device with polyaniline deposited. The isothermal operating point for a drain voltage of -6.00 V occurred for a gate voltage equal to -3.45 V. For the control device operating at the same drain bias, the isothermal operating point was found at a gate voltage of -2.95 V, as depicted in Figure 6.11.
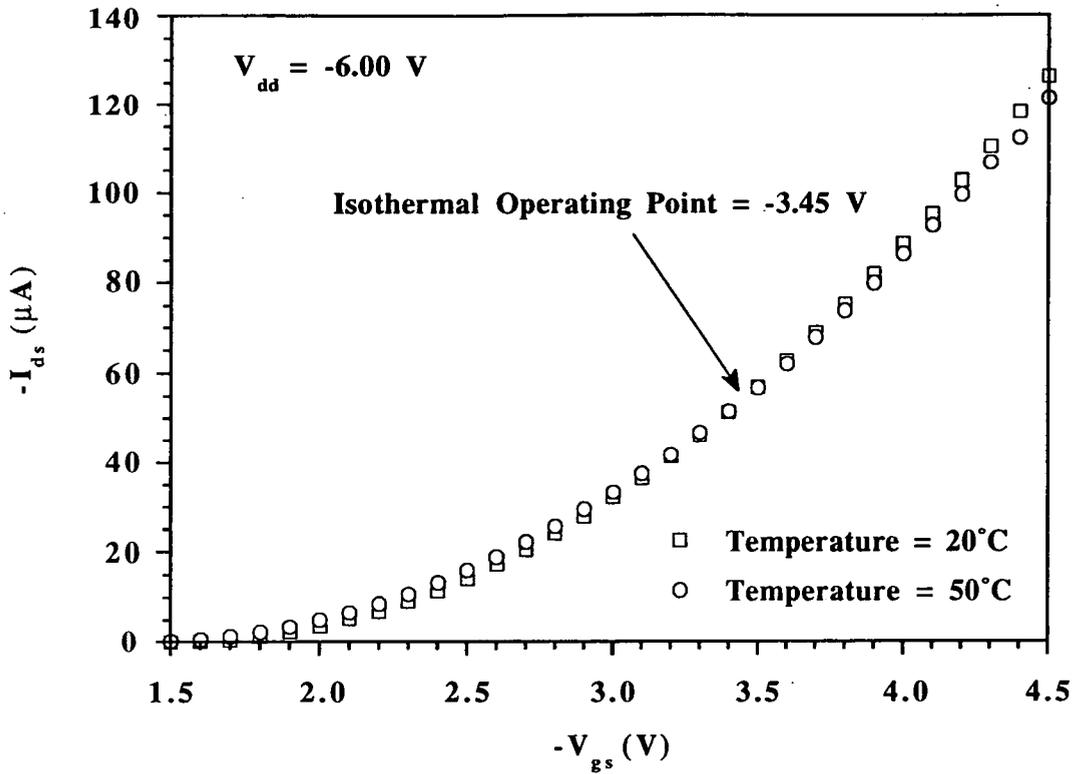
Figure 6.10 Source-drain current I_{ds} vs. gate voltage V_{gs} illustrating the isothermal operating point for the 35μm gate-hole FET with polyaniline deposited.
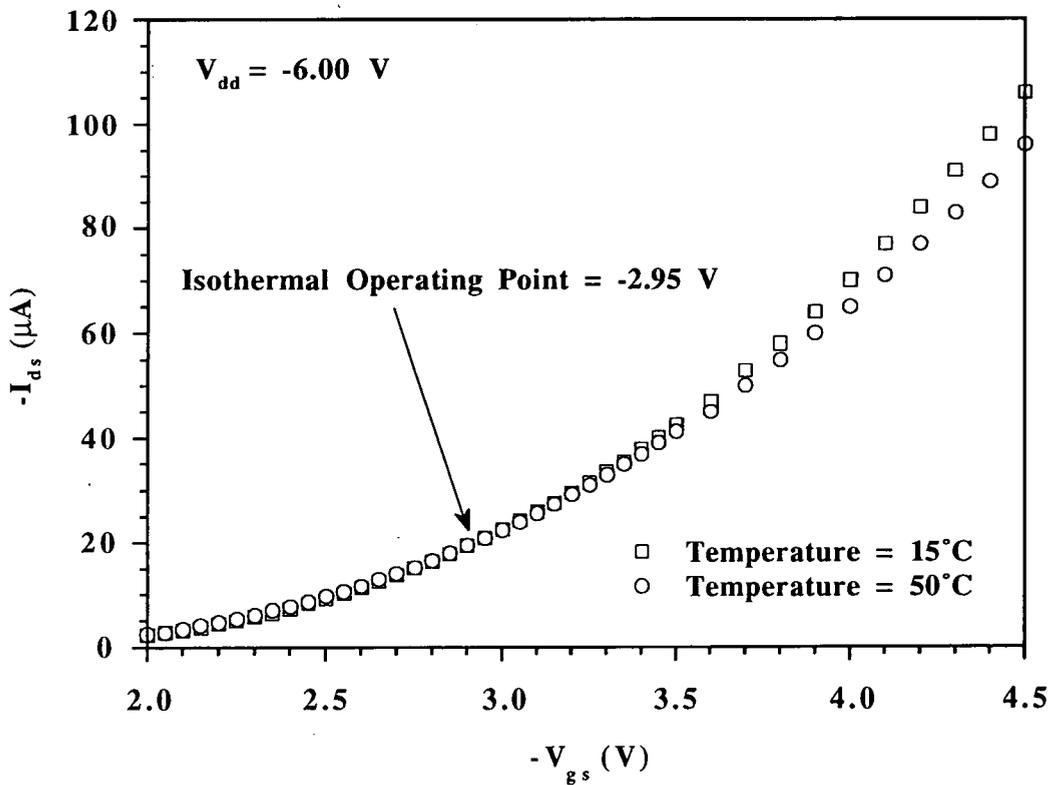
Figure 6.11 Source-drain current I_{ds} vs. gate voltage V_{gs} illustrating the isothermal operating point for the control device.

6.6 'TURN-ON' CHARACTERISTICS

Incorporating a charge-flow capacitor into the gate electrode of a p-channel MOSFET has been shown to modulate the time response of the drain current (§ 4.3).[12]

6.6.1 Room Temperature Response

Figure 6.12 illustrates the room temperature 'turn-on' responses for the array of devices without polyaniline deposited. The drain current saturates almost immediately for the control device whilst increasing the size of the air-gap from 15 μm to 35 μm considerably reduces the rate at which the current tends towards saturation for the remaining three FETs. The air-gap limits the extent of the electric field available to attract minority carriers to the semiconductor-insulator interface and create an inversion layer. The fringing field draws mobile carriers into the channel region over an extended period of time. A small drain current (~ 20 μA) was observed immediately after applying a gate voltage due to fixed charges and mobile ions very close to the channel creating a conducting path between the source and drain.

Figure 6.13 shows a comparison of the room temperature 'turn-on' response for the 25 μm gate-hole FET with and without polyaniline deposited. With an air-gap in the gate electrode the drain current was very close to saturation within 12 minutes. For the same device with polyaniline deposited and patterned in the gate electrode, saturation occurred after approximately 0.5 seconds. With the polymer present, the drain current will only reach saturation when the whole polymer surface is charged to the applied gate potential. Although highly resistive, the polymer was able to charge rapidly to the gate potential, forming a complete conducting channel considerably faster (approximately 2 seconds) than the same FET with an air-gap. Similar increases in the rate at which the drain current reached saturation were observed for the 15 μm and 35 μm gate-hole devices.
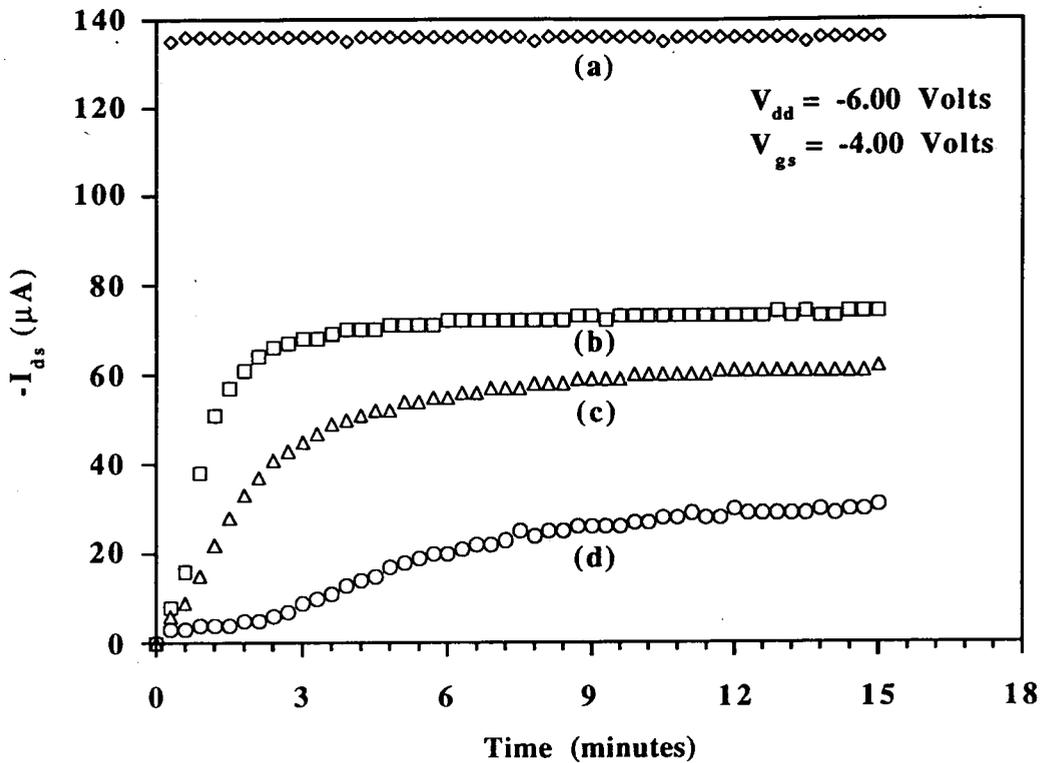
Figure 6.12 Source-drain current I_{ds} vs. time at room temperature for the four FET devices without polyaniline deposited: (a) control FET; (b) 15 μm gate-hole; (c) 25 μm gate-hole; (d) 35 μm gate-hole.
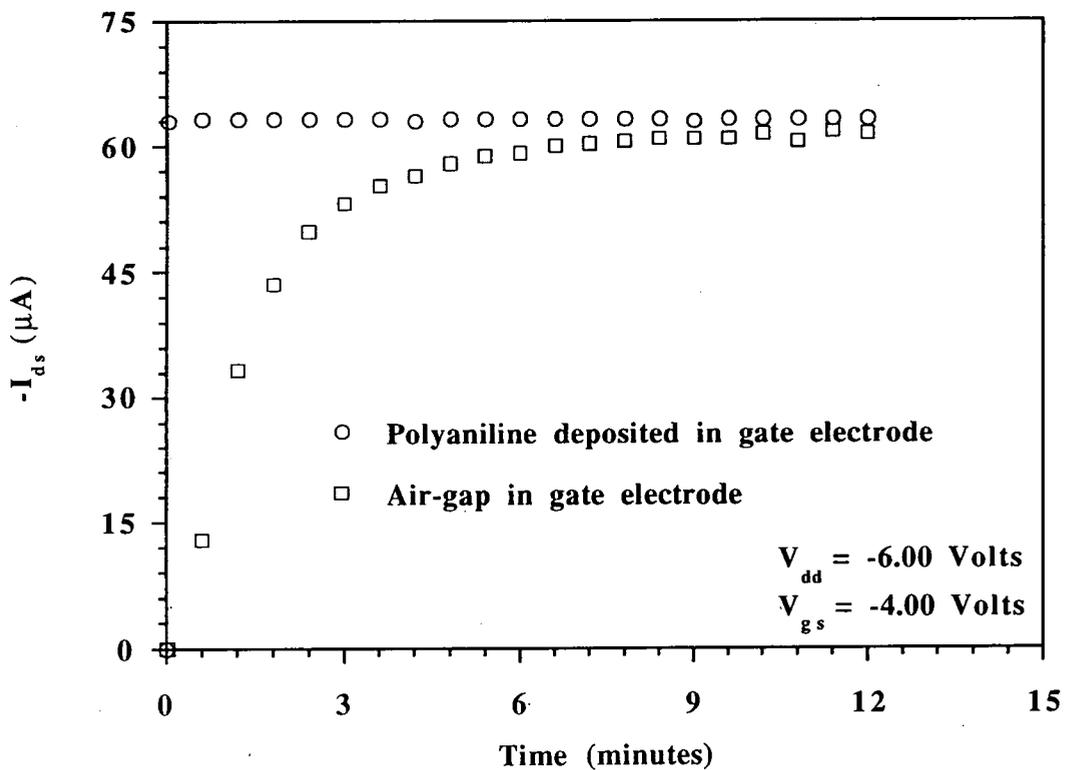
Figure 6.13 Source-drain current I_{ds} vs. time at room temperature for the 25 μm gate-hole FET with and without polyaniline deposited.

6.6.2 The Effect of Temperature on the 'Turn-on' Response

Figure 6.14 presents the 'turn-on' effect for the control device at operating temperatures of 14°C and 60°C. It has already been shown that increasing the operating temperature has a direct effect on the drain current (§ 6.4 and § 6.5) due to a decrease in the channel conductivity and a reduction in the threshold voltage. For a drain voltage of -6.00 V, the isothermal operating point for the control device occurred for a gate bias of -2.95 V (Figure 6.11). For a gate bias greater than this value it was shown that increasing the substrate temperature reduced the drain current. This effect is also observed in the 'turn-on' transient depicted in Figure 6.14. The rate at which the current increases after applying the gate voltage (at time equals 0.00 seconds) is more rapid at the lower operating temperature, and the near-saturated drain current at the end of the data sampling is greater. It can be deduced from these data that, for these operating conditions, the reduction in the threshold voltage as the temperature is increased has a smaller effect on the drain current than the decrease in the channel conductivity.

Figure 6.15 shows the 'turn-on' effect for a 35 μm gate-hole FET operating at several different temperatures, in the range +12°C to +60°C. For a drain voltage of -6.00 V, the isothermal operating point for this device occurred for a gate bias of -3.45 V (Figure 6.10). Therefore, the data displayed in Figure 6.15 show the device operating above the isothermal gate bias, at -4.00 V. It can be seen that the initial rate of 'turn-on' (from the application of the gate bias up to 0.04 seconds) became more rapid with increased temperature. This results from a greater number of available carriers in the semiconductor and an increase in the electrical conductivity of the polyaniline. Beyond this point in time, the rate at which the drain current increases begins to decline at higher substrate temperatures. It would be expected that extrapolating the curves in Figure 6.15 would show the largest saturated drain current occurring when the device was functioning at the lowest temperature.
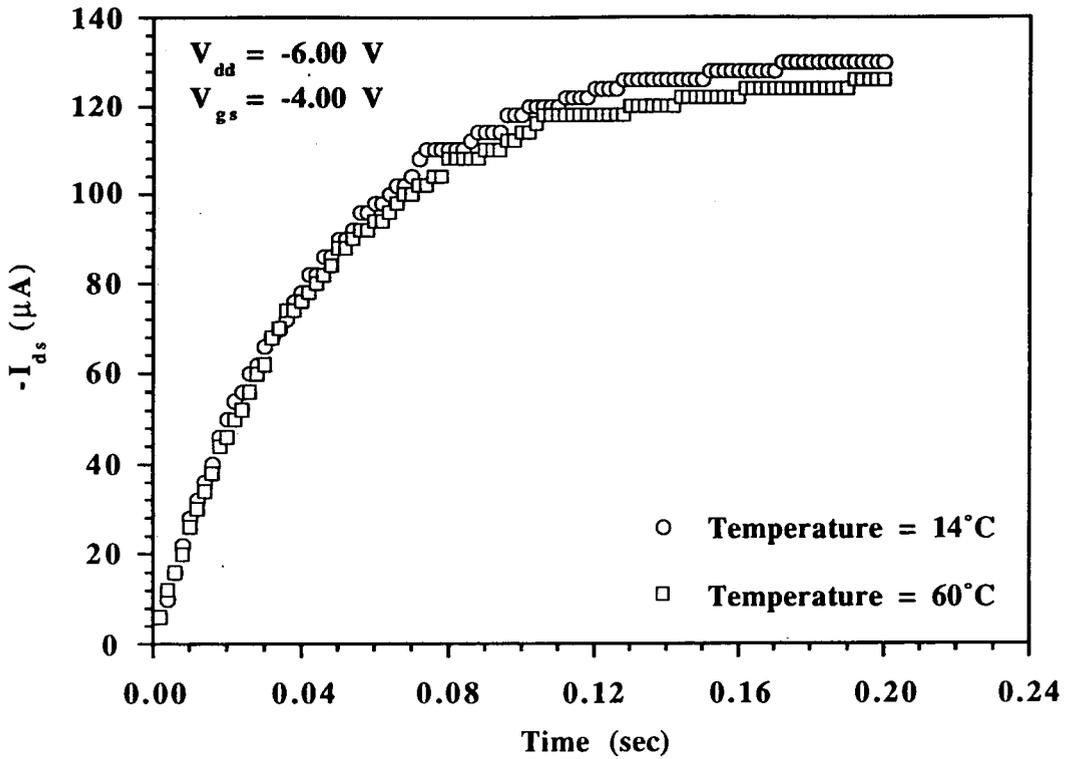
Figure 6.14 Source-drain current I_{ds} vs. time for the control device at operating temperatures of 14°C and 60°C.
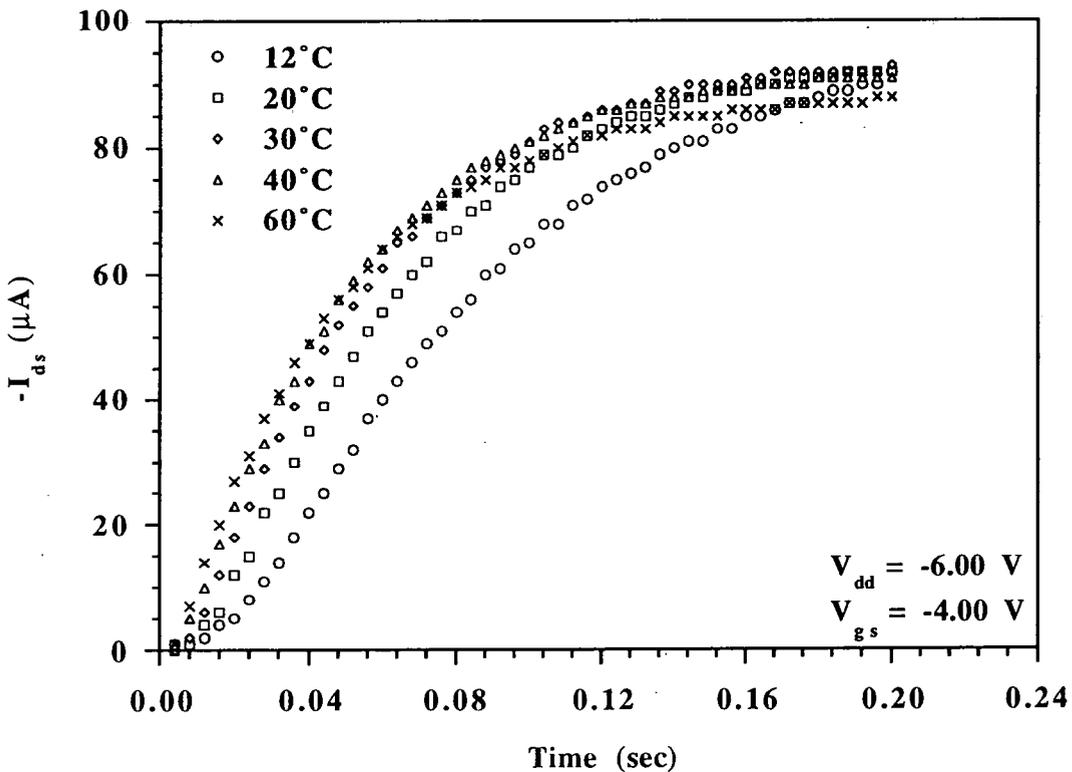
Figure 6.15 Source-drain current I_{ds} vs. time for the 35µm gate-hole FET with polyaniline deposited for several operating temperatures.

6.7 HUMIDITY DEPENDENCY OF THE 'TURN-ON' RESPONSE

It has been shown that the room temperature conductivity of both polyaniline[13-16] (§ 3.1.5 [c]) and phthalocyanines[17-19] is sensitive to different ambient humidities.

(a) The Response for an FET with Polyaniline Deposited within the Air-gap

Figure 6.16 shows the room temperature variation in the initial gradient of the 'turn-on' response for relative humidities in the range 15% - 50% for a 35μm gate-hole device with polyaniline deposited. To raise the level of humidity, nitrogen gas was bubbled through water before entering the gas-tight chamber. Admitting dry nitrogen reduced the relative humidity within the chamber, allowing the 'turn-on' response to be recorded for several stabilised values in the range referred to previously. Figure 6.17 illustrates how the 'turn-on' response is used to calculate the initial gradient (or sensitivity) of the FET to different levels of humidity: the initial linear section of the curve, resulting from the application of the gate bias, has been found to be characteristic of the response of the sensor to increasing concentrations of certain gases or, in this instance, levels of humidity.
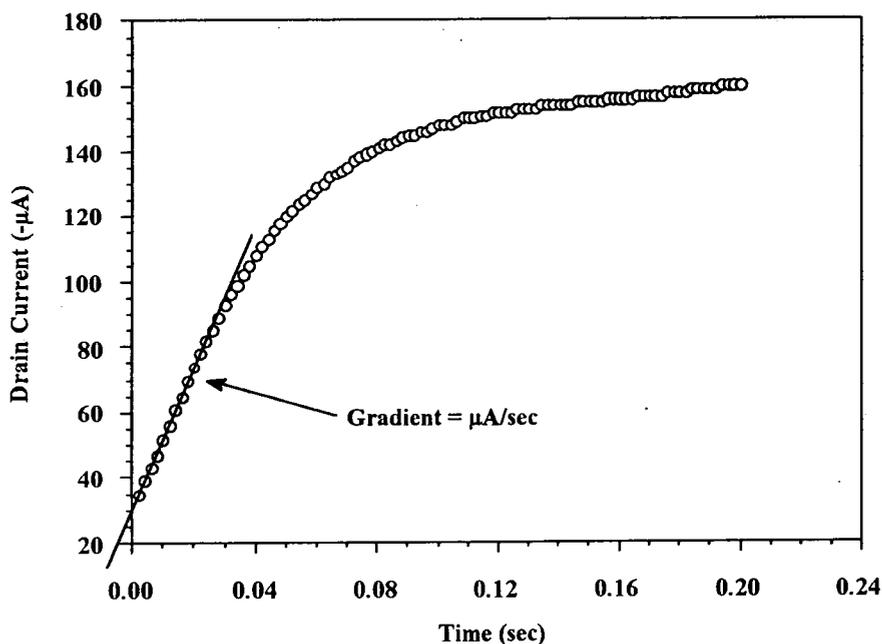
Figure 6.17 An example of how the 'turn-on' response is used to calculate the initial gradient for several values of humidity.
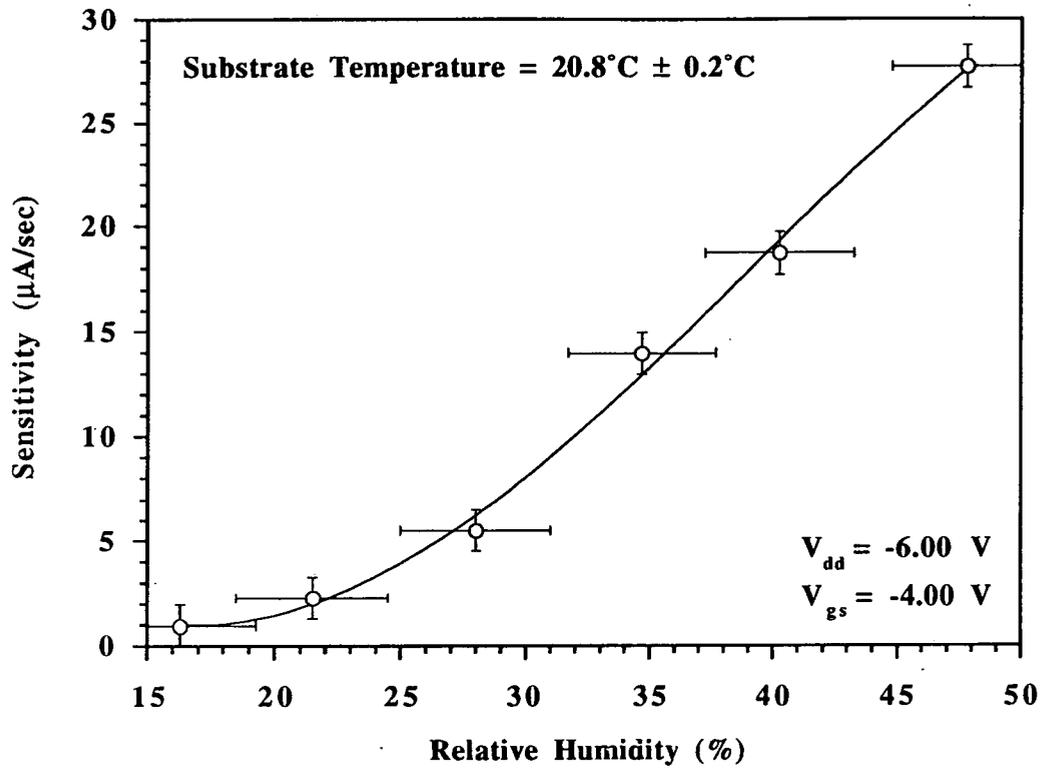
Figure 6.16 Initial gradient of the 'turn-on' response, at various levels of humidity, for the 35μm gate-hole FET with polyaniline deposited.
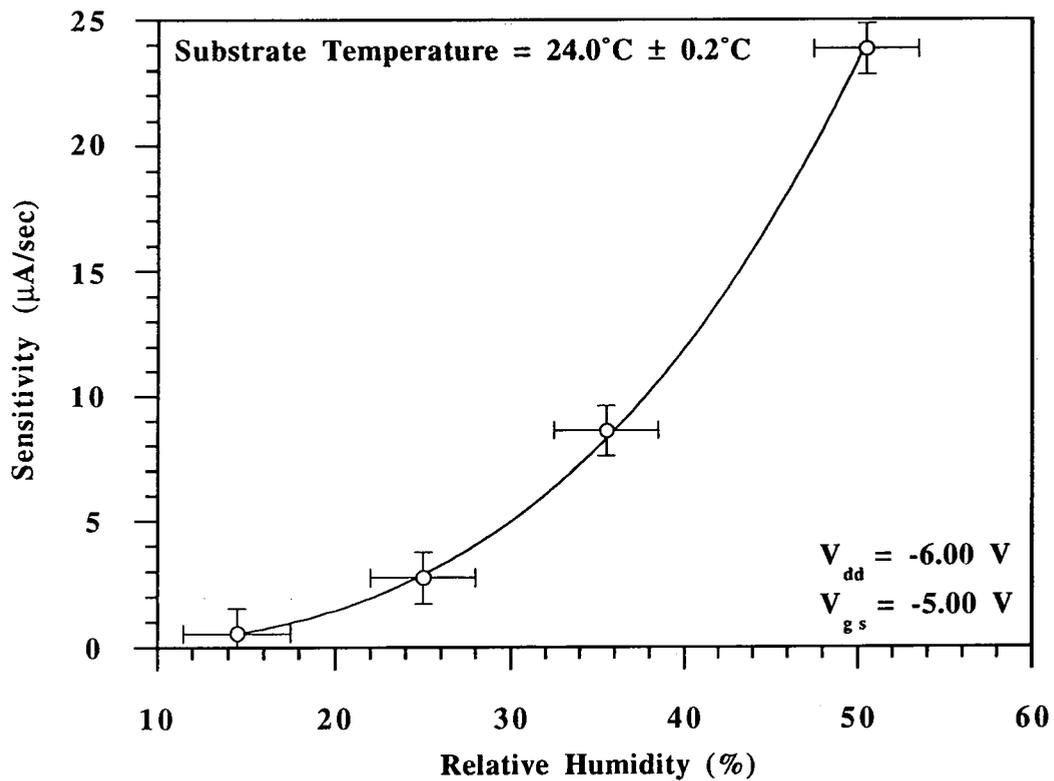
Figure 6.18 Initial gradient of the 'turn-on' response, at various levels of humidity, for the 35μm gate-hole FET with metal-free phthalocyanine deposited.

It can be seen from Figure 6.16 that the initial gradient (i.e. sensitivity) does not vary linearly over the humidity range to which the device was exposed. At low humidity (15% to 30%) the initial gradient increases only gradually, before demonstrating a near-linear relationship for humidity levels above 30% and up to approximately 50%.

A suggested mechanism for the increased conductivity of polyaniline upon exposure to water vapour, in turn leading to a faster 'turn-on' response has already been discussed (§ 3.1.5 [c]). The effect observed in Figure 6.16 was entirely reversible but illustrates an important parameter that needs to be considered when using the device for gas sensing in atmospheric conditions.

(b) The Response for an FET with Phthalocyanine Deposited within the Air-gap

Figure 6.18 presents the humidity response of a 35 μm gate-hole FET with octa-substituted metal-free phthalocyanine (with a chemical structure as shown in Chapter Three, Figure 3.7) deposited. The initial gradient of the 'turn-on' response can be seen to increase with increasing humidity, confirming that the conductivity of the phthalocyanine film is increased by the presence of absorbed water molecules. Since water alone cannot create charge carriers, it has been proposed[17] (for a similar phthalocyanine derivative) that the water facilitates the formation of free charge carriers from trapped charges already within the film.

The curve fit shown in Figure 6.18 is of the form

$$y = Cx^n, \qquad [6.2]$$

where $C \cong 1.7 \times 10^{-4}$ and $n \cong 3.02$. Whilst this near-cubic relationship does indeed provide an accurate fit for the data, there is not a valid scientific explanation for why it should be so. For this reason the curve fit is primarily present as a guide to the eye.

6.8 SUMMARY

The results from the physical and electrical characterisation of an array of organic/silicon hybrid field-effect transistors have been discussed. The dependence of film thickness on spin speed and the effect of chemical patterning techniques have been examined for polyaniline. Capacitance-voltage characteristics for the devices, with and without polyaniline, have been presented. The variation in the threshold voltage with temperature and the isothermal operating points were determined. A delay in the response of the drain current, inherent with the incorporation of an organic material into the transistor, has been examined for various operating conditions. These included the effects of increasing operating temperature and the exposure to several different levels of humidity. In the next chapter, the results for the effect on the array of sensors to various concentrations of NO_x are presented and discussed.

REFERENCES

1. M. Scully, M.C. Petty and A.P. Monkman, *Synth. Met.*, **55** (1993) 183-187.

2. D.E. Bornside, C.W. Macosko and L.E. Scriven, *J. Appl. Phys.*, **66** (1989) 5185-5193.

3. W.W. Flack, D.S. Soong, A.T. Bell and D.W. Hess, *J. Appl. Phys.*, **56** (1984) 1199-1206.

4. C. Di Bartolomeo, P.S. Barker, M.C. Petty, P. Adams and A.P. Monkman, *Advanced Materials for Optics and Electronics*, **2** (1993) 223-236.

5. K.J. Skrobis, D.D. Denton and A.V. Skrobis, *Polymer Engineering and Science*, **30** (1990) 193-196.

6. A.P. Monkman and P. Adams, *Synthetic Metals*, **40** (1991) 87-96.

7. M. Wan and J. Yang, *J. Poly. Sci.*, **55** (1995) 399-405.

8. E.H. Nicollian and A. Goetzberger, *IEEE Trans. on Electron Devices*, **ED-12** (1965) 108-117.

9. A. Goetzberger, E. Klausmann and M.J. Schultz, *CRC Critical Review in Solid-State Science*, **6** (1976) 1-43.

10. L. Vadasz and A.S. Grove, *IEEE Trans. on Electron Devices*, **ED-13** (1966) 863-867.

11. R. Wang, J. Dunkley, T. De Massa and L. Jelsma, *IEEE Trans. on Electron Devices*, **ED-18** (1971) 386-388.

12. S.D. Senturia, C.M. Sechen and J.A. Wishneusky, *Appl. Phys. Lett.*, **30** (1977) 106-108.

13. M. Nechtschein, C. Santier, J.P. Travers, J. Chroboczek, A. Alix and M. Ripert, *Synth. Met.*, **18** (1987) 311-316.

14. M. Angelopoulos, A. Ray, A.G. MacDiarmid and A.J. Epstein, *Synth. Met.*, **21** (1987) 21-30.

15. O.N. Timofeeva, B.Z. Lubenstov, Y.Z. Sudakova, D.N. Chernyshov and M.L. Khidekel, *Synth. Met.*, **40** (1991) 111-116.

16. T. Taka, *Synth. Met.*, **57** (1993) 5014-5019.

17. C. Gu, L. Sun, T. Zhang, T. Li and M. Hirata, *Thin Solid Films*, **244** (1994) 909-912.

18. A. Belghachi and R.A. Collins, *J. Phys. D: Appl. Phys.*, **23** (1990) 223-237.

19. P. Bassoul, T. Toupance and J. Simon, *Sensors and Actuators B*, **26** (1995) 150-152.

CHAPTER SEVEN

RESPONSE TO NO$_x$: RESULTS AND DISCUSSION

This chapter describes the results obtained from experiments with the hybrid sensors. The response and recovery of the devices after exposure to concentrations of NO$_x$ up to 8 parts per million (ppm) was examined. Data obtained for a polyaniline-based device are compared to those from a structure incorporating phthalocyanine.

7.1 GAS SENSING USING A POLYANILINE/SILICON HYBRID FIELD-EFFECT TRANSISTOR

When characterising a sensor it is necessary to control external parameters including the temperature and humidity within the test chamber. Any response then observed after admitting the test gas can be attributed entirely to the gas.

One of the primary difficulties when using nitrogen dioxide is its propensity for dimerising by the following reversible reaction

$$2NO_2 \Leftrightarrow N_2O_4.$$
[7.1]

The equilibrium is affected by both temperature and pressure. Figure 7.1 shows some typical results for pure nitrogen dioxide, illustrating the contribution of each variable over a range of temperatures and pressures. For this reason it is usual to assign the chemical formula NO$_x$ when referring to 'nitrogen dioxide' since the exact amount of nitrogen tetroxide and nitrogen dioxide is variable.
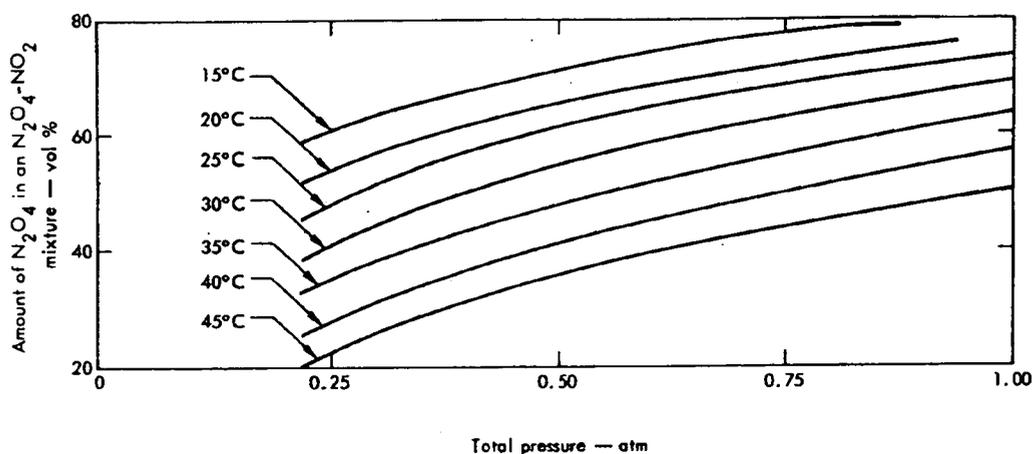
Figure 7.1 Dimerization of pure nitrogen dioxide vs. pressure at seven isotherms. [Ref. 1.]

In this work, the nitrogen dioxide used was supplied diluted to 0.1% in nitrogen. Further dilution was achieved using a gas blender as described in Chapter Five. Because the nitrogen dioxide admitted to the gas chamber was diluted in nitrogen, the N_2O_4/NO_2 ratio displayed in Figure 7.1 will be displaced. This shift will depend on the fraction of nitrogen dioxide present in the sample.

7.1.1 Characterisation of the Sensors

The experimental procedure used to test a device with a gas has been described in Chapter Five (§ 5.4). Whilst the response of the sensor to NO_x was found to be reversible, the baseline that was re-established was at a lower level than it was before exposure. For this reason, some of the data presented in this chapter required normalising to allow valid comparisons for the different concentrations of test gas.

7.1.2 Normalisation of the Data

The normalisation was accomplished by scaling the second data set by the ratio of the equivalent points in time (i.e. source-drain current values) on the two baselines, as illustrated on the following page.

At time x :

$$\frac{\text{Original Baseline } (x)}{\text{New Baseline } (x)} \times \text{New Data Point } (x) = \text{Normalised Data Point } (x).$$ [7.2]

For example, if at time x the following values of current were obtained for the three variables:

Original Baseline = -96 µA,

New Baseline = -76 µA,

New Data Point = -103 µA,

then the normalised data point would be calculated from Equation 7.2 as follows,

$$\frac{-96}{-76}\mu A \times -103\mu A = -130 \ \mu A.$$

The above normalisation procedure can be repeated for all the data values over the period of sampling. Figure 7.2 (a) illustrates some typical raw data, while Figure 7.2 (b) shows the same data after normalisation.

7.1.3 Response of the 35 µm Gate-Hole Device

Figure 7.3 shows the room temperature 'turn-on' response for the 35 µm gate-hole device, following exposure to increasing concentrations of NO_x. The data have been normalised to the 1 ppm baseline. (In Equation 7.2 the 'original baseline' would therefore be the one recorded before the device was exposed to 1 ppm NO_x. The baselines recorded before exposure to 2-, 4-, and 8 ppm NO_x would be substituted for the 'new baseline' for each appropriate data set, to obtain the normalised values.)

It can be seen that there is a detectable response for concentrations of NO_x as low as 1 ppm, though the effect cannot be readily distinguished from the response to 2 ppm. The complete 'turn-on' response (i.e., until the drain current saturates) was not recorded, since the most useful and characteristic data are accumulated in the initial part of the 'turn-on' transient. It was found that the final saturated drain current was
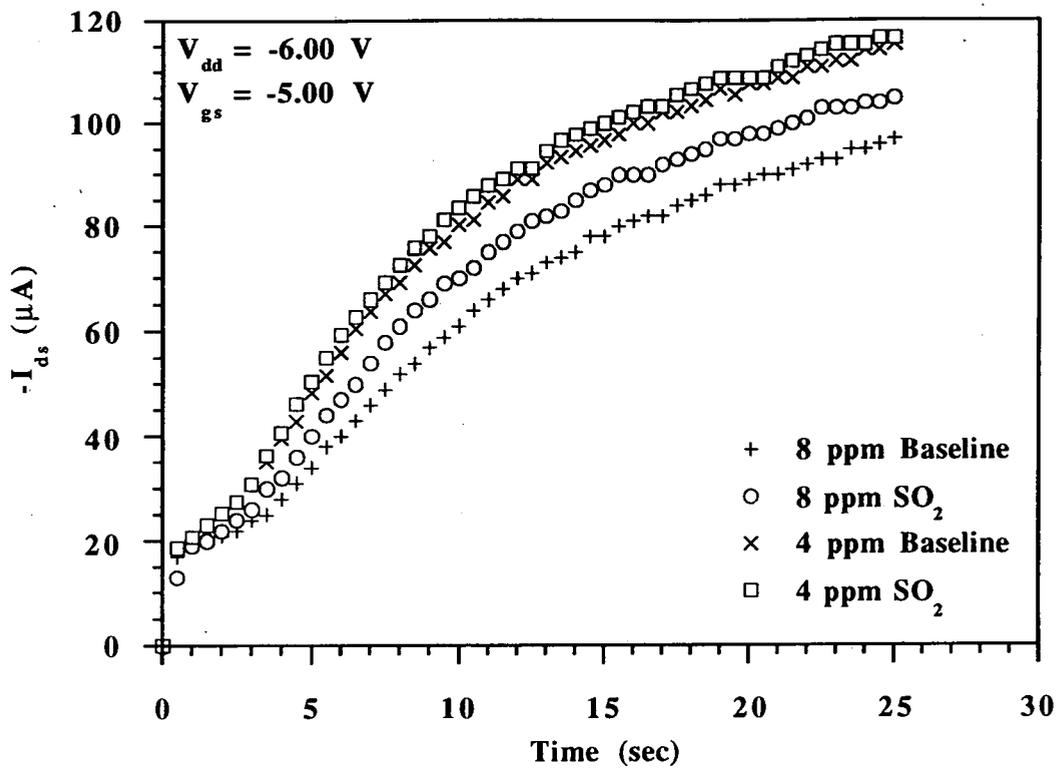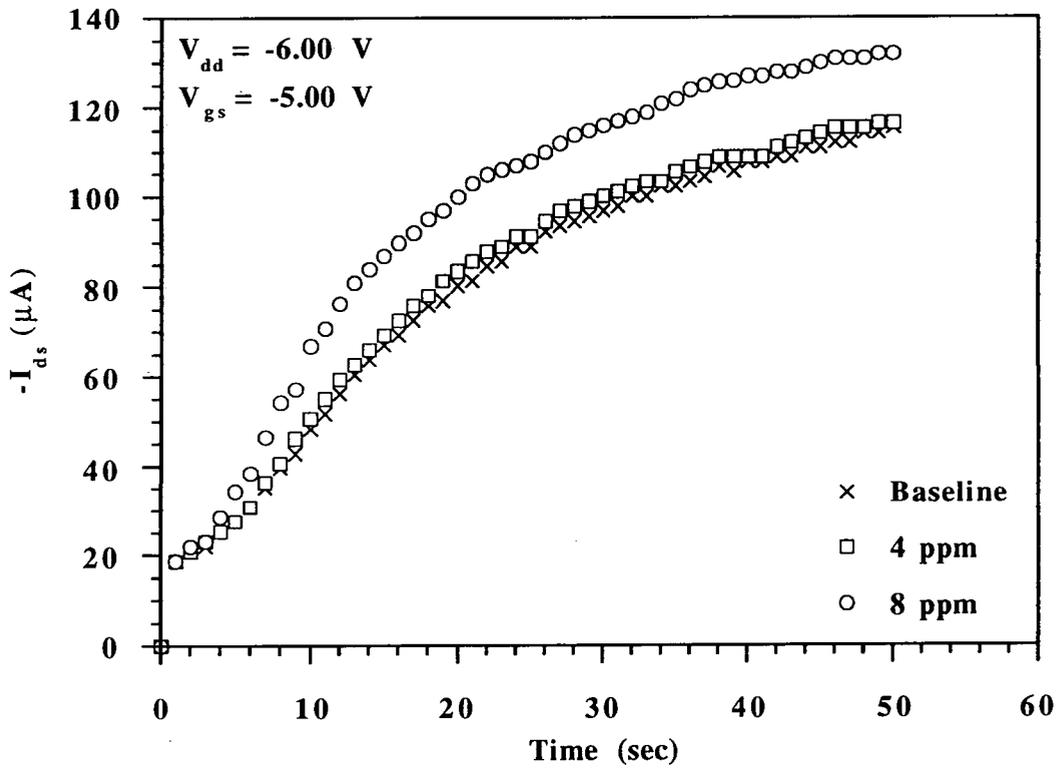
Figure 7.2 Source-drain current I_{ds} vs. time for a 35 µm gate-hole device with polyaniline deposited: (a) typical raw data after exposure to SO_2 and (b) the same data normalised to the 4 ppm baseline.
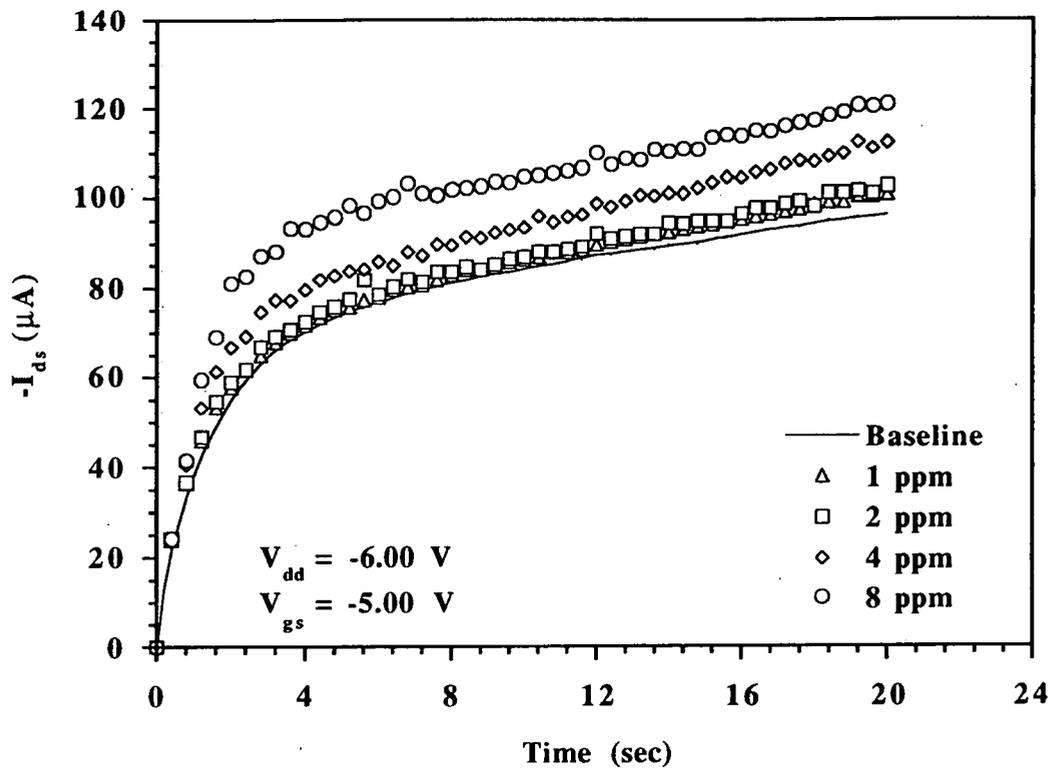
Figure 7.3 Source-drain current I_{ds} vs. time for the 35 μm gate-hole device with polyaniline deposited in various NO_x atmospheres. These data have been normalised to the 1 ppm baseline.
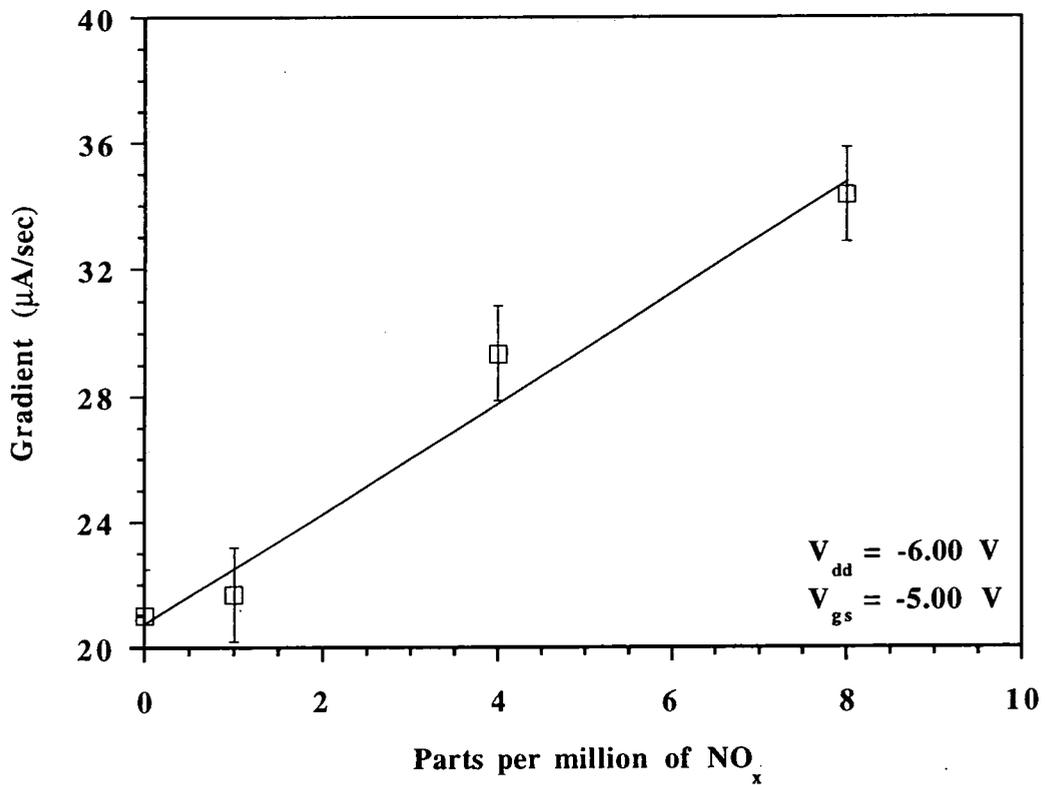
Figure 7.4 Initial gradient for the normalised 'turn-on' response.

not greatly changed by the presence of NO_x (typically no more than ±1%). This result will be presented in § 7.1.6.

Figure 7.4 illustrates the initial gradient for the 'turn-on' response. (These data were obtained by the method already described in § 6.7 (a) for the response of a similar device to various levels of humidity.) This curve shows that there is a linear relationship for the initial rate of increase in drain current as the concentration of NO_x is increased, and is indicative of the sensitivity of the FET to this gas.

A chemiresistor with a spin-coated film of emeraldine base polyaniline deposited has been shown to have a 4 ppm detection threshold for NO_x at room temperature.[2] The increase in current for a 10 ppm exposure was 0.8 pA. Figure 7.3 shows that the 35 μm gate-hole device (normalised) drain current increased by approximately 20 μA after 8 ppm NO_x. This significantly greater change in the measured signal considerably reduces problems associated with signal detection. A thick-film tin oxide sensor operating at a temperature of approximately 200 °C, has been demonstrated to be sensitive to a mixture of NO_x in nitrogen at a concentration of 1 ppm.[3] Changes in conductance of over two orders of magnitude occured at this optimum temperature. This sensitivity is comparable to the 35 μm FET sensor, but the device does not function at room temperature. An amperometric electrochemical gas sensor (discussed in § 2.3.1 [b]) with a layer of H^+-form Nafion gel as the electrolyte has been used to detect NO_x. This device was shown to exhibit a rapid response, with a detection limit of 5 ppm.[4]

7.1.4 Response of the 25 μm Gate-Hole Device

Figure 7.5 shows the normalised room temperature 'turn-on' response for the 25 μm gate-hole sensor, following exposure to increasing concentrations of NO_x. A 5 second sampling period (c.f. 20 seconds for the 35 μm gate-hole FET) allowed sufficient information to be obtained to characterise the device. This is because the ratio of polyaniline-to-metal in the gate electrode is smaller than for the 35 μm gate-hole transistor. For this reason the conducting channel was able to form more rapidly.

Figure 7.5 Source-drain current I_{ds} vs. time for the 25 µm gate-hole device with polyaniline deposited in various NO_x atmospheres. These data have been normalised to the 1 ppm baseline.

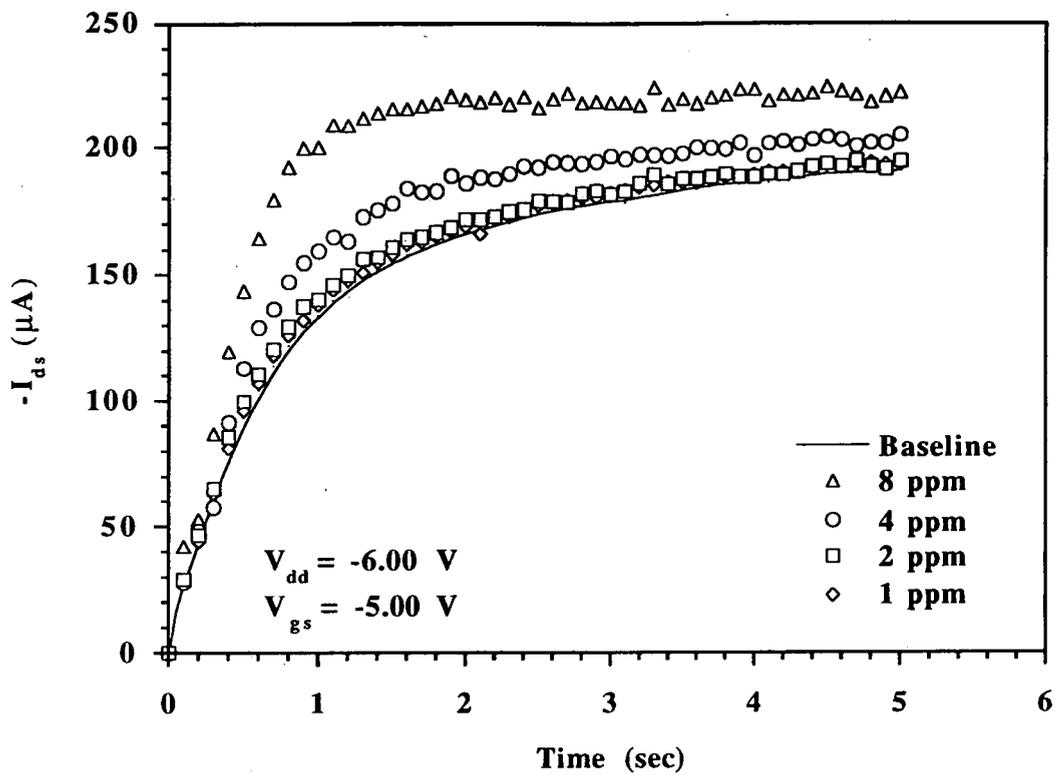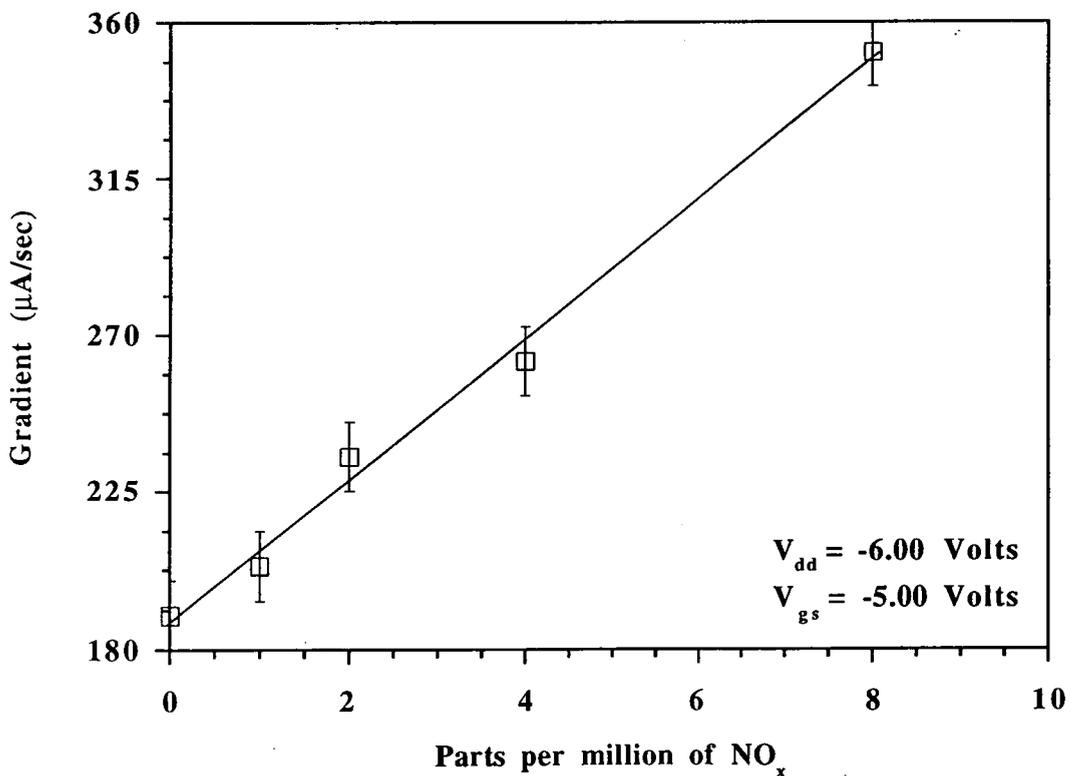**Figure 7.6** Initial gradient for the normalised 'turn-on' responses to NO_x.

This device was also sensitive to concentrations of NO_x as low as 1 ppm, though this response was virtually the same as that recorded for a 2 ppm exposure. (A similar effect as shown in Figure 7.3 for the 35 µm gate-hole FET.)

Figure 7.6 depicts the initial gradient of the 'turn-on' response. The rate at which the drain current increases with time is much greater than that shown in Figure 7.4 for the 35 µm gate-hole device. Again, this is because the ratio of polymer-to-metal is smaller, allowing a significantly greater drain-current to flow in a shorter period of time.

7.1.5 Response of the 15 µm Gate-Hole Device

Figure 7.7 illustrates the room temperature response of the 15 µm gate-hole device to NO_x. In this case, there was no observable effect for concentrations of NO_x less than 8 ppm. The increase in the 'turn-on' response was very marginal, even at 8 ppm, hence Figure 7.8 displays the same data with the y-axis re-scaled to highlight the effect. From this result it is evident that at low concentrations (< 8 ppm) of NO_x there is too small a surface area of polyaniline to modulate the 'turn-on' transient sufficiently at the micro-ampere level.

7.1.6 The Effect of 8 ppm NO_x on the Saturated Value of the Drain Current

For the normalised 'turn-on' responses presented for the 35 µm (Figure 7.3) and 25 µm (Figure 7.5) gate-hole sensors it can be seen that the drain currents have not reached saturation. It has been stated that the complete response, until I_{ds} saturates, was not necessary to satisfactorily characterise the devices. To determine what effect the exposure to NO_x had on the saturated drain current, a 30 minute 'turn-on' response was recorded for the 25 µm gate-hole device in a nitrogen ambient. This was followed by sampling a second 30 minute response, once the chamber had been equilibrated to an 8 ppm NO_x atmosphere. Figure 7.9 compares the two 'turn-on' transients, with the inset highlighting the initial period of the responses. It is evident that saturation has occurred after approximately seven minutes (420 seconds). It can also be seen that whilst the initial rate of increase (time = 0 to 80 seconds) of the
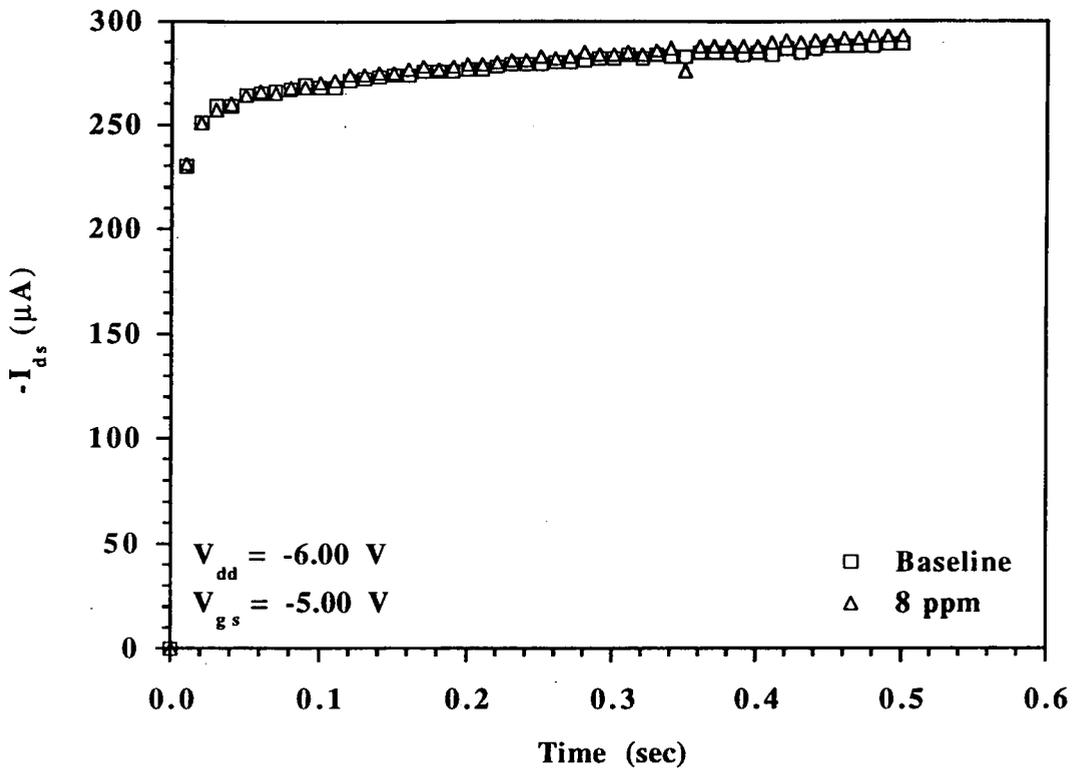
Figure 7.7 Source-drain current I_{ds} vs. time for the 15 μm gate-hole device with polyaniline deposited after exposure to 8 ppm NO_x.
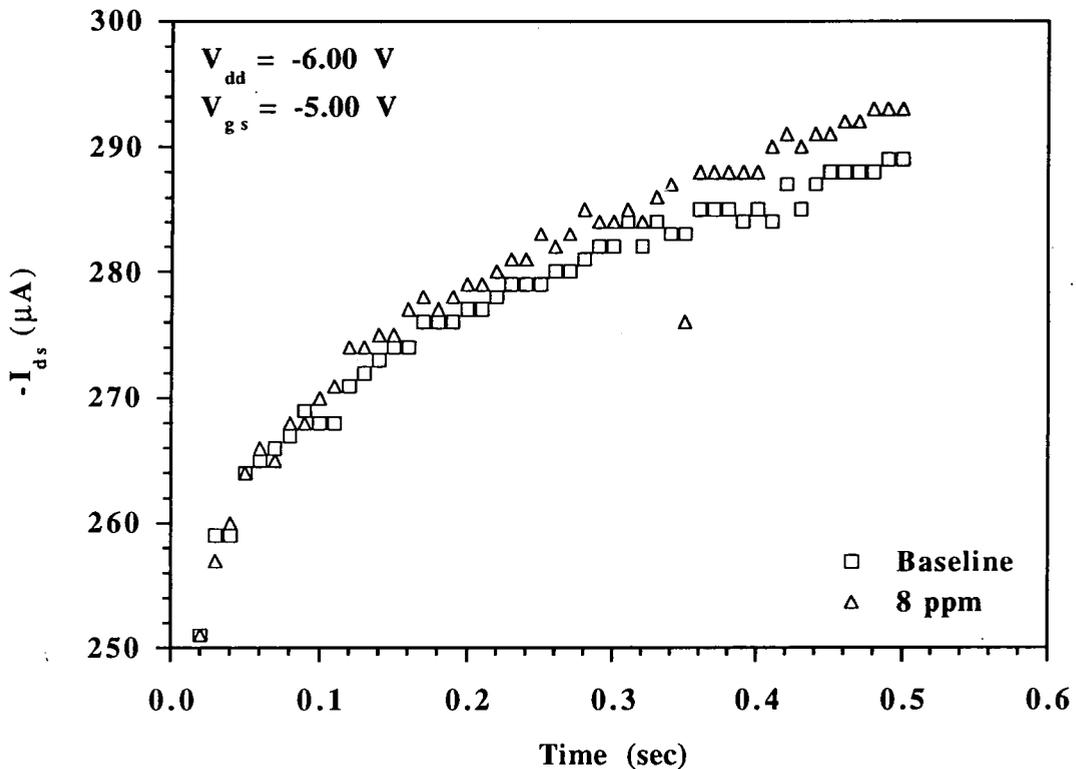
Figure 7.8 Source-drain current I_{ds} vs. time for the 15 μm gate-hole device with polyaniline deposited after exposure to 8 ppm NO_x. This is the data presented in Figure 7.7, above. The range of drain current represented on the y-axis has been reduced to improve the clarity of the data.
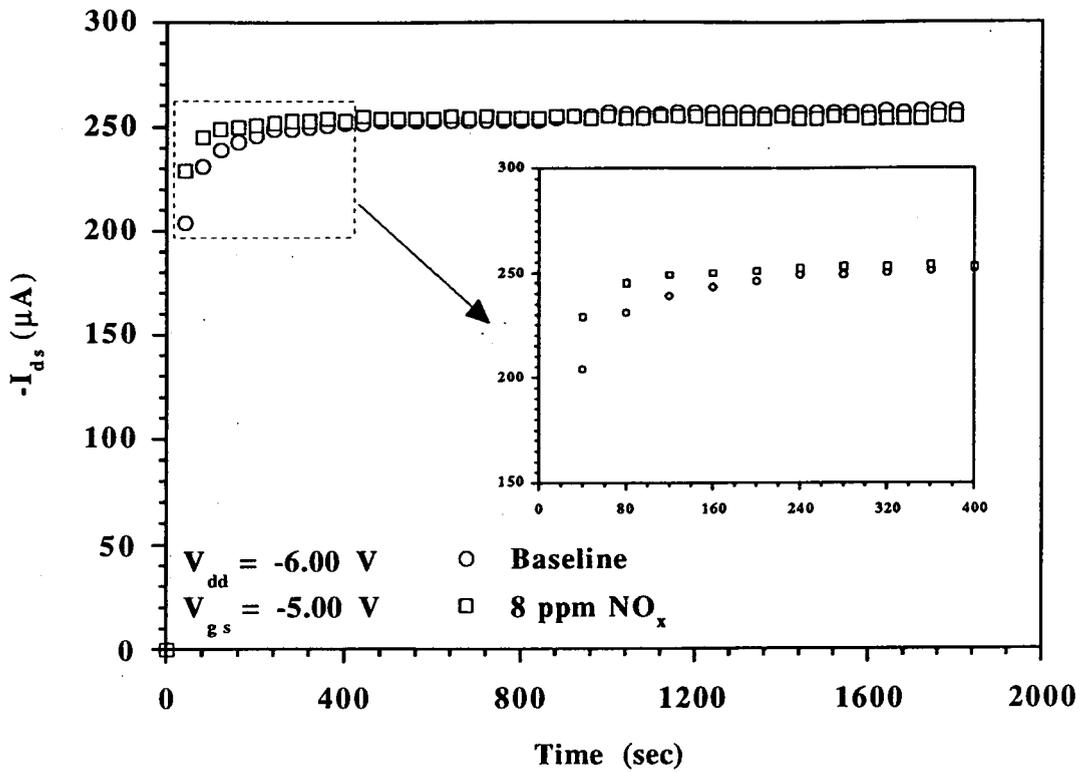
Figure 7.9 Source-drain current I_{ds} vs. time for the 25μm gate-hole device with polyaniline deposited, before and after exposure to 8 ppm NO_x. This illustrates that the saturated drain current is unaffected by the gas.

Figure 7.10 Source-drain current I_{ds} for one point on the 'turn-on' transient (t = 4.0 secs) following the termination of the supply of 4 ppm NO_x. This result was obtained at room temperature for the 35 μm gate-hole FET with polyaniline deposited.

source-drain current is significantly greater after exposure to the gas, the final saturated values are very similar for both cases.

7.1.7 The Recovery of the Sensor after Exposure to 4 ppm NO$_x$

An vital aspect for a commercial gas sensor is whether or not it can be re-used after exposure to a gas. For recovery to occur it is necessary that the surface adsorption of the gas by the organic film is an entirely reversible process. If a chemical reaction should occur, producing a permanent change in the conductivity of the organic material, the sensor cannot be considered to be a practical device.

Figure 7.10 shows the room temperature recovery (15 °C) for a 35 μm gate-hole device with polyaniline deposited after exposure to 4 ppm NO$_x$. The restoration of the baseline was achieved by continuously purging the gas-tight chamber with pure nitrogen gas.

The points on the curve represent one current value obtained from each of the 'turn-on' transients recorded over the period of recovery. In this example, the value of current at t = 4.0 seconds was used to determine the recovery of the sensor illustrated in Figure 7.10. Within two and a half hours 50% recovery was achieved. This initial rate of recovery was not sustained and it took a further five and a half hours before the complete restoration of the baseline response. During the initial recovery it is believed that NO$_x$ was desorbing rapidly from the surface of the film. Whilst the longer period, until complete recovery, was due to the more difficult process of desorbtion of the gas from the bulk of the film.

The recovery times of other reported devices used for the detection of NO$_x$ vary from a few minutes to several hours. For a field-effect transistor sensor with a Langmuir-Blodgett film of porphyrin deposited as the gate electrode, recovery required between 45 and 60 minutes.[5] For a spun polyaniline chemiresistor, a period of over 90 minutes purging with nitrogen was required.[2] A rapid reversal in the response after exposure to 100 ppm NO$_x$ of half of one second has been shown for an amperometric electrochemical gas sensor operating at room temperature.[4] The eight hours recovery

required for the device reported in this work is long in comparison to those reported above. A possible explanation is the large capacity of the gas-tight chamber in comparison to the flow rate from the gas blender. (The volume of the chamber was approximately 4.17 litres while the gas flow from the blender was approximately 0.55 litres min^{-1}.) To purge the chamber with pure nitrogen in order to expel the test gas therefore required several minutes. In contrast, many of the reported devices with a fast recovery time have been characterised in small gas cells that can be purged in seconds.

In § 7.1.10 the effect of raising the operating temperature on the 'turn-on' response in gaseous environments and the subsequent recovery will be discussed and compared with the results obtained at room temperature.

7.1.8 The Outcome of Prolonged Exposure of the Sensor to 8 ppm NO$_x$

Figure 7.11 illustrates the effect of a five hour exposure for a 25 µm gate-hole device in an 8 ppm NO$_x$ ambient. Because the modulation of the 'turn-on' response is entirely dependent on the change in the conductivity of the polyaniline film, it can be deduced from Figure 7.11 that the increase in conductivity due to the gas, tends towards a maximum. This is reflected in the increases in the rate of 'turn-on' of the drain current shown for the five successive responses: those recorded for the first three hours of exposure show significant increases in the initial 'turn-on' transient, whilst the final two (four hours and five hours) show only a small change from the one obtained after three hours.

Figure 7.12 presents the same data in such a way that this saturation in the turn-on response is more obvious. In this figure, each curve comprises a single data point taken from each of the 'turn-on' transients recorded over the five hour period. This set of five curves represents a 'snap-shot' of the drain current at one point in time over the five second 'turn-on' response. It is clearly evident (from the levelling off of the curves) that further exposure to NO$_x$, beyond three hours, does not notably increase the drain current.
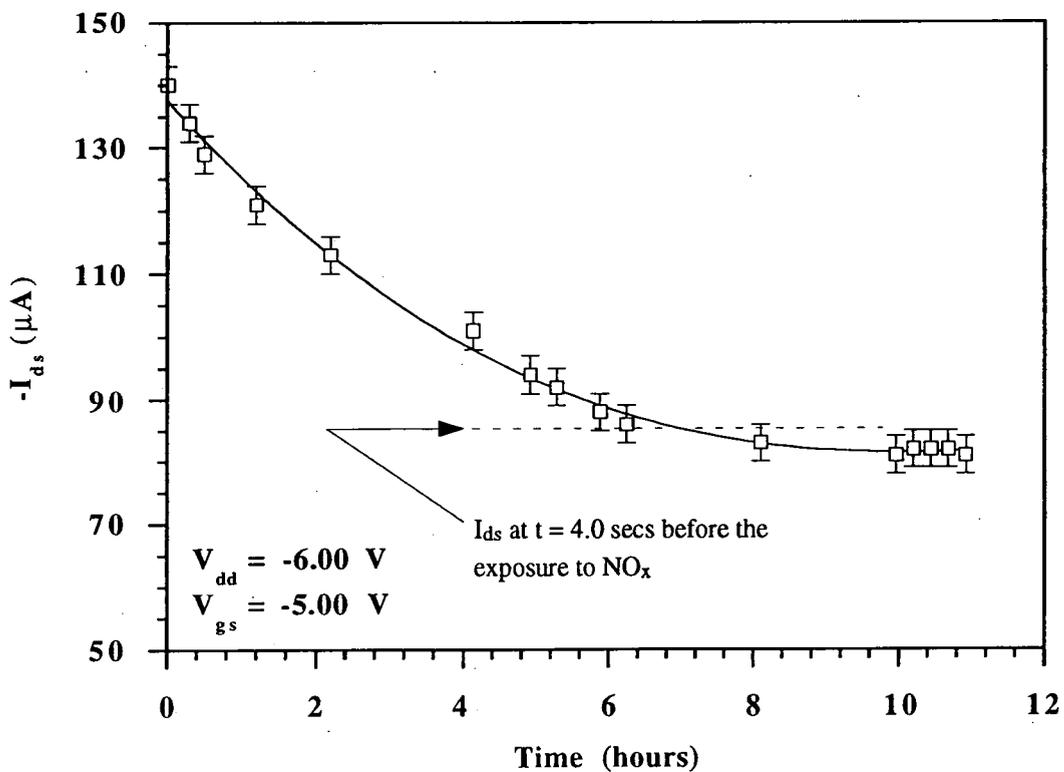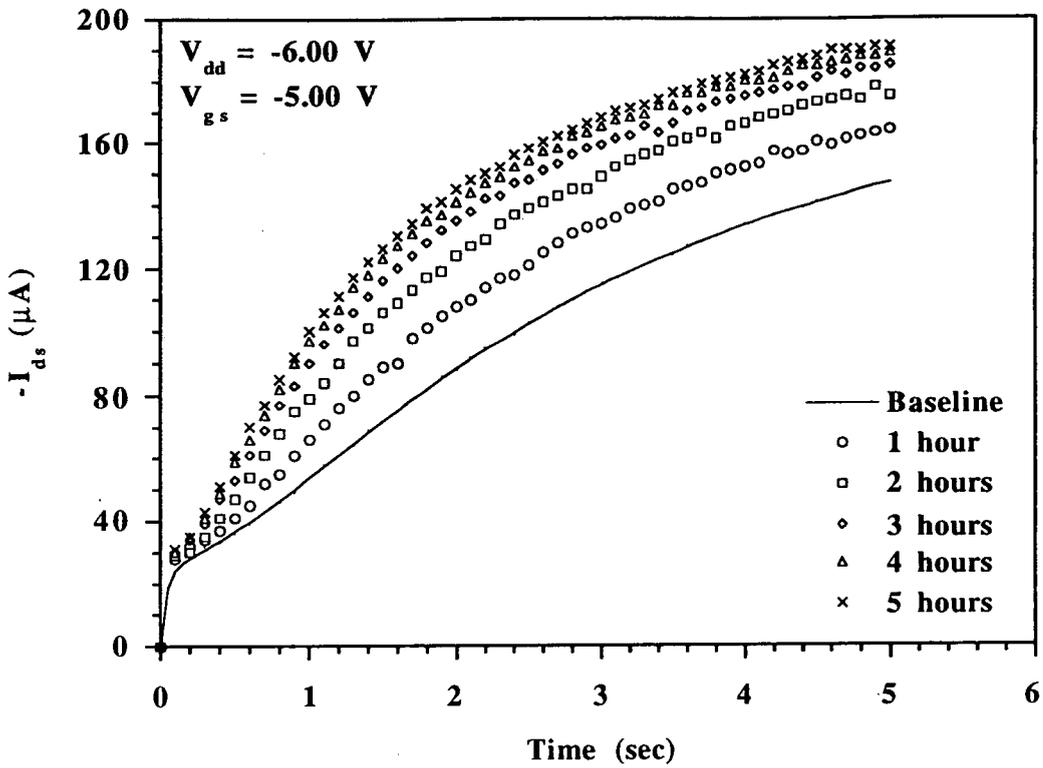
Figure 7.11 Source-drain current I_{ds} vs. time for the 25 μm gate-hole device with polyaniline deposited for five hours exposure to 8 ppm NO_x.
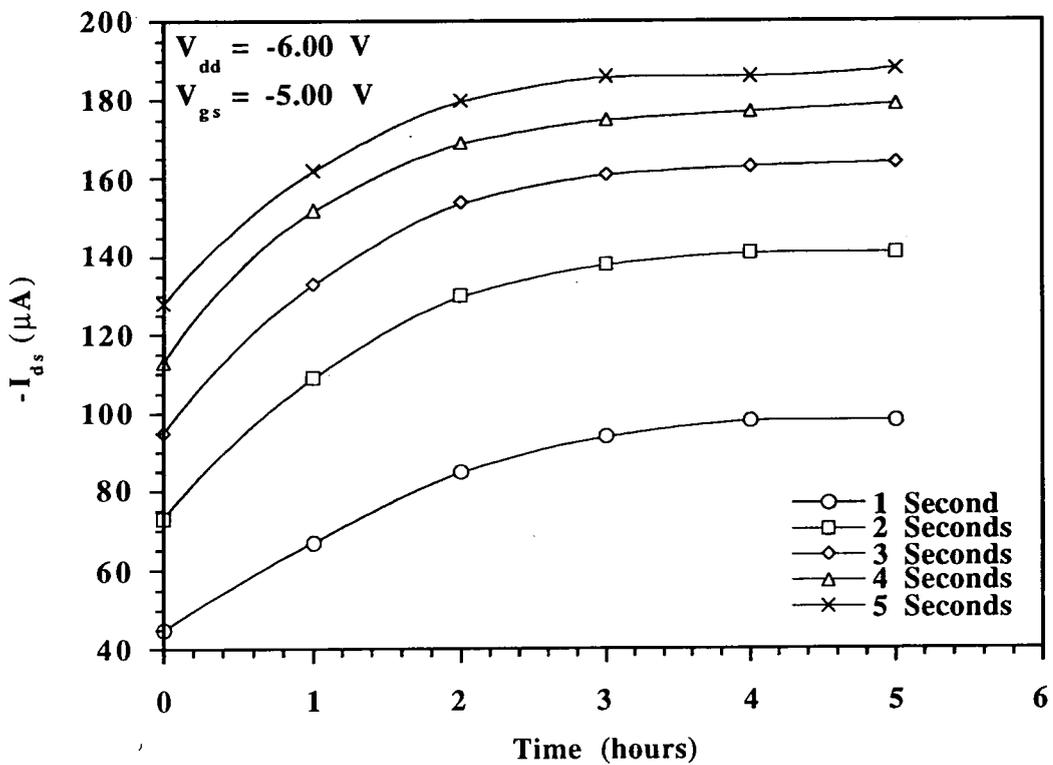
Figure 7.12 Source-drain current I_{ds} over the five hour exposure to 8 ppm NO_x at five, one second intervals extracted from the 'turn-on' transients shown in Figure 7.11, above.

This observation that the conductivity of the polyaniline tends towards a limit for a specific concentration of a gas suggests that there are a finite number of sites available, over the surface of the film and within its bulk, that are able to absorb the gaseous molecules. There will be no further increase in the conductivity of the polyaniline film once the gas has interacted with all of the available sites.

7.1.9 The Effect of Repeated Exposure to 8 ppm NO$_x$

In § 7.1.1 it was stated that the baseline response re-established after purging with nitrogen was found to be at a lower level than it was before exposure. To investigate this phenomenon further, a series of exposures to 8 ppm NO$_x$ followed by purging with nitrogen gas were carried out to monitor the successive baseline and 'turn-on' responses. The following results were obtained at room temperature for a 25 μm gate-hole device with polyaniline deposited.

Figure 7.13 shows the baseline responses recorded over six consecutive cycles of exposure and recovery. A significant fall in the response can be seen between the first and second cycles but the decrease is much smaller between the second and third. The remaining responses show that a degree of stability has been achieved, with an average variation of $\pm$ 2 μA in the baselines. Figure 7.14 illustrates the corresponding 'turn-on' transients obtained after exposure to 8 ppm NO$_x$ for the final three cycles. It can be seen that the response to the gas is similar for each cycle, although variations become more visible towards the end of the recorded transient. An important feature of these responses is that the initial rate of 'turn-on' of the drain current, used to characterise the sensitivity of a device, are the same (up to time = 1 second).

Because there was still a small variation in the baselines, Figure 7.15 presents the results for cycles four through to six after normalising the data to the baseline recorded for the first cycle. Figure 7.16 depicts the sensitivity of the sensor (i.e. the initial gradient of the 'turn-on' response) for the final three cycles. Within experimental error these data are the same, indicating that the response to 8 ppm NO$_x$ was reproducible at room temperature.
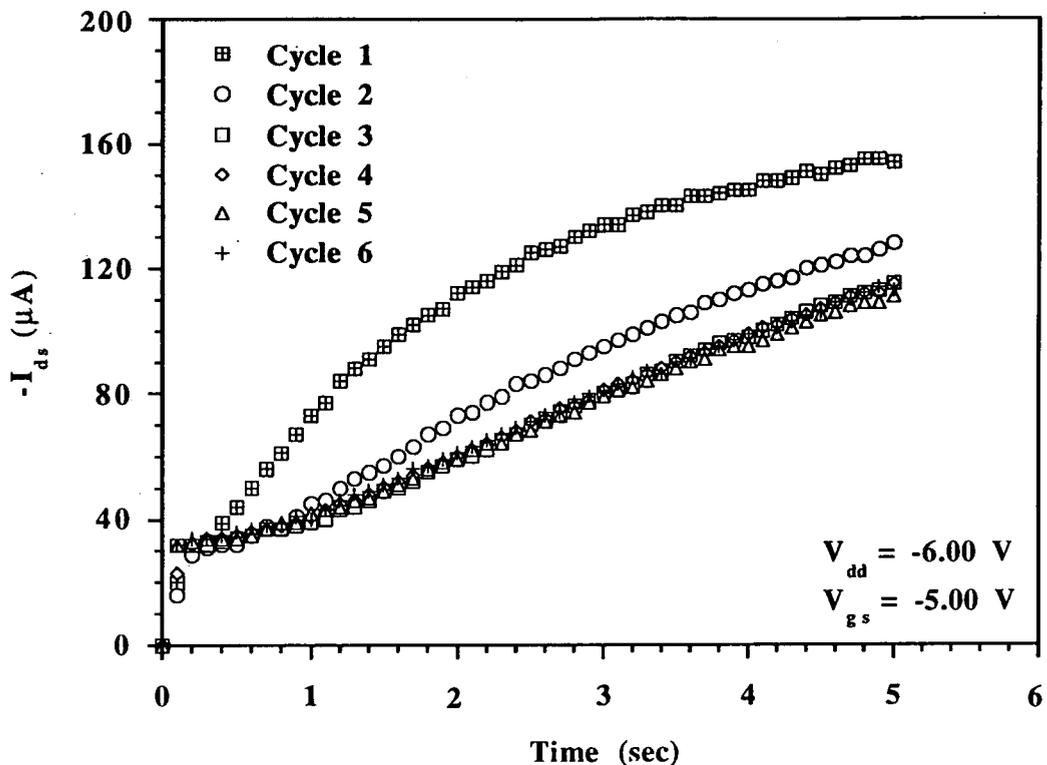
Figure 7.13 An illustration of how the baseline response stabilises after repeated exposure to 8 ppm NO_x followed by purging with nitrogen to re-establish a baseline. These results were obtained at room temperature for a 25 μm gate-hole device with polyaniline deposited.
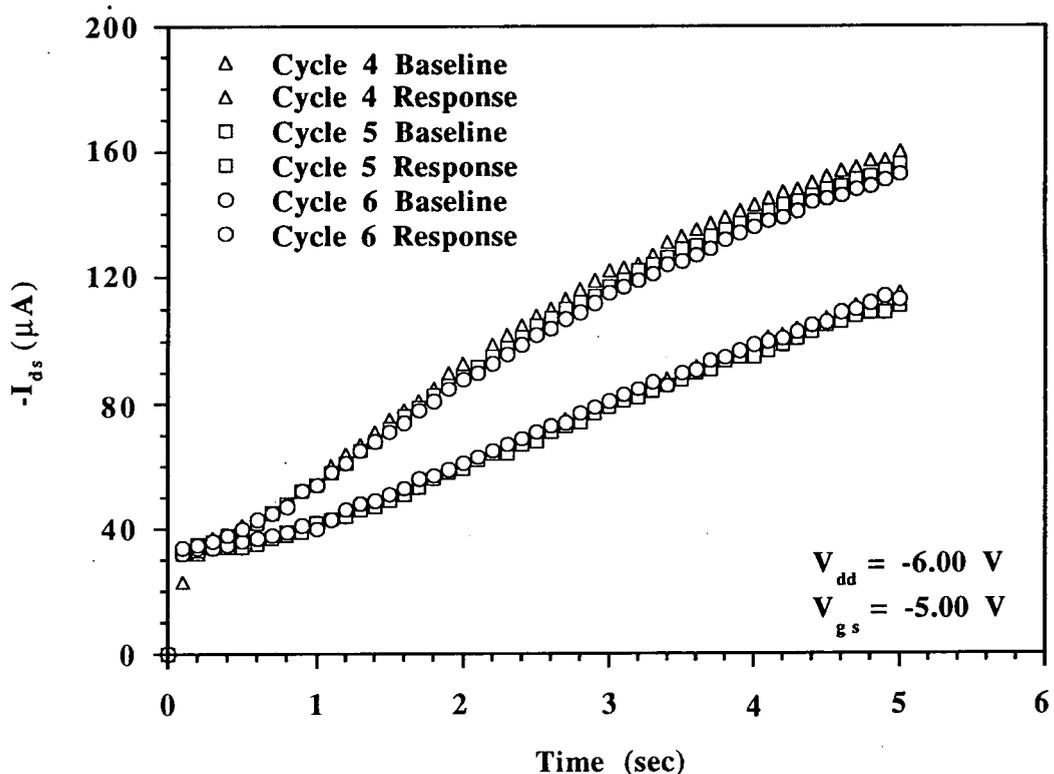
Figure 7.14 The baseline response and equivalent 'turn-on' transient after exposure to 8 ppm NO_x for three consecutive cycles. (The upper set of traces are the responses after exposure to the gas.) These results were obtained at room temperature for a 25 μm gate-hole device with polyaniline deposited.
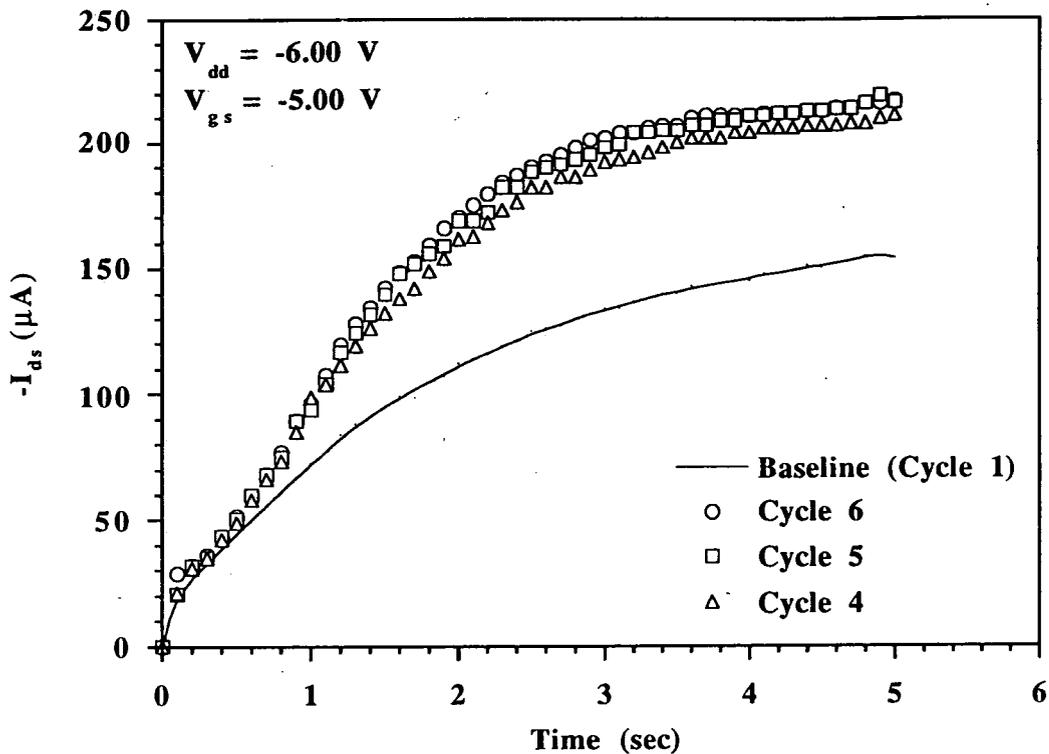
Figure 7.15 Source-drain current I_{ds} vs. time for three consecutive exposures to 8 ppm NO_x. These results were obtained at room temperature for a 25 μm gate-hole device with polyaniline deposited. These data have been normalised to the cycle 1 baseline.
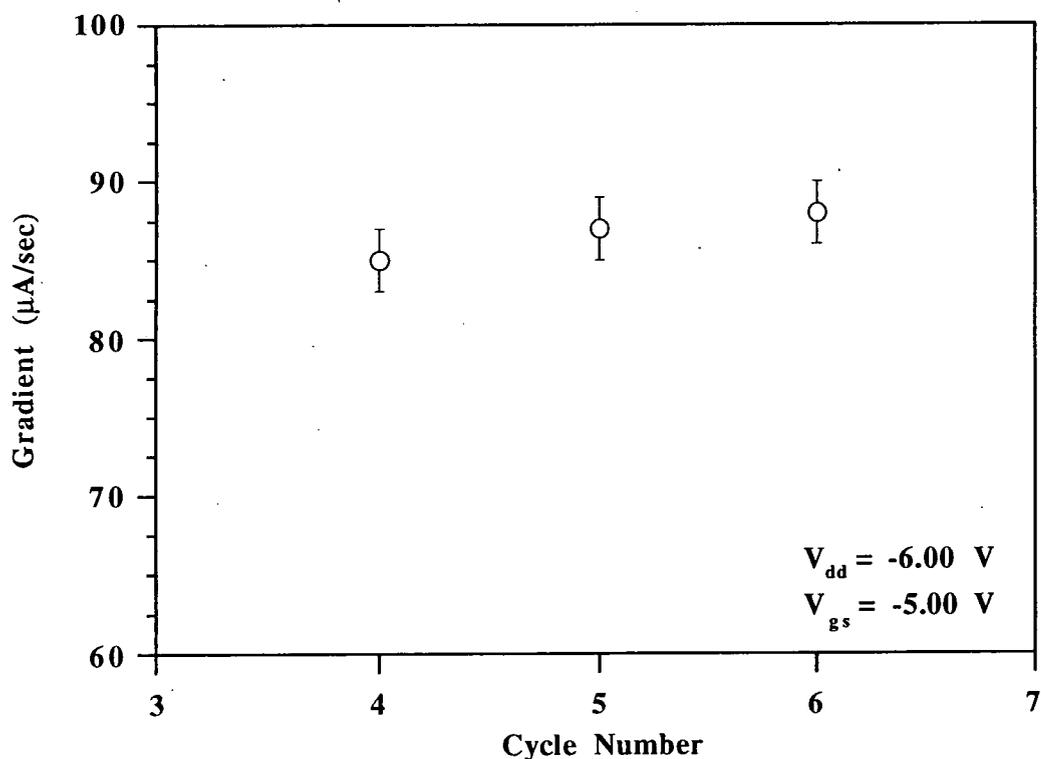
Figure 7.16 Initial gradient for the normalised 'turn-on' response for three consecutive exposures to 8 ppm NO_x.

For ammonia gas sensors using polyaniline as the active material, it has been reported that a period of surface activation can improve the response and recovery characteristics for a device.[6,7] Although no explanation has been offered for this phenomenon, it is conceivable that a similar effect has occurred between polyaniline and NO_x, evident in the results presented in this work. It is possible that initial exposure of the polymer to NO_x could lead to a very small irreversible chemical reaction on certain molecular sites within the film. In time, all of these sites will become occupied coinciding with the stability observed in both the baseline and 'turn-on' response:

7.1.10 The Effect of Raising the Operating Temperature on the Response and Recovery of the Sensor

It has been found that certain gas sensitive materials demonstrate greater sensitivities and/or selectivities when operated at elevated temperatures. (This was discussed in Chapter Two.) Unfortunately, the power required to raise the temperature of a device up to, in the case of tin oxide films, several hundred degrees Centigrade limits the potential portability of a commercial sensor. An ideal device is one that can be operated at room temperature. The results presented in this chapter for the organic/silicon hybrid FET sensor have already shown a successful room temperature response and subsequent recovery upon exposure to NO_x.

Figure 7.17 illustrates the 'turn-on' response at room temperature (15°C) and at an elevated temperature of 30°C, for the 35 μm gate-hole device with polyaniline deposited. It has been shown in Chapter Six (§ 6.6.2), that increasing the operating temperature modulates the 'turn-on' response. For this reason, the data shown in Figure 7.17 have been normalised to the room temperature baseline. It can be seen that the 'turn-on' response is marginally slower at 30°C in comparison to the room temperature response obtained at 15°C. This implies that the sensitivity of the sensor is reduced with increased operating temperature.

In contrast, the recovery of the device at 30°C (presented in Figure 7.18) is substantially more rapid than the recovery of a similar device recorded at room
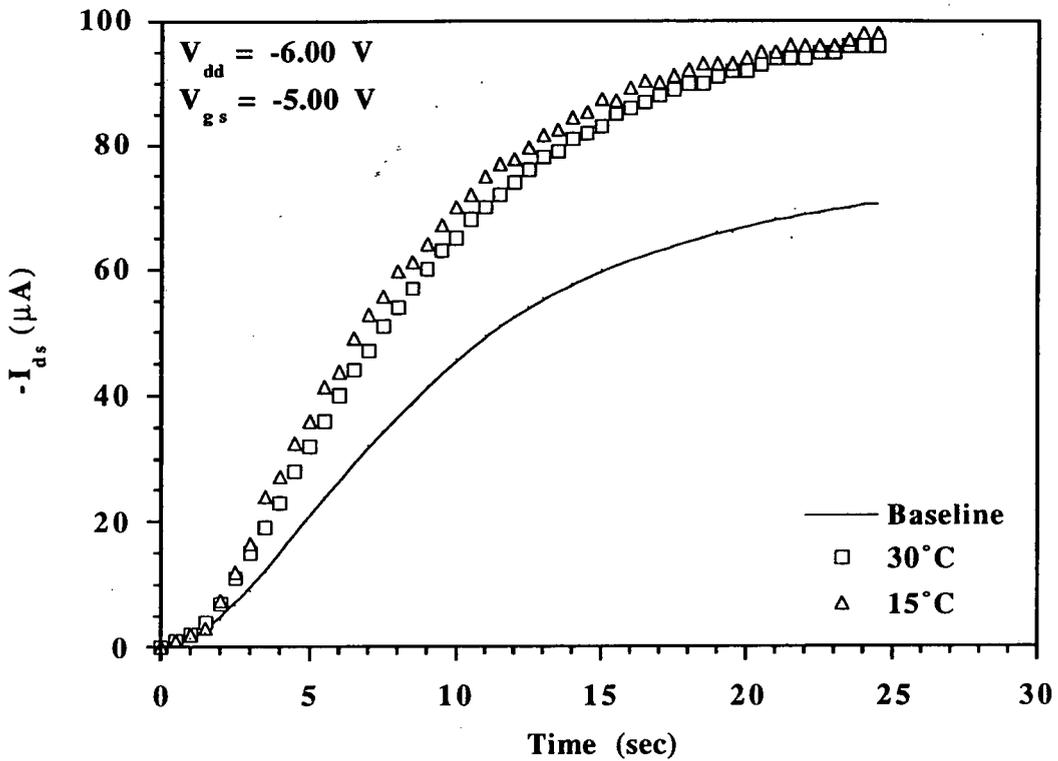
Figure 7.17 Source-drain current I_{ds} vs. time for the 35 μm gate-hole device with polyaniline deposited. The 'turn-on' responses after exposure to 8 ppm NO_x at two operating temperatures are shown. These data have been normalised to the room temperature baseline.
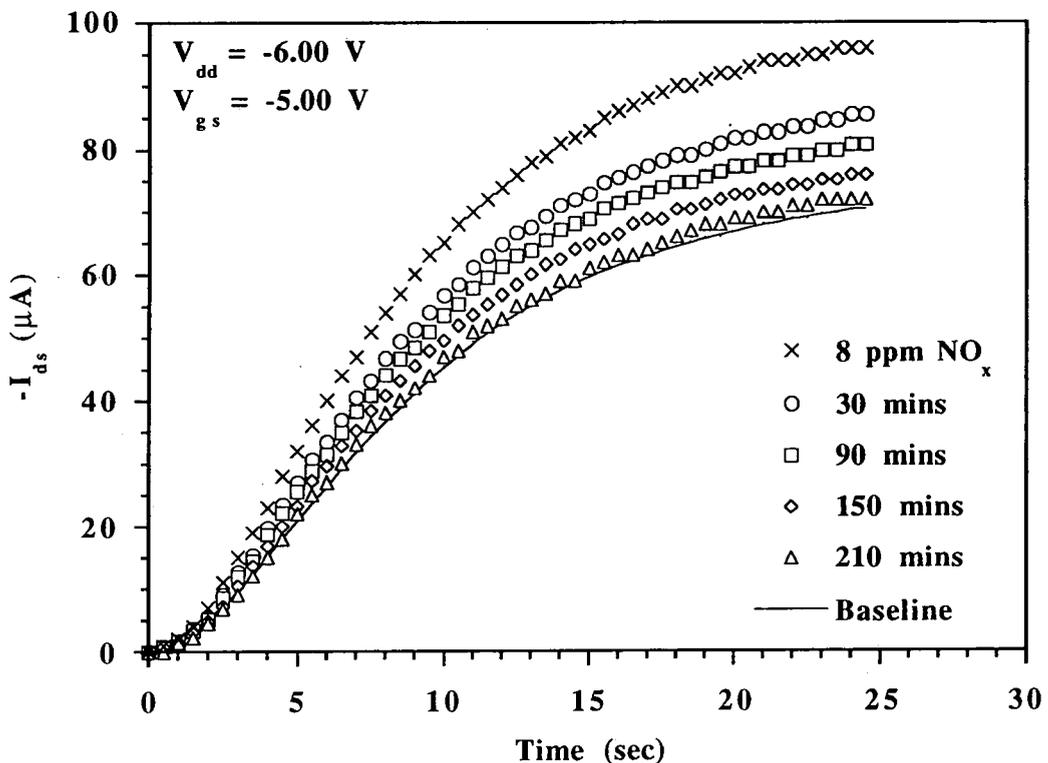
Figure 7.18 The recovery of the 35 μm gate-hole device by purging with pure nitrogen gas, following exposure to 8 ppm NO_x. The operating temperature of the sensor was maintained at 30°C throughout the experiment.

temperature (shown in Figure 7.10). At 15°C, an eight hour period purging the gas-tight chamber with nitrogen gas was required to re-establish a stable baseline response. At 30°C, recovery was achieved within four hours. The reduction in the time required for the device to recover after exposure to a gas suggests that the desorption of gaseous molecules from the bulk and surface of the polyaniline film is enhanced at elevated temperatures. It is expected that the extra energy available to the gas molecules due to the increased substrate temperature is responsible for this improvement in the reversibility of the sensor.

7.2 NO_x SENSING USING A PHTHALOCYANINE/SILICON HYBRID FIELD-EFFECT TRANSISTOR

The chemical properties and structure of the octa-substituted metal-free phthalocyanine compound used in this work (full name- 1, 4, 11, 15, 22, 25-octa-hexylphthalocyanine) were presented in Chapter Three (§ 3.2).

Figure 7.19 shows the 'turn-on' response for the 35 μm gate-hole device on exposure to increasing concentrations of NO_x. Unlike the devices incorporating polyaniline, the baseline established (and re-established after exposure to the gas) was reproducible from the commencement of the characterisation of the sensor. Because of this it was unnecessary to normalise the data. The increase in the rate of 'turn-on' of drain current, as the concentration of NO_x increases, can be attributed to an increase in the conductivity of the phthalocyanine film within the gate electrode. (Chapter Three, § 3.2.3, presents an explanation of the gas-phthalocyanine interaction mechanism.)

It was found that before a virgin device could be used, it was necessary to activate the sensor. This was achieved by exposing the device to 16 ppm NO_x for one hour. Prior to the activation, the lowest detectable concentration of gas was 8 ppm. It can be seen in Figure 7.19 that once activated, there was a detectable response for concentrations of NO_x as low as 2 ppm. It has been proposed for films of a lead phthalocyanine compound that rapid adsorption of NO_x is facilitated by the presence of residual traces of strongly-bound NO_x, which must be built up on fresh films before the normal
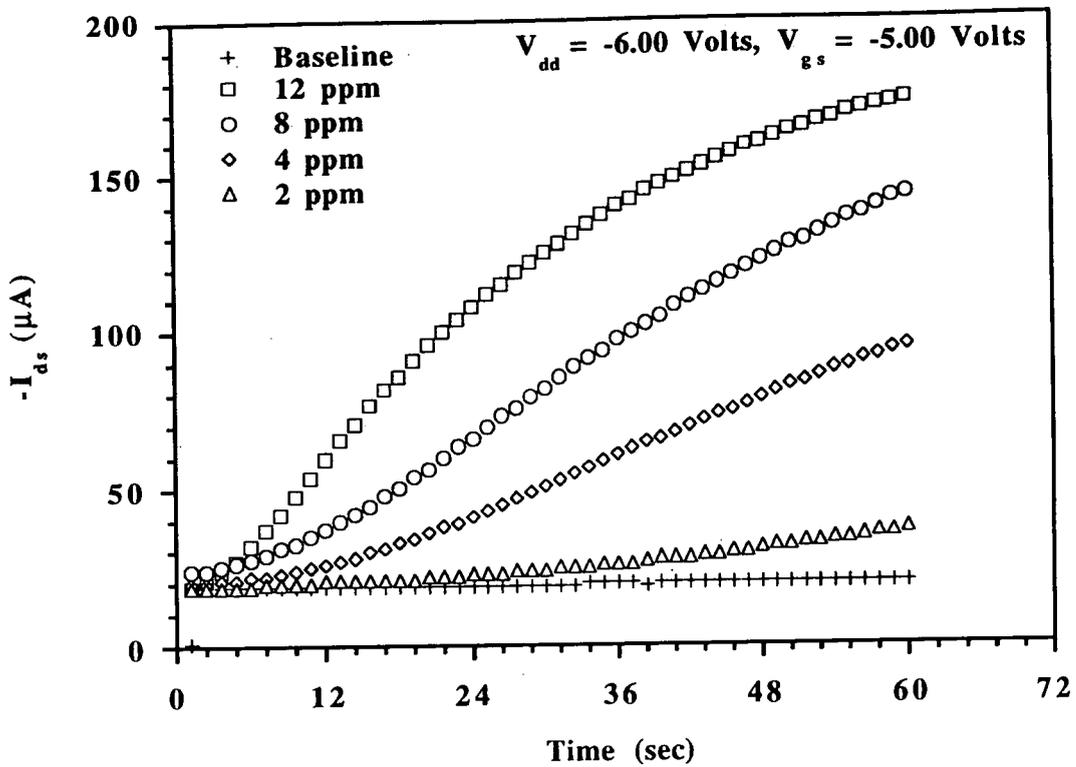
Figure 7.19 Source-drain current I_{ds} vs. time for the 35 μm gate-hole device with phthalocyanine deposited in various NO_x atmospheres.
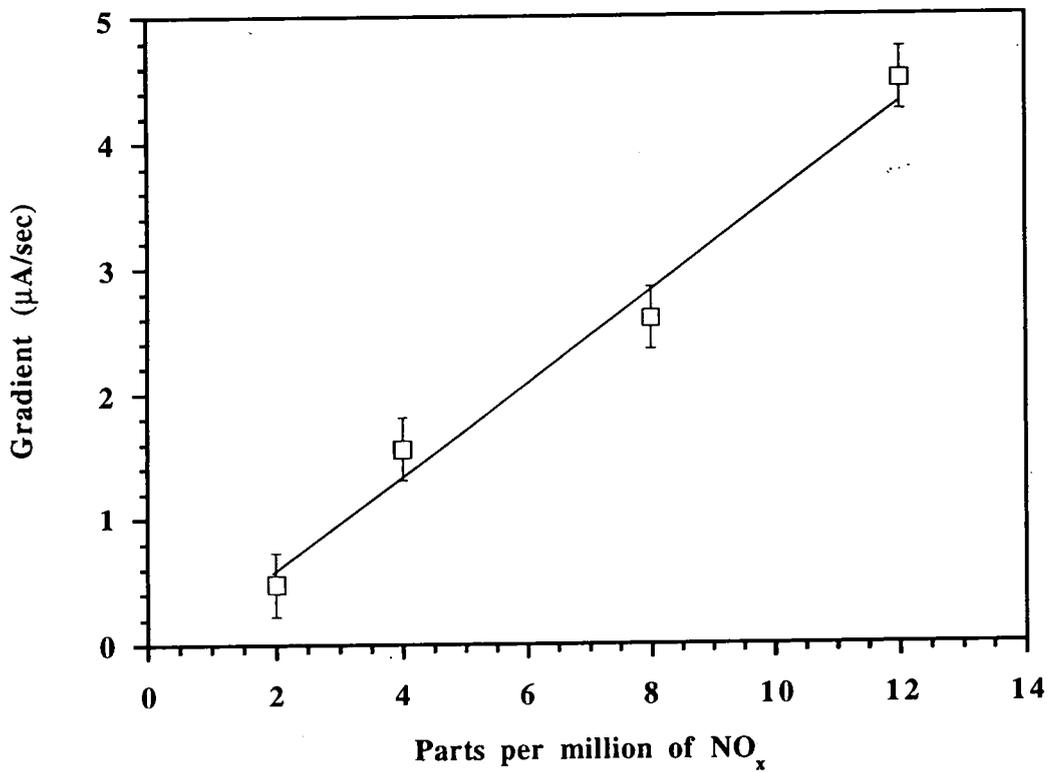
Figure 7.21 Initial gradient for the normalised 'turn-on' responses to NO_x.

response is obtained.[8] In effect, traces of adsorbed NO_x act as a catalyst for the adsorption of subsequent NO_x molecules. (This type of effect is comparable to the eventual stability in the response achieved for an equivalent device incorporating a film of polyaniline, as shown in § 7.1.9.)

The reversibility of the phthalocyanine device, compared to the polyaniline device, was initially rapid, but entirely complete. Within the first hour, approximately 80% recovery was achieved, and fully achieved after a further four hours. This can be seen in Figure 7.20.
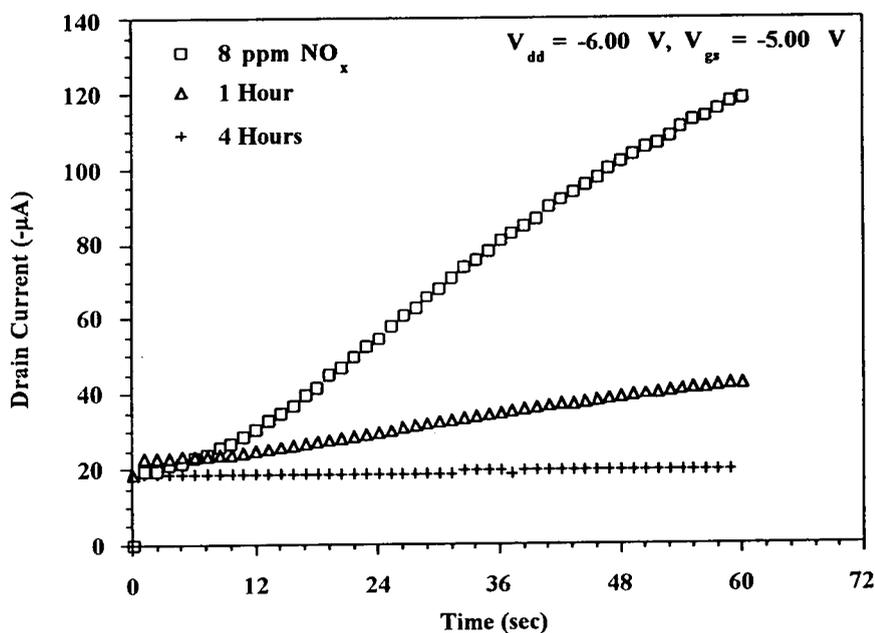
Figure 7.20 Drain current I_{ds} vs. time for the 35 μm gate-hole device with phthalocyanine deposited showing the recovery after exposure to 8 ppm NO_x.

During the first hour it is thought that NO_x was desorbing rapidly from the surface of the film. In contrast, the longer period (until complete recovery) was due to the more difficult process of desorbtion of the gas from the bulk of the film. (This is similar to the explanation provided in § 7.1.7 for the polyaniline sensor.)

The initial gradient of the 'turn-on' response (i.e. the sensitivity of the device), calculated in microamperes per second is illustrated in Figure 7.21. The sensitivity for

the phthalocyanine device is lower than for the equivalent 35 μm gate-hole device with polyaniline deposited. This suggests that the conductivity of the phthalocyanine film, in an inert nitrogen atmosphere, was lower than for the polyaniline film.

The thickness and physical structure of the two films are important factors in determining how readily the gas molecules will be adsorbed by the organic films. Typically, the phthalocyanine film thickness within the air-gap in the gate electrodes was greater than the spin-coated polyaniline films ($\approx$60 nm compared to $\approx$35 nm). The thicker film may inhibit the flow of charge through the bulk of the film leading to a slower increase in the drain current upon the application of a gate bias.

Scanning electron micrographs of spin-coated films of polyaniline have revealed a highly fibrous mesh-like structure with a large density of pores separating the fibres.[9] For gas sensing applications, it is likely that the fibrous mesh network will increase the surface area available for interaction between the polymer and the gas. Furthermore, the large number of pores observed in the film could enable a higher rate of gas diffusion into the bulk of the film. In Chapter Three (§ 3.2.2), evidence of the crystalline structure exhibited in spin-coated films of the phthalocyanine used in this work was presented. It is accepted that the conduction of charge is facilitated by films with a more ordered structure. An organised film with an ordered structure will, in general, allow a gas to diffuse through the bulk at a more rapid rate than an amorphous film of a similar compound.

Various substituted phthalocyanine compounds have been successfully used as NO_x sensors. In general, sensors utilising phthalocyanine films are more sensitive to this gas than those using conductive polymers. Thin films produced by thermal evaporation and the Langmuir-Blodgett (LB) technique have been deposited on various structures and the change in room temperature conductivity measured after exposure to the gas. Lead phthalocyanine demonstrates the highest sensitivity to NO_x, permitting measurements down to between 1 and 10 parts per billion (ppb) in air.[10,11] Complete recovery for these sensors was reported after approximately 90 seconds. LB films of an asymmetrically substituted phthalocyanine have been shown to have a room

temperature response to NO_x to 1 ppm. Recovery after this exposure required approximately 2 minutes, though increasing the concentration and/or the duration reduced the rate of recovery. These films are not affected by the presence of other gases or from water vapour.[12,13]

The phthalocyanine compound used in this work was not as sensitive as those reported above (2 ppm compared with 10 ppb). The deposition technique used, (e.g. evaporation, LB or spin coating) determines the physical structure, and in some cases the chemical properties of the films. Both the device sensitivity and the rate of recovery depend upon these parameters. The choice of a central metal-ion and the substituted groups around the periphery of the molecule can also be used to enhance the response of a sensor. These considerations, as well as the type of sensor structure utilised explain why different results have been reported for NO_x phthalocyanine sensors.

7.3 SUMMARY

The results for exposing the polyaniline sensing devices to low concentrations of NO_x have been presented. It has been shown that the sensor incorporating the greatest surface area of polymer (i.e. the gate-electrode with the largest gap in the metallisation) demonstrates the highest sensitivity to NO_x: the 35 µm gate-hole device was found to be sensitive to 1 ppm at room temperature. The recovery of the sensors, including the observed drift in the baseline characteristics, has been examined with a possible explanation for these effects presented. The variation in the response and recovery of the sensor when operated at an elevated temperature has been discussed. The effect of NO_x on a device incorporating a metal-free phthalocyanine film has been investigated and compared to a similar sensor incorporating polyaniline. Table 1 overleaf, summarises the different sensing properties obtained for the various devices. In the next chapter, the responses of the devices to SO_2 and H_2S are discussed. An investigation of the capacitance-voltage characteristics and the optical absorption spectra of thin films of polyaniline deposited on glass substrates after exposure to a gas are also presented.

DEVICE (GATE-HOLE)	SENSING MATERIAL	RESPONSE TIME	MINIMUM SENSITIVITY	RECOVERY TIME
35 μm	Polyaniline	20 secs	1 ppm	50% - 2.5 hours 100% - 8 hours
35 μm	Phthalocyanine	60 secs	2 ppm	80% - 2 hours 100% - 6 hours
25 μm	Polyaniline	5 secs	2 ppm	N/A
15 μm	Polyaniline	0.5 secs	8 ppm	N/A

Table 1 A Summary of the Room Temperature Response to NO_x of the Sensing Devices

REFERENCES

1. G.O. Nelson *Gas Mixtures: Preparation and Control* (Lewis Publishers 1992) 191.

2. N.E. Agbor, M.C. Petty and A.P. Monkman, *Sensors and Actuators B*, **28** (1995) 173-179.

3. G. Sberveglieri, S. Groppelli,P. Nelli, V. Lantto, H. Torvela, P. Romppainen and S. Leppävuori, *Sensors and Actuators B*, **1** (1990) 79-92.

4. M.J. Tierney and H.L. Kim, *Anal. Chem.*, **65** (1993) 3435-3440.

5. L. Sun, C. Gu, K. Wen, X. Chao, T. Li, G. Hu and J. Sun, *Thin Solid Films*, **210** (1992) 486-488.

6. W. Jiakun and M. Hirata, *Sensors and Actuators B*, **12** (1993) 11-13.

7. M. Hirata and L. Sun, *Sensors and Actuators A*, **40** (1994) 159-163.

8. P.B.M. Archer, A.V. Chadwick, J.J. Miasik, M. Tamizi and J.D. Wright, *Sensors and Actuators*, **16** (1989) 379-392.

9. N.E. Agbor, Ph.D. Thesis (University of Durham UK) 1993.

10. B. Bott and T.A. Jones, *Sensors and Actuators*, **5** (1984) 43-53.

11. C. Hamann, A. Mrwa, M. Müller, W. Göpel and M. Rager, *Sensors and Actuators B*, **4** (1991) 73-78.

12. A. Cole, R.J. McIlroy, S.C. Thorpe, M.J. Cook, J. McMurdo and A.K. Ray, *Sensors and Actuators B*, **13** (1993) 416-419.

13. D. Crouch, S.C. Thorpe, M.J. Cook, I. Chambrier and A.K. Ray, *Sensors and Actuators B*, **19** (1994) 411-414.

CHAPTER EIGHT

RESPONSE TO SO₂ AND H₂S: RESULTS AND DISCUSSION

This chapter describes further results obtained with the polyaniline/silicon hybrid FET sensors. The responses of the devices to various concentrations of SO_2 and H_2S are discussed. The effect of exposure to SO_2 and NO_x on the capacitance-voltage characteristic of one of the devices is also described. Finally, the optical absorption spectra of polyaniline thin films before and after exposure to all three gases are presented.

8.1 SO₂ SENSING USING A POLYANILINE/SILICON HYBRID FIELD-EFFECT TRANSISTOR

The SO_2 was supplied at a concentration of 1000 ppm, diluted in pure nitrogen. Lower concentrations were achieved, using the gas blender to mix the SO_2 with more nitrogen gas. The experimental procedure used to characterise a device has been described in Chapter Five (§ 5.4). To avoid inconsistencies when comparing the results, the data were normalised by the method described in Chapter Seven (§ 7.1.2).

8.1.2 Response of the 35 μm Gate-hole Device

Figure 8.1 shows the room temperature 'turn-on' response for the 35 μm gate-hole device, following exposure to increasing concentrations of SO_2. The data have been normalised to the 2 ppm baseline. SO_2 is a weaker oxidising gas than NO_x, which is reflected in the slower 'turn-on' responses shown in the figure. (A sixty second sample time was used rather than the 25 second period required for an equivalent device used for NO_x sensing.) This is indicative of a smaller increase in the conductivity of the polyaniline for comparable concentrations of the two test gases. It can be seen from Figure 8.1 that this device was capable of measuring concentrations down to 2 ppm
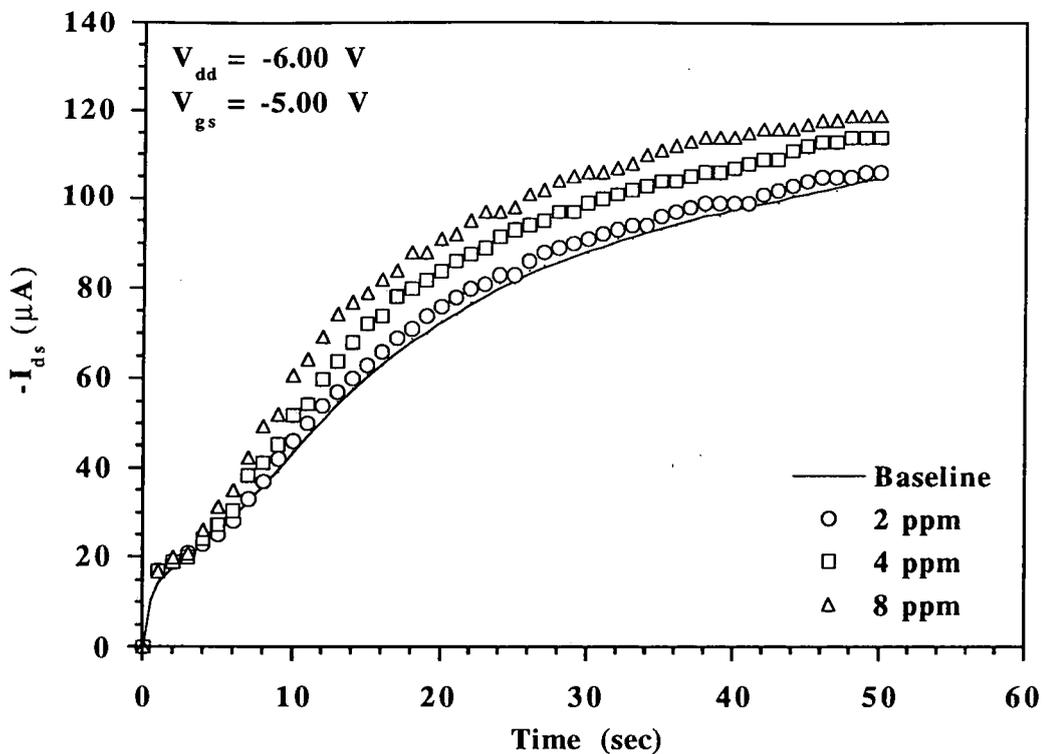
Figure 8.1 Source-drain current I_{ds} vs. time for the 35 μm gate-hole device with polyaniline deposited in various SO_2 atmospheres. These data have been normalised to the 2 ppm baseline.
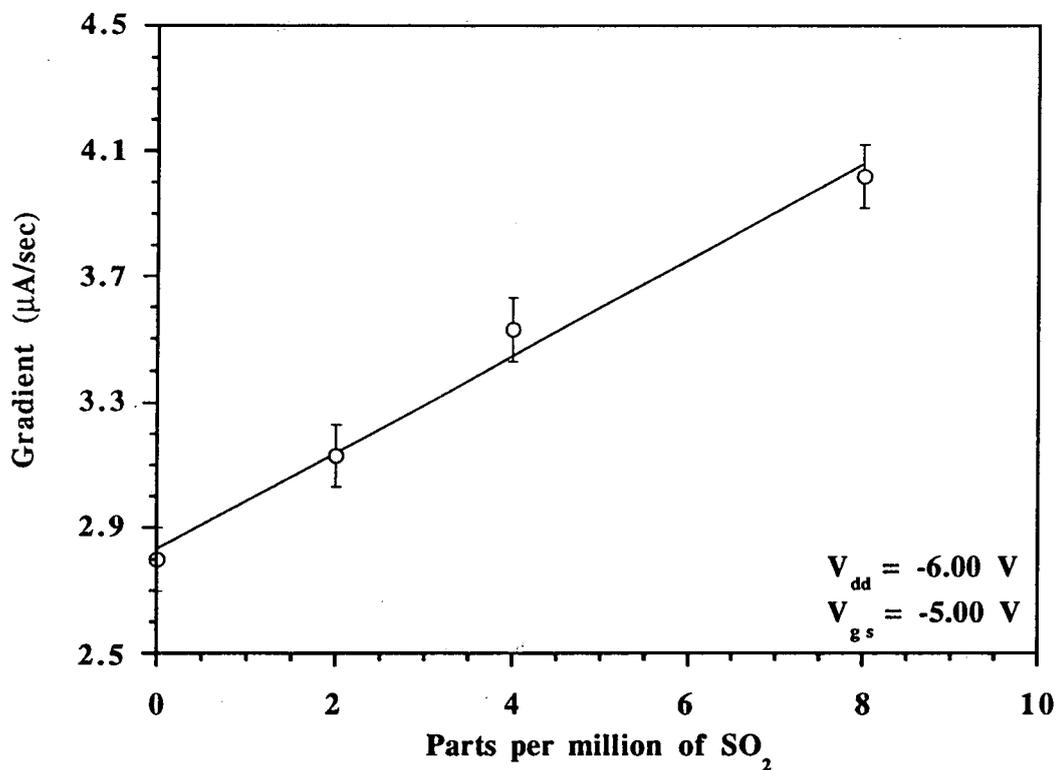
Figure 8.2 Initial gradient for the normalised 'turn-on' response.

(compared to 1 ppm for NO_x). The initial gradient of the 'turn-on' response is illustrated in Figure 8.2. Within experimental error, a straight-line fit can be ascribed to these data points. A comparison of the sensitivity of the 35 μm gate-hole device exposed to both NO_x and SO_2 is shown in Figure 8.3.
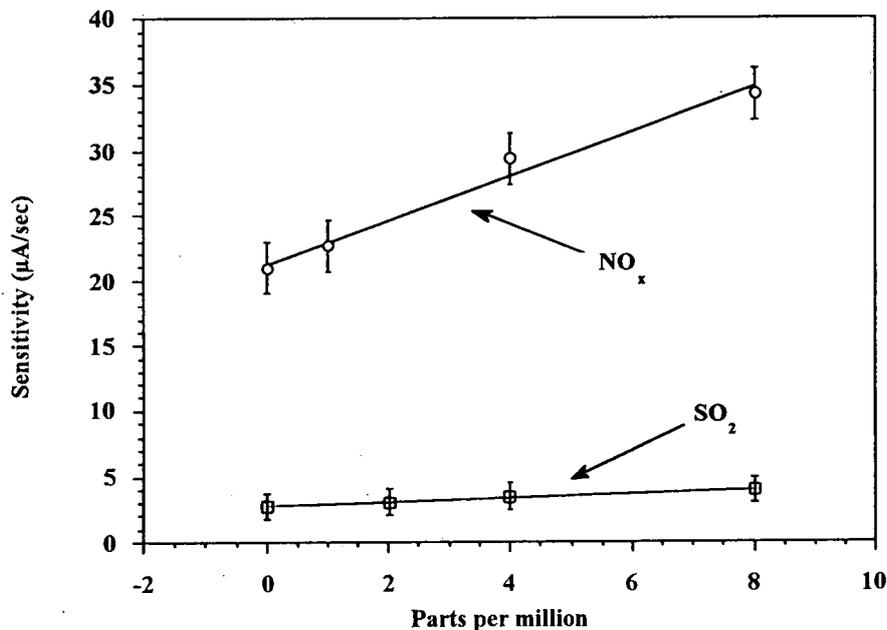
Figure 8.3 A comparison of the room temperature sensitivity for the 35 μm gate-hole device with polyaniline deposited after exposure to several concentrations of NO_x and SO_2.

It can be seen from this figure that the initial gradient of the 'turn-on' response is much greater for the stronger oxidising gas, NO_x. This difference in the initial gradient (i.e. sensitivity) could be used to distinguish between these two gases.

A comparable detection threshold has been reported at room temperature for a spun polyaniline chemiresistor.[1] A response was observed after exposure to 2 ppm SO_2, with complete recovery occurring after 100 minutes in air. An interdigital capacitor coated with an organically modified ceramic has demonstrated a sensitivity to 1 ppm SO_2 when operated at 50 °C.[2]

8.1.3 Response of the 25 μm Gate-hole Device

Figure 8.4 shows the normalised room temperature 'turn-on' response for the 25 μm gate-hole sensor following exposure to increasing concentrations of SO_2. For this device, the lowest detectable concentration of SO_2 was 8 ppm. Exposure to 16 ppm SO_2 produced a response that could be visually identified from the 8 ppm 'turn-on' transient. However, the resolution of the data collected was insufficient to distinguish further concentrations between 8 ppm and 16 ppm. (The inset of Figure 8.4 highlights the small change in the 'turn-on' response for the two gas concentrations.) This lower sensitivity in comparison to the 35 μm gate-hole device can be explained by the smaller surface area of polyaniline available for the gas to react with.

Experiments with the 15 μm gate-hole sensor showed no response in the concentration range of interest in this work.

8.1.4 Reproducibility of the Sensor Response to SO_2

Figure 8.5 illustrates two 'turn-on' transients obtained for the same 35 μm gate-hole sensor recorded four weeks apart. The data were acquired at room temperature after the device had been exposed to 8 ppm SO_2. It can be seen that the two responses are quite similar. This indicates good chemical stability of the polyaniline film over an extended period of time, including several other exposures to test gases.

8.2 H_2S SENSING USING A POLYANILINE/SILICON HYBRID FIELD-EFFECT TRANSISTOR

Figure 8.6 presents the response of the 25 μm gate-hole device after exposure to several concentrations of H_2S. The range of concentrations used in this experiment was different from those used for NO_x and SO_2. It was found that significantly large increases in the gas concentration produced only small changes in the 'turn-on' responses for the device. The initial gradient of the 'turn-on' response is illustrated in
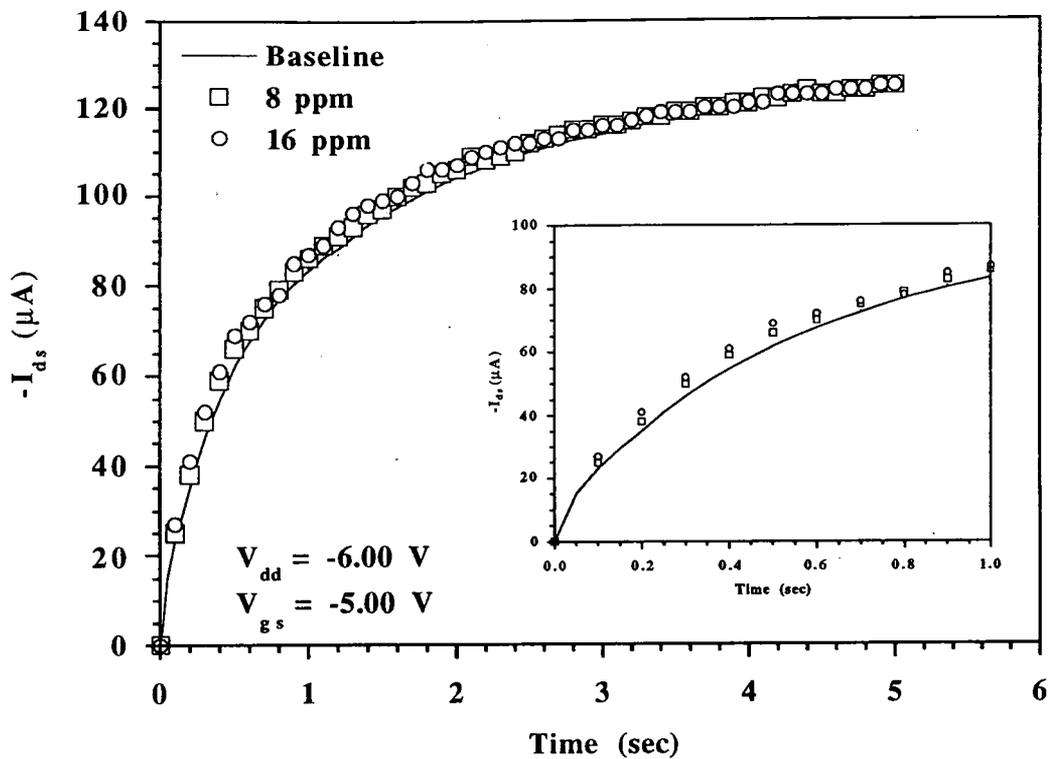
Figure 8.4 Source-drain current I_{ds} vs. time for the 25 μm gate-hole device with polyaniline deposited after exposure to SO_2. These data have been normalised to the 8 ppm baseline.
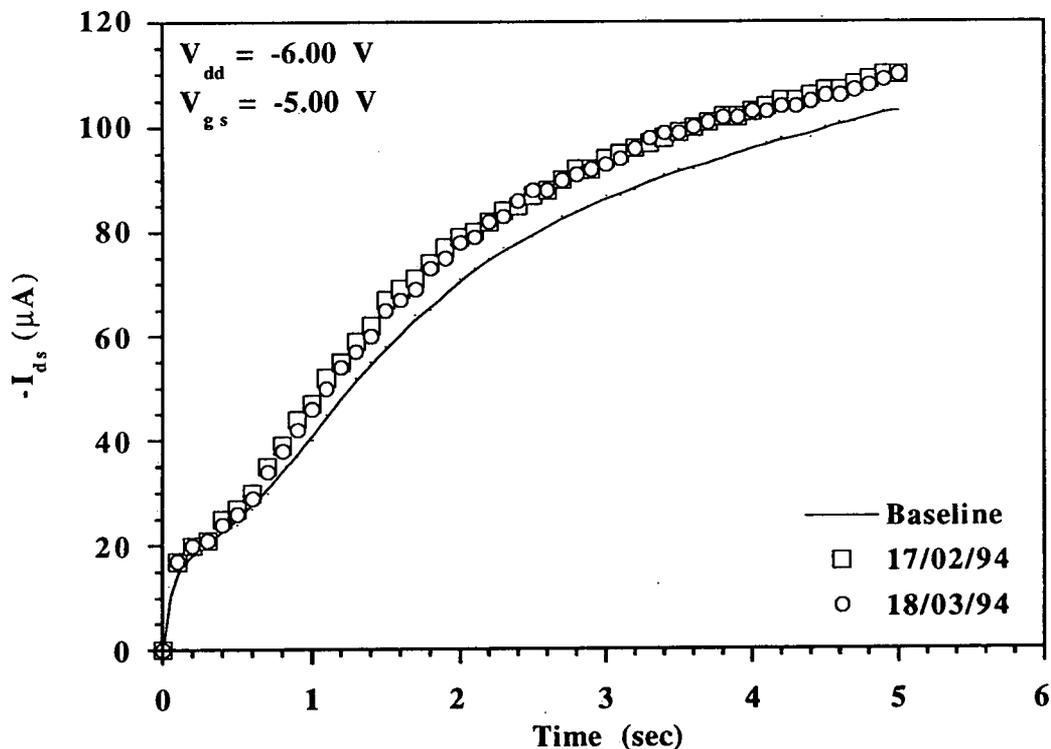
Figure 8.5 Source-drain current I_{ds} vs. time for the 35 μm gate-hole device with polyaniline deposited after exposure to 8 ppm SO_2. The second set of data (18/03/94) were obtained four weeks after the first (17/02/94) using the same device. These data have been normalised to the 17/02/94 baseline.
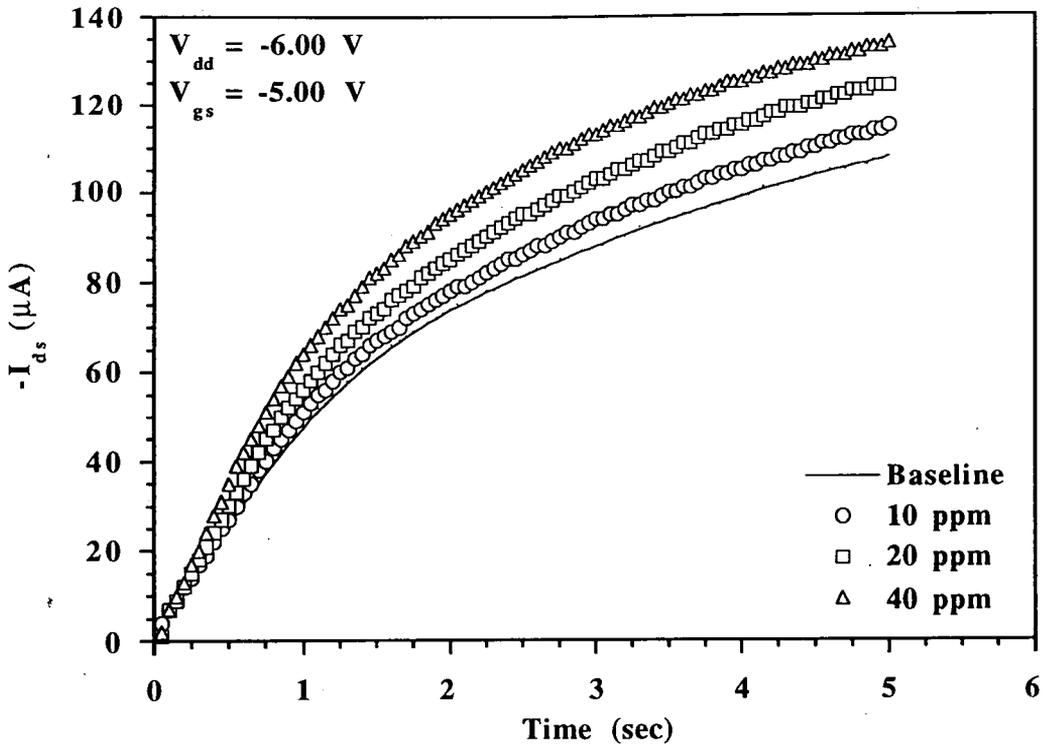
Figure 8.6 Source-drain current I_{ds} vs. time for the 25 µm gate-hole device with polyaniline deposited in various H_2S atmospheres. These data have been normalised to the 10 ppm baseline.
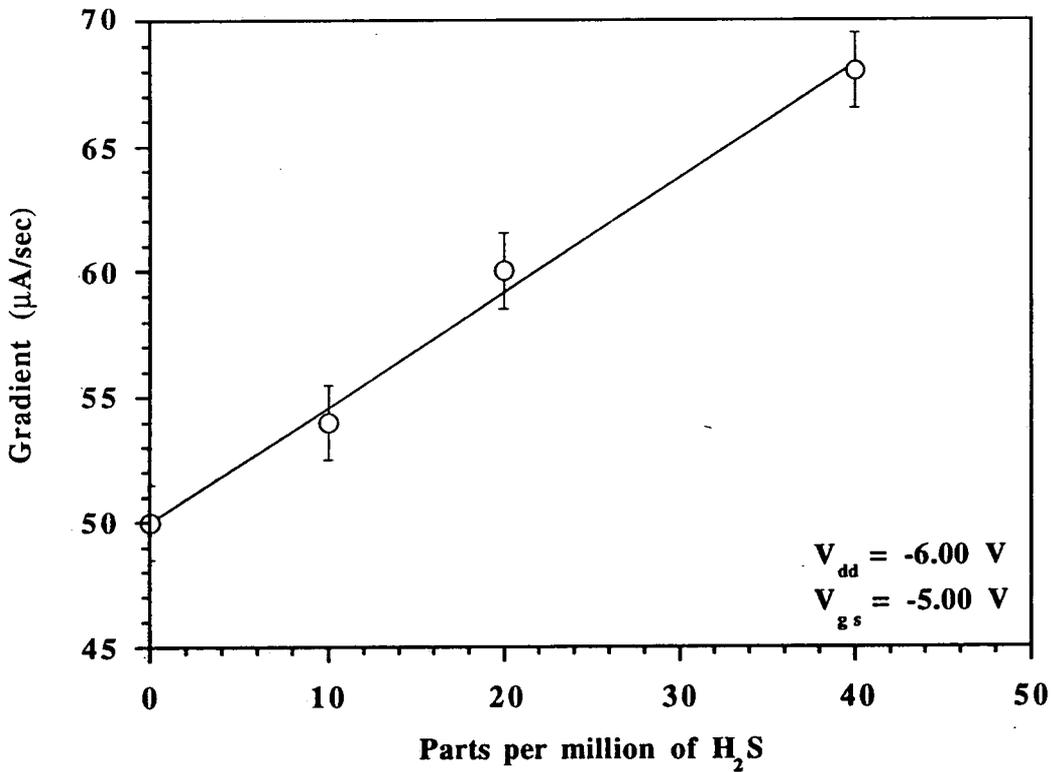
Figure 8.7 Initial gradient for the normalised 'turn-on' response.

Figure 8.7. Within experimental error, a straight-line fit can be ascribed to these data points.

The increase in the rate of 'turn-on' of the drain current shows that the presence of H_2S is increasing the conductivity of the polyaniline. Because H_2S is a known reducing gas, it may have been expected that exposure to this gas would have produced a decrease in conductivity and hence, a reduced rate of 'turn-on' when compared to the baseline response.

A similar increase in the conductivity of spin-coated films of polyaniline has been reported previously.[3] The effect may be attributed to the availability of more than one type of reaction site and/or the possibility of a number of different chemical reactions.

At room temperature and pressure, H_2S dissociates into H^+ and HS^- as illustrated in Figure 8.8.[4,5] The dissociation of H_2S is subsequently followed by H^+ protonating the polyaniline. As noted in Chapter Three (§ 3.1.4), this protonation reaction produces semiquinone radicals which are conjugated, increasing the d.c. conductivity.
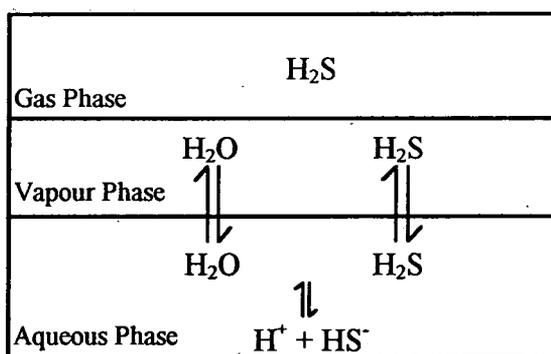
Figure 8.8 An illustration of the state of H_2S in different environments [Adapted from ref. 4]. In this work, the vapour phase is equivalent to H_2S/surface bound water molecules and the aqueous phase is equivalent to H_2S/water molecules trapped in the bulk of the film.

This is a possible explanation for the apparent increase in the conductivity of the polyaniline, leading to the observed increase in the rate of 'turn-on' of the drain current. Such a reaction can be considered to be a bulk dominated process because of the higher concentration of water molecules trapped in the bulk of the film.

A tin-oxide semiconductor gas sensor incorporating copper oxide has been reported for H_2S sensing with a detection limit of 10 ppm.[6] The maximum sensitivity for this device occurred for an operating temperature of 150 °C. The response to other gases (including methane, carbon monoxide and ethanol vapour) was negligible, illustrating the excellent selectivity of the sensor to H_2S. The recovery time of this device was shown to be approximately three minutes.[6] This is considerably faster than the polyaniline FET device used in this work, although the volume of the test chamber and the gas flow rates are not stated. Both of these parameters will have a direct effect on the rate of dissociation of the gas from the polyaniline film.

A spun polyaniline chemiresistor has been demonstrated with a 4 ppm detection threshold to H_2S. Because of the very high resistance of the polymer film, the recorded change in the current for this exposure was less than 0.4 pA. This is considerably less than the 10 μA increase in the drain current illustrated in Figure 8.6 (for the polyaniline FET) at the same gas concentration. Complete recovery after exposure to 10 ppm H_2S was achieved for the chemiresistor after 60 minutes.[1]

8.3 H_2S AND SO_2 SENSING USING A PHTHALOCYANINE/SILICON HYBRID FIELD-EFFECT TRANSISTOR

Exposing the sensor to concentrations of SO_2 and H_2S up to 30 ppm produced no measurable response. This selectivity at low concentrations of NO_x is a useful property of this device. Several other phthalocyanine sensors have been reported with similar selectivities. For example, an amphiphilic substituted phthalocyanine has been demonstrated to have a limited response to 10 ppm H_2S and 2 ppm SO_2, in contrast to the greater effect generated by 1 ppm NO_x.[7] Thermally evaporated films of metal-free and lead phthalocyanine compounds have shown reduced sensitivities to SO_2 (10 ppm) and H_2S (5 ppm), in comparison to NO_x (1 ppb).[8]

8.4 ULTRAVIOLET/VISIBLE SPECTROSCOPY OF EXPOSED FILMS OF POLYANILINE

Figure 8.9 shows the ultraviolet/visible spectrum of a spin-coated film of polyaniline before (solid line) and after (dashed line) exposure to 8 ppm NO_x. The spectrum acquired before exposure to the gas is typical of those obtained for the undoped emeraldine base material,[9-11] with absorption peaks centred at approximately 325 nm (3.8 eV) and 625 nm (2.0 eV). These are due to the $\pi \rightarrow \pi^*$ transition of the benzenoid ring along the polymeric backbone and the transition from a benzenoid ring to a quinoid ring, respectively. (This was discussed in Chapter Three, § 3.1.3.)

Exposure of the film to 8 ppm NO_x for one hour leads to a reduction in the intensity of the peak at 325 nm, whilst the peak at 625 nm has diminished and become part of a broad absorption band with a peak around 900 nm, indicative of partial protonation. The simultaneous presence of the 2 eV and 1.4 eV energy bands suggests phase segregation of fully protonated and unprotonated domains. In Figure 8.10 the spectrum for a similar spin-coated polyaniline film is shown after exposure to 30 ppm NO_x. As expected, the degree of protonation is greater, with the peak at 625 nm having now entirely disappeared. The intensity of the peak at 325 nm has further diminished whilst the peak at 900 nm is now clearly more pronounced. The lack of the peak at 630 nm (equivalent to doping the emeraldine base with an HCl solution of pH = 1) is confirmation of the complete protonation of the base to the emeraldine salt form of polyaniline.[9]

It has been suggested that the disappearance of the 625 nm absorption peak, and the formation of those at 420 nm and 900 nm, are indicative of the absence of the localised quinoid structure of emeraldine base and the formation of a polaron lattice.[12,13] The reduction in the absorption at 325 nm and the broad absorption band extending from approximately 800 nm into the infrared (i.e. a shift in the oscillator strength) is consistent with metallic behaviour.[14]

Figure 8.11 shows the ultraviolet/visible absorption spectra for a similar spin-coated film of polyaniline before (solid line) and after (dashed line) exposure to 8 ppm SO_2.
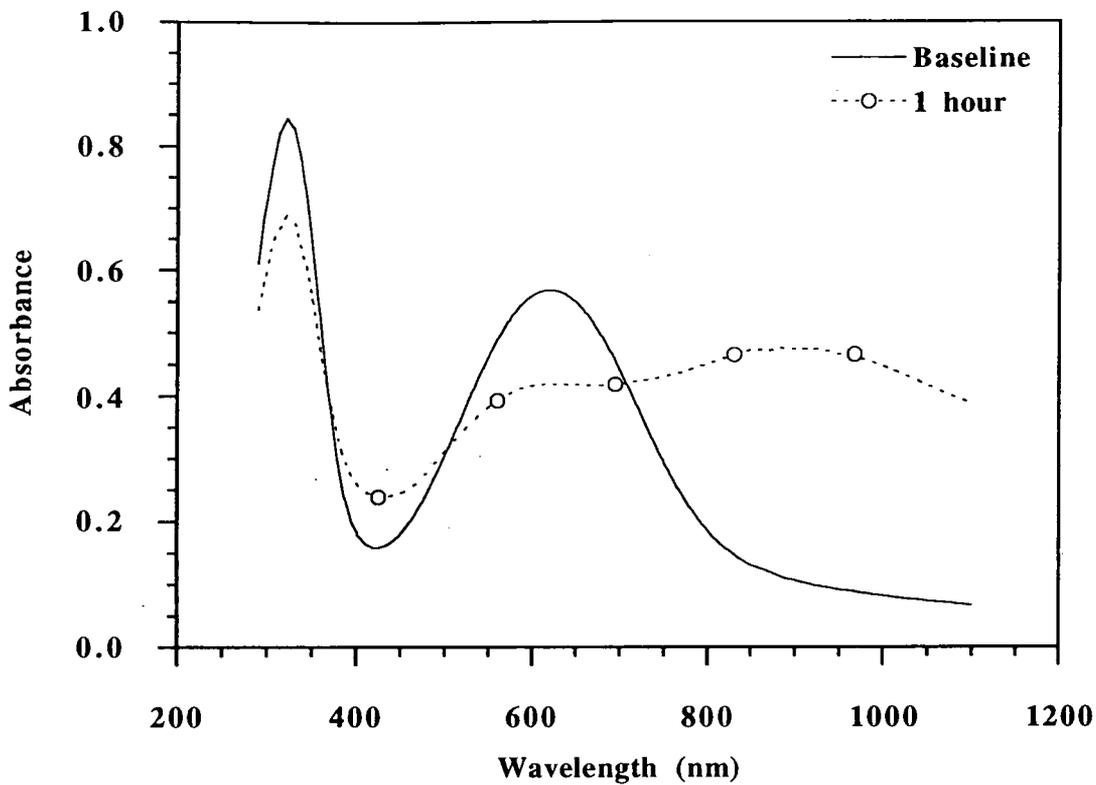
Figure 8.9 UV-visible absorption spectra of a 50 nm thick polyaniline film spin-coated on a glass substrate after one hours exposure to 8 ppm NO_x.
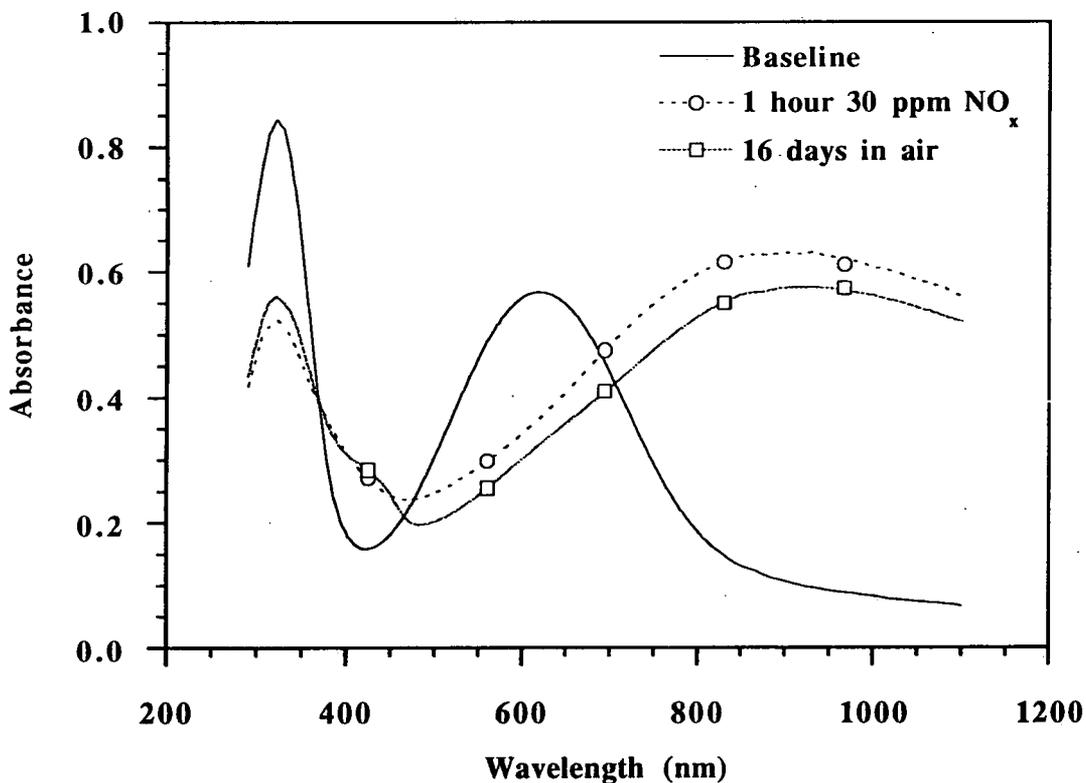
Figure 8.10 UV-visible absorption spectra of a 50 nm thick film polyaniline film spin-coated on a glass substrate after 1 hours exposure to 30 ppm NO_x. A second spectrum of the sample after 16 days in an air atmosphere is shown.
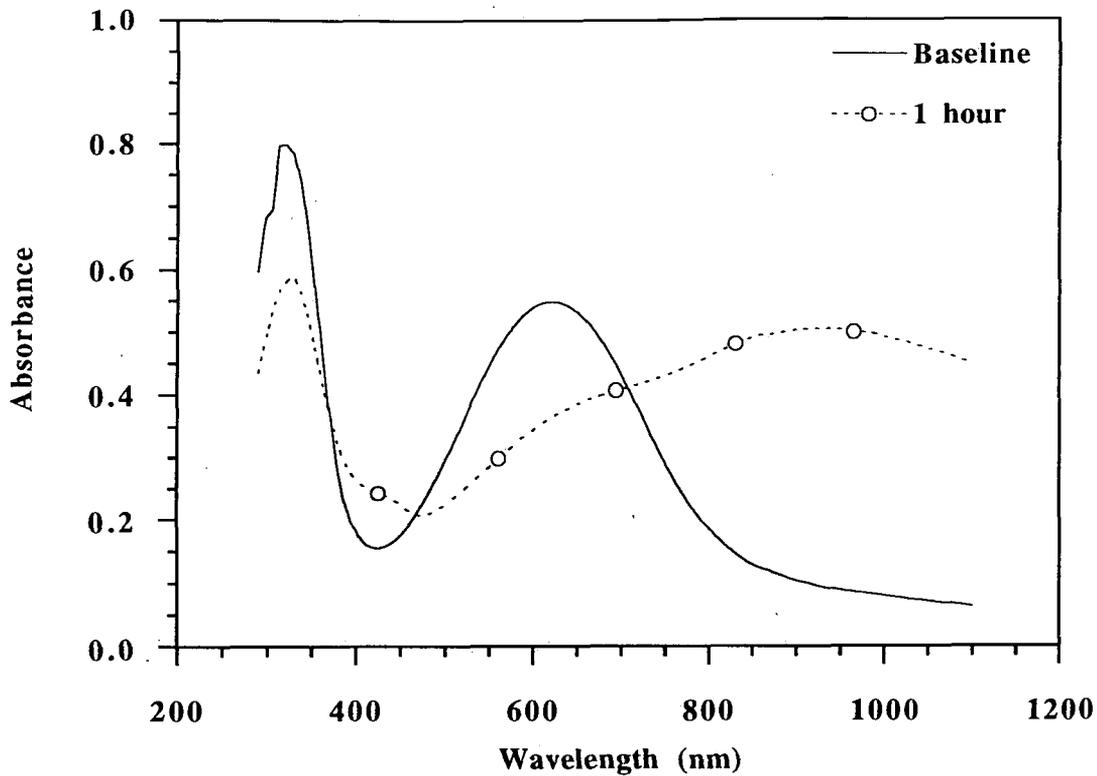
Figure 8.11 UV-visible absorption spectra of a 50 nm thick polyaniline film spin-coated on a glass substrate after exposure for one hour to 8 ppm SO_2.
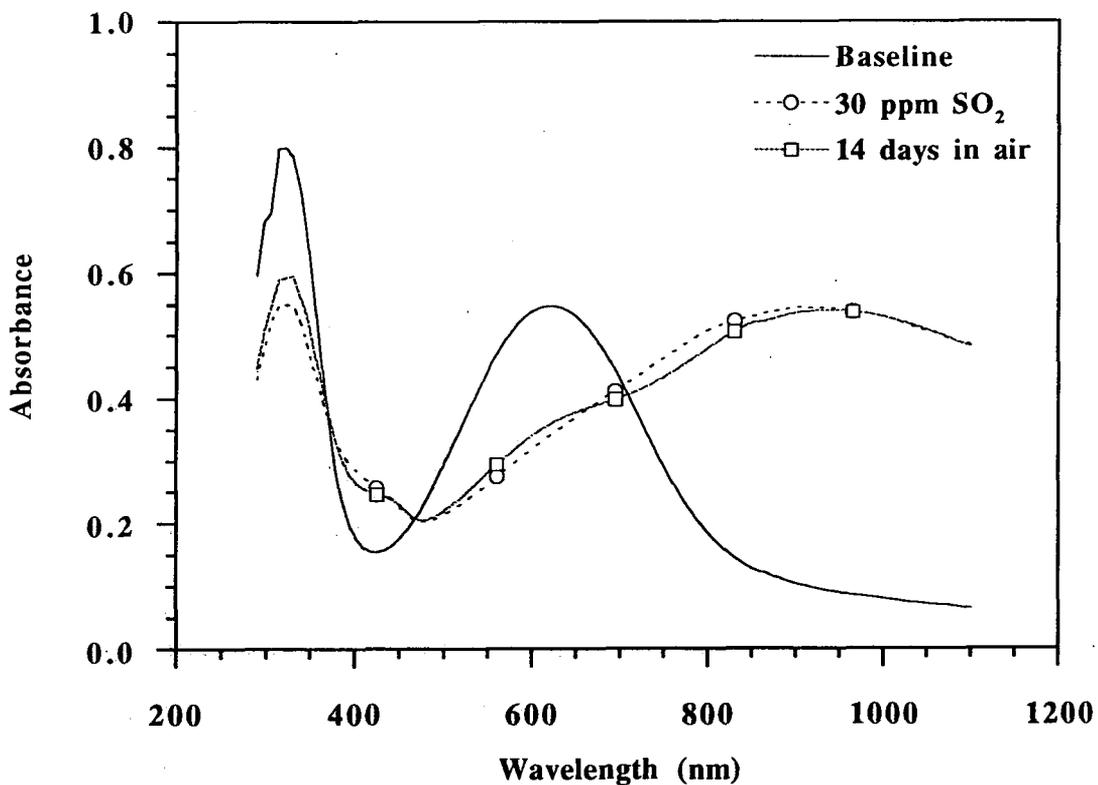
Figure 8.12 UV-visible absorption spectra of a 50 nm thick polyaniline film spin-coated on a glass substrate after 1 hours exposure to 30 ppm SO_2. A second spectrum of the sample after 14 days in an air atmosphere is shown.
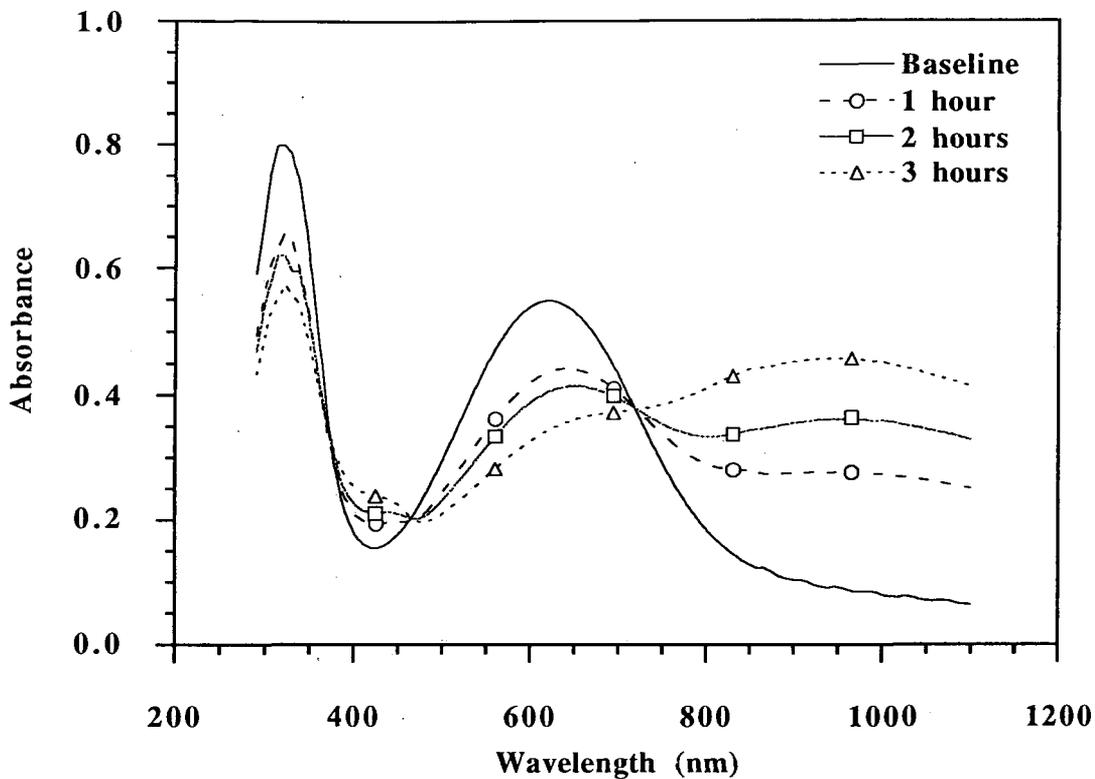
Figure 8.13 UV-visible absorption spectra of a 50 nm thick polyaniline film spin-coated on a glass substrate after exposure to 8 ppm H_2S for 3 hours.
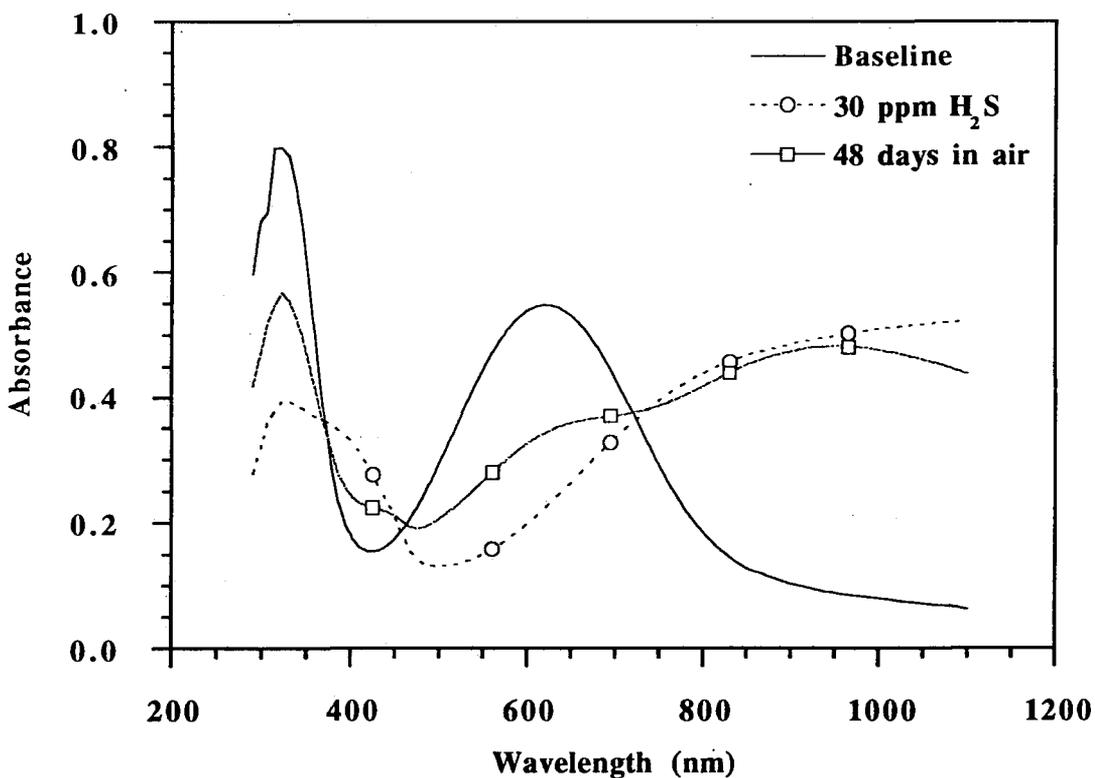
Figure 8.14 UV-visible absorption spectra of a 50 nm thick polyaniline film spin-coated on a glass substrate after 1 hours exposure to 30 ppm H_2S. A second spectrum of the sample after 48 days in an air atmosphere is shown.

The absorption spectra before and after exposure to 30 ppm SO_2 are presented in Figure 8.12. Finally, the equivalent data obtained for H_2S are illustrated in Figure 8.13 (for exposure to 8 ppm H_2S) and Figure 8.14 (for exposure to 30 ppm H_2S). A comparison of the spectra after exposure for one hour to each of the three gases is depicted in Figure 8.15.

From Figure 8.15 it can be seen that exposure for one hour to 8 ppm SO_2 produced the greatest degree of protonation. This is evident from the increase in the absorbance at and above 700 nm, extending into the near-infrared region, together with the appearance of a shoulder at 420 nm. Exposure to 8 ppm H_2S produced the smallest degree of protonation. Isosbestic points (those common to all curves produced in the spectra of a compound taken at several pH values) can be observed at 695 nm and 365 nm.
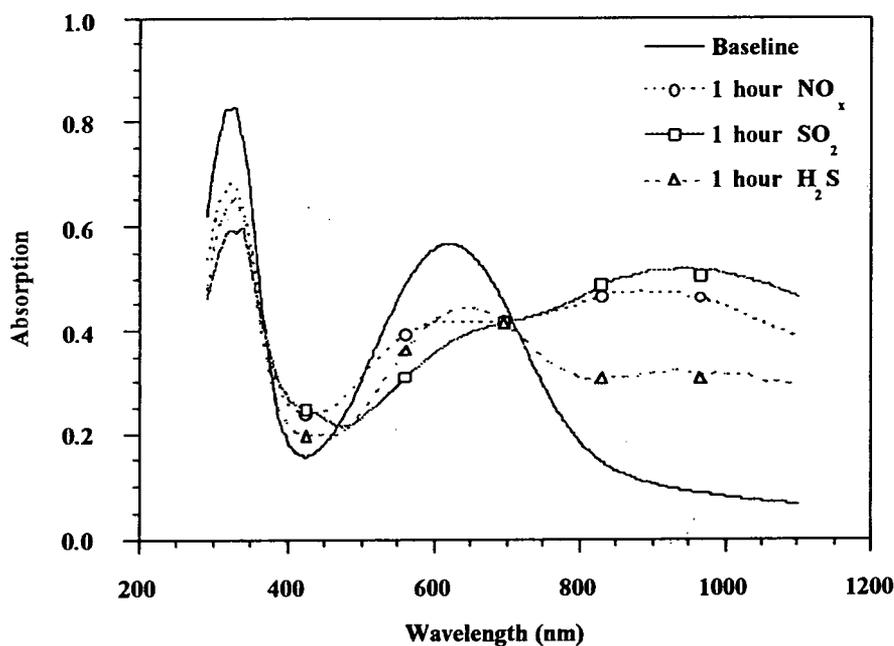
Figure 8.15 A comparison of the UV-visible absorption spectra for 50 nm thick spin-coated films of polyaniline exposed to 8 ppm NO_x, SO_2 and H_2S for one hour. These data have been normalised to the NO_x baseline spectrum.

From the results obtained for the polyaniline/silicon hybrid FET sensor, it may have been expected that NO_x would produce the greatest degree of protonation (i.e. since

the largest increase in the rate of 'turn-on', corresponding to a rise in the conductivity of the polyaniline was demonstrated for this gas). It has been shown though, that the electrical conductivity of polyaniline is not *directly* related to the degree of protonation.[15] This provides an explanation for the greater effect observed after exposure to 8 ppm SO_2 for one hour, compared to 8 ppm NO_x for the equivalent period.

It is known that the UV-visible spectra of polyaniline films for a given protonation state depend on the doping time.[9] In Figure 8.13, three absorption spectra over a three hour exposure to 8 ppm H_2S are presented. It is evident from this figure that the degree of protonation continues to increase over this period. Isosbestic points can be seen at approximately 718 nm and 365 nm. After this three hour exposure conversion to the emeraldine salt form of polyaniline is not complete. In time this would be achieved in the same way as the increase in the rate of 'turn-on' approached a limit after five hours exposure to NO_x (§ 7.1.8). In Figure 8.14 a greater degree of doping has been achieved after just one hours exposure to 30 ppm H_2S. This is entirely expected for a higher concentration of gas.

In Figure's 8.10, 8.12 and 8.14 the spectra after storing the exposed samples in air are presented. The polyaniline films were exposed to 30 ppm NO_x, SO_2 and H_2S, respectively with 16 days, 14 days and 48 days in air before the recovery spectra were recorded. For the samples exposed to NO_x and SO_2, the restoration towards the original baseline spectra is marginal. After 48 days stored in air the sample exposed to H_2S was significantly dedoped, as illustrated by the spectrum shown in Figure 8.14.

It was found that heat treating the samples in air at 80 °C accelerated the dedoping process. Results reported for HCl-doped polyaniline samples undergoing a 12 hour heat treatment process at 180 °C show complete dedoping.[11]

The dedoping for these spectra in air was <u>very</u> slow in comparison to the recovery of the 'turn-on' response for the FET sensors after similar exposures to the gases. This can be explained by the need to record the optical spectra directly after exposure to a gas. This allowed water vapour in the air to react with the absorbed gaseous molecules in the film creating an effect equivalent to acid doping of the polyaniline in aqueous

solutions. In contrast, the recovery of the sensor was monitored without opening the chamber to air, at a relative humidity close to 0%. This permitted the gaseous molecules to be completely desorbed from the polyaniline before exposure to ambient (and generally humid) air.

8.5 CAPACITANCE-VOLTAGE CHARACTERISTICS FOLLOWING EXPOSURE TO GAS

Capacitance-voltage curves (at room temperature) for a 35 μm gate-hole FET with polyaniline deposited are shown in Figure 8.16 (a) and (b). Figure 8.16 (a) illustrates the shift in the curve after exposure to 30 ppm SO_2 for 60 minutes, whilst Figure 8.16 (b) presents the change in the response after exposure to 30 ppm NO_x for an equivalent period. A small voltage shift (of approximately 0.2 V) occurs in the depletion region of both curves as a result of exposure to the gases. A similar shift was <u>not</u> observed for a device with an entirely metallic gate-electrode.

This shift could be the result of the gas modulating the gate-metal/polyaniline work function. Alternatively, if the gas permeates through the insulator to the interface with the semiconductor then the change in the surface potential would also produce the lateral shift observed in the two curves.

For an MOS hydrogen gas sensor with a palladium gate electrode (introduced in Chapter Two, § 2.1.1.2), hydrogen molecules dissociate into atoms on the metal surface. Some of these molecules then dissolve within the metal, a fraction of which are absorbed at the palladium-silicon dioxide interface, where they act as dipoles. The resultant charge layer produces a voltage drop that must be added to the external applied voltage. For n-type silicon, the dipoles attract negative charge to the surface, giving rise to accumulation at zero volts i.e. a capacitance rise which, when extended over the whole curve, corresponds to the observed leftward shift in the C-V characteristic.

A similar experiment exposing a device with an air-gap in the gate electrode to 30 ppm NO_x produced a much smaller shift of the C-V curve. This observation suggests that
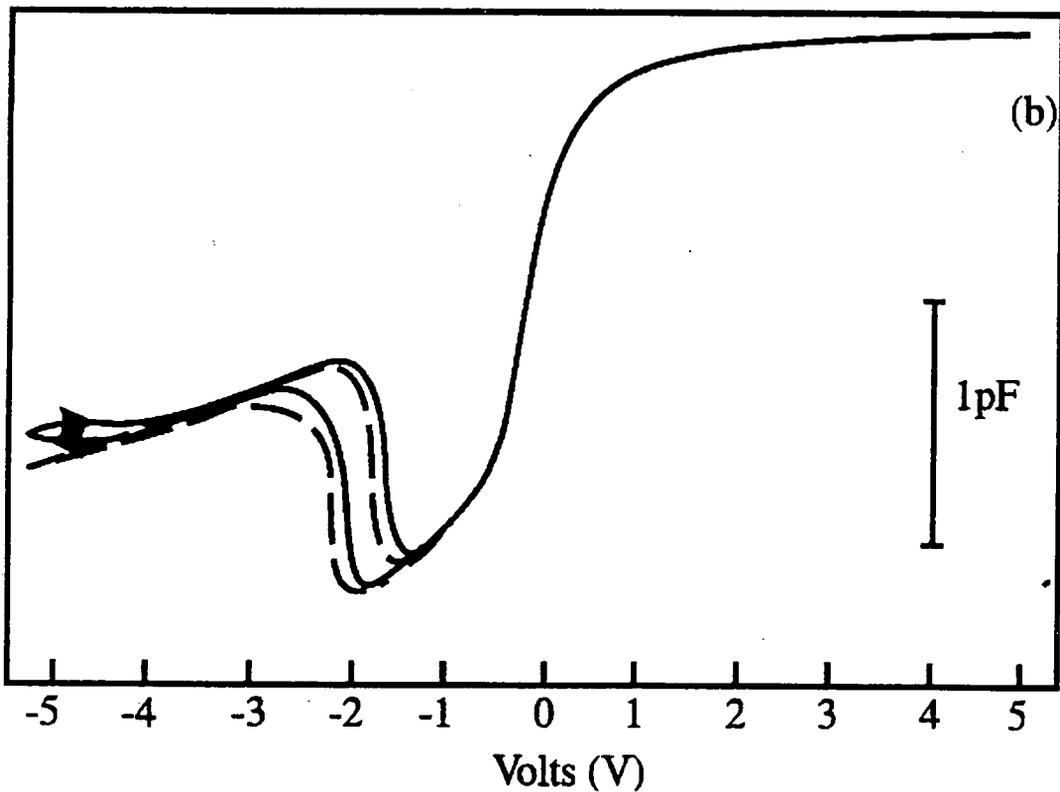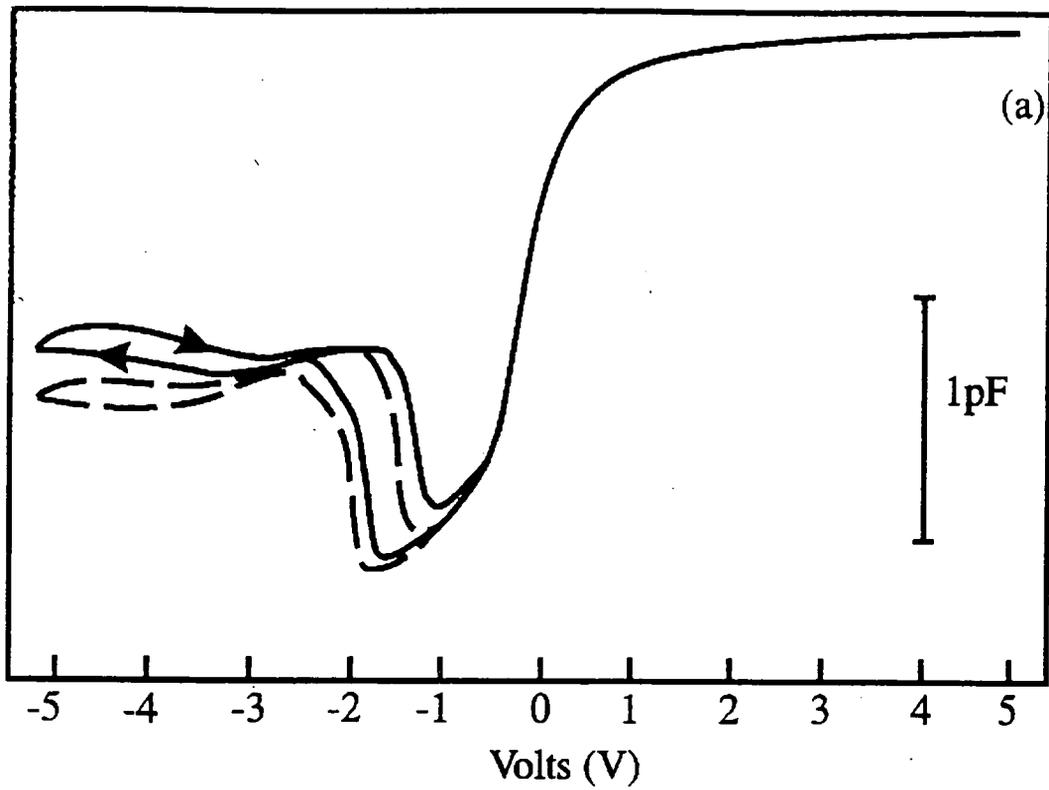
Figure 8.16 Room temperature capacitance-voltage curves for the 35 μm gate-hole FET with polyaniline deposited: (a) before (solid line) and after (dashed line) 60 minutes exposure to 30 ppm SO_2 and (b) before (solid line) and after (dashed line) 60 minutes exposure to 30 ppm NO_x.

the interaction of the gas molecules with the polyaniline film contributes to the change in the C-V response. After purging the system with pure nitrogen gas the original curve (before exposure to a gas) was recorded. Similar recovery times as those for the 'turn-on' response, of up to eight hours were required for this to occur.

8.6 SUMMARY

The results for exposing the polyaniline sensor devices to SO_2 and H_2S have been presented. In comparison to NO_x, the 25 μm gate-hole device was shown to have a lower sensitivity to both of these gases. A detection threshold of 8 ppm SO_2 and 10 ppm H_2S were demonstrated at room temperature. (This compares to a limit of 1 ppm NO_x for an equivalent device.) A sensor incorporating a metal-free phthalocyanine produced no measurable response to either SO_2 or H_2S up to concentrations of 30 ppm. UV-visible spectra of spin-coated films of polyaniline recorded before and after exposure to the three gases were presented. An understanding of the chemical and physical reactions occurring were gained from these results and applied to the response of the sensor. A brief study into the modulation of the capacitance-voltage characteristics after exposure to NO_x and SO_2 illustrated an alternative method for evaluating the sensor response of this hybrid device.

REFERENCES

1. N.E. Agbor, M.C. Petty and A.P. Monkman, *Sensors and Actuators B*, **28** (1995) 173-179.

2. J. Pichlmaier, *Sensors and Actuators B*, **27** (1995) 286-288.

3. N.E. Agbor, Ph.D. Thesis (University of Durham UK) 1993.

4. E.C.W. Clarke and D.N. Glew, *Canadian J. Chem.*, **49** (1971) 691-698.

5. J.A. Barbero, K.G. McCurdy and P.R. Tremaine, *Canadian J. Chem.*, **60** (1982) 1872-1880.

6. G. Sarala Devi, S. Manorama and V.J. Rao, *Sensors and Actuators B*, **28** (1995) 31-37.

7. D. Crouch, S.C. Thorpe, M.J. Cook, I. Chambrier and A.K. Ray, *Sensors and Actuators B*, **19** (1994) 411-414.

8. B. Bott and T.A. Jones, *Sensors and Actuators*, **5** (1984) 43-53.

9. M. Wan and J. Yang, *J. Appl. Polymer Sci.*, **55** (1995) 399-405.

10. A.P. Monkman and P. Adams, *Synth. Met.*, **40** (1991) 87-96.

11. Y Wang and M.F. Rubner, *Synth. Met.*, **47** (1992) 255-266.

12. A.J. Epstein, J.M. Ginder, F. Zuo, R.W. Bigelow, H.S. Woo, D.B. Tanner, A.F. Richter, W.S. Huang and A.G. MacDiarmid, *Synth. Met.*, **18** (1987) 302-309.

13. A.J. Epstein, J.M. Ginder, F. Zuo, H.S. Woo, D.B. Tanner, A.F. Richter, M. Angelopoulos, W.S. Huang and A.G. MacDiarmid, *Synth. Met.*, **21** (1987) 63-70.

14. Y. Cao, P. Smith and A.J. Heeger, *Synth. Met.*, **32** (1989) 263-281.

15. S. Ghosh and V. Kalpagam, *Solid State Ionics*, **60** (1993) 149-152.

CHAPTER NINE

CONCLUSIONS AND SUGGESTIONS FOR FURTHER WORK

9.1 CONCLUSIONS

Incorporating a conductive organic material into the gate electrode of a p-channel field-effect transistor has created a relatively successful gas sensor. One of the major advantages of this device is the amplification of the signal provided by the transistor. The currents measured in this work were in the microampere to milliampere range, compared to the picoamperes measured using a similar material on a simple chemiresistor.[1] This greatly reduces the problems associated with electrical noise. Another significant advantage was the ability to operate the device at room temperature. This removes the requirement for a substantial power source to heat the sensor element, which would limit the portability of a practical device.

The d.c. operating characteristics of the organic/silicon hybrid FET are comparable to those of a standard transistor. A delay observed in the ('turn-on') response of the drain current on application of a gate bias has been shown to be dependent on temperature, humidity and the presence of certain gases. This would not be observed in an entirely metallic device. Exposure to different gaseous ambients changes the conductivity of the organic films. This in turn modulates the rate at which the drain current tends towards saturation and has been demonstrated in this work and elsewhere to be an effective technique for gas sensing.[2,3]

From the array of four devices produced (in which the width of metallisation removed from the gate electrode, of total width 72 µm, varied from 0 µm to 35 µm) the 35 µm gate-hole sensor proved to have the greatest sensitivity to the three gases tested.

The threshold for detection varied from 1 ppm NO_x to 10 ppm H_2S for the polyaniline device. For the 35 µm gate-hole device with phthalocyanine deposited in the air-gap reversible detection of 2 ppm NO_x was realised. Exposure to SO_2 and H_2S up to

concentrations of 30 ppm produced no response, demonstrating a good selective property for this material.

The reversibility of the sensors was complete after exposure to all three gases. The recovery times were approximately eight hours for the polyaniline FET and five hours for the phthalocyanine device. These substantial recovery times represent a significant disadvantage for this device as a practical gas sensor. Raising the operating temperature improved the rate of recovery, though the need for a heating element would increase the overall power consumption of the sensor. Recovery times of existing sensors range from a couple of minutes to over an hour. The chemistry of the sensing material, the operating temperature and the thickness of the film are all factors that influence this process.

In this work the capacity of the gas-tight sample chamber was large in comparison to the flow rate from the gas blender. (The volume of the chamber was ≈ 4.17 litres while the gas blender output was ≈ 0.55 litres min^{-1}.) For this reason purging the chamber with pure nitrogen to expel the test gas took several minutes. If an individual array of sensors (of approximate area 4 mm^2) had been mounted on a substrate in a significantly smaller gas-cell, recovery times may have been substantially reduced.

Experimental results illustrated that both temperature and humidity modulated the 'turn-on' response of the devices. This made it necessary to monitor and control these parameters so that the effects caused by the test gases could be explicitly identified.

More fundamental investigations into the spin-coating and patterning of thin organic films plus the electrical characterisation of the FET arrays with and without organic material deposited were undertaken. A graphical relationship for the dependence of film thickness on spin speed was obtained for a 4% by weight solution of emeraldine base polyaniline. Using ultraviolet/visible optical spectroscopy it was shown that the chemical processing involved in patterning the organic films had no affect on the chemical properties of the material. Capacitance-voltage measurements, the d.c. operating characteristics and the modulation of the threshold voltage all demonstrated that the inclusion of the organic material in the gate electrode influenced the operation of this hybrid device.

9.2 SUGGESTIONS FOR FURTHER WORK

The fundamental results presented in this work show that the organic/silicon hybrid field-effect transistor can be used as a gas sensor. The cross-sensitivity to several gases (including water vapour) and the slow recovery times are the two significant problems to be overcome to create a practical device.

In order to discriminate between various gases, it will be necessary to incorporate organic materials with differing responses (i.e. conductivity changes) into the FET device. We have already shown that the metal-free phthalocyanine 1, 4, 11, 15, 18, 22, 25-octa-hexylphthalocyanine can discriminate 2 ppm NO_x from SO_2 and H_2S at concentrations less than 30 ppm. An alternative to discovering different materials is to chemically modify an existing one. For example, changing the central metal ion and/or the substituted groups on a phthalocyanine compound can alter the chemical response to particular gases.

A further technique for reducing the effect of cross-sensitivity is to use pattern recognition or artificial neural network software. Such systems use adaptive learning algorithms which can be 'trained' to recognise a range of gases or vapours from the electrical outputs of a sensor array. Small variations in the device response can be compensated for by the software, allowing the sensor a greater operating tolerance.

The design of a significantly smaller gas cell and a suitable interface to replace the bulky microprobes could be used to minimise the recovery time of the device. A cell capable of enclosing the 4 mm^2 array could be purged in seconds, compared to the several minutes required for the sample chamber used for this work.

The effects of variable operating temperature could be removed by arranging two devices in the form of a voltage gain amplifier. One device would be screened from the effects of the gas exposure and act as a reference while the other remains active. In such a configuration, the system monitors only changes to the output voltage which can be related to the gas effect. This would require the fabrication of two devices with identical operating characteristics. The controlled deposition of the organic films would be a critical process in achieving this.

REFERENCES

1. N.E. Agbor, M.C. Petty and A.P. Monkman, *Sensors and Actuators B*, **28** (1995) 173-179.

2. S.D. Senturia, J. Rubinstein, S.J. Azoury and D. Adler, *J. Of Appl. Phys.*, **52** (1981) 3663-3670.

3. P.S. Barker, C. Di Bartolomeo, A.P. Monkman, M.C. Petty and R. Pride, *Sensors and Actuators B*, **25** (1995) 451-453.

APPENDIX A

COMPUTER PROGRAMS

All the programs included in this appendix were written in Turbo Pascal. The software was used for aquiring and graphically analysing the 'turn-on' response data.

```
{ ** MENU PROGRAM TO RUN DATA COLLECTION AND DISPLAY SOFTWARE ** }
{                                                                 }
{ FILE NAME : MENU.PAS                                            }
{                                                                 }
{ PURPOSE    : To select the executable software                 }
{                                                                 }
{ REMARK     : Program allows the user to select either the data collection, }
{              the data view, or the data analyse software        }
{                                                                 }
{ LANGUAGE : TURBO PASCAL                                         }

Program menu_dvm;

{$M 65520,0,655360}

uses gpib, Crt, dos, datamanipulate, dvmcontrol, readarrays, graph, gkernel, gdriver;

var
   reply          :char;

begin
 repeat
  clrscr;
  writeln;
  writeln('*****DVM CONTROL MENU*****':48);
  writeln('PRESS ->':250);
  writeln('1. for DATA COLLECTION':115);
  writeln('2. for DATA READ':109);
  writeln('3. for DATA ANALYSE':112);
  writeln('X. to EXIT':103);
  repeat
   reply:= readkey;
  until (reply = '1') or (reply ='2') or (reply='3') or (reply ='x');
  if reply ='1' then dvm_read;
  if reply ='2' then data_display;
  if reply ='3' then data_manip;
 until reply ='x'
end.
```

```
{ FILE NAME : DATAMANI.PAS                                          }
{                                                                   }
{ Purpose   : This program averages two baseline responses          }
{               then calculates the percentage increase compared    }
{               to a third, datafile array. This can be repeated    }
{               multiple times before displaying all the data graphically. }
{                                                                   }
{ Language : Turbo Pascal                                           }
{                                                                   }
{ Author    : P.S. Barker                                           }

unit datamanipulate;

interface

uses gpib,Crt,dos,graph,gkernel,gdriver;

procedure data_manip;

implementation

procedure data_manip;

type
    garry = array[1..200] of integer;
    varry = array[1..200] of real;

var
    res,l,dummy,graphdriver   : integer;
    graphmode,p,q,h,count     : integer;
    scale,pfactor,gfactor     : integer;
    data                      : array[1..200] of lstring;
    result,avbase             : varry;
    delpoint                  : array[1..002] of longint;
    value,array1,array2       : garry;
    name                      : array[1..010] of string[8];
    points,del                : longint;
    filename,fullname         : string;
    f                         : text;
    maxpt                     : real;


Procedure getdata (var value :garry; points,del :longint; filename :string);

{This routine prompts the user to input the names of two baseline responses}
{and one datafile which are loaded into memory in three arrays.}
```

```pascal
var
  f                : text;
  fullname         : string;
  loop,code        : integer;

begin
fullname :='';
fullname :='c:\pascal\data\'+filename+'.dat';
assign (f,fullname);
reset(f);
readln(f,delpoint[1]);
del:= delpoint[1];
readln(f,delpoint[2]);
points:= delpoint[2];
for loop:= 1 to (points*2) do
 readln(f,data[loop]);
close(f);
writeln;
writeln('Number of data points sampled := ',points);
writeln('Delay between sample points   := ',del);
writeln;
for loop:=1 to (points*2) do
 begin
  data[loop]:= copy(data[loop],3,4);    { Extracts the 4 digits from the data }
  val (data[loop],value[loop],code);    { Converts to integer format }
  value[loop]:=round(value[loop]*(1000/(10*res)));
 end;
end;                       { END of procedure }
```

{*********************Graph Axis Drawing Routine*********************}

```pascal
Procedure graphdraw (var filename :string; del :longint);

var
  sec        :real;
  a          :integer;
  time,num   :string;

begin
 settextstyle (2,0,4);
 setviewport(0,0,640,400,clipon);
 setcolor (15);
 setbkcolor (0);
 textcolor (15);
 window (1,1,80,25);
 moveto (60,330);                { Draws x-axis }
 lineto (600,330);
 outtextxy (283,360,'Time (sec)');    { Label x-axis }
 sec :=((del/1250)*10);
```

```pascal
  for a:=0 to 10 do
   begin
    moveto ((50*a+60),332);          { Draw x-axis ticks }
    lineto ((50*a+60),328);
    str ((a*sec):2:2,time);
    outtextxy ((50*a+50),335,time);   { X-scale numbers }
   end;
  outtextxy (510,368,'* AUTOSCALE (Y/N) *');  { Gives user the choice of      }
  if readkey ='n' then begin                   { having the graph autoscaled   }
   scale:=7;                                    { to optimise the screen dipslay. }
   gfactor:=40;
   pfactor:=4;
  end
  else begin                      ʒ
   scale:= trunc(maxpt/10)+1;
   gfactor:= trunc(300/scale);
   pfactor:= trunc(300/(scale*10));
  end;
  moveto (60,330);                 { Draws y-axis }
  lineto (60,20);
  for a:= 0 to scale do
   begin                           { Draws y-axis ticks }
    moveto (58,(330-(gfactor*a)));
    lineto (62,(330-(gfactor*a)));
    str ((a*10),num);
    outtextxy (40,(330-(gfactor*a)-5),num);  { Y-scale numbers }
   end;
  settextstyle (2,1,4);
  outtextxy (25,160,'% Change');    { Label y-axis }
 end;


{************************Graph Plotting Routine********************}

Procedure graphplot (var points :longint; result :varry);

var
  x,b      :integer;

begin
 x:=0;
 for b:= 1 to (points*2) do
  begin
   x:=x+1;                     { Plots data on graph }
   if result[b]= -999 then
    x:=x-1
   else putpixel ((60+(x*5)),(330-round(result[b]*pfactor)),(16-h));
  end;
 setcolor(16-h);
 textcolor (16-h);
```

```pascal
      settextstyle (2,0,4);
      outtextxy ((h*60),368,filename);      { Labels the graph with filename }
    end;
```

{************************Read in Three Data Files************************}

```pascal
Procedure filegrab;

var l  :integer;

  begin
  clrscr;
  write('Enter the FIRST Baseline file for averaging: ');
  readln(filename);
  getdata (value,points,del,filename);
  points:=delpoint[2];
  del:=delpoint[1];
  for l:= 1 to (points*2) do
   array1[l]:= value[l];
  write('Enter the SECOND Baseline file for averaging: ');
  readln(filename);
  getdata (value,points,del,filename);
  for l:= 1 to (points*2) do
   array2[l]:= value[l];
  for l:= 1 to (points*2) do
   begin
    if ((array1[l] <> 0) and (array2[l] <> 0)) then
     avbase[l]:=((array1[l]+array2[l])/2)
    else avbase[l]:= 0;
   end;
  write ('Enter the DATA filename: ');
  readln(filename);
  getdata (value,points,del,filename);
  for l:= 1 to (points*2) do
   array1[l]:= value[l];
 end;
```

{********************Calculate Drain-Source Current********************}

```pascal
Procedure draincalc;

{ This routine calculates the percentage change of the datafile to the }
{ averaged baseline responses; storing the result in a text array.      }

var l  :integer;

 begin
 for l:= 1 to (points*2) do
  begin
```

```pascal
   if ((array1[l] <> 0) and (avbase[l] <> 0)) then
    result[l]:= (((array1[l]-avbase[l])/avbase[l])*100)
    else result[l]:= -999;
    str(result[l]:3:2,data[l]);
    if result[l]>maxpt then
     maxpt:=result[l]
   end;
   if maxpt>100 then
    maxpt:=100;
   writeln('Press <RETURN> to display data');
   repeat
   until readkey <> '';
  end;
```

{***********************Data Display Routine**************************}

```pascal
Procedure display;

var p,q   :integer;

{ This routine outputs the calculated % changes in a 10 x 10 format }

begin
 l:=round((points/10)-1);
 graphdriver:=detect;
 initgraph (graphdriver,graphmode,' ');
 settextstyle (2,0,5);
 for p:=0 to l do
  for q:=1 to 20 do
   if result[((p*20)+q)] <> -999 then
    outtextxy ((p*60),(q*16),data[((p*20)+q)]+'%')
    else dummy:=q;
 settextstyle (0,0,1);
 outtextxy(10,370,'** Press any key to read in more data/display a graph of the data **');
 repeat
 until readkey <> '';
 closegraph;
end;
```

{***********************Save Result Array to disk**********************}

```pascal
Procedure saveresult;

var l :integer;

begin
 fullname:='c:\pascal\data\'+filename+'.res';
 assign(f,fullname);
 rewrite(f);
```

```pascal
  writeln(f,delpoint[1]);
  writeln(f,delpoint[2]);
  for l:= 1 to (points*2) do
   writeln (f,result[l]);
  close(f);
 end;
```

{*********************Read in Result Array*****************************}

```pascal
Procedure readresult;

var l   :integer;
 begin
  fullname:='';
  fullname:='c:\pascal\data\'+filename+'.res';
  assign(f,fullname);
  reset(f);
  readln(f,delpoint[1]);
  del:=delpoint[1];
  readln(f,delpoint[2]);
  points:=delpoint[2];
  for l:=1 to (points*2) do
   readln(f,result[l]);
  close(f);
 end;
```

{*************************MAIN PROGRAM************************}

```pascal
begin
 res:=0555;                 { Defines the value of load resistance }
 count:=0;
 maxpt:=00;
 repeat
 begin
  count:=count+1;
  filegrab;
  name[count] :=filename;
  draincalc;
  display;
  saveresult;
  writeln;
  writeln('Press "Y" to analyse more data OR "N" to plot results.');
 end;
 until readkey ='n';
 graphdriver:=detect;
 initgraph (graphdriver,graphmode,'');
 repeat
 clearviewport;
 graphdraw(filename,del);
```

```pascal
  for h:=1 to count do
   begin
    filename:=name[h];
    readresult;
    graphplot(points,result);
   end;
  textcolor (15);
  setcolor (15);
  outtextxy (510,385,'* REPLOT DATA (Y/N) *');
 until readkey ='n';
 closegraph;
 end;
end.
```

```
{********* DVM CONTROL PROGRAM WRITTEN BY P.S. BARKER *********}
{                                                              }
{ FILE NAME : PSB_DVM.PAS                                      }
{                                                              }
{ PURPOSE    : This program triggers the voltmeter to take a series of voltage }
{              measurements.                                   }
{                                                              }
{ REMARK     : The program is written for the HP3437A DVM.     }
{              Refer to the operating manual for IEEE device control commands }
{              when modifying this program.                    }
{                                                              }
{ LANGUAGE : TURBO PASCAL                                      }

unit dvmcontrol;

interface

 uses gpib, Crt, dos;

 procedure dvm_read;

implementation

procedure dvm_read;
var
   ioerr: integer;


   procedure iochk;                         {  I/O error check routine  }

begin
  case ioerr of
   0 : ;
   1 : writeln('TIME OUT !!');
   else
      writeln('INTERFACE ERROR !!');
  end;
end;                                        { End of iochk }

var
  cmdstr,instr1            : lstring;
  i,s,dvm1,loop,points     : integer;
  data                     : array [1..200] of lstring;
  delpoint                 : array [1..002] of longint;
  f                        : text;
  fullname,filename        : string;
  hour,minute,second,sec100 : word;
  deloop,endloop,del       : longint;
  newdel                   : real;
```

```
begin
 clrscr;
 ioerr:=ieabort;
 dvm1:=24;
 writeln('Enter the integer value for the required frequency of readings,');
 write('[125 = 1 sample per 100ms : 1250 = 1 sample per second.] :- ');
 readln(del);
 delpoint[1] := del;                               { Stores info of sample rate }
 if del < 65535 then endloop :=1 else
  begin
   newdel :=(del/10);
   endloop :=10;
   del :=round (newdel)
  end;
 writeln;
 write('Enter the number of data points to be sampled, [1-100] :- ');
 readln(points);
 writeln;
 delpoint[2] := points;                            { and number of sample points }

 { **Set the DVM** }

 cmdstr:='DCL';
 ioerr:=ieoutput(dvm1,cmdstr);                     { Clear device to turn-on state }
 iochk;                                            { Error check }
 cmdstr:='F1T2R1N1S';
 ioerr:=ieoutput(dvm1,cmdstr);                     { Send DVM #1 setting string }
 iochk;                                            { Error check }
 repeat
  s:=iespoll(dvm1);                                { Wait for external trigger }
 until s>0;

 { **Measurement Start** }

 cmdstr:='UNL UNT MTA LISTEN 24 GET';
 gettime(hour,minute,second,sec100);
 writeln('Start time (Hour:min:sec.100sec)= ',hour,':',minute,':',second,'.',sec100);
 writeln;
 for i:=1 to points do
 begin
  for deloop :=1 to endloop do
   begin
    delay(del)
   end;
  ioerr:=iesend(cmdstr);                           { Trigger the DVM }
  instr1:='            ';
  ioerr:=ieenter(dvm1,instr1);                     { Enter DVM #1 reading }
  iochk;                                           { Error check }
```

```pascal
    data[i] := instr1;
    write('*');
  end;

  gettime(hour,minute,second,sec100);
  writeln;
  writeln('End time   (Hour:min:sec.100sec)= ',hour,':',minute,':',second,'.',sec100);
  writeln;
  writeln('Press <RETURN> to display data');
  repeat
  until readkey <>'';


{ **Routine to output data stored in 'data' array** }

for i:=1 to points do
begin
  write(data[i],' ');
end;

{ **Routine to store data in array on to hard drive** }

writeln;
writeln('Enter filename data should be saved under...');
readln(filename);
fullname := 'c:\pascal\data\'+filename+'.dat';
assign(f,fullname);
rewrite(f);
writeln(f,delpoint[1]);
writeln(f,delpoint[2]);
for loop :=1 to points do
  writeln(f,data[loop]);
close(f);
writeln;
writeln('The data has been saved in ',filename);
writeln;
writeln('** Press any key to return to MENU **');
repeat
until readkey <> '';
 end;
end.
```

```
{ FILE NAME : READVALU.PAS                                                   }
{                                                                            }
{ Purpose   : This program reads and displays data, both graphically and in tabular   }
{             form, from disc, taken from CFT turn-on characteristic.        }
{                                                                            }
{ Language : TURBO PASCAL                                                    }
{                                                                            }
{ Author    : P.S. Barker                                                    }

unit readarrays;

interface

uses gpib,Crt,dos,graph,gkernel,gdriver;

procedure data_display;

implementation

procedure data_display;

var
   code,res,count                       : integer;
   dummy,loop,graphdriver,graphmode     : integer;
   f                                    : text;
   data                                 : array[1..200] of lstring;
   delpoint                             : array[1..002] of longint;
   value                                : array[1..200] of integer;
   name                                 : array[1..010] of string[8];
   fullname,filename,num,time           : string;
   ymax,x,y,ytitle,maxvalue             : integer;
   factor,step,scale,del,points         : longint;
   sec                                  : real;


{ ***********************Routine to Load Data + Calculate I_{ds}***************}

Procedure grabdata;

var l :integer;

begin
  write('Enter filename of data array to read: ');
  readln(filename);
  fullname :='c:\pascal\data\'+filename+'.dat';
  assign(f,fullname);
  reset(f);
```

```
    readln(f,delpoint[1]);
    del:= delpoint[1];
    readln(f,delpoint[2]);
    points:= delpoint[2];
    for l:=1 to 200 do                          { Reads the data from the hard drive }
     readln(f,data[l]);
    close(f);
    writeln;
    writeln('Data successfully retrieved from file.');
    writeln;
    writeln('Number of data points sampled := ',points);
    writeln('Delay between sample points   := ',del);
    writeln;
    for l:=1 to (points*2) do
     begin
     data[l]:= copy(data[l],3,4);               { Extracts the 4 digits from the data }
     val (data[l],value[l],code);               { Converts to integer format }
     value[l]:=round((value[l])*(1000/(10*res)));
     if value[l]>maxvalue then
      maxvalue :=value[l];
     str(value[l],data[l]);                     { Converts back to string format }
     end;
    end;


{******************Routine to Display Data in a 10 x 10 Grid****************}

Procedure datadisplay;

var p,q   :integer;

 begin
 loop:=round((points/10)-1);
 graphdriver:=detect;                           { Routine to display the data in ten  }
 initgraph (graphdriver,graphmode,'');          { columns of ten data items          }
 settextstyle (2,0,5);
 for p:=0 to (loop) do
  for q:=1 to 20 do
   if value[((p*20)+q)] <> 0 then
    outtextxy((p*60),(q*16),'-'+data[((p*20)+q)]+'uA')
   else
    dummy:=q;
 settextstyle (0,0,1);
 outtextxy(10,370,'** Press any key to read in more data/display a graph of the data **');
 repeat
 until readkey <> '';
 closegraph;
end;
```

{********************* Graph Axis Drawing Routine *********************}

Procedure graphaxis (var maxvalue :integer);

var l :integer;

```
begin
 graphdriver:=detect;
 initgraph (graphdriver,graphmode,");
 settextstyle (2,0,4);
 setviewport (0,0,630,400,clipon);
 setcolor (15);
 setbkcolor (0);
 textcolor (15);
 rectangle (5,5,630,380);
 window (1,1,80,25);
 moveto (60,330);                          { Draws x-axis }
 lineto (600,330);
 outtextxy (283,360,'Time (sec)');         { Label x-axis }
 sec :=((del/1250)*10);
 for l:=0 to 10 do
  begin
   moveto ((50*l+60),332);                 { Draws x-axis ticks }
   lineto ((50*l+60),328);
   str ((l*sec):2:2,time);
   outtextxy ((50*l+50),335,time);         { X-scale number }
  end;
 ymax :=maxvalue;                          { Scales y-axis data }
 factor := trunc(300/ymax);
 scale :=trunc(ymax/10);
 step :=(scale*factor);
 moveto (60,330);                          { Draws y-axis }
 lineto (60,(320-(step*11)));
 for l:= 0 to 11 do
  begin                                    { Draws y-axis ticks }
   moveto (58,(330-step*l));
   lineto (62,(330-step*l));
   str ((l*scale),num);                    { Y-scale numbers }
   outtextxy (40,(330-(step*l)-5),num);
  end;
 settextstyle (2,1,4);
 ytitle :=trunc(330-(((step*11)+10)/2)-22);  { Calculates point to label }
 outtextxy (25,ytitle,'-Ids (uA)');
end;
```

```
{**********************Graph Point Plotting Routine******************}

Procedure pointplot (var p :integer);

var l  :integer;

 begin
  x:=0;
  for l:= 1 to (points*2) do
   begin
    x:=x+1;
    if trunc(l/2)*2 <> l then
     putpixel ((60+(x*5)),(330-(value[l]*factor)),(16-p))     { Plots points }
    else
     x:=x-1;
   end;
  settextstyle (2,0,4);
  setcolor(16-p);
  textcolor(16-p);
  outtextxy((p*50),368,filename);                    { Labels graph with filename }
 end;

{********************Read in Value Array*************************}

Procedure readvalue;

var l :integer;
 begin
  fullname:='';
  fullname:='c:\pascal\data\'+filename+'.val';
  assign(f,fullname);
  reset(f);
  readln(f,delpoint[1]);
  del:=delpoint[1];
  readln(f,delpoint[2]);
  points:=delpoint[2];
  for l:=1 to (points*2) do
   readln(f,value[l]);
 end;

{********************Save Value Array to Disk*******************}

Procedure savevalue;

var l  :integer;

 begin
  fullname:='c:\pascal\data\'+filename+'.val';
  assign(f,fullname);
```

```pascal
  rewrite(f);
  writeln(f,delpoint[1]);
  writeln(f,delpoint[2]);
  for l:=1 to (points*2) do
   writeln (f,value[l]);
  close(f);
 end;


{*************************Main Program****************************}

var p   :integer;

begin
 res:=0555;                                    { Defines value of load resistance   }
 x:=0;
 maxvalue:=0;
 count:=0;
 ClrScr;
 repeat
  begin
   count:=count+1;
   grabdata;
   name[count] :=filename;
   writeln(' Press <RETURN> to display data');
   repeat
   until readkey <> '';
   datadisplay;
   savevalue;
   writeln;
   writeln('Press "Y" to analyse more data OR "N" to plot out results.');
  end;
 until readkey='n';
 graphaxis(maxvalue);
 for p:=1 to count do
  begin
   filename:=name[p];
   readvalue;
   pointplot(p);
  end;
 setcolor(15);
 textcolor(15);
 outtextxy (180,385,'** Press any key to return to the MENU **');
  repeat
  until readkey <> '';
  closegraph;
 end;
end.
```

APPENDIX B

PUBLICATIONS

"A photolithographic technique for patterning spin-coated polyaniline films", C. Di Bartolomeo, P.S. Barker, M.C. Petty, P. Adams and A.P. Monkman, *Advanced Materials for Optics and Electronics*, **2** (1993), pp. 233-236.

"Vapour recognition using organic films and artificial neural networks", P.S. Barker, J.R. Chen, N.E. Agbor, A.P. Monkman, P. Mars and M.C. Petty, *Sensors and Actuators B*, **17** (1994), pp. 143-147.

"Gas sensing using a charge-flow transistor", P.S. Barker, C. Di Bartolomeo, A.P. Monkman, M.C. Petty and R. Pride, *Sensors and Actuators B*, **24-25** (1995), pp. 451-453.

"A hybrid phthalocyanine/silicon field-effect transistor sensor for NO_2", P.S. Barker, M.C. Petty, A.P. Monkman, J. McMurdo, M.J. Cook and R. Pride, *Thin Solid Films*, in press.

"Electrical characteristics of a polyaniline/silicon hybrid field-effect transistor gas sensor", P.S. Barker, A.P. Monkman, M.C. Petty and R. Pride, *IEE Proceedings: Circuits, Devices and Systems*, in press.

"A polyaniline/silicon hybrid field effect transistor humidity sensor", P.S. Barker, A.P. Monkman, M.C. Petty and R. Pride, *Synthetic Metals*, in press.